

Doctoral Dissertation

Tailoring the microporous structure of a ceramic composite for development of molecular sieving membranes

(セラミック複合物のマイクロポラス制御による分子ふるい膜の開発)

Sulaiman Oladipo Lawal

**Department of Chemical Engineering,
Graduate School of Engineering, Hiroshima University**

(広島大学 大学院工学研究科 化学工学専攻)

September 2021

Abstract of this dissertation

In this thesis, organic coordination/complexation ligands have been applied to the modification of a SiO₂-ZrO₂ ceramic composite. The various sections seek to deepen the understanding and access further opportunities offered by organic coordination/complexation ligands modification of ceramic composite membranes.

First, the chemical modification of SiO₂-ZrO₂ via the sol-gel method was successfully accomplished by chelating acetylacetonate (acac⁻) with zirconium tetrabutoxide (ZrTB) prior to co-hydrolysis and condensation with tetraethoxysilane (TEOS), which was then used to fabricate a gas separation layer. The acac⁻-modified SiO₂-ZrO₂-derived membrane showed a high H₂ permeance of $9.9 \times 10^{-7} \text{ mol m}^{-2} \text{ s}^{-1} \text{ Pa}^{-1}$ with a H₂/SF₆ permeance ratio of 7,600, which was better than the results when using a pure SiO₂-ZrO₂-derived membrane (H₂ permeance: $1.4 \times 10^{-6} \text{ mol m}^{-2} \text{ s}^{-1} \text{ Pa}^{-1}$, H₂/SF₆ permeance ratio: 11).

In the next phase, the microstructural control of ligand-modified SiO₂-ZrO₂ composite membranes was attempted. Hybrid materials with crosslinking between the organic moieties were made by utilizing network forming Si precursor and chelating ligands. The effects of using a network-forming and network-modifying ligand were studied. Gas permeation experiments showed that the organic crosslink-derived membranes possess molecular sieving properties (H₂ permeance: $\approx 10^{-7} \text{ mol m}^{-2} \text{ s}^{-1} \text{ Pa}^{-1}$; H₂/N₂ selectivity: $\approx 20-30$) that are superior to those of non-crosslink-derived membranes (H₂ permeance: $\approx 10^{-7} \text{ mol m}^{-2} \text{ s}^{-1} \text{ Pa}^{-1}$; H₂/N₂ selectivity: $\approx 7-11$).

Furthermore, the preparation of a carbonized SiO₂-ZrO₂ composite membrane was studied. The sol synthesis of the precursor SiO₂-ZrO₂-acetylacetonate composite was optimized by studying the effect of water/alkoxide molar ratio and relative Si/Zr atomic ratio on the final carbon-SiO₂-ZrO₂ properties. A combination of SiO₂ and ZrO₂ in a ratio of 9/1 in a carbon-SiO₂-ZrO₂ membrane showed an H₂ permeance of $16 \times 10^{-7} \text{ mol m}^{-2} \text{ s}^{-1} \text{ Pa}^{-1}$ over a similarly pore-distributed unmodified SiO₂-ZrO₂ membrane with an H₂ permeance of $3 \times 10^{-7} \text{ mol m}^{-2} \text{ s}^{-1} \text{ Pa}^{-1}$. More interestingly, a combination of SiO₂ and ZrO₂ in a ratio of 5/5 displayed a unique pressure-induced CO₂ flow switching behaviour.

The various modification techniques offered more insights for molecular separations.

TABLE OF CONTENTS

	Page
Chapter 1	
General introduction	
1.1 A brief background on membranes	1
1.1.1 Synthetic membranes	1
1.1.2 Gas separation membranes	4
1.1.3 Gas separation mechanisms through membranes	4
1.1.3.1 Bulk fluid flow	5
1.1.3.2 Knudsen flow	5
1.1.3.3 Surface diffusion	6
1.1.3.4 Gas translational diffusion	6
1.1.3.5 Solid-state diffusion	6
1.1.4 Classification of gas separation membranes	7
1.1.4.1 Classification by membrane material	8
1.1.4.2 Classification by physical configuration	10
1.1.4.3 Classification by material composition	11
1.2 Silica and composite matrix ceramic membranes	15
1.2.1 State of the art of ceramic composite materials and membranes	18
1.2.2 Organic coordination ligands: a broad field of opportunities	20
1.2.2.1 Coordination ligands	20
1.2.2.2 Organic coordination ligands as molecular engineering agents	21
1.2.3 Ligand-modified ceramic composite membranes	23
1.3 The scope and outline of this thesis	25
Cited literature	29
Chapter 2	
Development of a molecular sieving membrane from an acetylacetonate-modified silica-zirconia ceramic composite	
2.1 Introduction	43
2.2 Experimental	46

2.3.1	Preparation of SiO ₂ -ZrO ₂ -acac ₂ sol and membrane fabrication	46
2.3.2	Characterizations of the SiO ₂ -ZrO ₂ -acac ₂ , the SiO ₂ -ZrO ₂ sol, the gel, and the membranes	48
2.3.3	Single-gas permeation measurements	48
2.3	Results and discussion	49
2.3.1	Sol-gel characterization	49
2.3.1.1	Chemical modification of a ZrTB precursor	49
2.3.1.2	Thermal analysis of acac ⁻ ligands in SiO ₂ -ZrO ₂ -acac ₂ gels	51
2.3.2	Effect of acetylacetonate ligands on the pore size controllability of SiO ₂ -ZrO ₂ (1:1) membranes	54
2.3.3	Heat-treatment effect on pore size and gas permeation properties of SiO ₂ -ZrO ₂ -acac ₂ membranes	58
2.4	Conclusions	66
	Cited literature	67

Chapter 3

Microstructure engineering of ligand-modified silica-zirconia membranes derived from network-forming precursors

3.1	Introduction	72
3.2	Experimental	75
3.2.1	Preparation of MAPTMS-SZ-LIGAND sols, powders, and films	76
3.2.1.1	Fabrication of MAPTMS-SZ-AAA and MAPTMS-SZ-ACAC membranes	77
3.2.2	Evaluation of gas permeation through membranes	78
3.3	Results and discussion	78
3.3.1	Evolution of organic cross-linking units via thermal radical polymerization	78
3.3.1.1	Facile control of particle size distribution and heterogeneity in sols	78
3.3.1.2	Microstructural evolution of organically cross-linked materials	80
3.3.2	Thermal stabilities and decomposition mechanisms: effect of organic crosslinking	85

3.3.3 Membranes fabricated from cross-linked hybrids and gas permeation analysis	89
3.3.3.1 Morphologies of supported membranes	89
3.3.3.2 Gas sieving properties at 200 °C and membrane microstructures	91
3.3.3.3 Analysis of microporous structures via the gas permeance ratio and activation energy	96
3.4 Conclusions	101
Cited literature	102

Chapter 4

Enhanced H₂-permselectivity in a carbon-silica-zirconia membrane derived from an acetylacetonate-ceramic composite pyrolysis

4.1 Introduction	108
4.2 Experimental	111
4.2.1 Materials preparation by sol-gel	111
4.2.2 Preparation of membrane separation layers	112
4.2.3 Material characterizations	112
4.3 Results and discussion	113
4.3.1 Control and optimization of ligand chelation degree via hydrolysis	113
4.3.1.1 Characterization of sols, films, and powders before carbonization	113
4.3.1.2 Characterization after carbonization	119
4.3.2 Microstructural transformation between SiO ₂ -ZrO ₂ -ACAC and Carbon-SiO ₂ -ZrO ₂ : effect of Si/Zr ratio	121
4.3.3 Carbonization-enhanced H ₂ -permselectivity in a SiO ₂ -ZrO ₂ composite membrane	128
4.4 Conclusions	132
Cited literature	133

Chapter 5

CO₂ flow-switching behaviour in a pyrolysis-derived carbon-silica-zirconia membrane promises a versatile high-temperature H₂/CO₂ separation

5.1 Introduction	138
-------------------------	------------

5.2	Experimental	141
5.2.1	Preparation and pyrolysis of SiO ₂ -ZrO ₂ -acac powder and C-SiO ₂ -ZrO ₂ membrane fabrication	141
5.2.2	Characterization of materials	142
5.2.3	Gas permeation measurement	143
5.3	Results and discussion	144
5.3.1	Carbonization of SiO ₂ -ZrO ₂ -acac into C-SiO ₂ -ZrO ₂ and identification of the carbon state	144
5.3.2	Unique permeation properties of CO ₂ in C-SiO ₂ -ZrO ₂ membranes	148
5.3.2.1	Understanding the interaction between CO ₂ and C-SiO ₂ -ZrO ₂	148
5.3.2.2	Pressure-induced transition of CO ₂ flow in C-SiO ₂ -ZrO ₂ membranes	151
5.3.3	Binary H ₂ /CO ₂ mixture separation performance of a C-SiO ₂ -ZrO ₂ -derived membrane	156
5.3.3.1	Effects of temperature, pressure, and CO ₂ feed mole fraction on the binary mixture separation performance	156
5.3.4	Outlook on the practical application of a C-SiO ₂ -ZrO ₂ membrane for H ₂ /CO ₂ separation	159
5.4	Conclusions	161
	Cited literature	162

Chapter 6

Conclusions and considerations for further studies

6.1	Summary and conclusions	168
6.2	Considerations for further studies	170

List of publications	173
-----------------------------	-----

Acknowledgements	175
-------------------------	-----

Chapter 1

General introduction

1.1 A brief background on membranes

The separation, concentration and purification of material mixtures is a major challenge facing industries such as chemical, petrochemical, petroleum, textile, food, and pharmaceutical industries [1]. For this reason, several separation techniques have been developed over the years for different applications. Such processes include distillation, adsorption, absorption, extraction, crystallization, cryogenic separation etc. In recent decades however, a growing attention and shift towards a new separation technique, membrane processes and membrane separation, has occurred [2]. This is because membranes provide a simple, cost effective and energy efficient alternative to the state-of-the-art techniques [3, 4].

A membrane in the general sense refers to a ‘thin’, selectively permeable, or semi-permeable barrier or boundary that allows some material species such as molecules, ions, or other similarly sized particles to pass through it and prevents the passage of others. Membranes are abundantly found in nature as part of our daily lives and are referred to as biological membranes [2]. The basic function of a biological membrane in biological systems is to define boundaries between and within cellular components. This ability to separate between components and allowing communication between them by a tightly regulated transport of materials make many cellular processes possible [5]. These biological membranes served as model systems that inspired the research into synthetic membranes [5]. Perhaps the first recorded study of a synthetic membrane inspired by pig’s bladder was in an ethanol-water mixture by A. Nollet in 1752 [6]. Thereafter, T. Graham in 1866 studied the diffusion of gases in a synthetic rubber membrane [7].

1.1.1 Synthetic membranes

A synthetic membrane, therefore, is a permeable or semi-permeable phase such as a polymer, inorganic material or metal fabricated as a selective or contacting barrier to control the relative transport of matter (such as gases, vapors, liquids, or a mixture of these) and energy through itself [2, 8]. Separation membranes serve as a third phase

creating a barrier between two bulk phases. The aim of membrane processes is to concentrate a component into a phase by mass transport into another phase through the permeable barrier as illustrated by Fig. 1-1 [9]. Mass transport is achieved by several driving forces of which pressure driving force is the most easily and economically applied to achieve global impact [10]. This broad definition of a membrane and the membrane process gives rise to a very wide application of membranes as shown in Table 1-1.

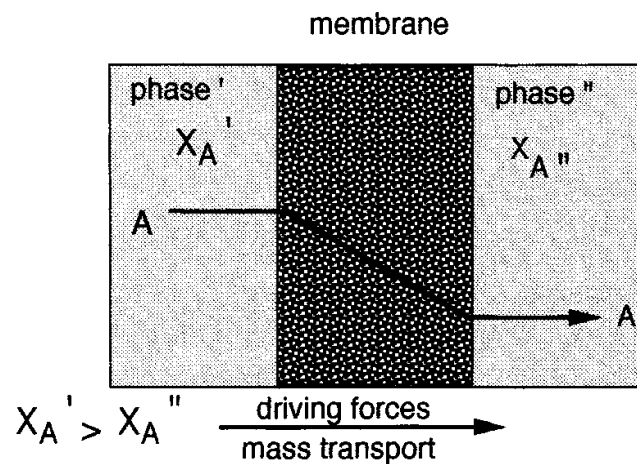


Fig. 1-1 Mass transport through a synthetic membrane [9]

From all the membrane separation processes listed in Table 1-1, perhaps one of the most important application of membranes is in the separation of gas mixtures [9, 11]. Table 1-2 lists the different membrane processes against their respective yearly growth in industrial sales. From these processes, gas separation shows the highest yearly growth of 15% [9].

Table 1-1 Types of synthetic membrane processes and applications [8, 10]

Membrane process	Driving force	Application(s)
Microfiltration (MF)	Transmembrane pressure difference	Clarification, sterile filtration
Ultrafiltration (UF)	Transmembrane pressure difference	Separation of macromolecular solutions
Dialysis (D)	Transmembrane conc. difference	Separation of macromolecular solutions and micro-solutes
Nanofiltration (NF)	Transmembrane pressure difference	Separation of small organic compounds and salt solutions
Reverse Osmosis (RO)	Transmembrane pressure difference	Separation of micro-solutes and salt solutions
Pervaporation (PV)	Transmembrane fugacity difference	Separation of volatile liquid mixtures
Gas or vapor separation (GS/VP)	Transmembrane pressure difference	Separation of gaseous/vapor mixtures
Electrodialysis (ED)	Transmembrane voltage difference	Dewatering of suspended solids in solution

Table 1-2 Membrane processes and yearly growth in sales

Membrane process	Growth [%/yr]
Dialysis	10
Microfiltration	8
Ultrafiltration	10
Reverse osmosis	10
Gas separation	15
Electrodialysis	5
Electrolysis	5
Miscellaneous	10

1.1.2 Gas separation membranes

As pointed out previously, gas separation processes are one of the most important applications of synthetic membranes. Sholl and Lively very importantly noted an ‘inexhaustive’ list of seven separation that could potentially change the world [12]. 3 among these separation processes include gas separation- light hydrocarbons from heavy ones, alkenes from alkanes and CO₂ capture from greenhouse gases. Apart from these, other very important gas separations in no order of importance include natural gas processing (acidic gas separation, C₃+ hydrocarbons removal, water separation, nitrogen separation, helium separation) [13-15], separation of hydrogen from light hydrocarbons, nitrogen/argon separation in ammonia plants [14-16]. Emerging important applications also include CO₂/N₂ separation, hydrogen/CO₂ separation, oxygen separation from air etc. [14, 15].

Gas separation membranes are usually tailored to specific applications as no one membrane type can be applied to all the gas separation scenarios. Therefore, processes are thoroughly understood before any useful membrane is to be designed [14]. Furthermore, to choose the best membrane, the interactive mechanism of the gases involved with the membrane material and its structure are important. Several gas/membrane interactive mechanisms have been proposed.

1.1.3 Gas permeation mechanisms through membranes

There are several mechanisms that have been proposed for the permeation of gases through thin-layer membranes. Some membrane materials exhibit mostly one type of gas permeation mechanism while others exhibit different kinds of mechanisms. Also, a single gaseous specie can be found to permeate a membrane by different mechanisms at the same time or at different temperature ranges as is common for CO₂ permeation through silica-based membranes [17-19]. The most encountered gas permeation mechanisms are shown in Fig. 1-2 [20].

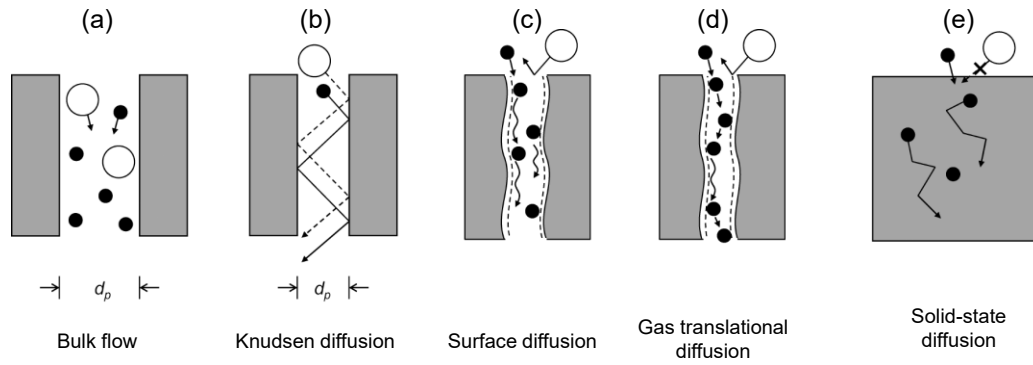


Fig. 1-2 Different mechanisms of gas permeation through membranes [20]

Generally, gas transport properties through porous media can be determined by the ratio of the number of molecule-molecule collisions to molecule-pore wall collisions [21]. This gave rise to the Knudsen number expressed as the ratio of the mean free path to the mean pore width as shown in Equation 1-1.

$$Kn = \frac{\lambda}{d_p} \quad (1-1)$$

Where Kn is the Knudsen number, λ is the mean free path and d_p is the mean pore diameter. The mean free path is defined as the mean distance travelled by a gas molecule between successive collisions. When $Kn \ll 1$, this indicates that the pore width is much larger than the mean free path and therefore, molecules tend to collide more frequently with each other than with the walls of the pore. In this situation, viscous flow results. On the other hand, when $Kn \gg 1$, the mean free path is much greater than the mean pore width and the gas molecules collide with the walls more frequently than they collide with themselves. Specific mechanisms are discussed in the following.

1.1.3.1 Bulk-fluid flow

Bulk-fluid or viscous flow through a membrane pore occurs by the Hagen-Poiseuille mechanism whereby the pore diameter of the membrane is very large compared to the mean free path of travel of the permeating gas molecules. In this situation, the Knudsen number, $Kn \ll 1$ and the gas molecules collide with each other more than they do with the pore walls [22]. Fig. 1-2a illustrates such a scenario.

1.1.3.2 Knudsen diffusion

A Knudsen permeation mechanism dominates when the Knudsen number, $Kn \gg 1$ and the gas molecules collide with the pore wall more than with themselves as illustrated in Fig. 1-2b. Knudsen mechanism is strictly dependent on the molecular weight of the permeating gas species and lighter weighing gas permeate faster than gases with higher molecular weights [21]. Here, the gas diffusivity is determined by the combined consideration of the gas kinetic velocity and the geometric parameters of the associated pores [20].

1.1.3.3 Surface diffusion

In the preceding Knudsen mechanisms discussed, it was assumed that the collisions occurring between the gaseous molecules and the pore walls are strictly and completely elastic without any interactions. However, this situation is not always the case. At low temperatures when the kinetic energy of the permeating gas molecules is not enough to escape the potential energy barrier of the pore surface, the gas molecules tend to adsorb onto the pore wall surface at the pore mouth and diffuse through the membrane via the surface of the pore wall (Fig. 1-2c). Gases like CO_2 , CH_4 , N_2 and CO show significant surface diffusion contribution to the overall transport mechanism at temperatures below $100\text{ }^\circ\text{C}$ [23, 24].

1.1.3.4 Gas translational diffusion

When the mean pore diameter of a membrane is very small in the region of micropores, mechanisms such as Knudsen diffusion, surface diffusion and molecular sieving combine to dictate the permeation of gas molecules [20, 25]. In microporous membranes, the diffusion of gaseous molecules is heavily affected by the molecule-lattice and molecule-molecule interactions. A unified mechanism was proposed by Xiao and Wei referred to as gas-translational diffusion mechanism [26, 27].

1.1.3.5 Solid-state diffusion

A solid-state diffusion also known as solution diffusion occurs with a further reduction in the mean pore size of the permeation medium. The pores become so small that the interaction of the permeating molecules with the membrane material becomes very significant to the transport of molecules. This phenomenon occurs in dense non-porous membranes. In solution-diffusion the permeating molecules

dissolve into the membrane material and transport through the material via a concentration gradient. Different molecules of similar sizes permeate at different rates because of their different relative solubilities [28, 29]. In this instance, the permeability is a combination of the solubility and diffusivity effects expressed in Equation 1-2.

$$P = S \times D \quad (1-2)$$

Where P is the observed permeability of the permeating specie, S is the solubility and D is the diffusivity. A solution-diffusion mechanism occurs in three steps [28]: (1) the adsorption of the permeating molecule onto the surface of the membrane in the upstream side (2) diffusion of the molecules through the membrane by a chemical potential gradient and (3) the desorption of the molecules from the membrane surface at the downstream end. This phenomenon is common in polymeric membranes, glassy membranes, and metallic membranes [20].

1.1.4 Classification of gas separation membranes

Today there exists hundreds of different membrane types used in different applications which makes it difficult to understand the trend in membrane development. To evaluate the state of the art in membrane development and drive further improvements in membrane science, technology and processes it is important to classify membranes into various categories. Many efforts have been directed towards this objective e.g., membranes for hydrogen separation by Ockwig and Nenoff [30]. They identified and categorized membranes for hydrogen separation by membrane material. However, this may still be limited in helping to get an overview of the whole membrane science landscape. In this section, it is proposed that membranes be categorized by material, configuration, and membrane composition. An overview of this categorization is displayed in Fig. 1-3.

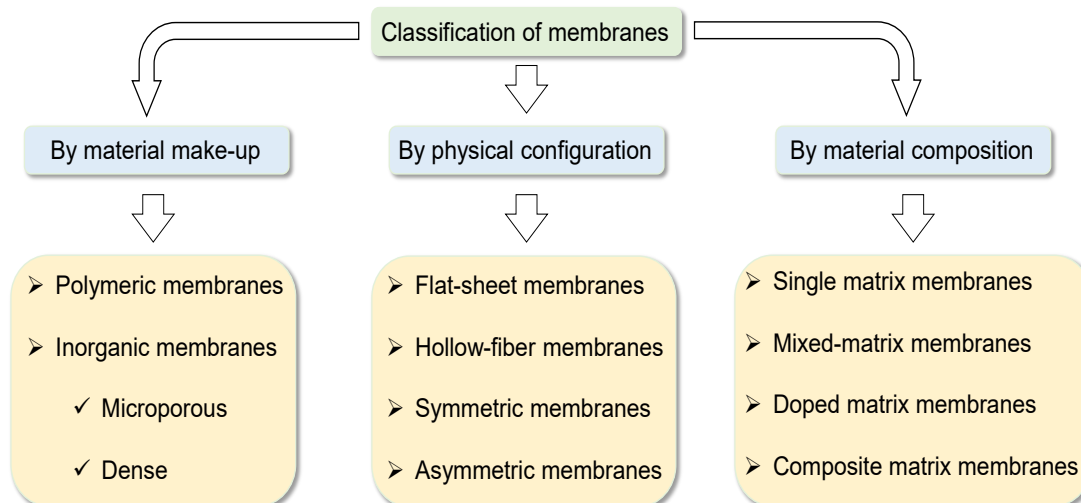


Fig. 1-3 An overview of the categorization of membranes by different parameters proposed here.

1.1.4.1 Classification by membrane material

The material make-up of a membrane refers to the chemical nature of its constituting matter and can provide a reasonable basis for categorization. A solid matter can be either organic or inorganic. Therefore, membranes can be generally classified by their material make-up into two large categories: polymeric and inorganic membranes. Several works have reported membranes from these two categories [6, 7, 31-36].

(a) Polymeric membranes

As pointed out earlier, a solution-diffusion mechanism of mass transport of permeating molecules occurs in polymer membranes. Polymers are dense macromolecular organic compounds composed of long sequences of one or more species of atoms or group of atoms linked to each other by usually covalent bonds [37]. Polymers can be formed into membranes as flat sheets or hollow fiber configurations [33] and are categorized majorly as glassy and rubbery polymers.

The performance and suitability of a polymer membrane to a specific application may depend on its structure. Rubbery polymers operate above the glass transition temperature. Above this temperature, the polymer chains have sufficient thermal energy to allow segmental motions [38]. These include silicone rubber, polyisoprene

[14], amide copolymers [11], neoprene, polyether, polyvinylchloride, polyurethane, polybutadiene [38, 39] etc. In glassy polymers, operating below the glass transition temperature means that the chains are rigid and possess lower free volume because the polymer chains are more restricted in their motions [38, 39]. Glassy polymers include cellulose acetate, polycarbonates, polyimides, polysulfone, polyethersulfone, polyethylene oxide [11, 14, 38, 40] etc.

Challenges: the challenges associated with polymer membranes include

1. Trade-off relationship. In an ideal membrane, a combination of high selectivity and permeability is desired. However, this is difficult to achieve with polymer membranes [14, 32, 41, 42]
2. Physical ageing and plasticization. Plasticization occurs when the polymer membrane is exposed to highly soluble gas species that result in considerable swelling of the polymer matrix overtime. This increases free volume which leads to higher flux and reduced selectivity. [43, 44]

(b) Inorganic membranes

Inorganic membranes can comprise of oxides (ceramic), metals or elemental carbon [45, 46]. Going by their nomenclature inorganic membranes comprise of inorganic matter which are arranged in either amorphous or crystalline form. They can be broadly divided into two categories: (i) microporous inorganic membrane and (ii) dense inorganic membranes.

(i) Microporous inorganic membranes

Microporous inorganic membranes comprise of amorphous and crystalline ceramic membranes with pore sizes less than 2 nm according to the IUPAC definition [47]. These membranes are capable of separating gas molecules by the molecular sieving mechanism because of the inherent range of pore sizes. Microporous inorganic membranes are prepared as thin layers on porous inorganic supports that present little permeation resistance but considerable mechanical strength [47]. Examples include amorphous silica [34, 48-51], zeolites (which contain silicon, aluminum, and oxygen atoms arranged into a lattice structure) [52-55] and alumina [56, 57].

(ii) Dense inorganic membranes

Dense inorganic membranes on the other hand contain pores whose size is less than 0.5 nm [45]. Dense inorganic membranes comprise majorly of metals that allow preferential permeation of certain molecules through their crystal lattice. Dense metal membranes can achieve exceptionally high H₂ selectivities and they typically include special metals and their alloys such as palladium [35], niobium, tantalum, vanadium, nickel, platinum [58], Pd-Au, Pd-Ag, Pd-Cu [35], Pd-Ta [59], Pd-Ru, Pd-Nb, Pd-Mo, Pd-Cu-Ag [60] etc.

Challenges: some challenges of inorganic membranes include [45]

1. Hydrothermal instability in silica membranes.
2. High cost of inorganic processing in zeolites and reproducibility issues.
3. High cost of fabricating thin metal films (>\$2000/m²). Instability of metal membranes against phase transition and contaminants such as H₂S.

1.1.4.2 Classification by physical configuration

Membranes can also be classified according to the manner in which the membrane module has been physically configured for application. Polymeric and inorganic membranes can be configured in various ways that are not particular to a membrane material, although a configuration may be more suited to a membrane material than another. The common configurations are discussed below and illustrated in Fig. 1-4 a-d.

(a) Flat-sheet membranes

Flat-sheet membranes are formed as plate-and-frame modules (Fig. 1-4a) [33] and various examples exist in applications such as ultrafiltration [61], forward osmosis [62], membrane distillation [63] etc.

(b) Hollow-fiber membranes

Hollow-fiber membranes are tubular in nature (Fig. 1-4b) with very high packing density [33]. Many polymeric membranes exist as hollow-fiber membranes [64, 65]. Many carbon molecular sieve membranes formed from hollow-fiber polymer modules

also exist in this configuration [66]. Li et al also reported a successful fabrication of an inorganic hollow-fiber membrane based on alumina [67].

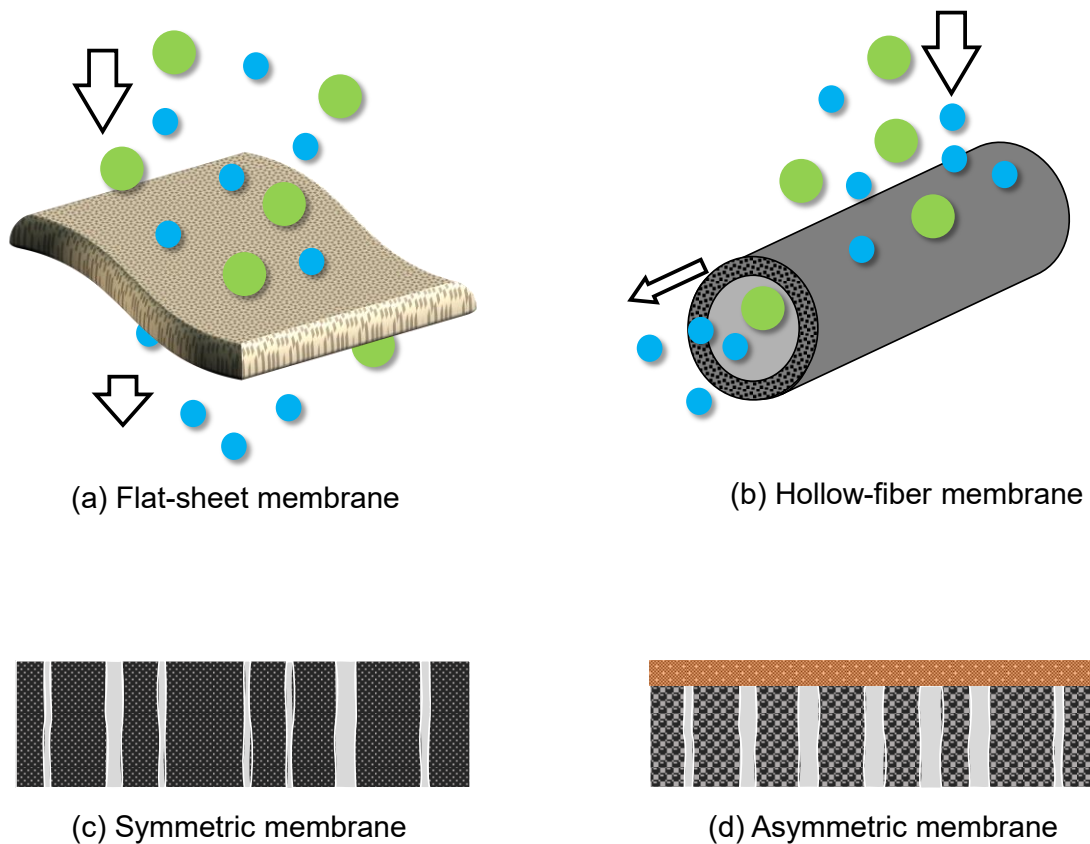


Fig. 1-4 The physical configurations of synthetic membranes

(c) Symmetric membranes

A symmetric membrane is also referred to as an isotropic membrane and is defined as one which is comprised of a uniform structure throughout the thickness of the membrane [33], as shown in Fig 1-4c. Membranes possessing symmetric configuration are usually free-standing unsupported membranes [68, 69].

(d) Asymmetric membranes

Asymmetric membranes also referred to as anisotropic membranes are configured as multilayer modules. The structure of these membranes is such that the layers are graded in porosity and particle size (Fig. 1-4c). The active separation layer is usually situated as the topmost densest layer which determines the gas separation ability of the whole membrane [33] while the underlying layers serve as supports. Many

supported membranes are asymmetric in nature [70, 71]. For example, Fig. 1-5a and b show a ZIF-8 [71] membrane supported on porous titania and a $\text{SiO}_2\text{-ZrO}_2$ supported on porous alumina, respectively.

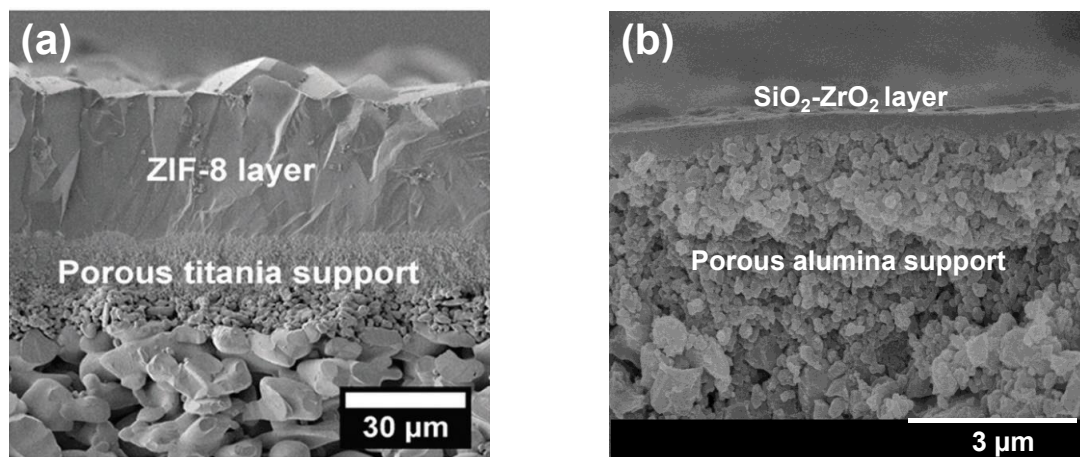


Fig. 1-5 SEM images of supported membranes showing asymmetric structure. (a) a ZIF-8 membrane supported on porous titania [71] (b) a $\text{SiO}_2\text{-ZrO}_2$ supported on porous alumina.

1.1.4.3 Classification by material composition

In the preceding sections, it has been established that membranes are made up differently in material and these membranes can be physically configured in different ways depending on the applications. A new class of materials (and thus new classification of membranes) is however necessary, borne out of the need to evolve membrane separation performances to a new generation [38, 72, 73]. This new generation of membranes are developed to give better performance metrics (selectivity, permeability, cost, handling etc.) over the previous generation membranes. Such evolutionary methodologies involve the combination of different matrices towards harnessing the strengths of each matrix for improved performance. Some of the possible classifications that can result are discussed further and illustrated in Fig. 1-6.

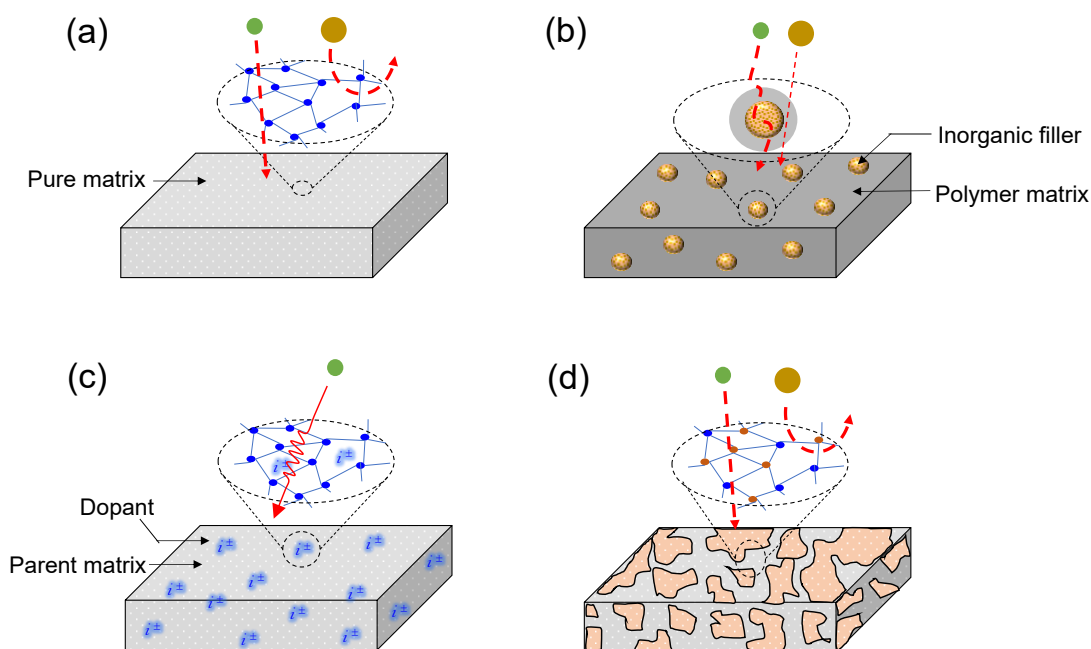


Fig. 1-6 Illustration of the categorization of membranes by material composition. (a) single matrix membranes (b) mixed matrix membranes (c) doped matrix membranes (d) composite matrix membranes.

(a) Single matrix membranes

This is the most basic form of a membrane matrix- a membrane comprising of only one type of material i.e., a single-component membrane. Many of the popular membrane types fall under this category as they serve as the bases for further development. Typically, single matrix membranes will include all various types of pure polymer membranes (polydimethoxysilane, polysulfone, polyimide, polyetherimide, cellulose acetate etc.), pure ceramic membranes and organosilica membranes (silica, zirconia, titania, alumina, bis(triethoxysilyl)ethane (BTESE) [74, 75], bis(triethoxysilyl)methane BTESM [76], bis(triethoxysilyl)propane BTESP [77], bis(triethoxysilyl)acetylene BTESA [78] etc.), pure metals (palladium, nickel, tantalum, molybdenum, niobium etc.), zeolites (ZIF, SAPO, AlPO₄, MeAPO structures etc.).

(b) Mixed-matrix membranes

Mixed-matrix membranes (MMM) are a combination of polymer and inorganic matrices. A pioneering work on MMMs was published by Koros and co-workers [79].

The concept of mixed-matrix membranes was introduced to overcome the limitations of both polymer membranes (vis trade-off, physical ageing, and plasticization) and inorganic membranes (vis brittleness and cost of inorganic processing) as enumerated in section 1.1.4.1 (a) and (b) [38, 39, 80, 81]. Typically, an MMM consists of a bulk polymer phase into which the inorganic phase is dispersed [80, 81]. The inorganic phase dispersed into the polymer bulk phase as shown in Fig. 1-6 (b) are referred to as fillers. The inorganic fillers traditionally incorporated can be categorized as zeolitic and non-zeolitic fillers [82]. The zeolitic fillers include conventional zeolites, AlPO and SAPO molecular sieves, while non-zeolitic fillers include carbon molecular sieves (CMS), porous and dense silica nanoparticles, metal oxide nanoparticles [82], activated carbon, metal-organic frameworks (MOFs), carbon nanotubes (CNTs), mesoporous materials, lamellar inorganic materials [39, 81].

(c) Doped matrix membranes

A membrane can acquire new characteristics and properties that improve its performance by introducing into it a metal or non-metal ion. Such an addition is referred to as doping. This strategy has been especially used in silica and silica-based membranes [83-86]. Doping a material with an anion or cation is used to direct a membranes microstructure or functionality towards enhanced performance. For example, fluorine as an anion is used to add a functionality to an organosilica membrane for improved propylene/iso-butane separation [85] or for improved hydrothermal stability of a silica membrane [87, 88], or for microstructural control of the membrane pore size [86]. On the other hand, Pd doping of a silica membrane has been used to improve the hydrogen-permselectivity [89]. Fig. 1-6 (c) shows the effect of a dopant interacting with the permeating molecule.

(d) Composite matrix membranes

In mixed-matrix membranes and doped matrix membranes, fillers or dopants are present as separate entities in the bulk of the primary matrix [82, 90]. In mixed-matrix membranes, the challenge of inorganic particles agglomeration in the polymer matrix especially in glassy polymers exists as a major concern [81]. In most doped matrix membranes (except for Pd-doped membranes for H₂-permselectivity), the dopants are not present as separate matrices but as functionality or microstructural change agents.

For composite matrix membranes, two separate structures are integrated into a single matrix and act as one matrix for active gas separation. Several examples of composite matrix membranes have been reported in literature. Such include ceramic composites ($\text{SiO}_2\text{-ZrO}_2$ [91-93], $\text{TiO}_2\text{-ZrO}_2$ [94-96], $\text{SiO}_2\text{-TiO}_2$ [97]). Furthermore, the different structures composing a composite matrix can act as structural, functional, or molecular sieving agents or a combination of these. These composites can be classified into two major categories: inorganic-organic composites and inorganic-inorganic composites.

(i) Inorganic-organic composites

Inorganic-organic composites are diphasic hybrids that can be grouped into two large categories: class I and class II inorganic-organic hybrids. A class I hybrid is such that the organic and inorganic matrices are linked by weak interactive forces such as hydrogen and van der Waals bonding [98, 99]. Examples of class I hybrids is interpenetrating polymer and inorganic networks (IPNs) [100]. In class II hybrids, on the other hand, the interaction between the inorganic and organic parts, which includes strong bonds like covalent and ionic-covalent bonds, serve to improve the inorganic matrix qualities such as improved hydrothermal stability [101], pore size controllability, [102, 103] targeted functionalization, [104] etc. Examples include organically modified transition metal oxides, metal-organic frameworks, etc. [102, 104]

(ii) Inorganic-inorganic composites

Inorganic-inorganic composites include several ceramic composites such as $\text{SiO}_2\text{-ZrO}_2$, $\text{TiO}_2\text{-ZrO}_2$, $\text{SiO}_2\text{-TiO}_2$. Composite $\text{SiO}_2\text{-ZrO}_2$ membranes have been used for pervaporation and nanofiltration applications [105-107]. Hydrogen separation performance of $\text{SiO}_2\text{-ZrO}_2$ hybrid membranes fabricated through chemical vapor deposition (CVD) has also been investigated [93].

1.2 Silica and composite matrix ceramic membranes

Amorphous silica membranes and their derivatives have drawn a lot of interest in the past few decades of gas separation membrane research due to their potential application to a wide variety of gas separation systems in general [34, 51, 108, 109],

and in particular to hydrogen separation due to their ease of fabrication, very high permselectivity and scalability [30]. Factors required for a permselective membrane are high flux, high selectivity, pore size controllability, and good physical and chemical stability. Silica membranes exhibit moderately high flux and excellent selectivity [34, 110, 111], but membranes based on silica still suffer from some problems [110]:

- (i) Pore size control for other gas separation applications beyond hydrogen separation
- (ii) Instability under hydrothermal conditions

Fig. 1-7 shows the typical performance of a silica membrane under a hydrothermal condition. Fig. 1-8a shows the single gas permeance at 200 °C as a function of kinetic diameter for a tetraethoxysilane (TEOS)-derived silica membrane measured for various gases before and after exposure to boiling water for 2 hours as carried out by ten Hove and co-workers [112]. Before exposure to boiling water, the membrane showed an impressive molecular sieving ability with high H₂-permselectivity. After an exposure of 72 hours to boiling water, this molecular sieving property all but disappeared with the performance now similar to that of the supporting alumina membrane. In a separate experiment by Castricum and coworkers, a 5% water by weight impure n-butanol was dehydrated by pure and hybrid silica at 150 °C by PV process and the separation performance observed for several days as shown in Fig. 1-8b [101]. Here, it can be seen that the dehydration performance of the inorganic silica membrane dropped off after just a few days because of the high hydrophilicity [113].

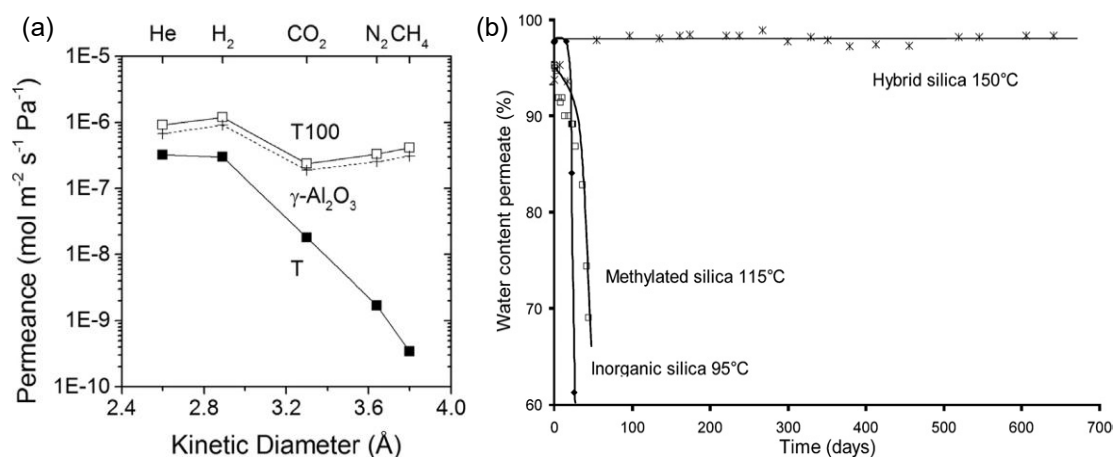


Fig. 1-7 Performance of silica membranes in hydrothermal conditions (a) single gas permeance at 200 °C as a function of kinetic diameter for a TEOS-derived silica membrane measured for various gases before and after exposure to boiling water for 72 hours [112] (b) long-term separation performance: water content of permeate of a hybrid silica membrane towards dehydration of n-butanol (5 wt% water) by pervaporation at 150 °C [113].

To develop silica, silica-based and other ceramic membranes with high perm-selectivity, pore size tunability, and hydrothermal stability, many researchers have studied various techniques such as:

- (i) Spacer methods (-Si-R-Si-) [108, 114],
- (ii) Templating methods (-Si-R') [102, 115],
- (iii) Anion and cation doping [83-90], and
- (iv) Hybridization of silica with other metal oxides such as ZrO₂ [91-93], TiO₂ [97], and Al₂O₃ [116, 117].

The hydrothermal, acidic, and basic stability of SiO₂-ZrO₂ ceramic composites have been particularly proven [91, 93, 107]. Fig. 1-8 shows the gas permeance for a SiO₂-ZrO₂ ceramic composite membrane as a function of kinetic diameter measured at 300 °C before and after exposure to steam at 40 and 100 kPa partial pressure and 500 °C for 20 hours, respectively, carried out by Yoshida and co-workers [91]. The membrane was made with a 9:1 mixture of SiO₂ to ZrO₂. When compared with a pure SiO₂ membrane exposed to boiling water for 72 hours as shown in Fig. 1-7a, it is seen here that the membrane quality of a composite SiO₂-ZrO₂ membrane withstands a hydrothermal atmosphere to a better degree.

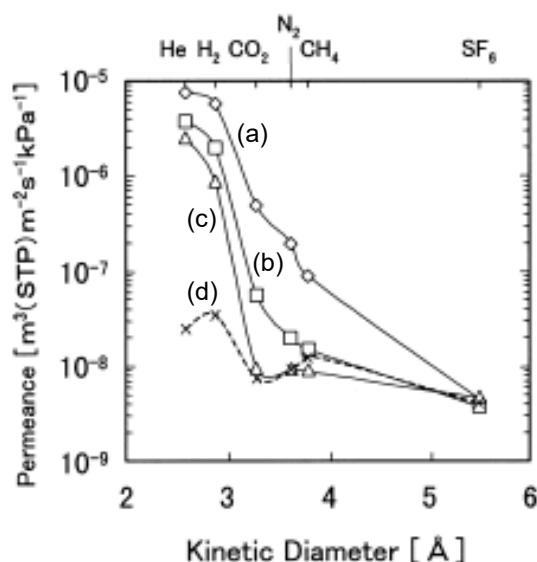


Fig. 1-8 Gas permeance for a $\text{SiO}_2\text{-ZrO}_2$ ceramic composite membrane as a function of kinetic diameter measured at 300 °C before and after exposure to steam: (a) fresh membrane (b) membrane after exposure to 500 °C steam at 40 kPa partial pressure for 10 hours (c) membrane after exposure to 500 °C steam at 100 kPa partial pressure for 10 hours (d) Knudsen diffusion (based on SF_6 permeance) [91].

1.2.1 State of the art of ceramic composite materials and membranes

Hybridization of silica with proven hydrothermally stable metal oxides such as Al_2O_3 , TiO_2 and ZrO_2 has been studied extensively [30, 91, 105, 117]. Initial specific studies into the effect of ZrO_2 and TiO_2 on SiO_2 nanoparticles were carried out by catalysis researchers [120-124]. It was extensively observed that the acidic properties of the composite oxides were considerably better than the individual component oxides. In another consideration, the presence of a second oxide containing a metal ion with a larger ionic radius tends to reduce the surface energy and hence the sintering rate in severe environmental conditions [125]. Therefore, there seems to be a synergistic effect between the contributing oxides as on one hand, an oxide may be present to improve the acidic conditions of the composite, on the other hand, the second oxide may be present to improve reduce the surface energy of the composite.

As mentioned before, the various combinations of these silica and metal oxides in membranes that have seen very extensive study include $\text{SiO}_2\text{-ZrO}_2$, $\text{TiO}_2\text{-ZrO}_2$, $\text{SiO}_2\text{-TiO}_2$ and $\text{SiO}_2\text{-Al}_2\text{O}_3$ [118] to a lesser degree. A ternary combination such as $\text{Al}_2\text{O}_3\text{-SiO}_2\text{-TiO}_2$ has also been investigated [119]. These ceramic composites have been

studied in various applications. Table 1-3 shows the various applications of ceramic composite membranes.

Table 1-3 Various applications of ceramic composite membranes (with preference for gas separation applications).

Ceramic composite	Composition (ratio)	Application system	Ideal selectivity [-]	Reference
SiO ₂ -ZrO ₂ (sol-gel)	9:1	GS ^a -H ₂ , N ₂	28 (H ₂ /N ₂)	[91]
SiO ₂ -ZrO ₂ (CVD)	5:5	GS ^a -He, H ₂ , N ₂	17 (He/N ₂), 25 (H ₂ /N ₂)	[92]
SiO ₂ -ZrO ₂ (CVD)	9:1	GS ^a -H ₂ , N ₂	1400 (H ₂ /N ₂)	[93]
ZrO ₂ -Y ₂ O ₃ -SiO ₂ (sol-gel)	9:0.5:0.5	GS ^a -H ₂ , N ₂	3 (H ₂ /N ₂)	[126]
SiO ₂ -ZrO ₂ (sol-gel)	5:5	NF-	-	[107, 107]
SiO ₂ -TiO ₂ (sol-gel)	5:5	NF- Hep/Tol.	-	[97]
TiO ₂ -ZrO ₂ (sol-gel)	5:5	GS- H ₂ , CO ₂ , N ₂	12 (H ₂ /CO ₂), 5 (H ₂ /N ₂)	[127]
TiO ₂ -ZrO ₂ (sol-gel)	5:5	NF-	-	[94, 95]
TiO ₂ -ZrO ₂ (sol-gel)	5:5	NF-	-	[128]
Al ₂ O ₃ -SiO ₂ -TiO ₂ (sol-gel)	4:1:1	-	-	[119]

^a Operated in a steam atmosphere, GS- gas separation, NF- nanofiltration, Hep.- Heptane, Tol.- Toluene

A few observations can be made from Table 1-3. The first is that only the composite of SiO₂ and ZrO₂ have been applied to gas separation. This is very likely due to the highly molecular sieving ability that SiO₂ can imbue the composite with. Consequently, it does seem that a SiO₂-ZrO₂ composite with a higher proportion of the SiO₂ component will achieve better selectivities as observed for references 91 and 93. Yoshida and co-workers [91] as well as Choi and co-workers [92], have demonstrated that although a composite of 5:5 of SiO₂ and ZrO₂ can achieve a very impressive hydrothermal stability, the selectivities can be low and sometimes

approaching Knudsen levels [91]. Furthermore, it also appears that other ceramic composites not SiO₂-ZrO₂ are limited to nanofiltration (NF) in their applications. Therefore, the challenges of improving the molecular sieving properties of an equimolar (5:5) ceramic composite and broadening their applicability are identified. Researchers have found a few opportunities in organic coordination ligands [129].

1.2.2 Organic coordination ligands: a broad field of opportunities

The versatility of sol-gel chemistry has been instrumental to the formation of new functional materials. One major aspect of this versatility is the ability to obtain products with predetermined characteristics based on the experimental conditions, and another aspect is that it allows for the synthesis of inorganic-organic hybrid materials through the introduction of organic groups in solution [130]. One way to add an organic group is to chemically modify a precursor prior to synthesis [120]. A good example of chemically modifying precursors is found in the use of coordination ligands to form coordinate complexes where the precursor to be modified is a transition metal ion compound. One of the pioneering works on the chemical modification and sol-gel chemistry of transition metal alkoxides were done by Sanchez, Livage and their co-workers [131-133]. They studied topics that included the partial charge model, gelation, coordination ligands, alcohol interchange etc.

1.2.2.1 Coordination ligands

As most transition metal alkoxides are very reactive in hydrolysis and condensation reactions, there arise the need to stabilize or slow them down in order to avoid precipitation or agglomeration especially when forming composite oxides [130, 132]. This is achieved by chemically modifying the alkoxides with complexing agents that are usually hydroxylated nucleophilic ligands such as carboxylic acids and β -diketones. For example, acetylacetonone ACAC (CH₃-CO-CH₂-CO-CH₃) in its enolic form contains hydroxyl groups which can react with metal alkoxides. According to the partial charge theory, the acetylacetonate group ACAC⁻ (CH₃-CO-CH₂-CO-CH₂) reacts with a titanium tetrapropoxide for example to give the oligomeric specie Ti (OPr)₃ (CH₃-CO-CH₂-CO-CH₂)-structurally depicted in Fig 1-9- and favors the release of the alcohol PrOH (propanol).

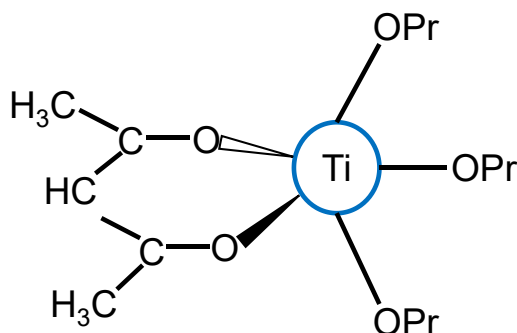


Fig. 1-9 Structural formula of an oligomer formed between a titanium tetrapropoxide and acetylacetonate.

Such nucleophilic reactions between hydroxylated ligands and transition metal alkoxides have been studied extensively: effect of acetylacetonate on the particle sizes of TiO_2 colloids [134], x-ray structures of titanium alkoxide β -diketones derivatives [135], ethyl acetoacetate distribution in the course of titanium alkoxide chelation [136], the influence of chemical modification on zirconium alkoxides as precursors in sol-gel process studied by EXAFS spectroscopy [137], hydrolytic stability of organic ligands in different alkoxide complexes [138] etc.

Since Hoebbel and co-workers [138] found that some of the ligands chelated to transition metals are hydrolytically stable to a very good extent in the range of a week period under continuous stirring in the presence of water, the opportunities for adoption of chelating ligands into composite ceramic membranes has drawn lots of attention beyond catalysis applications.

1.2.2.2 Organic coordination ligands as molecular engineering agents

Complexation of alkoxides with nucleophilic complexing ligands allows for the design of molecular precursors and the sol-gel synthesis of tailor-made materials [132]. Consequently, the role of a hydrolytically stable complexing ligand can be pre-designed according to two major functions: as a network modifier or network former [139] (Fig. 1-10).

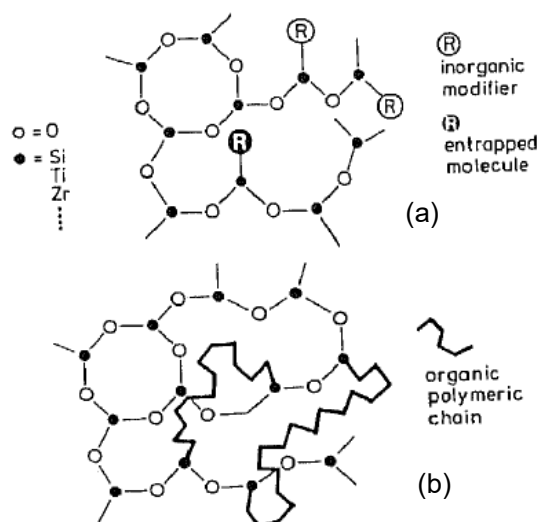


Fig. 1-10 Illustration of network modification and network formation organically modified ceramics [139]

(a) Network modifiers

When the complexing ligand is a simple non hydrolysable group, it will have a network modifying effect [140] (Fig. 1-10a). In this case, the ligand can create a physically or chemically different site [139]. Organic coordination ligands that fall in this category include acetylacetone, acetic acid, isoeugenol, ethyl acetoacetate etc. and they are depicted in Fig. 1-11a.

(b) Network formers

A complexing ligand working as a network former is when the ligand bears a reactive group that can, for example, polymerize or copolymerize [139, 140] (Fig. 1-10b). Complexing ligands that can serve as network formers include allyl acetoacetate, methacryloxyethyl acetoacetate, methacrylic acid etc. as shown in Fig. 1-11b.

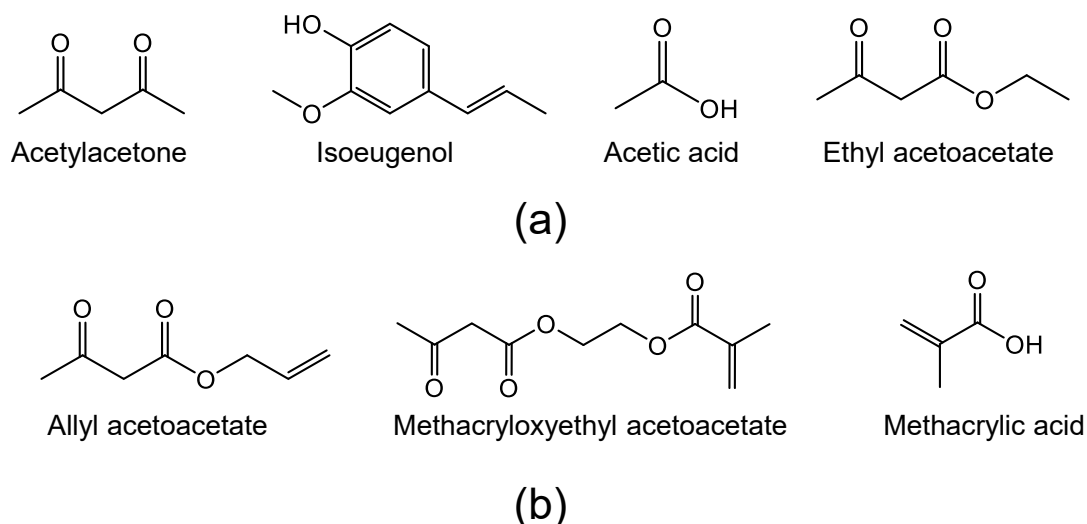


Fig. 1-11 Some organic coordination/ complexation ligands: (a) network modifiers (b) network formers.

1.2.3 Ligand-modified ceramic composite membranes

Embracing the unique chemistry between transition metal ions and organic coordination ligands, a number of researchers have been able to develop a new class of membranes that have shown promise in gas separation and filtration applications. The ligand-modified ceramic composites have shown better molecular sieving performance compared to the corresponding unmodified composites with the same mixed oxide composition. For example, Fukumoto *et al.*, prepared an isoeugenol-modified $\text{TiO}_2\text{-ZrO}_2$ composite membrane that showed superior molecular sieving selectivities compared to an unmodified $\text{TiO}_2\text{-ZrO}_2$ composite membrane [141]. The theory of the improved molecular sieving is that isoeugenol coordinated to the titanium and zirconium transition metal centers modify the intra-particle network pores by physically occupying the networks and serving as shield against the transport of large molecules. Fig. 1-12 illustrates this theory. Fukumoto *et al.* were able to prove this theory of intra-network occupation by changing the ligand/alkoxide molar ratio and they found that by increasing the ligand content, the molecular sieving was able to be improved. Elsewhere, Spijksma and co-workers also showed a diethanolamine-modified $\text{TiO}_2\text{-ZrO}_2$ composite membrane with H_2 permeance and H_2 /butane selectivity of $3.0 \times 10^{-7} \text{ mol m}^{-2} \text{ s}^{-1} \text{ Pa}^{-1}$ and 54, respectively [142].

This development has thus led to new applications of ligand-modified composite ceramic membranes to gas separation and filtration. Table 1-4 shows some of these membranes and their applications. Since one of the first research into the chemistry of transition metals and chelating ligands occurred between the 1940s and 1960s [143, 144] and the applications into composite ceramic membranes are relatively new (one of the earliest appearing in 2001 by Benfer and co-workers [145]), there seems to be a lot of gap in the scope of possibilities that can be achieved with organic coordination/complexation ligands and composite ceramic membranes.

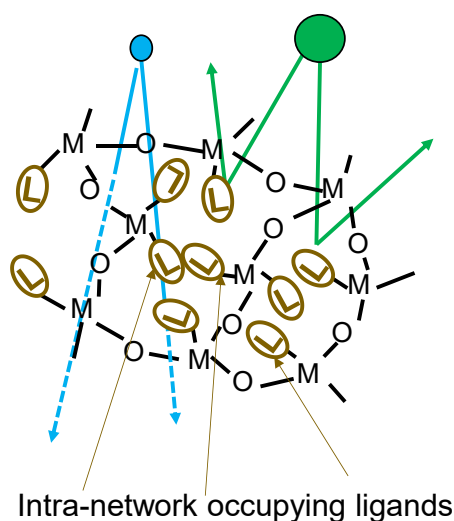


Fig. 1-12 Mechanism of molecular sieving in organic coordination ligand modified ceramic network

Table 1-4 Different ligand-modified ceramic composite membranes and their applications

Membrane	Modifying ligand	Appl.	Selectivity [-]	Reference
TiO ₂ -ZrO ₂	Isoeugenol	GS	65 (He/N ₂) 46 (CO ₂ /N ₂)	[141]
TiO ₂ -ZrO ₂	Diethanolamine (DEA)	GS	12 (He/N ₂) 1.1 (CO ₂ /N ₂)	[141]
TiO ₂ -ZrO ₂	Diethanolamine (DEA)	GS	54 (H ₂ /butane)	[142]
TiO ₂ -ZrO ₂	Methyl gallate	GS	62 (He/N ₂) 111 (He/CH ₄)	[146]
TiO ₂ -ZrO ₂	Ethyl ferrulate	GS	10.6 (He/N ₂) 13.6 (He/CH ₄)	[146]
SiO ₂ -TiO ₂	Acetylacetone	GS	2.43 (He/N ₂) 2.16 (N ₂ /CO ₂)	[147]
SiO ₂ -TiO ₂	Isoeugenol	GS	2.39 (He/N ₂) 2.22 (N ₂ /CO ₂)	[147]
TiO ₂ -ZrO ₂	Ethyl acetoacetate	NF		[129]
TiO ₂ -ZrO ₂	2,3-dihydroxynaphthalene	NF		[129]

Appl.- Applications, GS- gas separation, NF-nanofiltration

1.3 The scope and outline of this thesis

The overall objective of this dissertation is to engineer the microstructure of SiO₂-ZrO₂ ceramic composite towards the development of improved molecular separation membranes by applying diverse modification techniques. Organic coordination/complexation ligands have shown that the networks of ceramic composites can be tailored towards fabricating molecular sieving membranes, but a few concerns remain. First, most of the reported works on ligand-modified ceramic composite membranes have been limited to TiO₂-ZrO₂ when opportunities may lie elsewhere. Also, the engineered modifications of ceramic composite membrane networks have stopped at the ligand modification phase with no further investigation into more modification opportunities by the ligand transformation. Fig. 1-13 shows the possible modification directions considered during this research period. Therefore,

this work seeks to deepen the understanding and access further opportunities in organic coordination/complexation ligands modification of ceramic composite membranes.

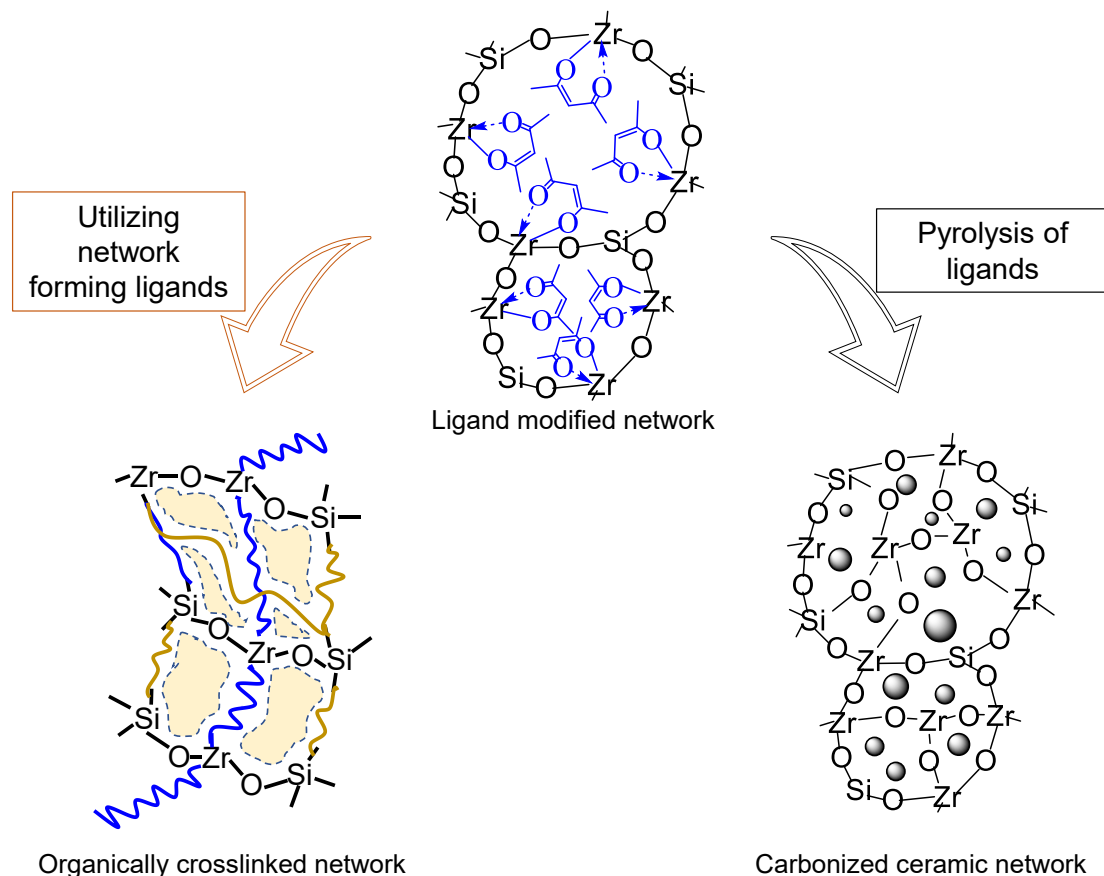


Fig. 1-13 Alternative modification opportunities offered by ligand-modified ceramic networks

The scope of this work is comprised of the following contents:

1. Preparation of organic ligand-modified $\text{SiO}_2\text{-ZrO}_2$ films, gels and membranes and evaluation of gas permeation characteristics
2. Evaluation of the effect of organic ligand types for microstructural engineering of $\text{SiO}_2\text{-ZrO}_2$ membranes
3. Pyrolysis transformation of organic coordination/complexation ligands chelated to $\text{SiO}_2\text{-ZrO}_2$ membranes and evaluation of gas permeation characteristics

This dissertation is outlined in 6 chapters thus:

Chapter 1 is the “**General introduction**”, which presents a brief overview of separation membranes and a detailed look at silica and composite ceramic membranes for gas separation.

Chapter 2 is titled “**Development of a molecular sieving membrane from an acetylacetonate-modified silica-zirconia ceramic composite**”. In this work, an acetylacetonate-modified equimolar SiO₂-ZrO₂ composite-derived membrane with molecular sieving properties was successfully fabricated. The sol-gel method was successfully employed to chemically modify zirconium tetrabutoxide prior to co-hydrolysis and -condensation with tetraethoxysilane, and it was then used to fabricate a gas separation layer. An acetylacetonate-modified SiO₂-ZrO₂-derived membrane prepared at 300 °C showed H₂ permeance of 9.9 x 10⁻⁷ mol m⁻² s⁻¹ Pa⁻¹ with a H₂/SF₆ permeance ratio of 7,600, which was a significant improvement over pure SiO₂-ZrO₂-derived membranes (H₂ permeance: 1.4 x 10⁻⁶ mol m⁻² s⁻¹ Pa⁻¹, H₂/SF₆ permeance ratio: 11). Heat-treatment of an acac⁻-modified SiO₂-ZrO₂-derived membrane prepared at temperatures that ranged from 250 °C (H₂ permeance: 4.5 x 10⁻⁸ mol m⁻² s⁻¹ Pa⁻¹, H₂/CH₄: 100, CO₂/CH₄: 60, H₂/SF₆: > 18,000 at 50 °C) to 550 °C resulted in an improved H₂ permeance of 3.4 x 10⁻⁶ mol m⁻² s⁻¹ Pa⁻¹ with reduced permeance ratios (H₂/CH₄: 3, H₂/SF₆: 9) at 50 °C. A membrane prepared by heat-treating a 250 °C-fired membrane at 300 °C showed the best trade-off with H₂ permeance-H₂/SF₆ permeance ratios above the trade-off line compared with membranes prepared at other temperatures.

Chapter 3 is titled “**Microstructure engineering of ligand-modified silica-zirconia membranes derived from network-forming precursors**”. In this study an easy template was devised for the fabrication and microstructural control of ligand-chelated, silica-zirconia-based composite membranes with a thickness of less than 400 nm. Hybrid materials with crosslinking between the organic moieties were successfully fabricated via the sol-gel co-condensation of 3-(trimethoxysilyl)propyl methacrylate and zirconium (IV) butoxide chelated via acetylacetonate and allyl acetoacetate ligands using an azobisisobutyronitrile radical initiator as a crosslinking agent. Characterization of the films and gels via FTIR, XRD and thermogravimetry indicated that both the polymerization and hybridization of the networks was achieved. Gas permeation experiments showed that the organic crosslink-derived

membranes possess molecular sieving properties (H_2 permeance: $\approx 10^{-7}$ mol m⁻² s⁻¹ Pa⁻¹; H_2/N_2 selectivity: $\approx 20-30$) that are superior to those of non-crosslink-derived membranes (H_2 permeance: $\approx 10^{-7}$ mol m⁻² s⁻¹ Pa⁻¹; H_2/N_2 selectivity: $\approx 7-11$). Quantitative analysis of the microstructures of the membranes based on the permeation behaviors of H_2 and N_2 revealed that organic crosslinking led to significant control of the microstructural characteristics of the membranes.

Chapter 4 is titled “**Enhanced H_2 -permselectivity in a carbon-silica-zirconia membrane derived from an acetylacetonate-ceramic composite pyrolysis**”. One viable technique for the retardation of high-temperature densification of H_2 -permselective inorganic silica-derived membranes is the combination with ZrO_2 . However, while ZrO_2 successfully inhibits SiO_2 phase densification, H_2 permeance is sacrificed. This work reports the preparation of a carbonized SiO_2 - ZrO_2 composite membrane with enhanced H_2 permselectivity via a sol-gel process. The sol synthesis of the precursor SiO_2 - ZrO_2 -acetylacetonate composite was optimized by studying the effect of water/alkoxide molar ratio on the final carbon- SiO_2 - ZrO_2 properties. Characterization by thermogravimetry, XRD and N_2 adsorption revealed that utilizing a water/alkoxide molar ratio of 60 was optimal for the retention of carbon, amorphousness and microporosity. Furthermore, by combining SiO_2 and ZrO_2 in a ratio of 9/1 in a carbon- SiO_2 - ZrO_2 membrane, a high H_2 -permselectivity could be achieved. This membrane showed an H_2 permeance of 16×10^{-7} mol m⁻² s⁻¹ Pa⁻¹ and H_2/N_2 and H_2/CH_4 ideal selectivities of 75 and 148, respectively. More importantly, the carbon- SiO_2 - ZrO_2 membrane’s H_2 -permselectivity exceeded that of a similarly pore-distributed unmodified SiO_2 - ZrO_2 membrane with an H_2 permeance of 3×10^{-7} mol m⁻² s⁻¹ Pa⁻¹. This enhanced H_2 -permselectivity was attributed to the increase in pore volume contributed by ultra-micropore-bearing carbon nanoparticles.

Chapter 5 is titled “ **CO_2 flow-switching behaviour in a pyrolysis-derived carbon-silica-zirconia membrane promises a versatile high-temperature H_2/CO_2 separation**”. Many researchers regard silica, silica-based and zeolite membranes as the agents that will accomplish H_2 separation. These membranes are expected to be productive in various mixture systems and under very high temperatures. This work reports the successful fabrication of a composite carbon- SiO_2 - ZrO_2 ceramic membrane with a unique pressure-induced switching of CO_2 flows that allows

versatile H₂/CO₂ separation at elevated temperatures. TG-MS, DTG-TGA, FT-IR, CP-MAS-¹³C-NMR, and TEM provide corroborative evidence of the carbonization of starting material SiO₂-ZrO₂-acetylacetonate into C-SiO₂-ZrO₂. The resultant C-SiO₂-ZrO₂ displayed significant hysteresis in CO₂ adsorption isotherm at a temperature well above the critical temperature of CO₂ (31 °C), which indicates structural conformation. Furthermore, single-gas permeation measurements showing upstream pressures of 200 and 500 kPa reveal different permeation values for CO₂ at 300 °C. In separating a H₂/CO₂ mixture at 50 and 300 °C under upstream pressures of 200 and 500 kPa, respectively, the flow of H₂ permeance reduces as the concentration of CO₂ increases in the feed side at 50 °C (1.14 x 10⁻⁸ down to 3.9 x 10⁻⁹ mol m⁻² s⁻¹ Pa⁻¹ at 200 kPa). The pressure-induced surface flow of CO₂ at 300 °C and 500 kPa, however, reduces the hindrance to H₂ flow and results in H₂/CO₂ selectivity of ~20-30 for all CO₂ concentrations, which is on a par with molecular sieving membranes. This novel C-SiO₂-ZrO₂ material shows promise for many interesting applications.

Chapter 6 is the “**Conclusions and considerations for further studies**”. In this chapter the major conclusions from chapters 2 through 5 are summarised and closed with itemisation of the aspects that may be studied in the future.

Cited literature

1. R. W. Rousseau, Handbook of separation process technology, John Wiley and Sons, New York, 1987.
2. H. Strathmann, L. Giorno, E. Drioli, An introduction to membrane science and technology, Consiglio Nazionale Delle Ricerche, Rome, 2006.
3. R. Bounaceur, N. Lape, D. Roizard, C. Vallieres, E. Favre, Membrane processes for post-combustion carbon dioxide capture: a parametric study, Energy, 31 (2006) 2556–2570.
4. C. Charcosset, A review of membrane processes and renewable energies for desalination, Desalination, 245 (2009) 214–231
5. Y.-H. M. Chan, S. G. Boxer, Model membrane systems and their applications, Curr. Opin. Chem. Biol., 2007, 11:581–587

6. J. A. Nollet, Extract of the observations made in Italy, by the Abbé Nollet, F. R. S. on the Grotta de Cani, *Philos. T. R. Soc.*, 47 (1752) 48-61
7. T. Graham, On the absorption and dialytic separation of gases by colloid septa, *Philos. T. R. Soc.*, 156 (1866) 399-439
8. K. Scott, *Handbook of industrial membranes*, Elsevier Advanced Technology, Oxford, United Kingdom, 2006.
9. H. Strathmann, Membrane separation processes: current relevance and future opportunities, *AIChE J.*, 47 (2001) 1077-1087
10. W. J. Koros, Evolving beyond the thermal age of separation processes: membranes can lead the way, *AIChE J.*, 50 (2004) 2326-2334
11. P. Bernardo, E. Drioli, G. Golemme, Membrane gas separation: a review/state of the art, *Ind. Eng. Chem. Res.*, 48 (2009) 4638-4663
12. D. S. Sholl, R. P. Lively, Seven chemical separations to change the world, *Nature*, 532 (2016) 435-437
13. C. A. Scholes, G. W. Stevens, S. E. Kentish, Membrane gas separation in natural gas processing, *Fuel*, 96 (2012) 15-28
14. R. W. Baker, B. T. Low, Gas separation membrane materials: a perspective, *Macromolecules*, 47 (2014) 6999-7013
15. R. W. Baker, Future directions of membrane gas separation technology, *Ind. Eng. Chem. Res.* 41 (2002) 1393-1411
16. D. F. Sanders, Z. P. Smith, R. Guo, L. M. Robeson, J. E. McGrath, D. R. Paul, B. D. Freeman, Energy-efficient polymeric gas separation membranes for a sustainable future: A review, *Polymer* 54 (2013) 4729-4761
17. M. Kanezashi, J. O'Brien-Abraham, and Y. S. Lin, Gas permeation through DDR-type zeolite membranes at high temperatures, *AIChE J.* 54 (2008) 1478-1486
18. L. Yu, M. Kanezashi, H. Nagasawa, J. Ohshita, A. Naka, T. Tsuru, Fabrication and microstructure tuning of a pyrimidine-bridged organoalkoxysilane membrane for CO₂ separation, *Ind. Eng. Chem. Res.*, 56 (2017) 1316-1326

19. D. Lee, S. T. Oyama, Gas permeation characteristics of a hydrogen selective supported silica membrane. *J. Membr. Sci.*, 210 (2002) 291–306
20. S. T. Oyama, M. Yamada, T. Sugawara, A. Takagaki, R. Kikuchi, Review on mechanisms of gas permeation through inorganic membranes, *J. Jpn. Petrol. Inst.*, 54 (2011) 298-309
21. Y. Wall, Ompe-Aime-Mudimu, G. Braun, G. Brunner, Gas transport through ceramic membranes under super-critical conditions, *Desalination* 250 (2010) 1056–1059
22. D. W. Stops, The mean free path of gas molecules in the transition régime, *J. Phys. D: Appl. Phys.*, 3 (1970) 685
23. P. F. Zito, A. Caravella, A. Brunetti, E. Drioli, G. Barbieri, Knudsen and surface diffusion competing for gas permeation inside silicalite membranes, *J. Membr. Sci.*, 523 (2017) 456–469
24. P. F. Zito, A. Caravella, A. Brunetti, E. Drioli, G. Barbieri, Discrimination among gas translation, surface, and Knudsen diffusion in permeation through zeolite membranes, *J. Membr. Sci.*, 564 (2018) 166–173
25. H. Nagasawa, T. Niimi, M. Kanezashi, T. Yoshioka and T. Tsuru, Modified gas-translation model for prediction of gas permeation through microporous organosilica membranes, *AIChE J.*, 60 (2014) 4199-4210
26. J. Xiao, J. Wei, Diffusion mechanisms of hydrocarbons in zeolites- I. Theory, *Chem. Eng. Sci.*, 47 (1992) 1123-1141
27. J. Xiao, J. Wei, Diffusion mechanisms of hydrocarbons in zeolites- II. Analysis of experimental observations, *Chem. Eng. Sci.*, 47 (1992) 1143-1159
28. P. Pandey, R. S. Chauhan, Membranes for gas separation, *Prog. Polym. Sci.*, 26 (2001) 853-893
29. J. G. Wijmans, R. W. Baker, The solution-diffusion model: a review, *J. Membr. Sci.* 107 (1995) 1-21
30. N. W. Ockwig, T. M. Nenoff, Membranes for hydrogen separation, *Chem. Rev.* 107 (2007) 4078-4110

31. J. K. Mitchel, On the penetrativeness of fluids, *J. Membr. Sci.*, 100 (1995) 11-16
32. L. M. Robeson, Correlation of separation factor versus permeability for polymeric membranes, *J. Membr. Sci.*, 62 (1991) 165-185
33. I. Pinnau, B. D. Freeman, Formation and modification of polymeric membranes, ACS Symposium Series; American Chemical Society: Washington, DC (1999) 1-22
34. R. M. de Vos, H. Verweij, Improved performance of silica membranes for gas separation, *J. Membr. Sci.*, 143 (1998) 37-51
35. Ø. Hatlevik, S. K. Gade, M. K. Keeling, P. M. Thoen, A. P. Davidson, J. D. Way, Palladium and palladium alloy membranes for hydrogen separation and production: History, fabrication strategies, and current performance, *Sep. Purif. Technol.* 73 (2010) 59–64
36. Z. Tang, J. Dong, T. M. Nenoff, Internal Surface Modification of MFI-Type Zeolite Membranes for High Selectivity and High Flux for Hydrogen, *Langmuir* 25 (2009) 4848–4852
37. R. J. Young, P. A. Lovell, Introduction to polymers, CRC Press, Taylor and Francis Group, Boca Raton, 2011.
38. M. R. Abdul Hamid, H.-K. Jeong, Recent advances on mixed-matrix membranes fro gas separation: opportunities and engineering challenges, *Korean J. Chem. Eng.*, 35 (2018) 1577-1600
39. G. Dong, H. Li, V. Chen, Challenges and opportunities for mixed-matrix membranes for gas separation, *J. Mater. Chem. A*, 1 (2013) 4610-4630
40. X. Feng, P. Shao, R. Y. M. Huang, G. Jiang, and R. -X. Xu, A study of silicone rubber/polysulfone composite membranes: correlating H₂/N₂ and O₂/N₂ permselectivities, *Sep. Purif. Technol.* 27 (2002) 211-223
41. L. M. Robeson, Polymer membranes for gas separation, *Curr. Opin. Solid St. M.* 4 (1999) 549-552

42. L. M. Robeson, The upper bound revisited, *J. Membr. Sci.*, 320 (2008) 390-400
43. M. Galizia, W. S. Chi, Z. P. Smith, T. C. Merkel, R. W. Baker, B. D. Freeman, 50th anniversary perspective: polymers and mixed matrix membranes for gas and vapor separation: a review and prospective opportunities, *Macromolecules*, 50 (2017) 7809-7843
44. D. F. Sanders, Z. P. Smith, R. Guo, L. M. Robeson, J. E. McGrath, D. R. Paul, B. D. Freeman, Energy-efficient polymeric gas separation membranes for a sustainable future: a review, *Polymer* 54 (2013) 4729-4761
45. H. Verweij, Inorganic membranes, *Curr. Opin. Chem. Eng.* 1 (2012) 156–162
46. G. Q. Lu, J. C. Diniz da Costa, M. Duke, S. Giessler, R. Socolow, R. H. Williams, T. Kreutz, Inorganic membranes for hydrogen production and purification: a critical review and perspective, *J. Colloid Interf. Sci.* 314 (2007) 589–603
47. Y. S. Lin, Microporous and dense inorganic membranes: current status and prospective, *Sep. Purif. Technol.* 25 (2001) 39–55
48. G. Cao, Y. Lu, L. Delattre, C. J. Brinker, G. P. Lopez, Amorphous silica molecular sieving membranes by sol-gel processing, *Adv. Mater.* 8 (1996) 588-591
49. Y. Iwamoto, K. Sato, T. Kato, T. Inada, Y. Kubo, A hydrogen-permselective amorphous silica membrane derived from polysilazane, *J. Eur. Ceram. Soc.* 25 (2005) 257–264
50. T. Tsuru, T. Morita, H. Shintani, T. Yoshioka, M. Asaeda, Membrane reactor performance of steam reforming of methane using hydrogen-permselective catalytic SiO₂ membranes, *J. Membr. Sci.*, 316 (2007) 53-62
51. G. Li, M. Kanezashi, T. Yoshioka, T. Tsuru, Ammonia decomposition in catalytic membrane reactors: simulation and experimental studies, *AIChE J.* 59 (2013) 168-179
52. A. Tավարո, E. Drioli, Zeolite membranes, *Adv. Mater.*, 11 (1999)975-996

53. J. Caro, M. Noack, P. Kolsch, R. Schafer, Zeolite membranes - state of their development and perspective, *Micropor. Mesopor. Mat.* 38 (2000) 3-24
54. J. Caro, M. Noack, Zeolite membranes – recent developments and progress, *Micropor. Mesopor. Mat.* 115 (2008) 215–233
55. N. Rangnekar, N. Mittal, B. Elyassi, J. Caro and M. Tsapatsis, Zeolite membranes – a review and comparison with MOFs, *Chem. Soc. Rev.*, 44 (2015) 7128—7154
56. H. P. Hsieh, R. R. Bhave, H. L. Fleming, Microporous alumina membranes, *J. Membr. Sci.*, 39 (1988) 221-241
57. A. F. M. Leenaars, K. Keizer, A. J. Burggraaf, The preparation and characterization of alumina membranes with ultra-fine pores. Part 1- Microstructural investigations on non-supported membranes, *J. Mater. Sci.* 19 (1984) 1077-1088
58. N. A. Al-Mufachi, N. V. Rees, R. Steinberger-Wilkens, Hydrogen selective membranes: a review of palladium-based dense metal membranes, *Renew. Sust. Energ. Rev.* 47 (2015) 540–551
59. N. M. Peachey, R. C. Snow, R. C. Dye, Composite Pd/Ta metal membranes for hydrogen separation, *J. Membr. Sci.*, 111 (1996) 123-133
60. T. A. Peters, T. Kaleta, M. Stange, R. Bredesen, Development of thin binary and ternary Pd-based alloy membranes for use in hydrogen production, *J. Membr. Sci.*, 383 (2011) 124– 134
61. N. Pezeshk, D. Rana, R.M. Narbaitz, T. Matsuura, Novel modified PVDF ultrafiltration flat-sheet membranes, *J. Membr. Sci.*, 389 (2012) 280– 286
62. J. Wei, C. Qiu, C. Y. Tang, R. Wang, A. G. Fane, Synthesis and characterization of flat-sheet thin film composite forward osmosis membranes, *J. Membr. Sci.*, 372 (2011) 292–302
63. M. Tomaszewska, Preparation and properties of flat-sheet membranes from poly(vinylidene fluoride) for membrane distillation, *Desalination* 104 (1996) 1-11

64. I. U. Khan, M. H. D. Othman, A. F. Ismail, T. Matsuura, H. Hashim, N. Abdul Hadi Md Nordin, M. A. Rahman, J. Jaafar, A. Jilania, Status and improvement of dual-layer hollow fiber membranes via coextrusion process for gas separation: a review, *J. Nat. Gas Sci. Eng.*, 52 (2018) 215–234
65. X. Y. Chen, S. Kaliaguine, D. Rodrigue, A Comparison between Several Commercial Polymer Hollow Fiber Membranes for Gas Separation, *Journal of Membrane and Separation Technology*, 6 (2017) 1-15
66. L. Lei, F. Pan, A. Lindbrathen, X. Zhang, M. Hillestad, Y. Nie, L. Bai, X. He, M. D. Guiver, Carbon hollow fiber membranes for a molecular sieve with precise-cutoff ultramicropores for superior hydrogen separation, *Nat. Comm.*, 12 (2021) 268
67. X. Tan, S. Liu, K. Li, Preparation and characterization of inorganic hollow fiber membranes, *J. Membr. Sci.*, 188 (2001) 87–95
68. S. Kumbar, T. Selvam, C. Gellermann, W. Storch, T. Ballweg, J. Breu, G. Sextl, ORMOCERs (organic-inorganic hybrid copolymers)-zeolite beta (BEA) nanocomposite membranes for gas separation applications, *J. Membr. Sci.*, 347 (2010) 132-140
69. H. Lu, S. Zhu, Interfacial synthesis of free-standing metal–organic framework membranes, *Eur. J. Inorg. Chem.* (2013) 1294–1300
70. J. A. van 't Hof, A. J. Reuvers, R. M. Boom, H. H. M. Rolevink, C. A. Smolders, Preparation of asymmetric gas separation membranes with high selectivity by a dual-bath coagulation method, *J. Membr. Sci.*, 70 (1992) 17-30
71. J. Caro, Hierarchy in inorganic membranes, *Chem. Soc. Rev.*, 45 (2016) 3468
72. W. J. Koros, Evolving beyond the thermal age of separation processes: membranes can lead the way. *AIChE J.*, 50 (2004) 2326-2334
73. W. J. Koros, A more aggressive approach is needed for gas separation membrane development. *Membrane*, 31 (2006) 157-160
74. N. Moriyama, H. Nagasawa, M. Kanezashi, K. Ito, T. Tsuru, Bis(triethoxysilyl)ethane (BTESE)-derived silica membranes: pore formation

- mechanism and gas permeation properties, *J. Sol-Gel Sci. Technol.*, 86 (2018) 63-72
75. H. F. Qureshi, R. Besselink, J. E. ten Elshof, A. Nijmeijer, L. Winnubst, Doped microporous hybrid silica membranes for gas separation, *J Sol-Gel Sci Technol* 75 (2015) 180–188
76. M. Kanezashi, W. N. Shazwani, T. Yoshioka, T. Tsuru, Separation of propylene/propane binary mixtures by bis(triethoxysilyl)methane (BTESM)-derived silica membranes fabricated at different calcination temperatures, *J. Membr. Sci.*, 415–416 (2012) 478–485
77. R. Inoue, M. Kanezashi, H. Nagasawa, K. Yamamoto, T. Gunji, T. Tsuru, Pore size tuning of bis(triethoxysilyl)propane (BTESP)-derived membrane for gas separation: Effects of the acid molar ratio in the sol and of the calcination temperature, *Sep. Purif. Technol.*, 242 (2020) 116742
78. M. Guo, M. Kanezashi, H. Nagasawa, L. Yu, K. Yamamoto, T. Gunji, J. Ohshita, T. Tsuru, Tailoring the microstructure and permeation properties of bridged organosilica membranes via control of the bond angles, *J. Membr. Sci.*, 584 (2019) 56–65
79. C. M. Zimmerman, A. Singh, W. J. Koros, Tailoring mixed matrix composite membranes for gas separations, *J. Membr. Sci.*, 137 (1997) 145-154
80. M. A. Aroon, A. F. Ismail, T. Matsuura, M. M. Montazer-Rahmati, Performance studies of mixed matrix membranes for gas separation: a review, *Sep. Purif. Technol.*, 75 (2010) 229-242
81. P. S. Goh, A. F. Ismail, S. M. Sanip, B. C. Ng, M. Aziz, Recent advances of inorganic fillers in mixed matrix membrane for gas separation, *Sep. Purif. Technol.*, 81 (2011) 243–264
82. H. Vinh-Thang, S. Kaliaguine, Predictive models for mixed-matrix membrane performance: a review, *Chem. Rev.* 113 (2013) 4980–5028
83. M. Kanezashi, M. Asaeda, Hydrogen permeation characteristics and stability of Ni-doped silica membranes in steam at high temperature, *J. Membr. Sci.*, 271 (2006) 86–93
84. D. Uhlmann, S. Liu, B. P. Ladewig, J. C. Diniz da Costa, Cobalt-doped silica membranes for gas separation, *J. Membr. Sci.*, 326 (2009) 316–321

85. M. Takenaka, H. Nagasawa, T. Tsuru, M. Kanezashi, Hydrocarbon permeation properties through microporous fluorine-doped organosilica membranes with controlled pore sizes, *J. Membr. Sci.*, 619 (2021) 118787
86. M. Kanezashi, M. Murata, H. Nagasawa, T. Tsuru, Fluorine doping of microporous organosilica membranes for pore size control and enhanced hydrophobic properties, *ACS Omega* 3 (2018) 8612–8620
87. M. Kanezashi, T. Matsutani, H. Nagasawa, T. Tsuru, Fluorine-induced microporous silica membranes: Dramatic improvement in hydrothermal stability and pore size controllability for highly permeable propylene/propane separation, *J. Membr. Sci.*, 549 (2018) 111–119
88. M. Kanezashi, N. Hataoka, R. Ikram, H. Nagasawa, T. Tsuru, Hydrothermal stability of fluorine-induced microporous silica membranes: effect of steam treatment conditions, *AIChE J.* (2021) e17292.
89. J. Yanga, W. Fana, C.-M. Bell, Effect of calcination atmosphere on microstructure and H₂/CO₂ separation of palladium-doped silica membranes, *Sep. Purif. Technol.*, 210 (2019) 659–669
90. M. Kanezashi, M. Sano, T. Yoshioka, T. Tsuru, Extremely thin Pd–silica mixed-matrix membranes with nano-dispersion for improved hydrogen permeability, *Chem. Commun.*, 46 (2010) 6171–6173
91. K. Yoshida, Y. Hirano, H. Fujii, T. Tsuru, M. Asaeda, Hydrothermal stability and performance of silica-zirconia membranes for hydrogen separation in hydrothermal conditions, *J. Chem. Eng. Jpn.*, 34 (2001) 523-530
92. H.-S. Choi, C.-H. Ryu, G.-B. Hwang, Obtention of ZrO₂-SiO₂ hydrogen permselective membrane by chemical vapor deposition method, *Chem. Eng. J.*, 232 (2013) 302-309
93. S.-J. Ahn, A. Takagaki, T. Sugawara, R. Kikuchi, S. T. Oyama, Permeation properties of silica-zirconia composite membranes supported on porous alumina substrates, *J. Membr. Sci.*, 526 (2017) 409-416
94. S. Anisah, W. Puthai, M. Kanezashi, H. Nagasawa, T. Tsuru, Preparation, characterization, and evaluation of TiO₂-ZrO₂ nanofiltration membranes fired

- at different temperatures, *J. Membr. Sci.*, 564 (2018) 691-699.
95. S. Anisah, M. Kanezashi, H. Nagasawa, T. Tsuru, Hydrothermal stability and permeation of TiO₂-ZrO₂ (5/5) nanofiltration membranes at high temperatures, *Sep. Purif. Technol.*, 212 (2019) 1001-1012.
96. H. Guo, S. Zhao, X. Wu, H. Qi, Fabrication and characterization of TiO₂/ZrO₂ ceramic membranes for nanofiltration, *Micropor. Mesopor. Mater.* 260 (2018) 125–131.
97. C. Guizard, A. Ayrat, A. Julbe, Potentiality of organic solvents filtration with ceramic membranes. A comparison with polymer membranes, *Desalination* 147 (2002) 275-280
98. P. Judeinstein, C. Sanchez, Hybrid organic-inorganic materials: a land of multidisciplinary, *J. Mater. Chem.*, 6 (1996) 511-525
99. C. Sanchez, J. de A. A. Soler-Illia, F. Ribot, T. Lalot, C. R. Mayer, V. Cabuil, Designed Hybrid organic-inorganic nanocomposites from functional nanobuilding blocks, *Chem. Mater.*, 13 (2001) 3061-3083
100. K. Nakahiro, L. Yu, H. Nagasawa, T. Tsuru, M. Kanezashi, Pore structure controllability and CO₂ permeation properties of silica-derived membranes with a dual-network structure, *Ind. Eng. Chem. Res.*, 60 (2021) 8527–8537
101. H. L. Castricum, A. Sah, R. Kreiter, D. H. A. Blank, J. F. Vente, J. E. ten Elshof, Hydrothermally stable molecular separation membranes from organically linked silica, *J. Mater.Chem.*, 18 (2008) 2150-2158
102. N. K. Raman, C. J. Brinker, Organic “template” approach to molecular sieving silica membranes, *J. Membr. Sci.*, 105 (1995) 273-279
103. M. Kanezashi, M. Kawano, T. Yoshioka, T. Tsuru, Organic-inorganic hybrid silica membranes with controlled silica network size for propylene/propane separation, *Ind. Eng. Chem. Res.* 51 (2012) 944-953
104. L. Yu, M. Kanezashi, H. Nagasawa, J. Oshita, A. Naka, T. Tsuru, Pyrimidine-bridged organoalkoxysilane membrane for high-efficiency CO₂ transport via mild affinity, *Sep. Purif. Technol.*, 178 (2017) 232-241
105. M. Asaeda, Y. Sakou, J. Yang, K. Shimasaki, Stability and performance of porous silica-zirconia composite membranes for pervaporation of aqueous organic solutions, *J. Membr. Sci.* 209 (2002) 163-175.

106. W. Puthai, M. Kanezashi, H. Nagasawa, K. Wakamura, H. Ohnishi, T. Tsuru, Effect of firing temperature on water permeability of SiO₂-ZrO₂ membranes for nanofiltration, *J. Membr. Sci.* 497 (2016) 348-356.
107. W. Puthai, M. Kanezashi, H. Nagasawa, T. Tsuru, SiO₂-ZrO₂ nanofiltration membranes of different Si/Zr molar ratios: stability in hot water and acid/alkaline solutions, *J. Membr. Sci.* 524 (2017) 700-711.
108. A. P. Dral, J. E. ten Elshof, Organic groups influencing microporosity in organosilicas, *Micropor. Mesopor. Mater.* 267 (2018) 267–273
109. H. L. Castricum, G. G. Paradis, M. C. Mittelmeijer-Hazeleger, R. Kreiter, J. F. Vente, J. E. ten Elshof, Tailoring the separation behavior of hybrid organosilica membranes by adjusting the structure of the organic bridging group, *Adv. Funct. Mater.* 21 (2011) 2319–2329
110. M. Kanezashi, Sol-Gel Derived Silica Membranes, *Encyclopedia of Membrane Science and Technology*, John Wiley and Sons, 2013
111. R. M. de Vos, H. Verweij, High-selectivity, high-flux silica membranes for gas separation, *Science*. 279 (1998) 1710-1711
112. M. ten Hove, M. W. J. Luiten-Olieman, C. Huiskes, A. Nijmeijer, L. Winnubst, Hydrothermal stability of silica, hybrid silica and Zr-doped hybrid silica membranes, *Sep. Purif. Technol.*, 189 (2017) 48–53
113. Q. Wei, F. Wang, Z.-R. Nie, C.-L. Song, Y.-L. Wang, Q.-Y. Li, Highly hydrothermally stable microporous silica membranes for hydrogen separation, *J. Phys. Chem. B*, 112 (2008) 9354–9359
114. M. Kanezashi, Y. Yoneda, H. Nagasawa, T. Tsuru, K. Yamamoto, J. Ohshita, Gas permeation properties for organosilica membranes with different Si/C ratios and evaluation of microporous structures, *AIChE J.* 63 (2017) 4491-4498.
115. Y. E. Lee, B. S. Kang, S. H. Hyun, C. H. Lee, Organic-templating approach to synthesis of nanoporous silica composite membranes (ii): MTES-templating and CO₂ separation, *Sep. Sci. Technol.*, 39 (2004) 3541–3557
116. B. N. Nair, K. Keizar, W. J. Elferink, M. J. Gilde, H. Verweij, A. J. Burggraaf, Synthesis, characterization and gas permeation studies on microporous silica

- and alumina-silica membranes for separation of propane and propylene, *J. Membr. Sci.*, 116 (1996) 161-169
117. Y. Gu, P. Hacırlıođlu, S. T. Oyama, Hydrothermally stable silica-alumina composite membranes for hydrogen separation, *J. Membr. Sci.*, 310 (2008) 28-37
118. M. Amanipour, E. G. Babakhani, A. Safekordi, A. Zamaniyan, M. Heidari, Effect of CVD parameters on hydrogen permeation properties in anano-composite $\text{SiO}_2\text{-Al}_2\text{O}_3$ membrane, *J. Membr. Sci.*, 423-424 (2012)530-535
119. Z.-Q. Zeng, X.-Y. Xiao, Z.-L. Gui, L.-T. Li, $\text{Al}_2\text{O}_3\text{-SiO}_2\text{-TiO}_2$ composite ceramic membranes from sol-gel processing, *Mater. Lett.*, 35 (1998) 67-71
120. D. A. Ward, E. I. Ko, Preparing catalytic materials by the sol-gel method, *Ind. Eng. Chem. Res.* 34 (1995) 421-433
121. J. Navarrete, T. Lopez, R. Gomez, Surface acidity of sulfated $\text{TiO}_2\text{-SiO}_2$ sol-gels, *Langmuir*, 12 (1996) 4385-4390
122. F. Garbassi, L. Balducci, R. Ungarelli, Sol-gel preparation and characterization of spherical $\text{ZrO}_2\text{-SiO}_2$ particles, *J. Non-Cryst. Solids*, 223 (1998) 190-199
123. T. Lopez, F. Tzompantzi, J. Navarrete, R. Gomez, J. L. Boldu', E. Mun~oz, O. Novaro, Free radical formation in $\text{ZrO}_2\text{-SiO}_2$ sol-gel derived catalysts, *J. Catal.*, 181 (1999) 285-293
124. Z.-G. Wu, Y.-X. Zhao, D.-S. Liu, The synthesis and characterization of mesoporous silica-zirconia aerogels, *Micropor. Mesopor. Mater.* 68 (2004) 127-132
125. Y.-S. Lin, C.-H. Chang, R. Gopalan, Improvement of thermal stability of porous nanostructured ceramic membranes, *Ind. Eng. Chem. Res.* 33 (1994) 860-870
126. J. Fan, H. Ohya, T. Suga, H. Ohashi, K. Yamashita, S. Tsuchiya, M. Aihara, T. Takeuchi, Y. Negishi, High flux zirconia composite membrane for hydrogen separation at elevated temperature, *J. Membr. Sci.*, 170 (2000) 113-125

127. T. Van Gestel, D. Sebold, F. Hauler, W. A. Meulenbergh, H.-P. Buchkremer, Potentialities of microporous membranes for H₂/CO₂ separation in future fossil fuel power plants: evaluation of SiO₂, ZrO₂, Y₂O₃-ZrO₂ and TiO₂-ZrO₂ sol-gel membranes, *J. Membr. Sci.*, 359 (2010) 64-79
128. H. Guo, S. Zhao, X. Wu, H. Qi, Fabrication and characterization of TiO₂/ZrO₂ ceramic membranes for nanofiltration, *Micropor. Mesopor. Mater.*, 260 (2018) 125-131
129. Y. Sada, T. Yoshioka, K. Nakagawa, T. Shintani, R. Iesako, E. Kamio, H. Matsuyama, Preparation and characterization of organic chelate ligand (OCL)-templated TiO₂-ZrO₂ nanofiltration membranes, *J. Membr. Sci.*, 591 (2019) 117304
130. C. A. Milea, C. Bogatu, A. Duta, The influence of parameters in silica sol-gel process, in: *Bulletin of the Transilvania University of Brasov, Series I: Engineering sciences*, 4 (2011) 59-66
131. C. Sanchez, J. Livage, M. Henry, F. Babonneau, Chemical modification of alkoxide precursors, *J. Non-Cryst. Solids*, 100 (1988) 65-76
132. J. Livage, C. Sanchez, Sol-gel chemistry, *J. Non-Cryst. Solids.*, 145 (1992) 11-19
133. J. Livage, M. Henry, C. Sanchez, Sol-gel chemistry of transition metal oxides, *Prog. Solid St. Chem.*, 18 (1988) 25-341
134. H.-J. Chen, L. Wang, W.-Y. Chiu, Chelation and solvent effect on the preparation of titania colloids, *Mater. Chem. Phys.*, 101 (2007) 12-19
135. R. J. Errington, J. Ridland, W. Clegg, R. A. Coxall, J. M. Sherwood, β -diketonate derivatives of titanium alkoxides: x-ray crystal structures and solution dynamics of the binuclear complexes [$\{\text{Ti}(\text{OR})_3(\text{dik})\}_2$], *Polvhedron*, 17 (1998) 659-674
136. S. Kurajica, I. Skoric, I. Lozic, V. Mandic, Ethyl acetoacetate ligand distribution in the course of titanium *n*-butoxide chelation, *Mater. Chem. Phys.*, 147 (2014) 1058-1067

137. D. Peter, T. S. Ertel, H. Bertagnolli, EXAFS study of zirconium alkoxides as precursors in sol-gel process: II. The influence of the chemical modification, *J. Sol-Gel Sci. Technol.*, 5 (1995) 5-14
138. D. Hoebbel, T. Reinert, H. Schmidt, E. Arpac, On the hydrolytic stability of organic ligands in Al-, Ti- and Zr-alkoxide complexes, *J. Sol-Gel Sci. Technol.*, 10 (1997) 115-126
139. H. Schmidt, Preparation, application and potential of ORMOCERs, Sol-gel: science and technology; proceedings of the winter school on glass and ceramics from gels, São Carlos (SP), Brazil, 14 - 19 August 1989. Ed. by M. A. Aegerter. Singapore: World Scientific, (1989) 432-469
140. C. Sanchez, J. de A. A. Soler-Illia, F. Ribot, T. Lalot, C. R. Mayer, V. Cabuil, Designed Hybrid organic-inorganic nanocomposites from functional nanobuilding blocks. *Chem. Mater.*, 13 (2001) 3061-3083
141. T. Fukumoto, T. Yoshioka, H. Nagasawa, M. Kanezashi, T. Tsuru, Development and gas permeation properties of microporous amorphous TiO₂-ZrO₂-organic composite membranes using chelating ligands, *J. Membr. Sci.*, 461 (2014) 96-105.
142. G. I. Spijksma, C. Huiskes, N. E. Benes, H. Kruidhof, D. H. A. Blank, V. G. Kessler, H. J. M. Bouwmeester, Microporous zirconia–titania composite membranes derived from diethanolamine-modified precursors, *Adv. Mater.*, 18 (2006) 2165–2168
143. G. Klopman, A semiempirical treatment of molecular structures. I. electronegativity and atomic terms, *J. Am. Chem. Soc.*, 86 (1964) 1463-1469
144. W. H. Stockmayer, Theory of molecular size distribution and gel formation in branched-chain polymers, *J. Chem. Phys.*, 11 (1943) 45-55
145. S. Benfer, U. Popp, H. Richter, C. Siewert, G. Tomandl, Development and characterization of ceramic nanofiltration membranes, *Sep. Purif. Technol.*, 22-23 (2001) 231–237
146. T. Tachibana, T. Yoshioka, K. Nakagawa, T. Shintani, E. Kamio, H. Matsuyama, Gas permeation characteristics of TiO₂-ZrO₂-aromatic organic chelating ligand (aOCL) composite membranes, *Membranes*, 10 (2020) 388
147. J. Mendez-Vivar, R. Mendoza-Serna, SiO₂-TiO₂ membranes by the sol-gel process, *Silicon Chemistry* 3 (2006) 59–64

Chapter 2

Development of a molecular sieving membrane from an acetylacetonate-modified silica-zirconia ceramic composite

2.1 Introduction

The quest for a highly efficient and cost-effective means for separating important gases and liquids has gained prominence in the field of separation technology in the past century. Such research efforts have successfully yielded a variety of techniques such as membrane separation technology, which has attracted the most interest [1]. Inorganic membranes are currently in great demand for use in H₂ [2-5, 6], CO₂/CH₄ [7, 8], and CO₂/N₂ [9, 10] separation systems, as well as in olefin/paraffin systems [11, 12] and in the purification of natural gas [11]. Inorganic membranes can be broadly divided into porous and dense versions. Whereas dense membranes such as those fabricated from palladium and its alloys offer separation ability via a solution-diffusion mechanism, porous inorganic membranes such as silica, alumina, and zirconia separate gases by selective passage of molecules through a network of pores according to their size. Palladium membranes have shown high H₂ permeance, but they are difficult to fabricate and are plagued by high module costs [13, 22]. A mixed-matrix membrane consisting of palladium or palladium-cobalt particles dispersed in a network of amorphous inorganic silica is also possible as already reported by Kanezashi [14] and Ballinger *et al.* [15].

Much interest has been shown to inorganic amorphous membranes and their derivatives concerning their potential application to a wide variety of gas separation systems in general [2-11], and in particular to hydrogen separation due to their ease of fabrication, low cost of production and scalability [1]. Factors required for a perm-selective membrane are high flux, high selectivity, pore size controllability, and good physical and chemical stability. Silica membranes exhibit moderately high flux and excellent selectivity [14, 16, 17], but size control and instability under hydrothermal conditions are known problems [14]. To develop silica and silica-based membranes with high perm-selectivity, pore size tunability, and hydrothermal stability, many researchers have studied various techniques such as spacer methods [18, 19],

templating methods [20], anion and cation doping [6, 16, 23], and hybridization of silica with other metal oxides such as Al_2O_3 [12, 24], TiO_2 [25, 26], and ZrO_2 [5, 21].

Hybridization of silica with proven hydrothermally stable metal oxides such as TiO_2 and ZrO_2 has been studied extensively [1, 5, 21, 26, 27]. Hybrid SiO_2 - ZrO_2 membranes have been used for pervaporation and nanofiltration applications [27, 28]. Hydrogen separation performance of SiO_2 - ZrO_2 hybrid membranes fabricated through chemical vapor deposition (CVD) has also been investigated [5]. Zirconium oxide added to silica in an equi-molar ratio has shown the best hydrothermal stability to moderately high temperatures, but perm-selectivity remains very poor due to the large pore size created by adding a high zirconia content [21]. The large pores permit both large and small molecules to permeate as in Knudsen flow [29, 30]. However, a further modification to this network structure offers the possibility to change the molecular sieving characteristics of silica-zirconia (1:1) composite membranes.

In the fields of catalysis and separation technology, the versatility of sol-gel chemistry has been instrumental to the formation of new functional materials. One major aspect of this versatility is the ability to obtain products with predetermined characteristics based on the experimental conditions, and another aspect is that it allows for the synthesis of inorganic-organic hybrid materials through the introduction of organic groups in solution [31]. One way to add an organic group is to chemically modify a precursor prior to synthesis [32]. A good example of chemically modifying precursors is found in the use of chelating ligands to form coordinate complexes where the precursor to be modified is a transition metal ion compound. Coordinate polymer chemistry has been widely studied and found to be useful in synthesizing metal-organic frameworks (MOFs) [33-35]. Coordinate covalent bonds are formed in coordinate complexes by the occupation of d-orbitals belonging to a transition metal by free electron pairs donated by chelating ligands. For polydentate ligands, Metal-Organic Frameworks (MOFs) usually result [33-35]. In the case of mono- or bidentate ligands, MOFs are rarely formed [36, 37] and the formation of the coordinate complex chains will require other polymerization sites.

The formation of coordination complexes between zirconium ions and various chelating ligands has been studied [36, 38] with the most hydrolytically stable being the use of acetylacetonate (Hacac), a bidentate ligand, to form an acetylacetonate-

zirconium coordination complex [38], which implies the retention of acetylacetonate anions in the polymer sol even after hydrolysis and condensation have occurred for several hours. As such, a hydrolytically stable modified zirconium precursor can be co-polymerized and co-condensed with silica to achieve an acac⁻-modified equi-molar SiO₂-ZrO₂ polymer sol. The acetylacetonate ligand remaining in the modified SiO₂-ZrO₂ (1:1) is expected to translate into a modified pore structure applicable to gas separation. This possibility has been reported by both Fukumoto *et al.* [50] and Spijksma *et al.* [51], where the pore sizes of TiO₂-ZrO₂ were controlled using isoeugenol (isoH) and diethanolamine (DEA), respectively.

To study the possibility of a chemically modified silica-zirconia (1:1) membrane for gas separation applications, acetylacetonate-modified silica-zirconia (1:1) was prepared by the sol-gel method and used to fabricate a membrane. Single-gas permeation measurements were subsequently performed. Fig. 2-1 schematically shows the theoretical modification of zirconium tetra butoxide with acetylacetonate and the subsequent formation of an acac⁻-modified Si-O-Zr network. Theoretically, acetylacetonate is a bidentate ligand with two sites through which it can bond to transition metal zirconium ions in order to form a normal covalent bond with zirconium through one of the oxygen atoms and a coordinate covalent bond by donating a free pair of electrons from the other oxygen atoms that occupy the empty d-orbital. This theory assumes that acetylacetonate approaches the zirconium ions in its enol tautomer [36]. Furthermore, the thermal stability of the acetylacetonate modifying ligand was examined, and the pore modification effect that the addition of acetylacetonate ligands and heat-treatment exerted on the pore structure and on the gas permeation characteristics were explored. Activation energies were used to compare the SiO₂-ZrO₂-acac₂ (SZA₂) membrane performance with that of both a polymer membrane and a ligand-modified TiO₂-ZrO₂ membrane.

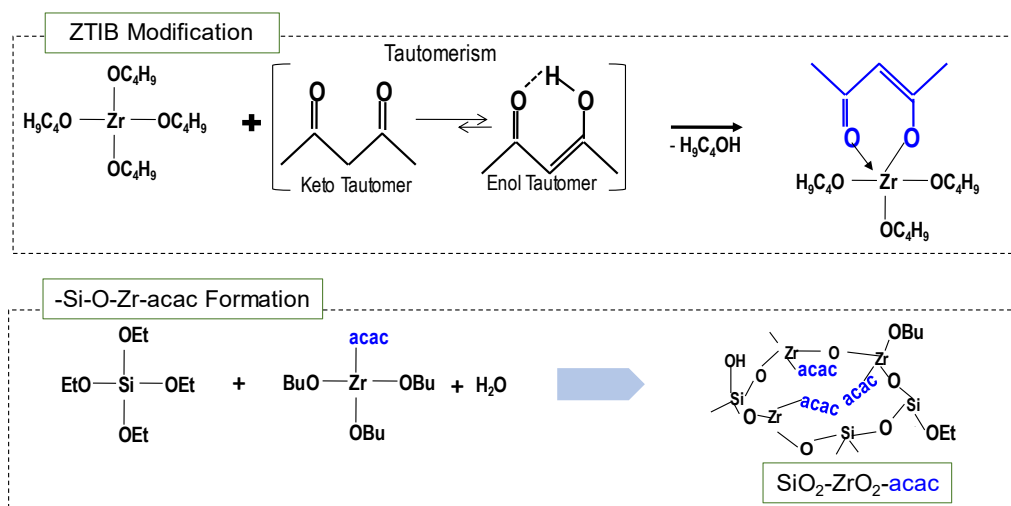


Fig. 2-1 Theoretical formation of the -Si-O-Zr-acac linkages in a polymer sol

2.2 Experimental

2.2.1 Preparation of $\text{SiO}_2\text{-ZrO}_2\text{-acac}_2$ sol and membrane fabrication

A 5 wt% modified $\text{SiO}_2\text{-ZrO}_2$ (1:1) polymeric sol (referred to as SZa₂ sol in later sections) and membranes were prepared and fabricated according to the following procedures. Modified $\text{SiO}_2\text{-ZrO}_2$ (1:1) sol was prepared in two stages. In the first stage, an 80% pure zirconium (iv) tert-butoxide (Aldrich) dissolved in ethanol (Aldrich) was modified by reacting with 99% pure acetylacetone (Aldrich) (ligand/ZrTB molar ratio 2) for one hour in the proportions listed in Table 2-1. In the second stage, a solution of 98% pure tetraethoxysilane (Aldrich) in ethanol was co-hydrolyzed with acetylacetone-modified zirconium (iv) tert-butoxide in a molar ratio of 1:1 using deionized water (water/ZrTB molar ratio 4) and hydrochloric acid (37%, Nacalai Tesque) as a catalyst (acid/alkoxide molar ratio 0.25). Hydrolysis and polycondensation were carried out by stirring the mixture at 500 rpm for more than 12 hours at room temperature.

In a similar manner, without pre-modification of zirconium (iv) tert-butoxide, a 5 wt% unmodified $\text{SiO}_2\text{-ZrO}_2$ (1:1) polymeric sol (referred to as SZ sol in later sections) was prepared in a process that required only one stage. The chemical reagents and their respective proportions are also summarized in Table 2-1. Dried gels were prepared by drying the sols slowly at a temperature of about 50 °C for a few days.

Table 2-1. Composition of chemical reagents and precursors for 5 wt% polymeric sol preparation

Sol Type (Ligand/Alkoxide)	Amount of Sol Precursors and Reagents [g]					
	TEOS	ZrTB	EtOH	Water (WR=4)	HCl (AR=0.25)	Hacac
0:1	1.77	4.06	94	0.61	0.207	0
2:1	1.77	4.06	94	0.61	0.207	1.7

SiO₂-ZrO₂-acac₂ membranes were fabricated by coating 3 graded layers of different suspensions/sols onto cylindrical α -alumina porous supports (60% porosity; 1.2 μ m pore size; outer diameter, 1 cm; and, length, 10 cm; Nikkato Corporation, Japan) connected to non-porous supports that were closed and open at either end. The first layer was prepared by coating a 10 wt% suspension of α -alumina particles (diameter 2-3 μ m and 0.2 μ m) onto a colloidal SiO₂-ZrO₂ sol for use as a binder prepared by ultrasonification. The preparation of colloidal SiO₂-ZrO₂ sol has been described elsewhere [28]. Each coating was repeated 6 times, and each coating was fired to a temperature of 550 °C for 15 – 20 min to solidify and bind the particle layer to the support and to cover the larger pores of the porous alumina support.

Next, pure SiO₂-ZrO₂ (1:1) sol diluted to 0.5 wt% with deionized water was coated onto the α -alumina particle layers using a hot coating method to form an intermediate layer, where the membrane was pre-heated to about 200 °C, and then coated almost immediately with the SiO₂-ZrO₂ sol followed by firing at 550 °C for 15 – 20 min to bind the intermediate layer to the particle layer. This process was repeated several times until large pores and defects from the particle layer were covered and a narrow pore size distribution suitable for the separation layer coating was achieved. The pore size distribution was obtained by nanoporometry [39]. The top separation layer was comprised of the acetylacetonate-modified SiO₂-ZrO₂ (1:1) polymeric sol (derived from diluting the as-prepared sol to 0.5 wt% in ethanol) coated onto the SiO₂-ZrO₂ intermediate layer followed by firing under a 600 ml min⁻¹ nitrogen gas flow at 250 °C for 15 min in a tube furnace. After this process was repeated 6 – 8 times, the membrane fabrication process was concluded, and the membranes were ready for single-gas permeation measurements. The same procedure

was followed for the fabrication of an unmodified SiO₂-ZrO₂ (1:1) membrane that was used for comparison.

2.2.2 Characterizations of the SiO₂-ZrO₂-acac₂, the SiO₂-ZrO₂ sol, the gel, and the membranes

The particle sizes of the as-prepared sols were analyzed at 25 °C via dynamic light scattering (DLS) using a Malvern Zetasizer Nano ZS (Malvern Instruments Ltd.). The presence and intensities of different functional groups were analyzed via Attenuated Total Reflection-Fourier Transform Infrared Spectroscopy (ATR-FTIR, FTIR-4100, JASCO, Japan). This analytical method was also used to track the thermal stability of ligands. Thermal stability of the acetylacetonate ligands in modified SiO₂-ZrO₂ was analyzed using thermogravimetry (TG, TG-50 Shimadzu Co., Japan) under a nitrogen gas flow of 80 ml min⁻¹ and a heating rate of 10 °C min⁻¹. The cross-section and surface morphologies were examined by Field Emission-Scanning Electron Microscopy (FE-SEM, Hitachi S-4800, Japan). Prior to examination, shared samples of the membranes were attached to sample holders via carbon tape and vacuum-dried at 50 °C for 48 hours.

2.2.3 Single-gas permeation measurements

A schematic representation of the gas permeation measurement setup is shown in Fig. 2-2. Prior to the gas permeation measurement, a membrane was fitted into its module immediately after fabrication and placed inside the furnace in the gas permeation measurement rig at a temperature of 150 or 200 °C under helium flow of 100 ml min⁻¹ for about 12 hours. This was done to ensure the removal of water adsorbed into the membrane pores after fabrication. To test for the molecular sieving properties of the membranes, high-purity gases (H₂, He, CO₂, N₂, CH₄, CF₄, SF₆ in that order) were flowed through molecular sieves to remove humidity and were then fed to the feed side of the membrane module at 100 kPa gauge pressure at temperatures ranging from 50 – 200 °C. Permeate side pressure was kept atmospheric and permeate gas flow was measured using a bubble film flow meter (HORIBA-STECC, Japan). Temperature dependence of gas permeance was examined by varying the temperature during the flow of a single gas and measuring the permeance flow at

each desired temperature. It should also be noted that permeate gas flow was only recorded after a steady state was attained.

Membrane heat-treatment was done by heating the membrane fired at 250 °C in the membrane module to a higher temperature (300, 400 or 550 °C) while flowing N₂ gas through the membrane. The flow of N₂ was maintained until a steady state was reached and the single-gas permeance was subsequently measured at 200 °C. This procedure was repeated for each heat-treatment temperature.

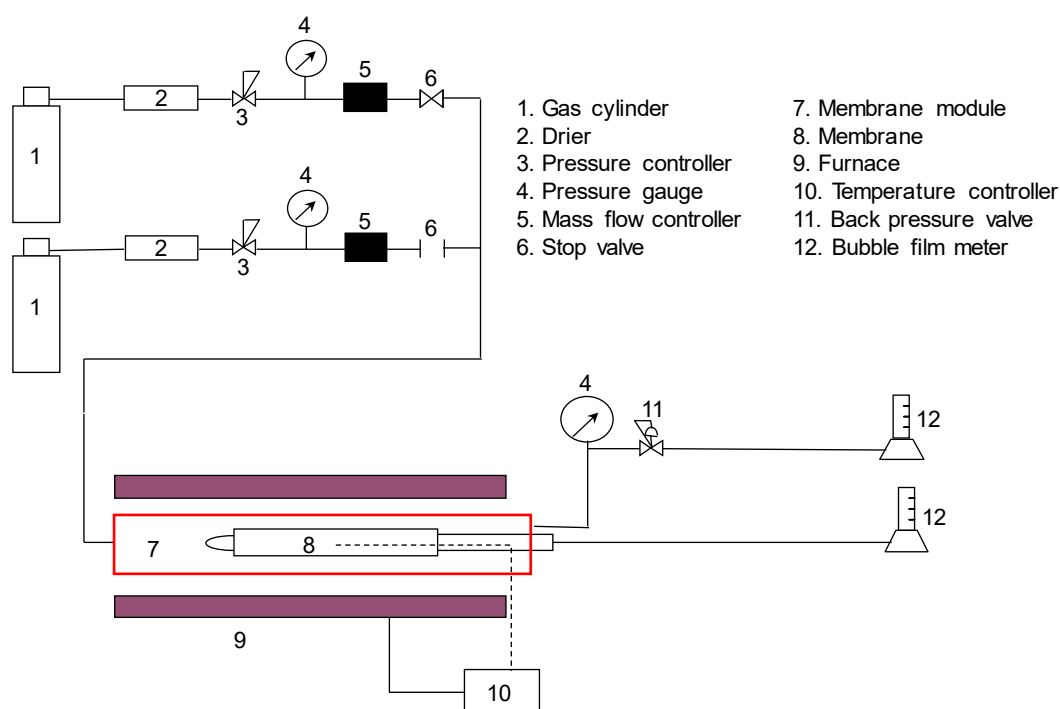


Fig. 2-2 Schematic diagram of single-gas permeation measurement.

2.3 Results and discussion

2.3.1 Sol-gel characterization

2.3.1.1 Chemical modification of a ZrTB precursor

Fig. 2-3 (a) shows the ATR-FTIR spectra of freshly prepared modified and pure zirconium tetrabutoxide precursors, measured directly on an ATR prism window that ranged from 4,000 to 500 cm⁻¹ compared with that of acetylacetone (Hacac). Peaks ranging from 1,700 to 1,500 cm⁻¹ are magnified for clarity in Fig. 2-3 (b). The two peaks that appear around 1,600 cm⁻¹ and 1,525 cm⁻¹ were assigned to the enol C=O

and C=C bonds that are characteristic of the acetone species [36, 38]. The presence of the C=C bond supports the assumption that Hacac approaches ZrTB in its enol tautomer. These peaks were not detected for the unmodified precursor and Hacac, which presented only the C=O (1615 cm^{-1}) peak of the keto tautomer. This clearly indicates the introduction of the acetylacetonate group to the chemical structure of zirconium tetrabutoxide. Furthermore, peaks assigned to the butoxide groups (-CH₂, -CH₃) in the range of $3,000$ to $2,750\text{ cm}^{-1}$ were observed for both modified and pure zirconium tetrabutoxide precursors, although different peak heights were exhibited. The -CH₂, -CH₃ peaks observed for the modified zirconium tetrabutoxide precursor were shorter than those observed for the unmodified precursor with representative absorbance peak ratios, A_{2960}/A_{1400} , of 0.29 and 0.56 for modified ZrTB and pure ZrTB, respectively. A_{2960} represents the absorbance peak height of a -CH₂ bond normalized by a common Zr-O-C peak observed at around A_{1400} ($1,400\text{ cm}^{-1}$). This indicates the replacement of some butoxy groups by the acetylacetonate groups that would have been otherwise present without modification.

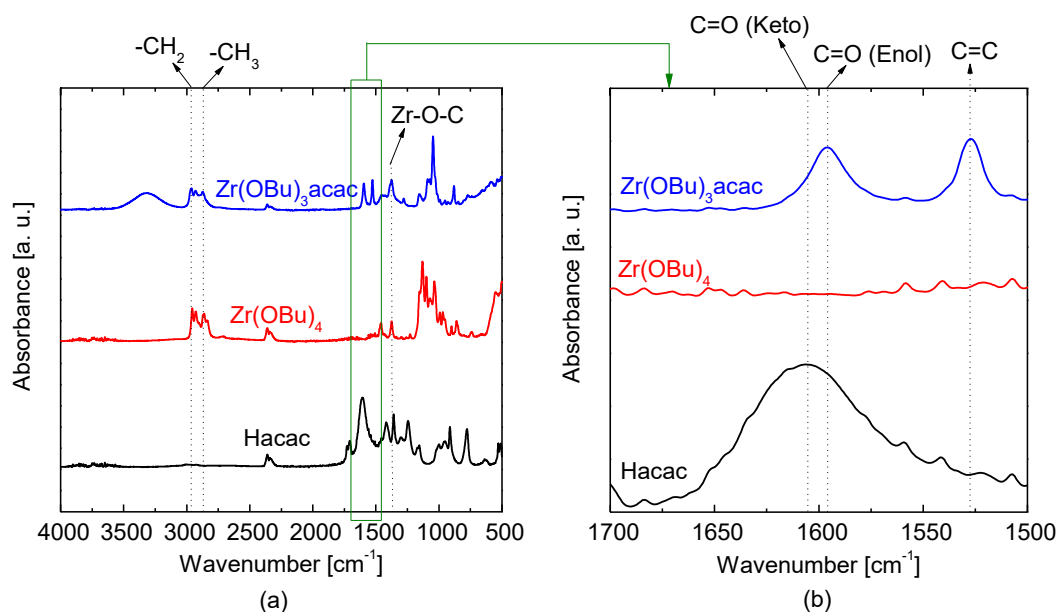


Fig. 2-3 ATR FT-IR spectra of ZrTB (zirconium tetrabutoxide) modification by acetylacetonate ligands ranging (a) from $4,000$ to 500 cm^{-1} and (b) from $1,700$ to $1,500\text{ cm}^{-1}$.

Fig. 2-4 also shows highly magnified ATR-FTIR spectra ranging from $1,700$ to 1500 cm^{-1} that compare modified zirconium tetrabutoxide, modified silica-zirconia,

and pure unmodified silica-zirconia sols. The C=O and C=C peaks characteristic of acetylacetonate ligands observed for the modified zirconium tetrabutoxide precursor were also detected for the modified silica-zirconia sol. This is an indication that the acetylacetonate-zirconium chelation structure was unaffected by the introduction of silica. Furthermore, the acetylacetonate characteristic peaks ($1,600\text{ cm}^{-1}$ and $1,525\text{ cm}^{-1}$) in the modified silica-zirconia sol were absent from the unmodified sol, which suggests that acac^- ligands are hydrolytically stable, and were not hydrolyzed by the addition of water under acidic conditions. This was previously observed during hydrolyzation of the acac-ZrTB coordinate complex polymer for several days [36]. The rate of ZrTB hydrolysis is much faster than that of TEOS, and one advantage of modifying the zirconium tetrabutoxide with a hydrolytically stable ligand prior to mixing with TEOS was that the hydrolysis rate of ZrTB was slowed considerably so that during co-hydrolysis of the ZrTB and TEOS mixtures, the rates of hydrolysis were similar, which improved the $-\text{Si-O-Zr}-$ composition degree [32].

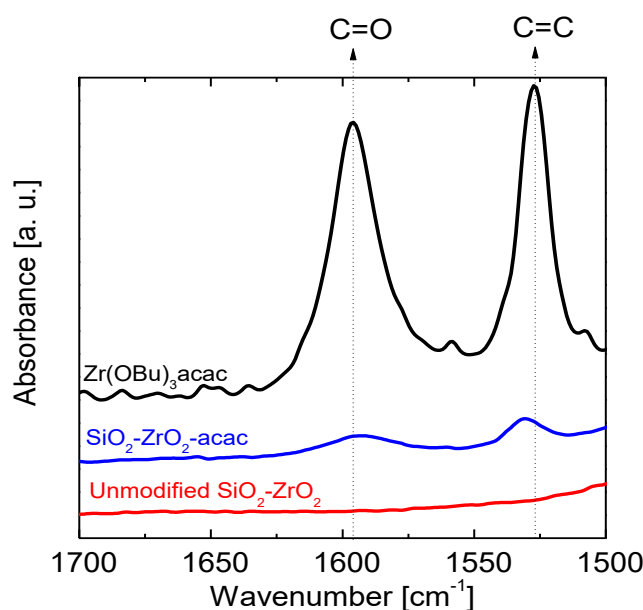


Fig. 2-4 ATR-FTIR spectra ranging from $1,700$ to $1,500\text{ cm}^{-1}$ for modified zirconium tetrabutoxide, modified silica-zirconia, and unmodified silica-zirconia sols.

2.3.1.2 Thermal analysis of acac^- ligands in $\text{SiO}_2\text{-ZrO}_2\text{-acac}_2$ gels

The hydrolytic stability of acac^- in the sol phase was expected, having been established in section 2.3.1.1, and this section discusses the thermal stability of the

acac⁻ ligands in the SZa₂ powder. The thermogravimetric (TG) curves of pure SiO₂-ZrO₂ and SiO₂-ZrO₂-acac₂ gels fired under a N₂ flow at temperatures as high as 1,000 °C (ramping rate: 10 °C min⁻¹) and the ATR-FTIR spectra of SZa₂ powders fired under N₂ at different temperatures are shown in Fig. 2-5. In Fig. 2-5 (a), the TG profile of SZa₂ powder can be divided into 3 sections according to their different slopes. Section i (100-300 °C) can be assigned to the decomposition of unhydrolyzed butoxy groups and to the partial decomposition of acetylacetonate linkages based on weight loss. This is supported by the ATR-FTIR profile of powders fired at different temperatures (Fig. 2-5 (b)).

In section ii (300 and 500 °C), pure SZ powder exhibited no further weight loss beyond 300 °C, indicating that weight loss was due only to the decomposition of unhydrolyzed butoxy groups. For SZa₂ powder, further weight loss was observed to a residual weight ratio that reached as high as 0.7, indicating the complete decomposition of acac ligands. This also appears in Fig. 2-5 (b) as the characteristic C=O and C=C bonds were decreased with temperature. Beyond 500 °C, as shown in section iii, free carbon from the decomposed acac⁻ ligands was released into the pore network, which resulted in no observed weight loss in this region. The dark appearance of the residual powders after TG measurement supports the theory of the encapsulation of free carbon in the SiO₂-ZrO₂ network, which is similar to carbon-encapsulated nickel nanoparticles prepared by the instant pyrolysis of nickel acetylacetonate reported by Chen *et al.* [40], as well as the C/C-ZrC composites fabricated by zirconium acetylacetonate pyrolysis [41]. The continued weight loss of SZa₂ powder beyond 300 °C indicates that an acac⁻-modified SiO₂-ZrO₂ layer can be fabricated even when fired to a temperature as high as 300 °C.

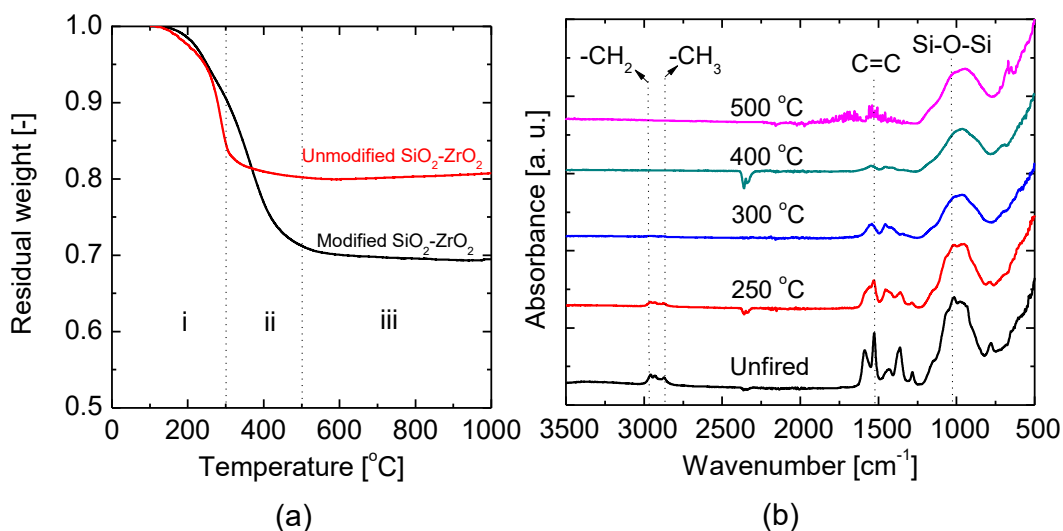


Fig. 2-5 TG curves of pure $\text{SiO}_2\text{-ZrO}_2$ and $\text{SiO}_2\text{-ZrO}_2\text{-acac}_2$ gels under N_2 at temperatures as high as $1,000\text{ }^\circ\text{C}$ (a) and Powder ATR-FTIR spectra of $\text{SiO}_2\text{-ZrO}_2\text{-acac}$ gels fired under a N_2 atmosphere at different temperatures (b)

Fig. 2-5 (b) shows the ATR-FT-IR spectra of SZa_2 powders fired under N_2 at different temperatures. The peak at around $1,500\text{ cm}^{-1}$ was assigned to the $\text{C}=\text{C}$ bond characteristics of an acetylacetonate ligand, as mentioned in a previous section [36, 38]. The presence of this peak is indicative of the fact that the acac-Zr chelation structure was unaffected by the change of state from sol to gel. The peak stretching between $1,100$ and 900 cm^{-1} was assigned to the $-\text{SiOSi}-$ ring while the $-\text{SiOH}$ group was assigned to the peak at about 800 cm^{-1} . The peaks between $2,800$ and $3,000\text{ cm}^{-1}$ were assigned to the unhydrolyzed ethoxy and butoxy groups [42-44]. The $-\text{SiOSi}-$ peaks were detected irrespective of the firing temperature, which is indicative of the formation of silica networks by hydrolysis and by the condensation of the ethoxy groups of TEOS. The $\text{C}=\text{C}$ peaks began to disappear as the firing temperature increased the $A_{\text{C}=\text{C}}/A_{\text{SiOSi}}$ absorbance peak ratio decreased as the firing temperature increased.

The simultaneous reduction and disappearance of $-\text{CH}_2$, $-\text{CH}_3$ and $-\text{SiOH}$ peaks at temperatures higher than $300\text{ }^\circ\text{C}$ was confirmed along with the subsequent $-\text{SiOSi}-$ peak shift and broadening. This can be attributed to the condensation of ethoxy, butoxy and silanol groups and the formation of more $-\text{SiOZr}-$ connections. The broadening and red shift of the $-\text{SiOSi}-$ peak in a silica-zirconia composite FT-IR spectrum is indicative of more $-\text{SiOZr}-$ connections, and the inclusion of Zr^{4+} ions

into the -SiOSi- ring caused a ring deformation and a resultant peak shift and broadening [45]. Fig. 2-6 shows the XRD patterns of pure SZ-derived and SZa₂-derived powders after firing at 700 °C under N₂. After firing at 700 °C, the tetragonal ZrO₂ peaks at $2\theta = 30^\circ$ and 50° indicated that the pure SZ-derived powder had begun to show an aggregation of ZrO₂ crystallites, whereas SZa₂-derived powder remained amorphous without aggregation of ZrO₂ crystallites indicating a better -Si-O-Zr- composition degree.

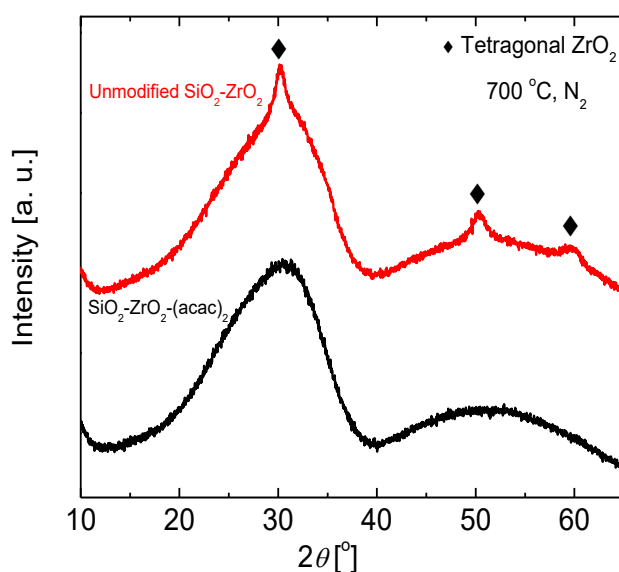


Fig. 2-6 XRD patterns of pure SZ- and SZa₂-derived powders before and after firing at 700 °C under N₂

2.3.2 Effect of acetylacetonate ligands on the pore size controllability of SiO₂-ZrO₂ (1:1) membranes

Fig. 2-7 shows the kinetic diameter dependence of single-gas permeance at 200 °C (a) and dimensionless permeance based on He (b) for SZ and SZa₂-derived membranes prepared at 300 °C under a N₂ atmosphere. Pure SZ-derived membranes showed a higher gas permeance compared with that of SZa₂-derived membranes, but He and H₂ selectivity over other gases was approximately the same as the Knudsen ratio. For example, a pure SZ-derived membrane showed a H₂ permeance of $1.4 \times 10^{-6} \text{ mol m}^{-2} \text{ s}^{-1} \text{ Pa}^{-1}$ with a H₂/SF₆ permeance ratio of 11.

The SZa₂-derived membrane showed a trend similar to that of the SZ-derived membrane; He (0.26 nm) permeance was lower than that of H₂ (0.289 nm), and N₂

(0.364 nm) permeance was lower than that of CH₄ (0.38 nm). This suggests a network pore size large enough for the separation of He-H₂ and N₂-CH₄ and Knudsen diffusion that is dominated by the permeation properties [29, 30]. However, the SZa₂-derived membrane showed a low SF₆ permeance of $1.3 \times 10^{-10} \text{ mol m}^{-2} \text{ s}^{-1} \text{ Pa}^{-1}$, with a high H₂/SF₆ permeance ratio of 7,600. This shows that the chelation of Zr⁴⁺ with acac⁻ ligands uniformly modified the pores of the SZa₂-derived membrane for molecular size-dependent permeation resistance. SZa₂-derived membranes, therefore, show promise for the separation of H₂/large organic gases, because the molecular size of SF₆ (0.55 nm) is similar to that of organic gases in benzene-cyclohexane and toluene-MCH systems (0.585 and 0.6 nm respectively) [46].

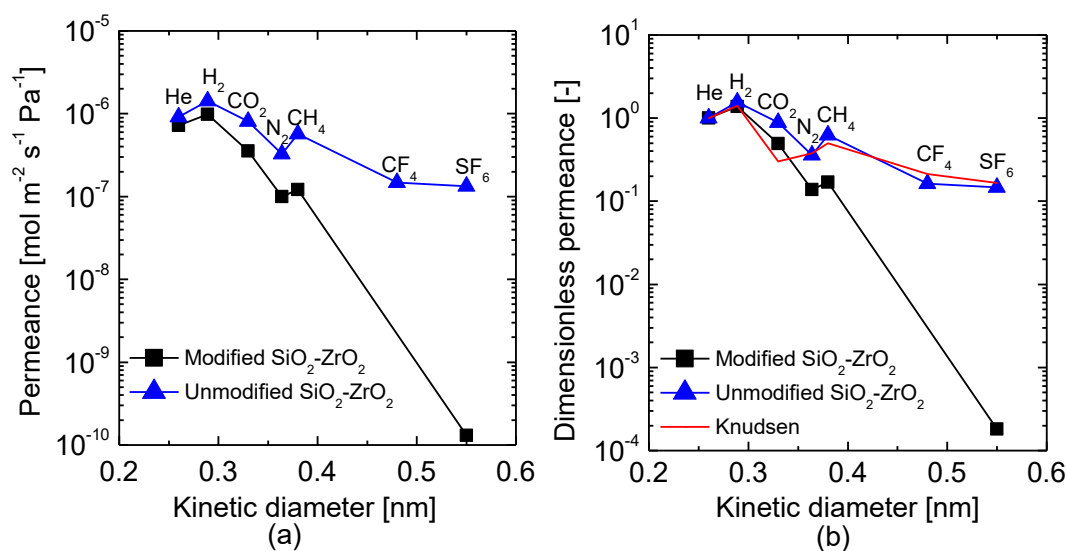


Fig. 2-7 Molecular size dependence of gas permeance (a) and dimensionless permeance based on He (b) at 200 °C of SiO₂-ZrO₂-acac₂ and pure SiO₂-ZrO₂ membranes all prepared at 300 °C under a N₂ atmosphere.

Fig. 2-8 shows the FE-SEM cross-sectional morphologies (x 50,000) of SZa₂ (a) and pure SZ (b)-derived membranes. A thin separation layer of acac⁻ modified silica-zirconia was successfully fabricated, although it was indistinguishable from the intermediate layer at this magnification. The α -Al₂O₃ particle layer (average 1 μm) was clearly distinguishable as a compact impenetrable support for the intermediate and top layers (< 400 nm) of both membranes. It should be noted that the FE-SEM images were taken after gas permeation experiments were performed. The lamination of the SZ and SZa₂ that topped the SiO₂-ZrO₂ intermediate layers was retained after

gas permeation experiments, which suggests a favorable interaction between silica-based top layers containing organic groups and the $\text{SiO}_2\text{-ZrO}_2$ layer. Therefore, the addition of the acac^- ligands to $\text{SiO}_2\text{-ZrO}_2$ had no structural effect on the top layer during long-term use.

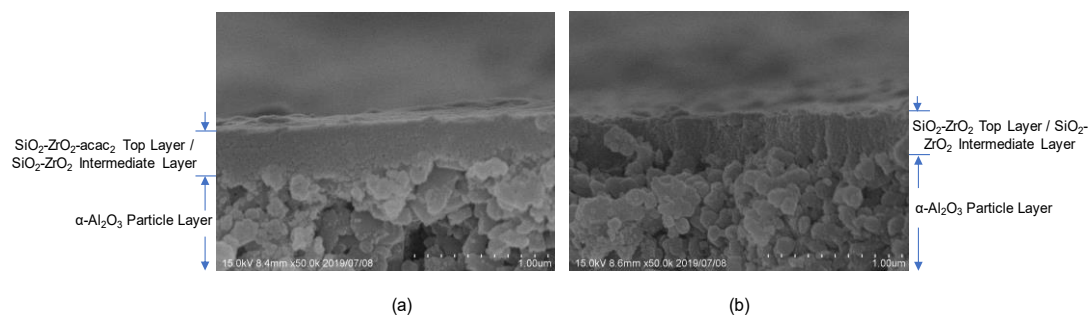
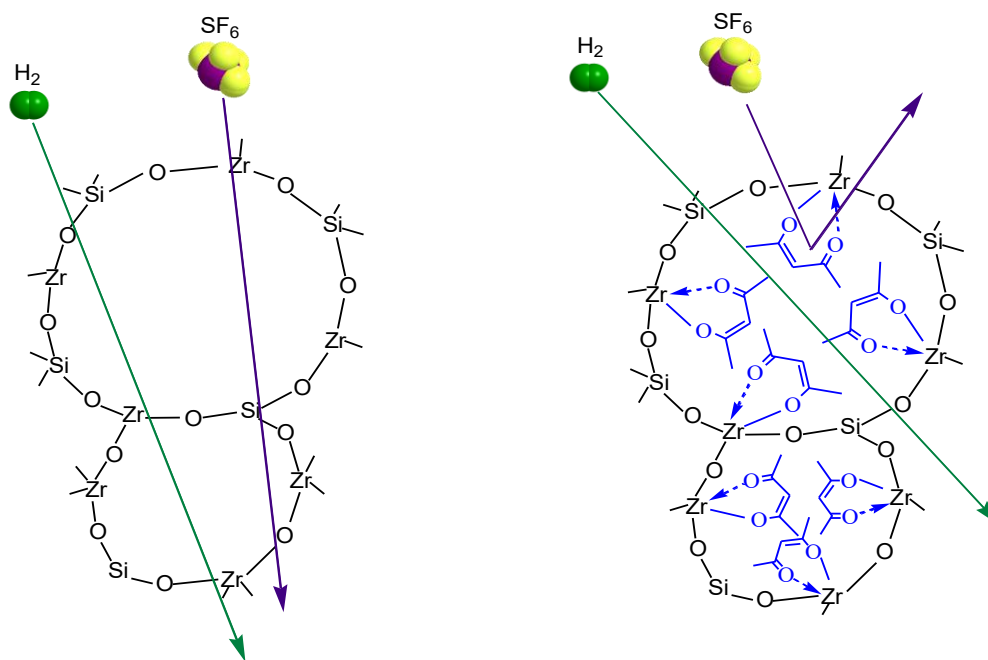
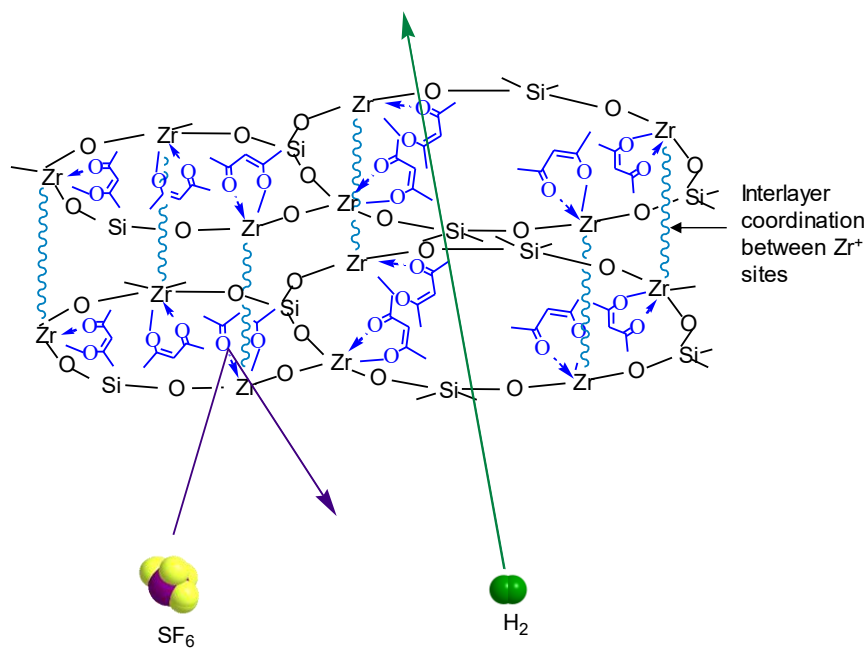


Fig. 2-8 FE-SEM micrographs of the cross-section for $\text{SiO}_2\text{-ZrO}_2\text{-acac}_2$ (a) and pure $\text{SiO}_2\text{-ZrO}_2$ (b) membranes.

The schematic diagram in Fig. 2-9 (a) summarizes the effect of the acac^- chelating ligands on the Si-O-Zr network. The chelation of acac^- ligands to Zr^+ sites created network spaces small enough to prevent permeation by large gases yet large enough to allow small gases to permeate, which created better molecular sieving properties. Hypothetically, as Fig. 2-9 (b) illustrates, interlayer condensation may occur between two successive layers when the free chelation sites in acac^- ligands on one layer chelate with the Zr^+ sites on another layer. Such interlayer interactions like the self-assembly of thiourea-crosslinked graphene oxide [47], topotactic dehydration-condensation of layered silicate into a zeolite [48], and hydrogen-covalent bond interaction between hybridized layers of PVA/TEOS [49] have been studied and proven. Characterization to prove these types of interaction is currently beyond the scope of this study and will require further inquiry. This phenomenon was not apparent in the SEM micrographs even at very high magnification.



(a)



(b)

Fig. 2-9 Schematic image of the intra-particle pore modification effect of acetylacetonate chelating ligands forming coordination complexes with Zr atoms and the influence on gas permeation ability; (a) network pore modification theory; (b) interlayer coordination theory.

2.3.3 Heat-treatment effect on pore size and gas permeation properties of SiO₂-ZrO₂-acac₂ membranes

The thermogravimetric results indicate different sections on the TG profile as discussed in section 2.3.1.2. Therefore, it was interesting to evaluate the gas permeation properties of SZa₂-derived membranes fired at different temperatures and the effect that firing temperature exerted on the membrane pore sizes. Fig. 2-10 shows the molecular size dependence of single-gas permeance at 200 °C (a) and the dimensionless permeance based on He (b) for SZa₂-derived membranes heat-treated at temperatures ranging from 250-550 °C under a N₂ flow, as mentioned in section 2.2.3. Fig. 2-11 shows the values for single-gas permeance and permeance ratios at 200 °C as a function of heat-treatment temperatures. Gas permeation properties changed as membranes were heat-treated at higher temperatures. A membrane fired at 250 °C showed a low H₂ permeance of 1.8×10^{-7} mol m⁻² s⁻¹ Pa⁻¹, but its H₂/CH₄ selectivity of 50 was higher than with heat-treatment ranging from 300-550 °C. It should be noted that the permeance for large gases such as CF₄ and SF₆ was below the detection levels of 10^{-11} mol m⁻² s⁻¹ Pa⁻¹, and the H₂/SF₆ permeance ratio was assumed to be within the acceptable range of 10^4 - 10^5 , which suggests that these membranes had very dense structures.

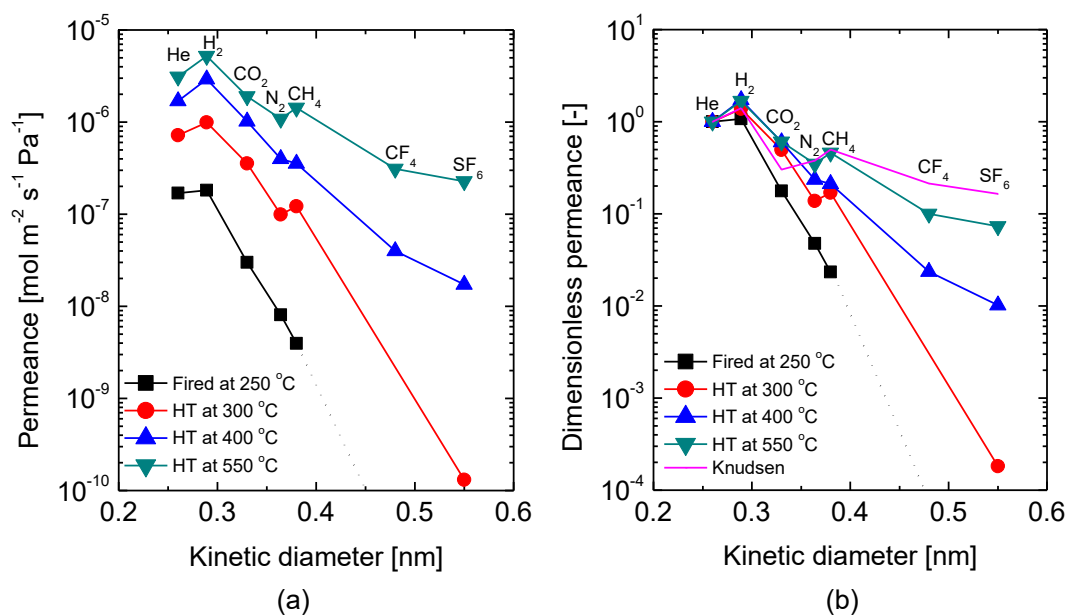


Fig. 2-10 Comparison of the kinetic diameter dependence of single-gas permeance (a) and dimensionless permeance based on He (b) at 200 °C for SiO₂-ZrO₂-acac₂ membranes fired at 250 °C and heat-treated at different temperatures (300-550 °C).

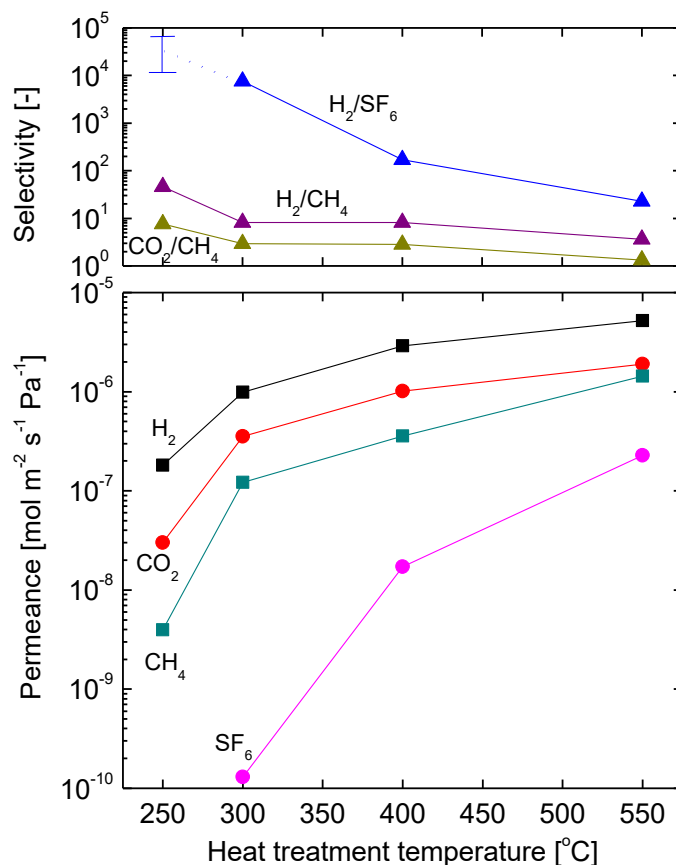


Fig. 2-11 Heat-treatment temperature (300-550 °C) dependence of gas permeance and selectivity (H₂/CH₄, H₂/SF₆, CO₂/CH₄) at 200 °C for SiO₂-ZrO₂-acac₂ membranes fired at 250 °C under a N₂ atmosphere.

After heat-treatment at 300 °C, developments such as a drastic increase in gas permeance and a decrease in gas selectivity were observed (H₂ permeance: $\sim 10^{-6}$ mol m⁻² s⁻¹ Pa⁻¹, H₂/SF₆ permeance ratio: $\sim 8,000$). At 300 °C and above, the changes to gas permeance and permeance ratios were more subdued. It should be noted that H₂ selectivity over large gases such as CF₄ and SF₆ remained above the Knudsen-based values until the membranes were heat-treated at 400 °C. However, a membrane heat-treated at 550 °C showed gas permeance on the order of values like that of the intermediate layer, and H₂ selectivity over large gases such as CF₄ and SF₆ approached Knudsen ratios.

The change in dimensionless permeance with increases in the firing temperature became more pronounced as molecular size increased from H_2 to SF_6 . This could have resulted from heat-treatment at higher temperatures causing the $acac^-$ ligands to decompose within the modified pores, which would make the pores larger, which is consistent with thermogravimetric results. The increased pore size increases the access to large gases. High-temperature heat-treatment of SZa₂-derived membranes fired at 250 °C, therefore, increases the pore size due to the decomposition of $acac^-$ ligand groups. This decomposition of organics behavior as heat-treatment temperature increases is consistent with the templating effect summarized in Fig. 2-12. The chelating ligands attached to the Zr^+ sites occupied the network pores in the $CH_3-CH-CH_2-CH-CH_3$ section of the $acac^-$ ligand. As heat-treatment temperature increased, these organic sections began to decompose opening the pores for gas passage, which increased the gas permeance, but reduced gas selectivity as larger gases were able to access the network pores. The occupation of network pores can be assumed to be both intraparticle and interparticle. Intraparticle pores exist within individual particles created by spaces between the atomic networks while interparticle pores are the spaces that exist between particles. The interparticle pore-containing ligands decomposed before the intraparticle pore-containing versions, which was inferred by the fact that the membranes continued to show gas selectivity higher than Knudsen ratios even after heat-treatment at 550 °C. This could have been because the intraparticle pore-containing ligands are relatively shielded from heat by the surrounding Si-O-Zr network, much like the encapsulation of carbon in nickel nanoparticles [40].

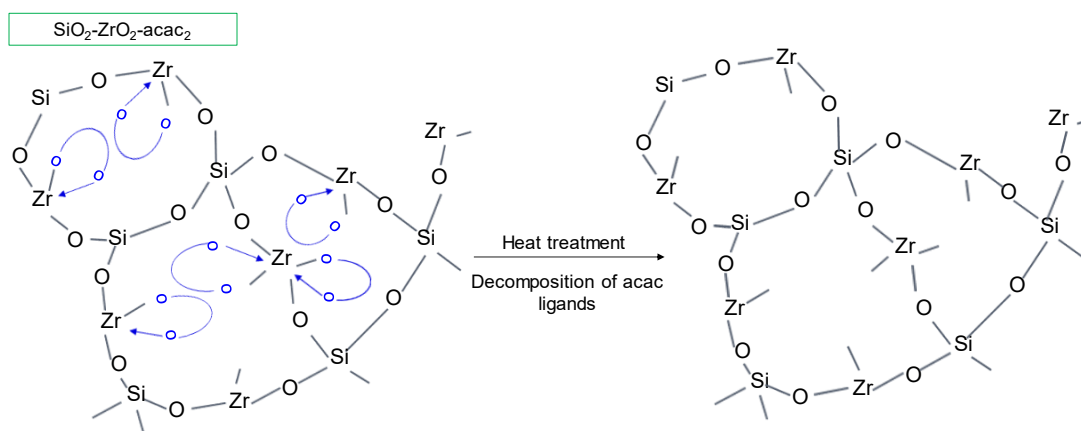


Fig. 2-12 Schematic diagram of the effect of heat-treatment on the pore size and gas permeation ability of a typical SiO₂-ZrO₂-acac₂ membrane.

Fig. 2-13 shows the single-gas permeance and permeance ratios as functions of temperatures between 50 and 200 °C for SZa₂-derived membranes fired at 250 °C (a) (He, H₂, CO₂, N₂, CH₄) and heat-treated at 300 °C (He, H₂, CO₂, N₂, CH₄, SF₆) and 550 °C (b) (He, H₂, CO₂, N₂, CH₄, CF₄, SF₆). The temperature dependence of permeance and the activation energies of gases were fitted and calculated using the modified gas translation model (Eq. 2-1). The model showed a very good fit with the experimental data and should be regarded as a viable representation of gas-membrane behavior.

$$P_i = \frac{k_{o,i}}{\sqrt{M_i RT}} \exp\left(-\frac{E_{p,i}}{RT}\right) \quad (2-1)$$

For membranes fired at 250 °C, the permeance of all gases (He, H₂, N₂, CH₄) increased with increases in temperature, suggesting an activated diffusion mechanism. The exception to this was CO₂, which showed an increase in permeance as the temperature decreased, which suggests a surface-diffusion mechanism. Gas selectivities (H₂/CH₄, CO₂/CH₄, CO₂/N₂) increased as temperature decreased. In particular, for gas permeance measured at 50 °C, H₂/CH₄ and CO₂/CH₄ selectivities reached 100 and 60, respectively.

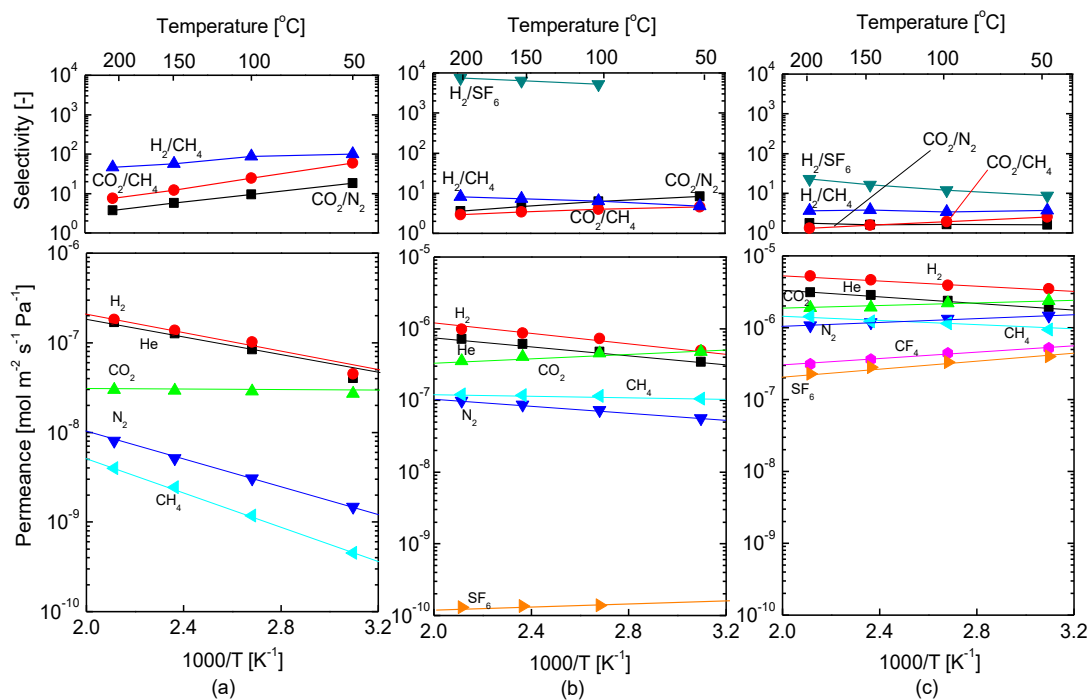


Fig. 2-13 Temperature dependence of gas permeance at temperatures ranging from 50–200 °C for SiO₂-ZrO₂-acac₂ membranes fired at 250 °C (a) and heat-treated at 300 °C (b) and 550 °C (c) under N₂.

Membranes heat-treated at 300 °C showed the same trend as the original membrane fired at 250 °C with gas permeance (He, H₂, N₂, CH₄) increasing as the temperature increased with the noted exception of CO₂ that exhibited a surface-diffusion mechanism. However, the slopes of the temperature dependence of gas permeance followed different trends, and membranes fired at 250 °C showed increases in the slope as the molecular size increased, but the slope decreased with molecular size for membranes heat-treated at 300 °C.

When heat-treated to 550 °C, the permeance of gases (N₂, CF₄, SF₆) decreased as temperature increased except for small gases (He, H₂ and CH₄) that continued to show smaller activation energies (He: 5.7, H₂: 5.1, CH₄: 5.07 kJ mol⁻¹) compared with 250 °C-fired membranes (He: 12, H₂: 13, CH₄: 20 kJ mol⁻¹). The transition in membrane permeation characteristics can be clearly observed in the gas selectivity plot. As a membrane is heat-treated to 300 °C, there is a drastic decrease in gas selectivity (H₂/CH₄, CO₂/CH₄, CO₂/N₂), which is reduced even further for membranes heat-treated at 550 °C with no considerable variation in permeation temperature. Based on

these results, it can be concluded that the pore morphology in a 250 °C-fired membrane is such that gas separation with high selectivity can be expected by altering the operating temperature, whereas membranes heat-treated to 550 °C can accomplish no gas separation at different operating temperatures since the pores are not selective for gases.

Fig. 2-14 shows the relationship between the activation energies of gases (He, H₂, N₂, CH₄, SF₆) and the kinetic diameter for SZa₂-derived heat-treatment ranging from 250-550 °C, for isoeugenol-modified TiO₂-ZrO₂-derived [50] and polyimide membranes [52, 53]. For SZa₂-derived membranes heat-treated at 250 °C, isoeugenol-modified, TiO₂-ZrO₂-derived, and polyimide membranes, the activation energy increases as the kinetic diameter increases, as indicated in Fig. 2-14 via the data points in the solid-line circle. These results indicate a similar gas permeation mechanism in these membranes, although the polymer membrane showed higher activation energies across all gases. This behavior (increased activation energy of gas permeance with kinetic diameter of gases) is a solution-diffusion mechanism that is accepted as the transport mechanism in polymer membranes [54, 55]. As for the polyimide membranes studied by Villaluenga [52] *et al.* and Hirayama *et al.* [56], the interaction between the polymer and each gas (He, H₂, N₂, CH₄) corresponding to the heat of sorption, ΔH_s , is very small so that the high activation energies of permeation observed should be attributed to diffusivity rather than to solubility, even if the solubility coefficient is thermodynamic in nature. The thermodynamic nature of gas diffusivity in polymer membranes can be explained by the fact that polymer chains corresponding to voids vibrate relative to temperature so that activation energy increases with kinetic diameter. Thus, based on the observed trend, this phenomenon could also be attributed to SZa₂-derived membranes fired at 250 °C.

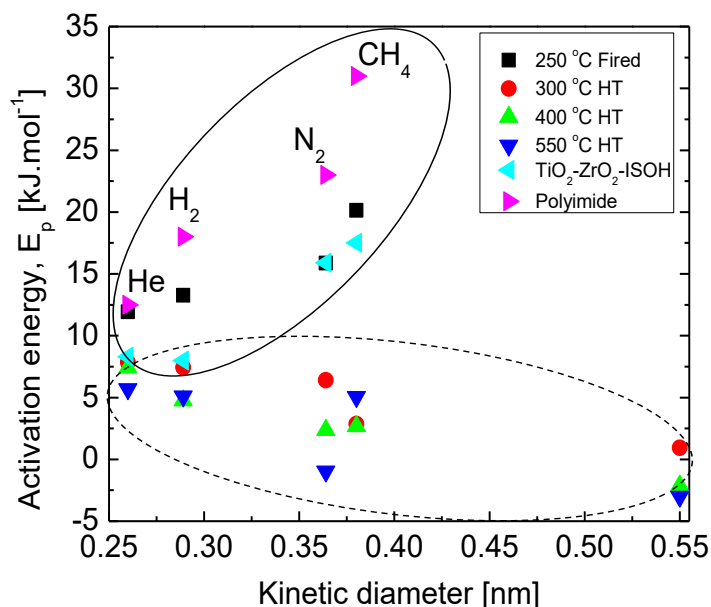


Fig. 2-14 Kinetic diameter dependence of gas activation energies (He, H₂, N₂, CH₄, SF₆) for SiO₂-ZrO₂-acac₂ membranes fired at 250 °C and heat-treated at 300, 400 or 550 °C under N₂ compares with that of isoeugenol (ISOH)-modified TiO₂-ZrO₂ [50] and polyimide [52, 53] membranes.

In contrast, as indicated by data points in the dashed-line circle in Fig. 2-14, the kinetic diameter dependence of the apparent activation energy of SZa₂-derived membranes heat-treated at 300-550 °C showed a trend whereby activation energy decreased with kinetic diameter. This was apparent because heat-treatment at higher temperatures decomposed the organic content in the modified network structure, which resulted in enlarged network pores that allowed easier access to larger gases for these membranes. Fig. 2-15 also compares the heat-treatment temperature dependence of the apparent activation energies of He and N₂, which clearly displays a sharper reduction in the activation energy of N₂ than that of He and suggests the creation of larger pores. However, small gases (He and H₂) showed higher activation energies indicating the presence of pores with sizes in the range of the kinetic diameters of He and H₂ even after firing at higher temperatures. These two observations are evidence of a bimodal pore structure. Therefore, the heat-treatment of membranes affects the pore structure enough to affect the permeation properties of the membrane.

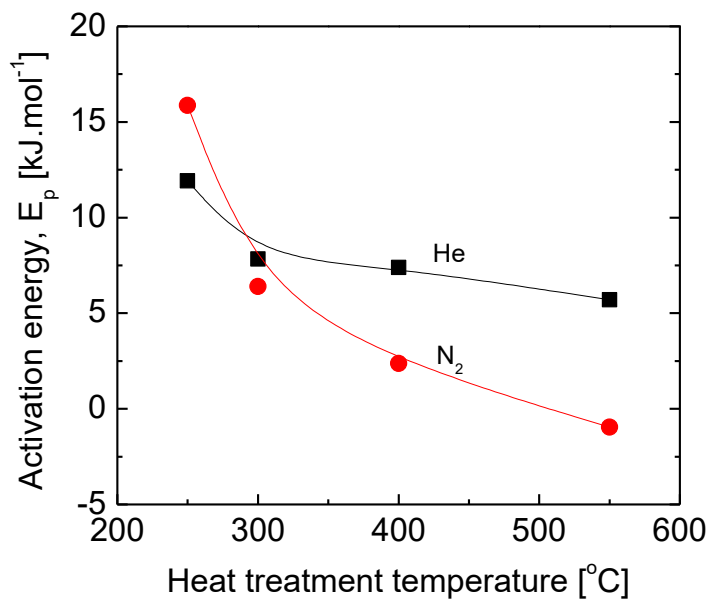


Fig. 2-15 Heat treatment temperature dependence of gas activation energies (He and N₂) for SZa₂-derived membranes

Fig. 2-16 shows the trade-off plot for the H₂/SF₆ permeance ratio as a function of H₂ permeance for two different membranes fired at 250 °C and heat-treated at 300, 400 or 550 °C. It should be noted that the SF₆ permeance for a membrane fired at 250 °C was assumed to be on the order of 10⁻¹¹, which is below the detection limit, and, therefore, the H₂/SF₆ permeance ratio was assumed to be within a reasonable limit of 10⁴ to 10⁵. It was apparent that all H₂/SF₆ permeance ratios were above the Knudsen ratio irrespective of heat-treatment temperature. The solid line in Fig. 2-16 is the trade-off line that can be drawn to align with the trade-off points. A membrane with high H₂/SF₆ selectivity generally shows a low H₂ permeance, and vice versa. When the trade-off line is considered, membranes heat-treated at 300 °C provided a favorable trade-off point by maintaining a good balance between H₂/SF₆ (1,800-7600) selectivity and H₂ permeance (0.4-1 × 10⁻⁶ mol m⁻² s⁻¹ Pa⁻¹). Although membranes fired at 250 °C exhibited a higher H₂/SF₆ selectivity (> 18,000), that for a membrane heat-treated at 300 °C was not far below, but with almost 10 times the order of H₂ permeance (1.8 × 10⁻⁷ mol m⁻² s⁻¹ Pa⁻¹). Thus, a membrane heat-treated at 300 °C delivers a better trade-off than other membranes with high H₂ permeance and H₂/SF₆ selectivity.

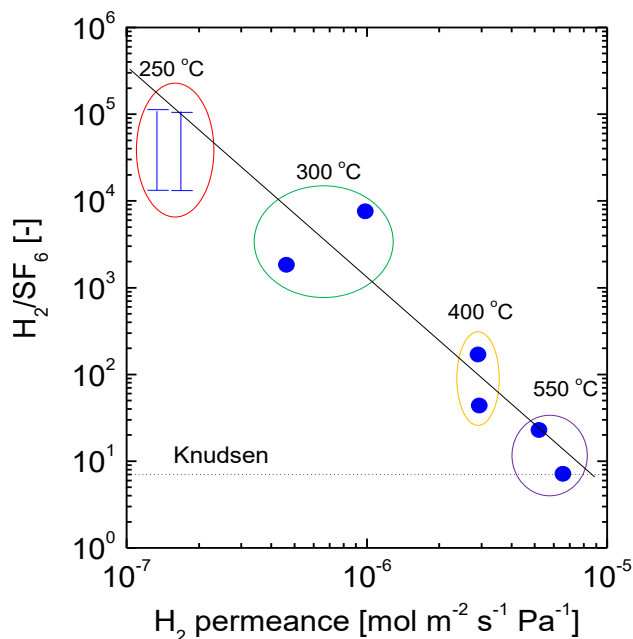


Fig. 2-16 H₂/SF₆ permeance ratio as a function of H₂ permeance at 200 °C for membranes fired at 250 °C and heat-treated at 300, 400 or 550 °C.

2.4 Conclusions

A chemical modification of SiO₂-ZrO₂ via the sol-gel method was successfully accomplished by chelating acetylacetonate (acac⁻) with zirconium tetrabutoxide (ZrTB) prior to co-hydrolysis and condensation with tetraethoxysilane (TEOS), which was then used to fabricate a gas separation layer by coating the acac⁻-modified SiO₂-ZrO₂ sol onto a SiO₂-ZrO₂ intermediate layer. Acac⁻-modified SiO₂-ZrO₂-derived membranes were then fabricated by firing under N₂ at 250 °C followed by heat-treatments that ranged from 300-550 °C under N₂. Single-gas permeation experiments were carried out to examine the effect of chelating agents on the resultant modification of the pores, which affected the gas permeation properties of the membrane.

The acac⁻-modified SiO₂-ZrO₂-derived membrane showed H₂ permeance of 9.9 × 10⁻⁷ with a H₂/SF₆ permeance ratio of 7,600, which was better than the results when using a pure SiO₂-ZrO₂-derived membrane (H₂ permeance: 1.4 × 10⁻⁶ mol m⁻² s⁻¹ Pa⁻¹, H₂/SF₆ permeance ratio: 11). When an acac⁻-modified SiO₂-ZrO₂-derived membrane prepared at 250 °C (H₂ permeance: 1.8 × 10⁻⁷ mol m⁻² s⁻¹ Pa⁻¹, H₂/CH₄: 100, CO₂/CH₄: 60 at 50 °C) was heat-treated at 550 °C, the result was improved H₂ permeance of 5.2

$\times 10^{-6} \text{ mol m}^{-2} \text{ s}^{-1} \text{ Pa}^{-1}$ with low permeance ratios (H_2/CH_4 : 3, H_2/SF_6 : 9) at 50 °C. The 250 °C-fired acac⁻-modified SiO₂-ZrO₂-derived membranes exhibited a gas permeation mechanism similar to polymer membranes, and the 300 °C-heat-treated version showed the best trade-off between H₂ permeance and the H₂/SF₆ permeance ratio.

Cited literature

1. N. W. Ockwig, T. M. Nenoff, Membranes for hydrogen separation, *Chem. Rev.* 107 (2007) 4078-4110.
2. S. Adhikari, S. Fernando, Hydrogen membrane separation techniques, *Ind. Eng. Chem. Res.* 45 (2006) 875-881
3. H. Li, Z. Song, X. Zhang, Y. Huang, S. Li, Y. Mao, H. J. Ploehn, Y. Bao, M. Yu, Ultrathin, molecular-sieving graphene oxide membranes for selective hydrogen separation, *Science* 342 (2013) 95-98
4. M. Kanezashi, D. Fuchigami, T. Yoshioka, T. Tsuru, Control of Pd dispersion in sol-gel-derived amorphous silica membranes for hydrogen separation at high temperatures, *J. Membr. Sci.* 439 (2013) 78-86
5. S.-J. Ahn, A. Takagaki, T. Sugawara, R. Kikuchi, S. T. Oyama, Permeation properties of silica-zirconia composite membranes supported on porous alumina substrates, *J. Membr. Sci.* 526 (2017) 409-416.
6. S.-W. Chuang, S. L.-C. Hsu, Y.-H. Liu, Synthesis and properties of fluorine-containing polybenzimidazole/silica nanocomposite membranes for proton exchange membrane fuel cells, *J. Membr. Sci.* 305 (2007) 353-363
7. Y. Zhang, J. Sunarso, S. Liu, R. Wang, Current status and development of membranes for CO₂/CH₄ separation: a review, *Int. J. Green Gas Control.* 12 (2013) 84-107
8. M. A. Carreon, S. Li, J. L. Falconer, R. D. Noble, Alumina-supported SAPO-34 membranes for CO₂/CH₄ separation, *J. Am. Chem. Soc.* 130 (2008) 5412-5413
9. C. E. Powell, G. G. Qiao, Polymeric CO₂/N₂ gas separation membranes for the capture of carbon dioxide for power plant flue gases, *J. Membr. Sci.* 279 (2006) 1-49

10. L. Zhao, E. Riensche, R. Menzer, L. Blum, D. Stolten, A parametric study of CO₂/N₂ gas separation membrane processes for post-combustion capture, *J. Membr. Sci.* 325 (2008) 284-294
11. D. C. Nymeyer, T. Visser, R. Assen, M. Wessling, Composite hollow fiber gas-liquid membrane contactors for olefin/paraffin separation, *Sep. Purif. Tech.* 37 (2004) 209-220
12. B. N. Nair, K. Keizar, W. J. Elferink, M. J. Gilde, H. Verweij, A. J. Burggraaf, Synthesis, characterization and gas permeation studies on microporous silica and alumina-silica membranes for separation of propane and propylene, *J. Membr. Sci.* 116 (1996) 161-169
13. S. Yun, J. H. Ko, S. T. Oyama, Ultrathin palladium membranes prepared by a novel electric field assisted activation, *J. Membr. Sci.* 369 (2011) 482-489.
14. M. Kanezashi, Sol-Gel Derived Silica Membranes, *Encyclopedia of Membrane Science and Technology*, John Wiley and Sons, 2013
15. B. Ballinger, J. Motuzas, S. Smart, J. C. Diniz da Costa, Palladium cobalt binary doping of molecular sieving silica membranes, *J. Membr. Sci.* 451 (2014) 185-191
16. R. M. de Vos, H. Verweij, High-selectivity, high-flux silica membranes for gas separation, *Science.* 279 (1998) 1710-1711
17. R. M. de Vos, H. Verweij, Improved performance of silica membranes for gas separation, *J. Membr. Sci.* 143 (1998) 37-51
18. A. Peta Dral, J. E. ten Elshof, Organic groups influencing microporosity in organosilicas, *Micr. Meso. Mater.* 267 (2018) 267-273.
19. M. Kanezashi, Y. Yoneda, H. Nagasawa, T. Tsuru, K. Yamamoto, J. Ohshita, Gas permeation properties for organosilica membranes with different Si/C ratios and evaluation of microporous structures, *AIChE J.* 63 (2017) 4491-4498.
20. N. K. Raman, C. J. Brinker, Organic “template” approach to molecular sieving silica membranes, *J. Membr.Sci.* 105 (1995) 273-279.
21. K. Yoshida, Y. Hirano, H. Fujii, T. Tsuru, M. Asaeda, Hydrothermal stability and performance of silica-zirconia for hydrogen separation in hydrothermal conditions, *J. Chem. Eng. Jpn.* 34 (2001) 523-530.
22. S. Yun, S. T. Oyama, Correlations in palladium membranes for hydrogen separation: a review, *J. Membr. Sci.* 375 (2011) 28-45.

23. D. Uhlmann, S. Liu, B. P. Ladewig, J. C. Diniz da Costa, Cobalt-doped silica membranes for gas separation, *J. Membr. Sci.* 326 (2009) 316-321
24. Y. Gu, P. Hacıoğlu, S. T. Oyama, Hydrothermally stable silica-alumina composite membranes for hydrogen separation, *J. Membr. Sci.* 310 (2008) 28-37
25. V. Tajer-Kajinebaf, H. Sarpoölaky, T. Mohammadi, Sol-gel synthesis of nanostructured titania-silica mesoporous membranes with photo-degradation and physical separation capacities for water purification, *Ceram. Int.*, 40 (2014) 1747-1757
26. Y. Gu, S. T. Oyama, Permeation properties and hydrothermal stability of silica-titania membranes supported on porous alumina substrates, *J. Membr. Sci.*, 345 (2009) 267-275
27. M. Asaeda, Y. Sakou, J. Yang, K. Shimasaki, Stability and performance of porous silica-zirconia composite membranes for pervaporation of aqueous organic solutions, *J. Membr. Sci.*, 209 (2002) 163-175.
28. W. Puthai, M. Kanezashi, H. Nagasawa, K. Wakamura, H. Ohnishi, T. Tsuru, Effect of firing temperature on water permeability of SiO₂-ZrO₂ membranes for nanofiltration, *J. Membr. Sci.*, 497 (2016) 348-356.
29. P. Pandey, R. S. Chauhan, Membranes for gas separation, *Prog. Polym. Sci.* 26 (2001) 853-893
30. L. Li, H. Qi, Gas separation using sol-gel derived microporous zirconia membranes with high hydrothermal stability, *Ch. J. Chem. Eng.*, 23 (2015) 1300-1306.
31. C. A. Milea, C. Bogatu, A. Duta, The influence of parameters in silica sol-gel process, in: *Bulletin of the Transilvania University of Brasov, Series I: Engineering sciences Vol. 4 (53)*, 2011, pp. 59-66
32. D. A. Ward, E. I. Ko, Preparing catalytic materials by the sol-gel method, *Ind. Eng. Chem. Res.* 34 (1995) 421-433.
33. N. Stock, S. Biswas, Synthesis of metal-organic frameworks (MOFs): routes to various MOF topologies, morphologies, and composites, *Chem. Rev.* 112 (2012) 933-969.
34. S. Basu, A. Cano-Odena, I. F. J. Vankelecom, MOF-containing mixed-matrix membranes for CO₂/CH₄ and CO₂/N₂ binary gas mixture separations, *Sep. Purif. Technol.* 81 (2011) 31-40.

35. O. G. Nik, X. Y. Chen, S. Kaliaguine, Functionalized metal organic framework-polyimide mixed matrix membranes for CO₂/CH₄ separation, *J. Membr. Sci.* 413-414 (2012) 48-61.
36. D. Hoebbel, T. Reinert, H. Schmidt, E. Arpac, On the hydrolytic stability of organic ligands in Al-, Ti- and Zr-alkoxide complexes, *J. Sol-Gel Sci. Technol.* 10 (1997) 115-126.
37. C. Janiak, Engineering coordination polymers towards applications, *Dalton Trans.* (2003) 2781-2804
38. D. Peter, T. S. Ertel, H. Bertagnolli, EXAFS study of zirconium alkoxides as precursors in sol-gel process: II. The influence of the chemical modification, *J. Sol-Gel Sci. Technol.* 5 (1995) 5-14.
39. T. Tsuru, Nano/subnano-tuning of porous ceramic membranes for molecular separations, *J. Sol-Gel Sci. Technol.* 46 (2008) 349-361
40. M. Chen, L. Bin, S. Huai-he, Z. Lin-jie, Preparation of carbon encapsulated metal magnetic nanoparticles by an instant pyrolysis method, *New Carbon Mater.* 25 (3) (2010) 199-204
41. Y. Li, S. Chen, H. Hu, C. Zou, Z. Chen, X. Ma, A meltable precursor for zirconium carbide ceramics and C/C-ZrC composites, *Ceram. Int.* 44 (2018) 10175-10180
42. R. W. Silverstein, G. C. Bassler, Spectrometric identification of organic compounds, *J. Chem. Ed.* 39 (1962) 546-553
43. A. L. Smith, Infrared spectra-structure correlations for organosilicon compounds, *Spectrochimica Acta.* 16 (1960) 87-105
44. J. Coates, Interpretation of infrared spectra, a practical approach, *Encyclopedia of Analytical Chemistry*, doi: 10. 1002/9780470027318. A5606
45. Z.-G. Wu, Y.-X. Zhao, D.-S. Liu, The synthesis and characterization of mesoporous silica-zirconia aerogels, *Micr. Meso. Mater.* 68 (2004) 127-132.
46. R. Lee, M. Kanezashi, Y. Shimomura, T. Yoshioka, T. Tsuru, Evaluation and fabrication of pore-size-tuned silica membranes with tetraethoxydimethyl disiloxane for gas separation, *AIChE J.* 57 (2011) 2755-2765.
47. J. Yang, D. Gong, G. Li, G. Zeng, Q. Wang, Y. Zhang, G. Liu, P. Wu, E. Vovk, Z. Peng, X. Zhou, Y. Yang, Z. Liu, Y. Sun, Self-assembly of thiourea-crosslinked graphene oxide framework membranes toward separation of small molecules, *Adv. Mater.* 30 (2018) 1705775 (1-8)

48. T. Ikeda, Y. Akiyama, Y. Oumi, A. Kawai, F. Mizukami, The topotactic conversion of a novel layered silicate into a new framework zeolite, *Angew. Chem. Int. Ed.* 43 (2004) 4892-4896
49. T. Uragami, K. Okazaki, H. Matsugi, T. Miyata, Structure and permeation characteristics of an aqueous ethanol solution of organic-inorganic hybrid membranes composed of poly(vinyl alcohol) and tetraethoxysilane, *Macromolecules* 35 (2002) 9156-9163
50. T. Fukumoto, T. Yoshioka, H. Nagasawa, M. Kanezashi, T. Tsuru, Development and gas permeation properties of microporous amorphous TiO₂-ZrO₂-organic composite membranes using chelating ligands, *Journal of Membrane Science.* 461 (2014) 96-105.
51. G. I. Spijksma, C. Huiskes, N. E. Benes, H. Kruidhof, D. H. A. Blank, V. G. Kessler, H. J. M. Bouwmeester, Microporous zirconia-titania composite membranes derived from diethanolamine-modified precursors, *Adv. Mater.* 18 (2006) 2165-2168
52. J. P. G. Villaluenga, B. Seoane, J. Hradil, P. Sysel, Gas permeation characteristics of heterogeneous ODPa-BIS P polyimide membranes at different temperatures, *J. Membr. Sci.* 305 (2007) 160-168.
53. K. Haraya, K. Obata, N. Itoh, Y. Shindo, T. Hakuta, Y. Yoshitome, Gas permeation and separation by an asymmetric polyimide hollow fiber membrane, *J. Membr. Sci.* 41 (1989) 23-35.
54. S. A. Stern, S. R. Sampat, S. S. Kulkarni, Test of a "free-volume" model of gas permeation through polymer membranes. II. Pure Ar, SF₆, CF₄, and C₂H₂F₂ in polyethylene, *J. Polym. Sci., Part B: Polym. Phys.* 24 (1986) 2149-2166
55. J. P. G. Villaluenga, B. Soane, Experimental estimation of gas-transport properties of linear low-density polyethylene membranes by an integral permeation method, *J. Appl. Polym. Sci.* 82 (2001) 3013-3021
56. Y. Hirayama, T. Yoshinaga, K. Kusuki, K. Ninomiya, T. Sakakibara, T. Tamari, Relation of gas permeability with structure of aromatic polyimides I, *J. Membr. Sci.* 111 (1996) 169-182

Chapter 3

Microstructure engineering of ligand-modified silica-zirconia membranes derived from network-forming precursors

3.1 Introduction

One critical element in separation membrane technology is the creation of advanced materials with tunable capabilities for molecular-level separation [1, 2] via the use of so-called evolutionary and revolutionary strategies [3]. Inorganic membranes are believed to possess the potential for revolutionary performances over polymeric membranes because polymeric membranes are limited by an ‘upper boundary’ [4, 5], which several examples of inorganic membranes have definitively surpassed. Porous inorganic membranes (silica, transition metal oxides, carbon, zeolites, etc.), however, are plagued by shortcomings such as the hydrothermal instability of silica and silica-based membranes [6-8], as well as that of zeolites [9], and also by low levels of packing density (membrane surface area per module volume) [10] and issues with the control of pore sizes [11, 12]. Therefore, inorganic materials have been modified with different organic moieties to address these shortcomings [6, 11, 13].

These organically modified inorganic materials are diphasic hybrids that can be grouped into two large categories: class I and class II inorganic-organic hybrids. A class I hybrid is such that the organic and inorganic moieties are linked by weak interactive forces such as hydrogen and van der Waals bonding [14, 15]. Examples of class I hybrids are mixed-matrix membranes, interpenetrating polymer and inorganic networks (IPNs) [16]. This class of hybrids is used more to improve the qualities of the polymer moiety. In class II hybrids, on the other hand, the interaction between the inorganic and organic parts, which includes strong bonds like covalent and ionic-covalent bonds, serve to improve the inorganic moiety qualities such as improved hydrothermal stability [6], pore size controllability [11,13], targeted functionalization [17], etc. Examples include pendant and bridged-type organically modified silicon alkoxides, organically modified transition metal oxides, metal-organic frameworks, etc. [14, 16]. Therefore, class II hybrids present a very wide field for membrane technology development.

Special types of class II hybrids that are referred to as ORMOCERs (hybrid inorganic-organic polymers) are fabricated by the sequential synthesis of inorganic and organic networks from different precursors [14-16, 18, 19]. Figure 1 shows a general framework for the fabrication of hybrid inorganic-organic polymers based on the work of K.-H. Haas [16]. This framework is comprised of four structural elements that include a siloxane network, a transition-metal oxide network (TMO) that provides chelation sites, an organic modifier, and cross-linking of the organic units. Traditionally, the organic R or (R) group can be bonded to the siloxane and/or TMO networks with two aims: as *network modifiers* and *network formers*. When R is a non-hydrolysable group, it will have a network-modifying effect. For example, a network can be modified by functionalization with a hydrophilic group (aminopropyltrimethoxysilane), a hydrophobic group (phenyltriethoxysilane), or with a combination of hydrophobicity and oleophobicity (tridekafluoro-1,1,2,2-tetrahydrooctyltriethoxysilane). In cases where R possesses a reactive group such as a polymerizable unit, it serves as a network former [15, 20]. For network formation, organic precursors such as methacryloxypropyltrimethoxysilane, vinyltrimethoxysilane, etc., can be utilized [16, 20].

Irrespective of their modifier role, hybrid inorganic-organic polymers have been used in many applications such as in protective and decorative coatings [21], barrier systems [22], dental applications [18], microelectronics [23] micro-optics [24], batteries [25], proton-exchange membrane fuel cells [26, 27], and gas separation membranes [19]. Extensive reviews of these applications can be found in the literature, with the exception of gas separation applications [15, 16, 18, 20]. It is unclear why the application of hybrid inorganic-organic polymer membranes has not been the focus of many studies; however, two reasons can be surmised. First, because the cross-linking of the organic modifiers is done mostly via photoinitiation of a radical polymerization initiator, the reaction can be very rapid, and conversion can be completed in a matter of seconds or a few minutes [28, 29] making it difficult to control the membrane microstructure. In another vein, a reported hybrid inorganic-organic polymer membrane was fabricated as a free-standing membrane with a thickness of 100 μm . 19 Fabrication of free-standing membranes usually results in brittle films that are difficult to handle. Thus, the choice of the radical polymerization

initiator type, the initiation process, and the organic modifiers can dramatically influence the positive fortunes of hybrid inorganic-organic polymer membranes.

In this study, the choice of the organic moieties as key structural elements for the fabrication of materials is illustrated in Fig. 3-1. As shown, 3-methacryloxypropyltriethoxysilane (MAPTMS) served a dual purpose, because it was the precursor for the siloxane network, and it contained a siloxane network modifier (methacrylate group). Two chelating ligands, allyl acetoacetate (AAA) and acetylacetone (ACAC), were instrumental in modifying the zirconium oxide network (zirconium (IV) butoxide as a precursor). For organic cross-linking, 2,2'-azobisisobutyronitrile (AIBN) was chosen as a thermal radical initiator, because it is known to thermally dissociate at temperatures between 60 and 80 °C, which makes it suitable for AAA co-polymerization reactions [30, 31].

Figure 3-2 shows the network formation schemes with and without organic cross-linking. For a network without organic cross-linking, the network structure is comprised of only three of the four structural elements of a hybrid inorganic-organic polymer. A network with organic cross-linking, however, possesses all the requisite structural elements. However, the nature of this organic cross-linking component is expected to differ based on the chelating ligand. In an ACAC-chelated network, since there are no reactive units for cross-linking, homopolymerization of the MAPTMS moiety results. In the case of an AAA-chelated network, polymerizable C=C units are present, and therefore a co-polymerization reaction can be expected with the MAPTMS methacrylate unit.

The evolution of these organic cross-linking networks and the effects on the microstructure were evaluated via various characterization methods. Furthermore, α -Al₂O₃-supported membranes were fabricated, and their gas permeation characteristics were evaluated. The performances of these membranes were compared vis-à-vis their microstructures against different defect-free polymers and organosilica membranes. Therefore, in this work we proposed a facile framework for the fabrication of defect-free, microstructure-controllable hybrid inorganic-organic composite membranes for use as templates in future work.

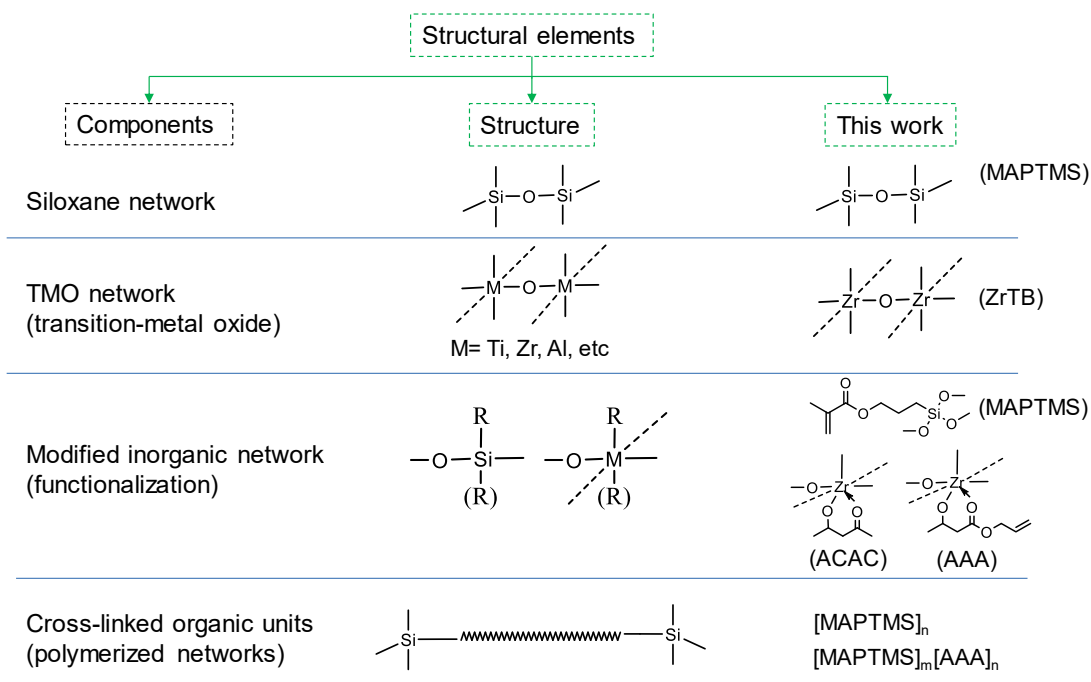


Fig. 3-1 Structural elements in the formation of hybrid inorganic-organic polymer materials

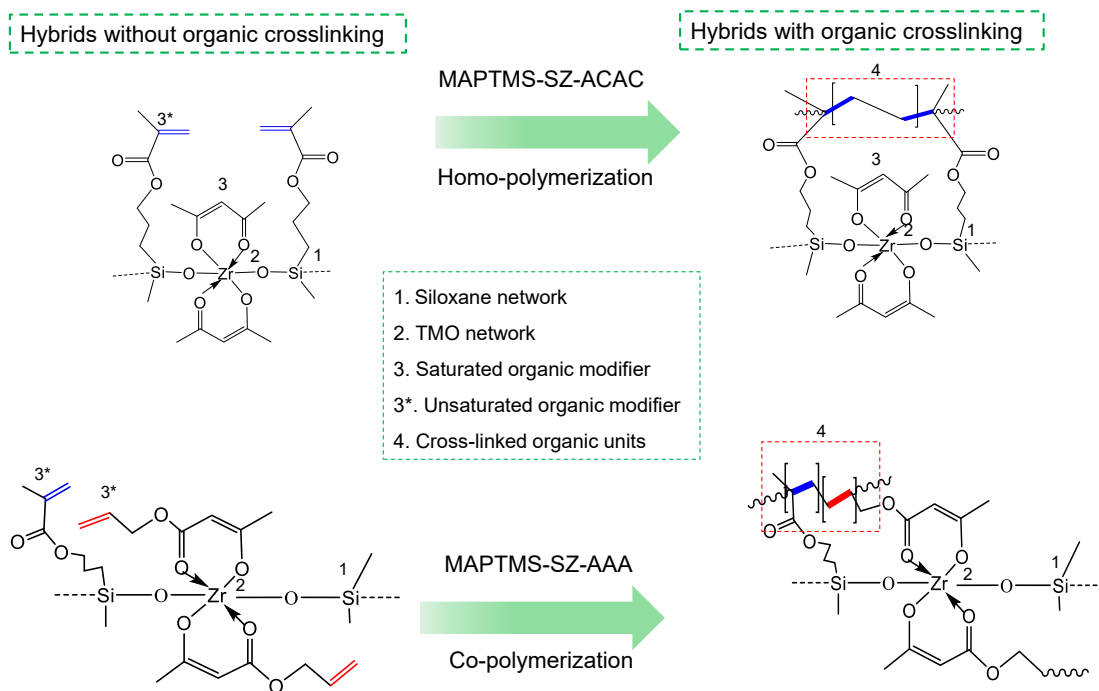


Fig. 3-2 Comparison of the structural elements of non-crosslinked and organic crosslinked MAPTMS-SZ-LIGAND materials

3.2 Experimental

In this study, samples (sol, film, powder, and membrane) derived from MAPTMS-SZ-AAA and MAPTMS-SZ-ACAC systems are named as follows: non-crosslinked samples are referred to as NC-AAA and NC-ACAC (sol, film, powder, or membrane), respectively, and crosslinked samples are referred to as CL-AAA and CL-ACAC (sol, film, powder, or membrane), respectively.

3.2.1 Preparation of MAPTMS-SZ-LIGAND sols, powders, and films

5 weight% of NC-AAA and NC-ACAC sols in ethanol were prepared in two stages as follows. First, zirconium (iv) tert-butoxide solution in ethanol (ZrTB, purity 80% in 1-butanol, Sigma-Aldrich) was pre-modified differently with two chelating ligands—acetylacetone (ACAC, purity 99%, Sigma-Aldrich) and allyl acetoacetate (AAA, purity >95 %, Tokyo Chemical Industries)—and stirred for one hour at room temperature in a ZrTB/LIGAND molar proportion of 1/4. Subsequently, the 5 weight% sols were realized by adding 3-methacryloxypropyltriethoxysilane (MAPTMS; 98% purity, Sigma-Aldrich; dissolved in ethanol), deionized water and hydrochloric acid (catalyst, purity 37%, Nacalai Tesque) dropwise into the ligand-modified ZrTB in a specific proportion (ZrTB/LIGAND/MAPTMS/H₂O/HCl = 1/4/1/8/0.25) to promote co-hydrolysis and co-condensation reactions. Hydrolysis and poly-condensation proceeded for more than 12 hours with stirring of the mixture in a closed vial at 500 rpm and room temperature.

To prepare the CL-AAA and CL-ACAC sols, the polymerization radical initiator, 2,2'-azobisisobutyronitrile (AIBN powder, purity 98 %, Sigma-Aldrich) was added to the previously prepared NC-AAA and NC-ACAC sols under room temperature with stirring at 600 rpm. Four different samples were prepared according to AIBN/C=C (methacrylate) molar ratios (0, 0.01, 0.1 and 1). Where a sol with an AIBN ratio of 0 represented the control sample. The crosslinking reaction was subsequently carried out at 80 °C in a thermostatic water bath for 24 hours. At the end of a 24-hour period, the CL-AAA and CL-ACAC sols (AIBN/C=C 0.1 and 1) had formed thick gels that were insoluble in pure ethanol. P-xylene solvent was carefully added to form a clear solution for further use.

Powders were prepared via a quick-drying method whereby the prepared sols (with and without crosslinking) were deposited dropwise into a platinum hot plate at 200 °C. Subsequently, the so formed powders were heated at 250 °C in a furnace under a 0.5 L min⁻¹ N₂ stream for 20 min. This is to ensure that solvents are

completely removed and to stabilize the material surface via further condensation reactions. To prepare the films used to evaluate the surface structural properties, the as-prepared sols were spin-coated onto UV-pretreated Si wafers at 2,000 rpm and then allowed to dry at room temperature prior to characterization.

3.2.2 Fabrication of MAPTMS-SZ-AAA and MAPTMS-SZ-ACAC membranes

Thin-layer membranes were formed onto prefabricated supports. Fabrication of the supports has been described in section 2.2.1. The active separation layers (MAPTMS-SZ-AAA and MAPTMS-SZ-ACAC membranes) were formed by hot-coating the prefabricated support with a 0.5 weight% concentration of respective sols (with and without crosslinking). After the coating process, each supported membrane was immediately calcined at 250 °C in a furnace with N₂ gas flowed at a rate of 0.5 L min⁻¹ for 15-20 min. This was to ensure that the solvents were completely removed and to stabilize the material surface via further condensation reactions. It is worth noting that although the NC-AAA and NC-ACAC sols were soluble in ethanol, all sols (with and without crosslinking) were dispersed in p-xylene to a 0.5 weight% prior to coating for consistent comparison.

3.2.3 Characterization of sols, powders, films, and membranes

The evolution of particle size distribution and particle dispersal in the pre-prepared sols, control sols, and organically crosslinked sols was evaluated at 25 °C via dynamic light scattering (DLS) using a Malvern Zetasizer Nano ZS (Malvern Instruments Ltd.). The surface and microstructural transformation of experimental samples were evaluated as follows. The presence and transformation of structural moieties in thin films supported on UV-treated Si-wafers were monitored using Fourier Transform-Infrared spectroscopy (FT-IR, FTIR-4100, JASCO, Japan). The amorphous structure nature and lattice spacing of as-prepared MAPTMS-SZ-LIGAND and MAPTMS-SZ-LIGAND+AIBN-derived powders were obtained via X-ray diffraction spectroscopy (D2 PHASER X-Ray Diffractometer, Bruker, Germany) using Cu K α as the radiation source with a wavelength of 1.54 Å. Furthermore, N₂ and CO₂ sorption isotherms of powders were analyzed at -196 and 25 °C, respectively, using BELMAX sorption equipment (BEL JAPAN INC., Japan). Prior to this measurement, adsorbed gases and vapors were evacuated from the samples at 200 °C for at least 12 hours. The thermal decomposition properties of non-crosslinked

and organic crosslinked powders were evaluated using thermogravimetry (DTG-60 Shimadzu Co., Japan). Finally, the supported membrane cross-sectional morphologies were obtained using Field Emission-Scanning Microscopy (FE-SEM, Hitachi S-4800, Japan). Prior to examination, sections were carefully cut from the supported membrane, attached to sample stages via special carbon tape, and vacuum dried at 50 °C for 24 hours.

3.2.4 Evaluation of gas permeation through membranes

A process-flow diagram of the gas permeation measurement setup has appeared in Chapter 2 Fig. 2-2. Immediately after preparing the top-layer MAPTMS-SZ-AAA and MAPTMS-SZ-ACAC membrane, it was carefully fitted into its steel module inside the furnace in the gas permeation measurement rig at 200 °C. Helium gas was then flowed through the module at 100 ml min⁻¹ for about 12 hours to remove adsorbed water vapor. Subsequently, single-gas permeation tests of the membranes were carried out using high-purity gases (H₂, He, CO₂, N₂, CH₄, CF₄, SF₆ in that order). Each gas was fed to the upstream side of the closed-end module at 200 kPa absolute pressure with temperatures ranging from 50 – 200 °C. Permeate side pressure was maintained at atmospheric levels, and the permeate gas-flow rate was measured using a bubble film flow meter (HORIBA-STEAC, Japan).

3.3 Results and Discussion

3.3.1 Evolution of organic cross-linking units via thermal radical polymerization

3.3.1.1 Facile control of particle size distribution and heterogeneity in sols

As previously mentioned, it was surmised that the study of hybrid inorganic-organic polymer membranes has been limited because of the difficulty associated with arresting the rate of photopolymerization reactions during organic crosslinking in the conversion of C=C bonds [28, 29]. Many researchers have demonstrated the importance of the particle size distribution of the coating sols in controlling a membrane's microstructure, and, hence, the molecular sieving properties [33, 34].

Fig. 3-3 (a) shows the observed polydispersity indexes (PDI) and z-average values of as-prepared NC-AAA and CL-AAA sols while Fig. 3-3 (b) shows the data for as-prepared NC-ACAC and CL-ACAC sols respectively. The PDI is a measure of the heterogeneity of a suspension based on particle size while the z-average represents the intensity weighted mean size of the dispersed particles to give the average size of

particle distribution. The particle size distributions by intensity are shown in Fig. 3-4 (a) and (b). Fig. 3-3 (a) clearly shows that after the crosslinking reaction, the PDI and z-average values of the CL-AAA (AIBN/C=C 0.1) showed a very high PDI (0.99) and z-average value (207 nm) compared with that of the control NC-AAA sol. The CL-ACAC sol showed a similar trend with respect to the z-average. The z-average value was increased to almost 100 nm. This indicates that the addition of the AIBN radical initiator induced a thermal polycondensation reaction. Furthermore, the PDI value of about 0.99 for the CL-AAA sol indicated a high level of polydispersity and suggested a very heterogeneous dispersion [35, 36]. For the CL-ACAC sol shown in Fig. 3-3 (b), however, the PDI showed only a slight change compared with the control NC-ACAC sol, which indicates that the heterogeneity that resulted from organic crosslinking was low. Therefore, the copolymerization of AAA with the MAPTMS created a high level of heterogeneity while the homopolymerization of MAPTMS in the MAPTMS-SZ-ACAC system resulted in little heterogeneity.

As previously established, the CL-AAA and CL-ACAC sols (AIBN/C=C 0.1 and 1) formed thick gels with intensity sol sizes of 700 and 200 nm, respectively, and these gels were insoluble in pure ethanol (Fig. 3-4). Particles within this range of sizes are unsuitable for membrane fabrication. The sizes were considerably reduced to within 2-8 nm (Fig. 3-4 (c)), however, via the careful addition of p-xylene solvent, and this range of sol sizes was suitable for coating onto the SiO₂-ZrO₂ intermediate layer substrate.

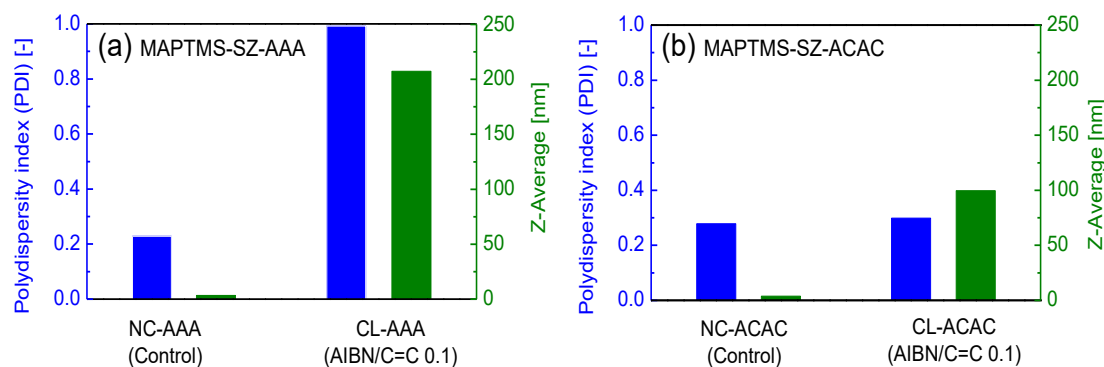


Fig. 3-3 Measured polydispersity index and Z-average values of control and crosslinked sols after a 24 h reaction at 80 °C for (a) MAPTMS-SZ-AAA and (b) MAPTMS-SZ-ACAC hybrid materials.

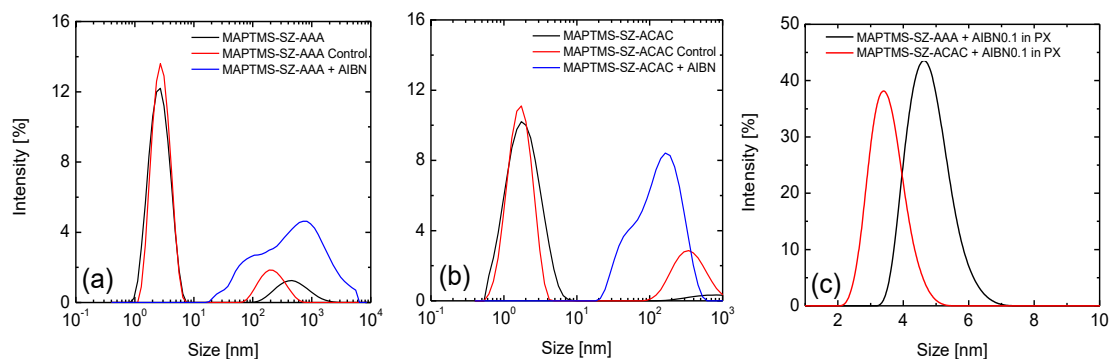


Fig. 3-4 Sol size based on intensity measured at room temperature for pre-prepared, control and AIBN-containing (a) MAPTMS-SZ-AAA and (b) MAPTMS-SZ-ACAC sols

3.3.1.2 Microstructural evolution of organically cross-linked materials

The structural transformations from non-crosslinked to organically crosslinked materials were confirmed according to the chemical and physical changes. FTIR spectroscopy represents a dependable method of monitoring the changes in chemical structure and was used to ascertain whether the growth in size and the evolution of polydispersity in CL-AAA and CL-ACAC sols were due to organic crosslinking reactions. Fig. 3-5 (a) and (b) show the observed FTIR profiles ranging from $1,800$ - $1,250$ cm^{-1} of different MAPTMS-SZ-AAA and MAPTMS-SZ-ACAC films, respectively, containing different AIBN/C=C ratios. The advancement of a polymerization reaction can be confirmed in a few ways: (1) the disappearance of C=C peaks ($1,638$ - $1,640$; and, $1,325$ cm^{-1}) belonging to MAPTMS [28, 29, 37] due to the organic crosslinking; (2) the broadening and shift of the C=O peak ($1,700$ - $1,720$ cm^{-1}) of MAPTMS to a higher wave number due to the loss of conjugation with C=C; [28, 29, 37] and, (3) the broadening and shift of peaks representative of ligand chelation to zirconium (AAA: $1,287$ cm^{-1} ; and, ACAC: $1,280$ cm^{-1}) in the cases where co-polymerization occurs between the MAPTMS and a ligand.

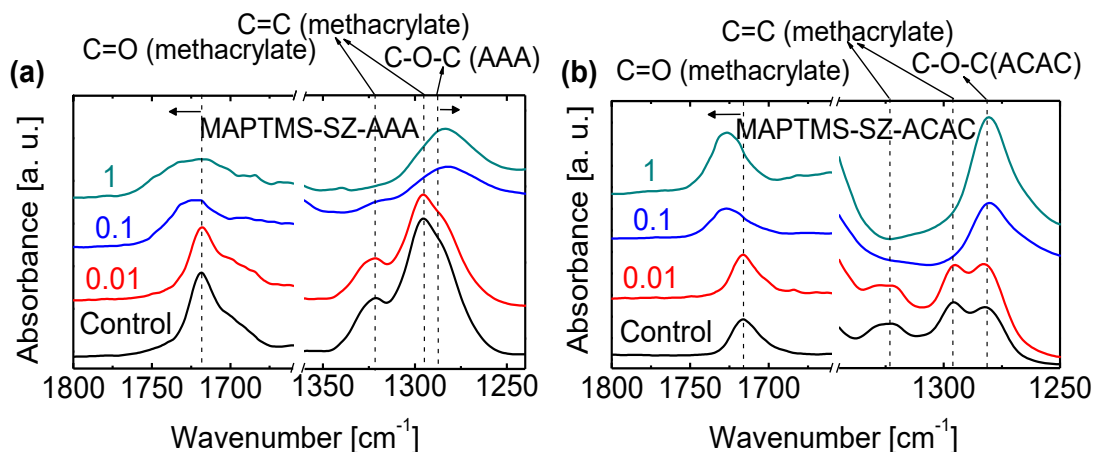


Fig. 3-5 Observed FTIR profiles of as-prepared (a) MAPTMS-SZ-AAA and (b) MAPTMS-SZ-ACAC films, respectively, at different AIBN/C=C ratios (0, 0.01, 0.1, 1), as measured at room temperature and presented in a range of from 1,800-1,250 cm^{-1} .

In Fig. 3-5 (a), three changes are evident as the AIBN/C=C ratio increased. The C=O (methacrylate) peak was shifted to higher wavenumbers and became broad, the C=C (methacrylate) peaks disappeared at an AIBN/C=C ratio of 1, and the AAA chelation peak became broad and shifted to lower wavenumbers. These changes were evident at the AIBN/C=C ratio of 0.1, which confirmed that organic crosslinking had taken place. The nature of this organic crosslinking can safely be assumed to be copolymerization since a transformation in the characteristic peak of AAA chelation to zirconium can be confirmed. On the other hand, as Fig. 3-5 (b) shows, the MAPTMS-SZ-ACAC samples displayed a similar trend with respect to the changes in C=C (methacrylate) and C=O (methacrylate) peaks but differed in the characteristic peak of ACAC chelation with zirconium as the peak showed no shift as the AIBN/C=C ratio increased. This underscores the fact that ACAC was not involved in organic crosslinking. With respect to ligand type, AAA was involved in a copolymerization crosslinking with MAPTMS because it possessed an allyl C=C unit while ACAC was not involved in any organic crosslinking since it possesses no organic crosslinking reactive units. Although it has been concluded that AAA is involved in copolymerization with MAPTMS, the occurrence of side homopolymerization reactions between AAA and MAPTMS reactive moieties cannot be ruled out. However, AAA in particular has been found to exhibit a ‘degradative monomer chain transfer’ where the $-\text{CH}_2-$ group adjacent to the allylic C=C bond causes a steric-induced resonance

stabilization thereby resulting in poor chain propagation [38]. Therefore, it is reasonable to opine that a co-polymerization between MAPTMS and AAA reactive moieties is the dominant reaction in this case.

After establishing the evolution of chemical structures via organic crosslinking and how this is affected by the ligand type, it would be interesting to determine the effect on the physical structure such as the microporosity and the correlation between them. Fig. 3-6 (a) shows the N_2 adsorption isotherms measured at $-196\text{ }^\circ\text{C}$ for NC-AAA and CL-AAA (AIBN/C=C 0.1) powders while Fig. 3-6 (b) shows the isotherms for NC-ACAC and CL-ACAC (AIBN/C=C 0.1) powders, all calcined at $250\text{ }^\circ\text{C}$, respectively. Table 3-1 also shows the experimentally obtained BET (Brunauer-Emmett-Teller) surface areas, pore volumes and average isosteric heats of CO_2 adsorption values for all samples. To calculate the isosteric heats of adsorption of CO_2 , the adsorption isotherms at three temperatures ($20, 25$ and $30\text{ }^\circ\text{C}$) were used and the respective isotherms and heats of adsorption plots are shown in Fig. 3-7.

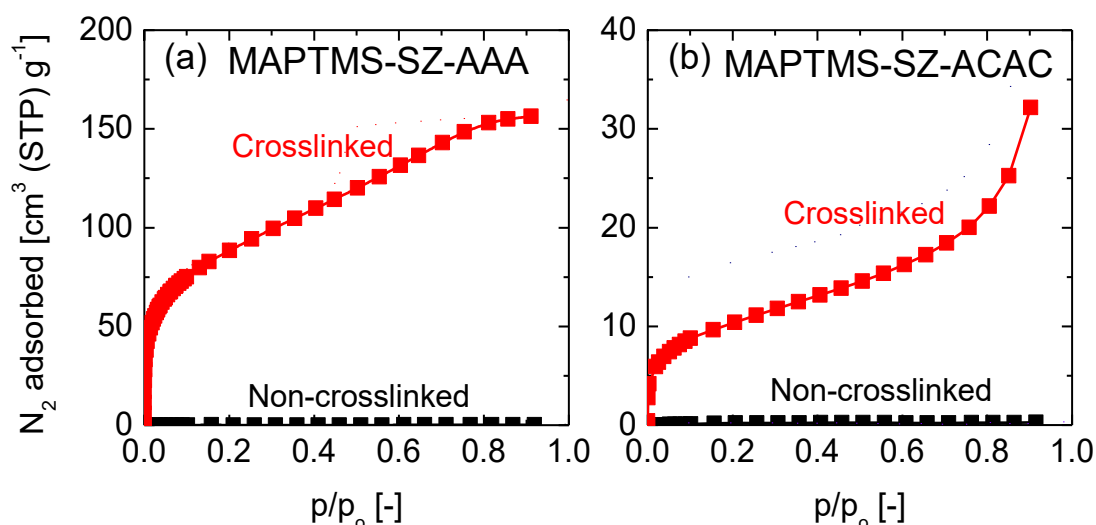


Fig. 3-6 (a) N_2 adsorption-desorption isotherms for non-crosslinked and organic cross-linked MAPTMS-SZ-AAA powders measured at $-196\text{ }^\circ\text{C}$; (b) CO_2 adsorption-desorption isotherms for non-crosslinked and organic cross-linked MAPTMS-SZ-AAA samples measured at $25\text{ }^\circ\text{C}$.

Table 3-1 Experimentally obtained BET (Brunauer-Emmett-Teller) surface areas (S_{BET}), pore volumes and average isosteric heats of CO_2 adsorption ($Q_{\text{st, Av}}$) values for powders calcined at 250 °C under a nitrogen gas stream.

Material	Non-crosslinked			Crosslinked		
	S_{BET} [$\text{m}^2 \text{g}^{-1}$]	Pore vol. [$\text{cm}^3 \text{g}^{-1}$]	$Q_{\text{st, Av}}(\text{CO}_2)$ [kJ mol^{-1}]	S_{BET} [$\text{m}^2 \text{g}^{-1}$]	Pore vol. [$\text{cm}^3 \text{g}^{-1}$]	$Q_{\text{st, Av}}(\text{CO}_2)$ [kJ mol^{-1}]
MAPTMS-SZ-AAA	< 1	0.1	20.8	320	73.4	27.7
MAPTMS-SZ-ACAC	< 1	0.2	23.3	40	8.6	28.0

Fig. 3-6 (a) and (b) show that NC-AAA and NC-ACAC powders adsorbed almost no N_2 . Correspondingly, the measured surface area and pore volume according to the BET method were less than $1 \text{ m}^2 \text{g}^{-1}$ and $0.2 \text{ cm}^3 \text{g}^{-1}$ respectively, as shown in Table 3-1, indicating a non-porous structure. On the other hand, after crosslinking, both samples showed a considerable increase in the amount of N_2 adsorbed compared with non-crosslinked samples with a corresponding increase in the BET surface area and pore volumes of $320 \text{ m}^2 \text{g}^{-1}$ and $73.4 \text{ cm}^3 \text{g}^{-1}$ for CL-AAA and $40 \text{ m}^2 \text{g}^{-1}$ and $8.6 \text{ cm}^3 \text{g}^{-1}$ for CL-ACAC powders, respectively (Table 3-1).

Moreover, at very low relative pressure ranges (P/P_0 : 0 – 0.001) a steep adsorption of N_2 was seen for organic crosslinked samples indicating the creation of microporosity. This was expected since mere organically modified -Si-O-Zr- chains or planar networks can be crosslinked into either extended planar networks or 3-dimensional structures creating a greater number of pores and preventing the densification of the -Si-O-Zr- networks, as illustrated in Fig. 3-8. This is a common phenomenon in hypercrosslinked polymers where the surface areas of non-crosslinked polymers increase immediately following chain crosslinking [39, 40]. The surface area measured for the CL-AAA powder sample was much higher than that measured for the CL-ACAC sample, however, which may be because following the homopolymerization of MAPTMS in a CL-ACAC sample, the ACAC ligands still occupied the intra-network spaces thereby reducing the effective surface areas (Fig. 3-8).

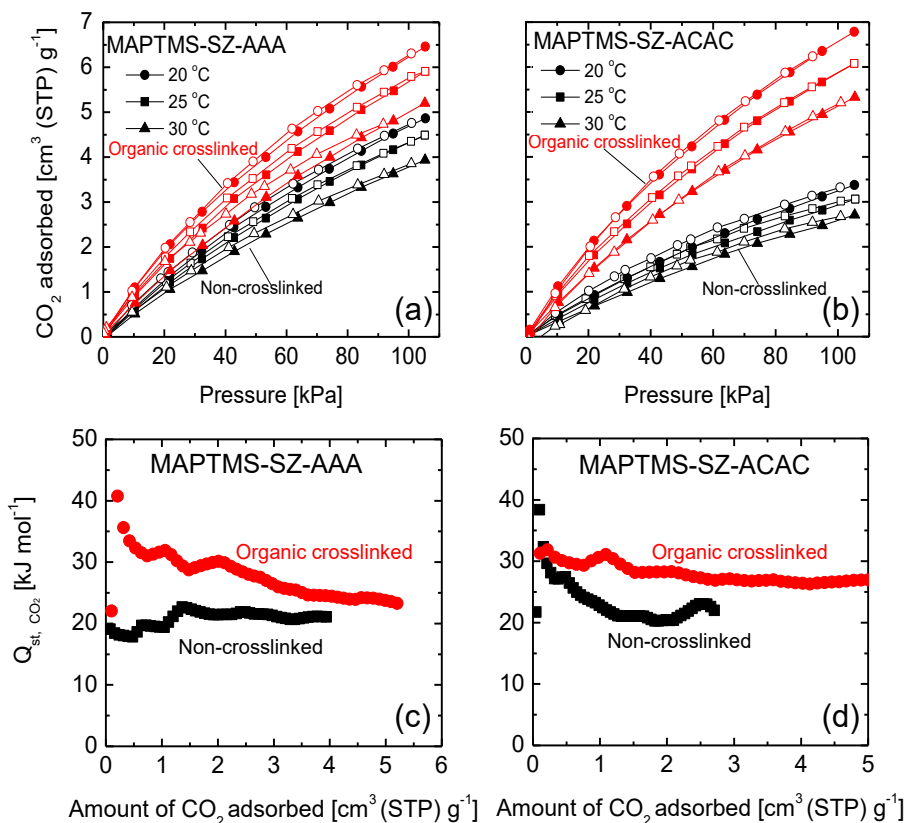


Fig. 3-7 CO₂ adsorption-desorption isotherms for non-crosslinked and organic cross-linked samples in (a) MAPTMS-SZ-AAA and (b) MAPTMS-SZ-ACAC measured at 20, 25 and 30 °C. Corresponding isosteric values for heat of CO₂ adsorption plots calculated based on the Clausius-Clapeyron equation are presented in panels (c) and (d), respectively.

Furthermore, the average isosteric heats of CO₂ adsorption increased from 20.8 for NC-AAA sample to 27.7 kJ mol⁻¹ for CL-AAA sample and from 23.3 for NC-ACAC sample to 28.0 kJ mol⁻¹ for CL-ACAC sample. This may be due to the increased attraction of CO₂ to Zr coordinatively unsaturated sites, which are made more accessible to CO₂ because the increased surface areas in crosslinked samples presents less hinderance for CO₂ access to Zr centers [41] Therefore, a correlation between the chemical and physical changes following crosslinking is established such that new connections accessible to N₂ are formed that prevent the tight ordering of -Si-O-Zr- chains or networks.

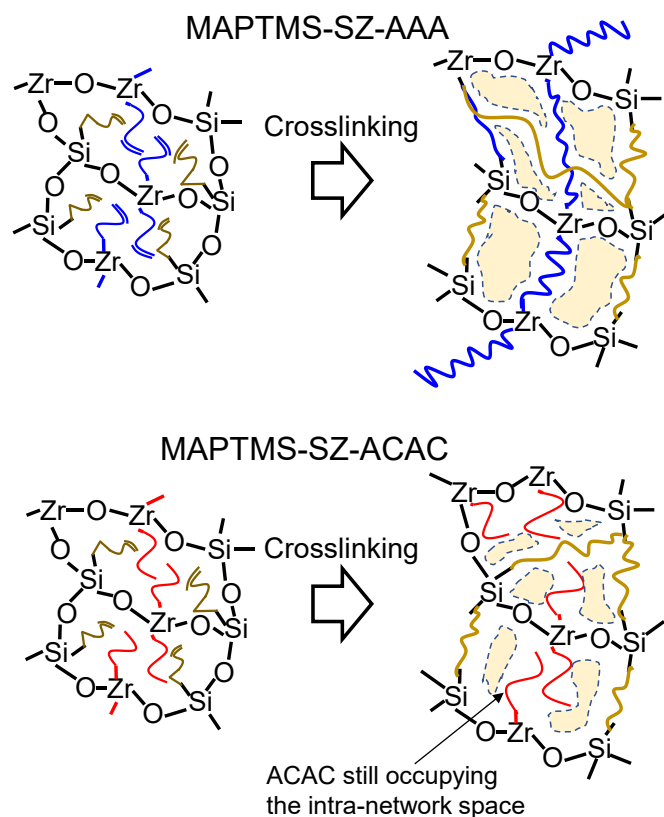


Fig. 3-8 Illustration of the network formation for non-crosslinked and organic crosslinked MAPTMS-SZ-LIGAND materials.

3.3.2 Thermal stabilities and decomposition mechanisms: effect of organic crosslinking

A key characteristic of membranes for robust applications is thermal stability at elevated temperatures, which has been widely substantiated for inorganic ceramic membranes. When inorganic materials are modified with organic moieties however, the thermal stability of the composite material becomes greatly dependent on the thermal stability of the organic modifier [42]. Fig. 3-9 (a) and (b) show the maximum decomposition temperatures and calculated activation energies of thermal decomposition for MAPTMS-SZ-AAA and MAPTMS-SZ-ACAC samples (crosslinked with different AIBN/C=C ratios of 0, 0.1 and 1), obtained from differential thermogravimetry (DTG) data.

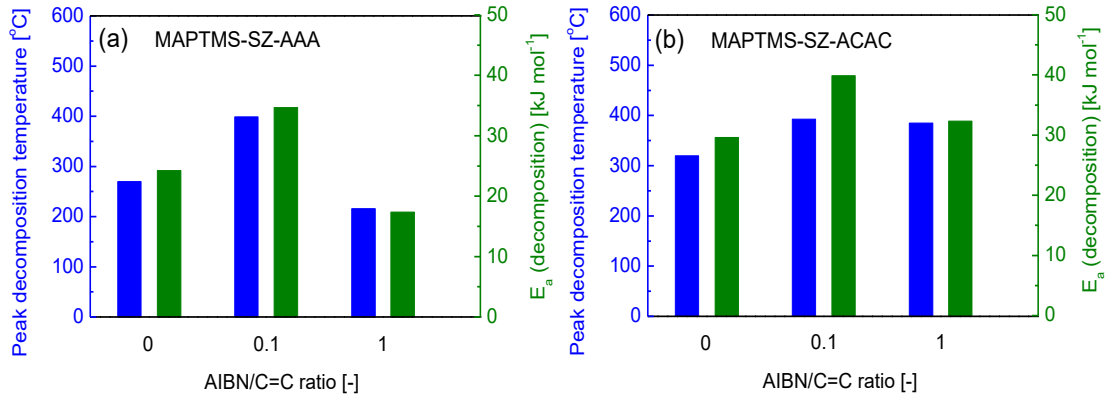


Fig. 3-9 DTG peak decomposition temperatures and calculated activation energies of thermal decomposition for MAPTMS-SZ-AAA and MAPTMS-SZ-ACAC powders crosslinked using different AIBN/C=C ratios.

The activation energies of thermal decomposition were calculated using the Horowitz-Metzger equation [43, 44] as shown below.

$$\log. \left[\log \frac{W_f}{W_f - W} \right] = \frac{\theta E_a}{2.303RT_s^2} - \log 2.303 \quad (3-1)$$

The equation describes a linear relationship such that the activation energy of thermal decomposition, E_a , can be calculated from the slope $\frac{E_a}{2.303RT_s^2}$ when $\log. \left[\log \frac{W_f}{W_f - W} \right]$ is plotted against θ , where W_f denotes the final weight loss after complete thermal decomposition, W is the weight loss at any temperature T , T_s is the maximum decomposition temperature as obtained from the DTG curve, θ denotes the difference $(T - T_s)$ and R is the universal gas constant. As shown in Fig. 3-9 (a) and (b) the peak decomposition temperatures and activation energies of thermal decomposition follow a similar trend. As the AIBN/C=C ratio in MAPTMS-SZ-AAA increased from 0 to 0.1, both T_s and E_a increased from 270 to 400 °C and 24.3 to 34.7 kJ mol⁻¹, respectively. However, as the AIBN/C=C ratio increased to 1, E_a and T_s decreased substantially to 17.4 kJ mol⁻¹ and 216 °C, respectively. This drastic reduction may be explained by a combined decomposition of excess AIBN and free non-crosslinked AAA. The same trend occurred in the case of MAPTMS-SZ-ACAC where both T_s and E_a increased from 320 to 393 °C and 29.6 to 40.0 kJ mol⁻¹, respectively, as AIBN/C=C increased from 0 to 0.1. Then, T_s and E_a were reduced to 385 °C and 32.3 kJ mol⁻¹, respectively, at an AIBN/C=C ratio of 1. This shows that the thermal stability of organic crosslinked materials increased and then decreased

with respect to AIBN content. This shows that the thermal stability of organic crosslinked materials increased and then decreased with respect to AIBN content. As indicated by FTIR, the presence of characteristic $C\equiv N$ peaks when the AIBN/C=C ratio was increased to 1 were identified. Considering the presence of free non-crosslinked AAA (having a lower thermal stability compared to ACAC), the decomposition of unreacted IBN radicals contributed to affect the MAPTMS-SZ-AAA at an AIBN/C=C ratio of 1 the most. Consequently, AIBN/C=C ratio close to 1 could be detrimental to the thermal stability of organic crosslinked materials. Therefore, for the fabrication of thermally stable and defect-free thin-layer membranes, an AIBN/C=C ratio of 0.1 guaranteeing no free unreacted IBN radicals was adopted.

Furthermore, the chemical structures of the organic moieties in NC-ACAC and CL-ACAC films for example decomposed differently when compared before and after calcination at 300 °C under N_2 , as shown in Fig. 3-10. MAPTMS-SZ-ACAC was chosen because it provides distinct peaks of the organic moieties involved in crosslinking (methacrylate) and those that are not (acetylacetonate). Since the C-C crosslinks cannot be identified via any peaks in FTIR, the stability of methacrylate C=O ($1,716-1,725\text{ cm}^{-1}$) was used as a representation since it is directly conjugated with the reactive C=C (methacrylate) involved in the crosslinking reaction. On the other hand, the characteristic peak of ACAC at C=C ($1,590\text{ cm}^{-1}$) represents the organic moiety not involved in crosslinking. For a consistent comparison the peak heights (absorbance values) of the organic moieties before and after calcination were normalized with the thermally stable Si-O-Si peaks ($1,080-1,090\text{ cm}^{-1}$) $\left(\frac{A_{C=O\text{ (methacrylate)}}}{A_{Si-O-Si}}, \frac{A_{C=C\text{ (ACAC)}}}{A_{Si-O-Si}}\right)$ and the obtained values are presented in Table 3-2.

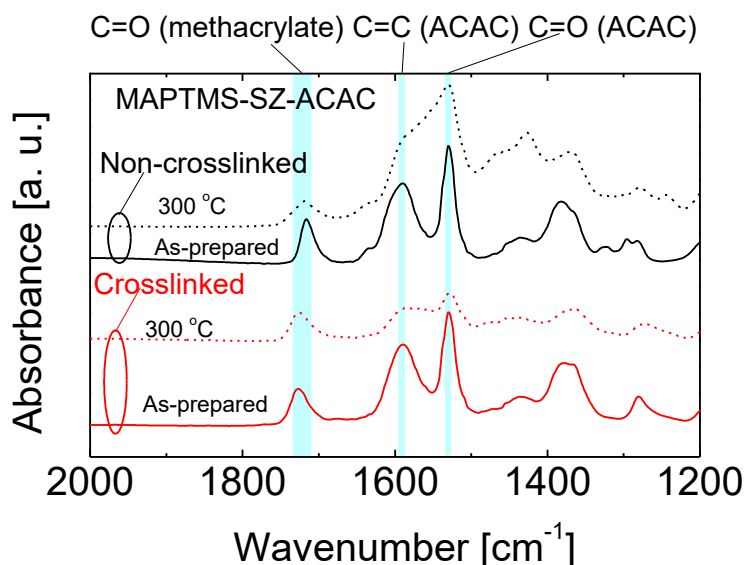


Fig. 3-10 Observed FTIR profiles of non-crosslinked and organic cross-linked MAPTMS-SZ-ACAC samples before and after calcination at 300 °C under a N₂ atmosphere.

Table 3-2 Normalized absorbance of organic moieties in non-crosslinked and crosslinked MAPTMS-SZ-ACAC films obtained from the FTIR spectra of Fig. 3-10.

Condition	Non-crosslinked		Crosslinked	
	$\frac{A_{C=O (meth.)}}{A_{Si-O-Si}}$	$\frac{A_{C=C (ACAC)}}{A_{Si-O-Si}}$	$\frac{A_{C=O (meth.)}}{A_{Si-O-Si}}$	$\frac{A_{C=C (ACAC)}}{A_{Si-O-Si}}$
	[-]	[-]	[-]	[-]
As prepared	1.1	1.9	0.8	1.7
Calcined (300 °C)	0.4	0.9	0.7	1.1

In the case of NC-ACAC before and after calcination at 300 °C, C=O (methacrylate) and C=C (ACAC) peaks both had reductions in intensity by 63 and 52%, respectively. However, for CL-ACAC after calcination at 300 °C, only the C=C (ACAC) peak was reduced by 39%. The C=O (methacrylate) peak, however, was only slightly decreased by 10% indicating that the C=O (methacrylate) peak was more stable at temperatures as high as 300 °C and by extension the organic crosslinked network to which it was conjugated. This indicates that the ACAC moieties in CL-ACAC samples that were uninvolved in organic crosslinking still decomposed within the same temperature range as that in the NC-ACAC sample. The MAPTMS moieties

in CL-ACAC and NC-ACAC, however, did not decompose in the same manner. Decomposition was delayed to a higher temperature in CL-ACAC, at which point the degradation was very rapid. Therefore, in organically crosslinked materials, the crosslinked moieties resulted in better stability.

Interestingly, the primary thermogravimetry (TG) profiles reveal different observations. The final residual weights after complete thermal decomposition become lower as the AIBN/C=C ratio increases, as shown in Fig. 3-11. It should be noted that the TG profile of a control sample is overlapped by that of a crosslinked sample with AIBN/C=C 0.01. This is a trend that is associated with a decrease in thermal stability. This disagrees with the previously established fact that organically crosslinked samples are more thermally stable. This can be explained by the addition of a crosslinking agent. AIBN radical initiators generate IBN radicals for the crosslinking process thus creating more crosslinking initiation sites as more AIBN is added. Therefore, as more AIBN radical initiators are added, more organically rich material results, which leads to more weight loss at the final decomposition stage.

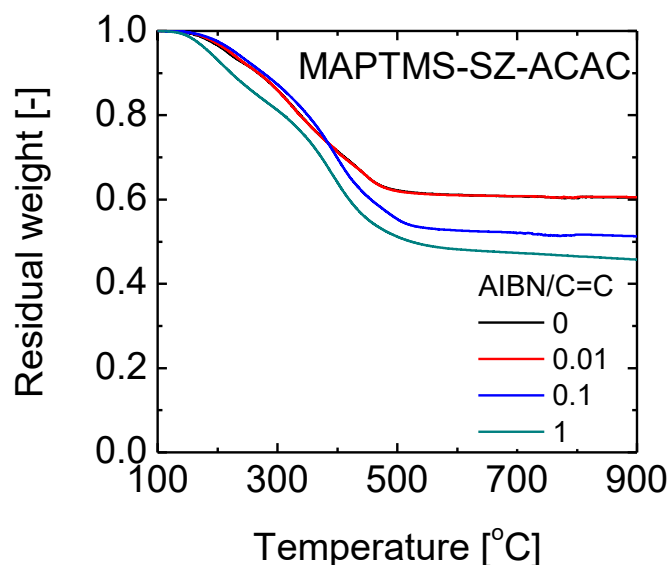


Fig. 3-11 Thermogravimetry (TGA) curves of MAPTMS-SZ-ACAC samples with different AIBN/C=C ratios fired under a N₂ atmosphere.

3.3.3 Membranes fabricated from cross-linked hybrids and gas permeation analysis

3.3.3.1 Morphologies of supported membranes

Fig. 3-12 (a) and (b) show the cross-sectional morphology of NC-AAA and CL-AAA membranes taken by FE-SEM on a scale of 100 nm (x300, 000 magnification). These images present a clear distinction between the active separation and SiO₂-ZrO₂ substrate layers. The SiO₂-ZrO₂ intermediate layer and active top separation layer were adequately controlled to within 400 nm. This is instructive since controlling the fabrication of membranes that are as thin as possible reduces permeation resistance while simultaneously maintaining a high level of molecular sieving properties. By contrast, a crack-free, free-standing, inorganic-organic hybrid membrane with a thickness of 100 μm had a very low H₂ permeance of 1.14 x 10⁻¹³ mol m⁻² s⁻¹ Pa⁻¹ [19].

As Fig. 3-12 (a) clearly demonstrates, the CL-AAA membrane formed a distinct layer about 20 nm at its thickest point over the SiO₂-ZrO₂ substrate. On the other hand, the NC-AAA membrane formed a much thinner, almost indistinct, layer less than 15 nm at its thickest point on the SiO₂-ZrO₂ substrate. This can be explained by the fact that the CL-AAA has a much higher polydispersity (Fig. 3-3 (a)) with an extensively crosslinked structure that is deposited much thicker and distinctly over a porous surface. When the NC-AAA is coated over a porous surface, its much lower polydispersity (Fig. 3-3 (a)) and non-crosslinked structure allows the particles to settle into the underlying surface thereby forming a thinner layer that is almost indistinct. To support this explanation, Fig. 3-12 (c) and (d) compare the deposition behaviors of CL-AAA and NC-AAA on a copper grid taken via transmission electron microscopy (TEM). As shown in Fig. 3-12 (c) and (d), after deposition the CL-AAA with its extended structure was deposited across the grid supports and spaces while the NC-AAA was deposited only on the grid supports and penetrated the spaces.

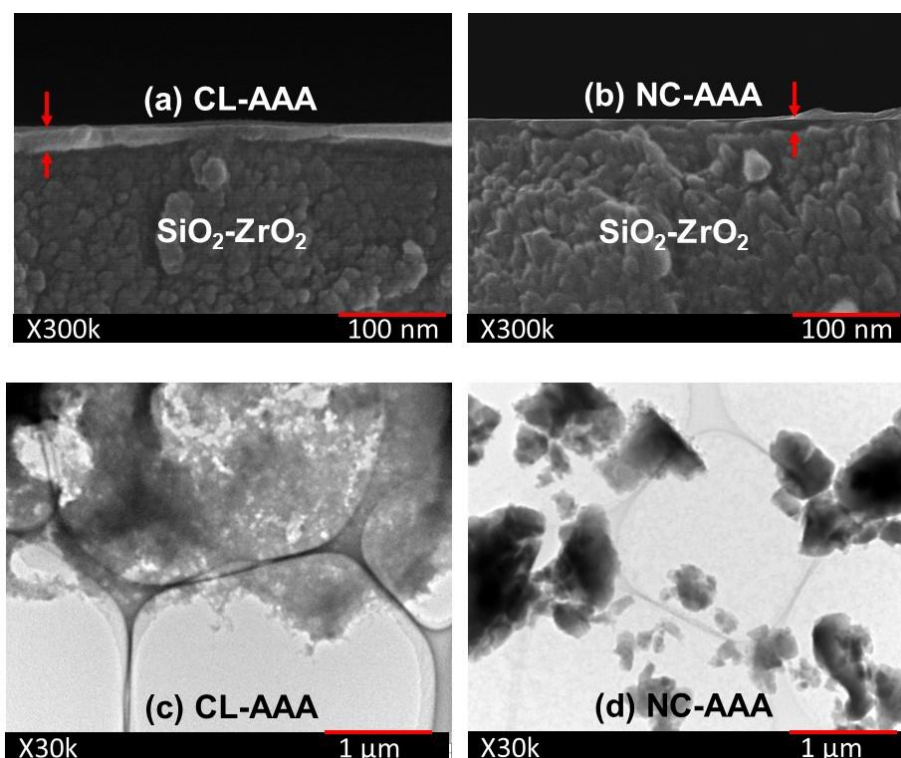


Fig. 3-12 Cross-sectional morphologies of (a) CL-AAA- and (b) NC-AAA-derived membranes obtained via field emission-scanning electron microscopy (FE-SEM-300,000x magnification) and the transmission electron microscopy (TEM- 30,000x magnification) images of deposited (c) CL-AAA- and (b) NC-AAA-derived films.

3.3.3.2 Gas sieving properties at 200 °C and membrane microstructures

Four different types of membranes were fabricated: non-crosslinked and organic crosslinked MAPTMS-SZ-AAA-derived membranes (NC-AAA and CL-AAA); non-crosslinked and organic crosslinked MAPTMS-SZ-ACAC-derived membranes (NC-ACAC and CL-ACAC). Fig. 3-13 (a) shows single-gas permeance as a function of kinetic diameter (He: 0.26 nm, H₂: 0.289 nm, CO₂: 0.33 nm, N₂: 0.364 nm, CH₄: 0.38 nm, CF₄: 0.48 nm, SF₆: 0.55 nm) at 200 °C. From Fig. 3-13 (a) it is evident that all membranes displayed molecular sieving properties such that gases with smaller kinetic diameters generally showed a higher permeance than gases with much larger kinetic diameters. Another observation is that non-crosslinked membranes generally showed higher permeance (H₂ permeance; NC-AAA: 5.4×10^{-7} mol m⁻² s⁻¹ Pa⁻¹, NC-ACAC: 8.7×10^{-7} mol m⁻² s⁻¹ Pa⁻¹) than the organic crosslinked versions (H₂ permeance; CL-AAA: 2.4×10^{-7} mol m⁻² s⁻¹ Pa⁻¹, CL-ACAC: 1.9×10^{-7} mol m⁻² s⁻¹ Pa⁻¹). This is consistent with the morphology of each membrane type as seen in Fig.

3-12 (a) and (b). The NC-AAA formed a thinner layer on the SiO₂-ZrO₂ substrate, and, thus, was expected to present a lower resistance to gas permeation. On the other hand, the CL-AAA formed a thicker layer and was expected to present higher resistance to gas permeation.

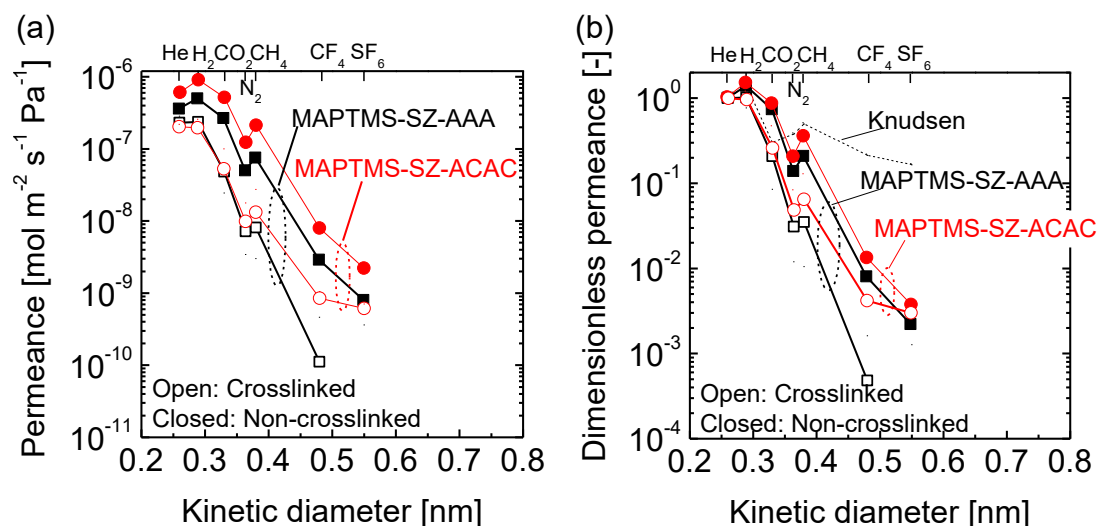


Fig. 3-13 Kinetic diameter dependence of (a) observed single-gas permeance and (b) dimensionless permeance (normalized on helium basis) of non-crosslinked and organic crosslinked MAPTMS-SZ-AAA- and MAPTMS-SZ-ACAC-derived membranes at 200 °C.

Table 3-3 H₂ permeance and H₂/X permeance ratio values for each membrane type at 200 °C

Membrane type	H ₂ permeance	H ₂ /X permeance ratio						
	[10 ⁻⁷ mol m ⁻² s ⁻¹ Pa ⁻¹]	He	CO ₂	N ₂	CH ₄	CF ₄	SF ₆	
NC-AAA	5.4	1.3	2.1	10.9	7.2	188.3	683.7	
CL-AAA	2.4	1.0	4.9	32.9	29.0	2117.0	-	
NC-ACAC	8.7	1.5	1.9	7.4	4.3	114.0	407.4	
CL-ACAC	1.9	1.0	3.7	19.8	14.9	230.6	319.4	

To get an idea of the pore size distribution and membrane microstructures after organic crosslinking, the plot of dimensionless permeance (normalized based on He

permeance) as a function of kinetic diameter of the different gases for different membranes at 200 °C is instructive, as shown in Fig. 3-13 (b). The plot reveals that NC-AAA- and NC-ACAC-derived membranes possessed similar dimensionless gas permeance values indicating similar pore size distribution. In contrast, CL-AAA- and CL-ACAC-derived membranes showed lower dimensionless gas permeance values indicating narrower pore size distribution. This suggests that the crosslinking in CL-AAA and CL-ACAC membranes modifies the microstructure enough to improve the molecular sieving properties (H_2/N_2 selectivity; CL-AAA: 33, CL-ACAC: 20) compared with non-crosslink-derived membranes (H_2/N_2 selectivity; NC-AAA: 11, NC-ACAC: 7). Table 3-3 presents the H_2/X permeance ratios for all gases. It is also worth noting that the molecular sieving properties were better for CL-AAA compared with that of CL-ACAC in that while the H_2 permeance was comparable H_2/N_2 selectivity was higher. This observation is instructive because according to the work of Schmidt [45] network formation by polymerization of modifying ligands can be complex, and some polymerization leads to a mere organic polymer chain that is almost independent of the main inorganic network while others will form truly interpenetrating chains with an inorganic superstructure, and both possibilities occur in the same material.

The modified gas translation model proposed by Lee *et al.* [46] was used to propose a way to estimate the mean pore size of <1 nm for membranes by employing a NKP (normalized Knudsen permeance) method based on the modified gas translation model expressed in Equation 3-2. Fig. 3-14 (a)-(d) show the calculated NKP values plotted as a function of kinetic diameter fitted to Equation 3-3 for NC-AAA, CL-AAA, NC-ACAC, and CL-ACAC-derived membranes, respectively. The figures reveal a rather interesting observation. Fig. 3-14 (a) and (c) show that two different mean pore diameters were estimated for the NC-AAA- (0.56 and 0.62 nm) and NC-ACAC-derived (0.65 and 0.70 nm) membranes, respectively, at 50 and 200 °C. In contrast, the estimated mean pore diameters for both CL-AAA- and CL-ACAC-derived membranes at 50 and 200 °C were very close (Fig. 3-14 (b) and (d)). This indicates that non-crosslink-derived membranes express different pore sizes depending on the permeation temperature. This may be explained by the fact that the non-crosslinked organic moieties in NC-AAA- and NC-ACAC-derived membranes are flexible and thus vibrate with an increase in temperature similar to polymer

matrices. Therefore, at low temperatures the flexible organic moieties are stiff and occupy much of the intraparticle free volume. High selectivity ($H_2/SF_6 \sim 1000$) can be obtained, but at high temperatures their continuous vibrations create more free volume for gas permeation. Therefore, it is difficult to estimate a single mean pore diameter in cases where organic moieties are not crosslinked and are free to vibrate.

$$P_i = \frac{1}{3} \frac{\varepsilon}{\tau L} (d_p - d_i) \frac{(d_p - d_i)^2}{d_p^2} \sqrt{\frac{8}{\pi M_i RT}} \exp\left(-\frac{E_{p,i}}{RT}\right) \quad (3-2)$$

$$f_{NKP} = \frac{P_i}{P_s} \sqrt{\frac{M_i}{M_s}} \approx \frac{\left(1 - \frac{d_i}{d_p}\right)^3}{\left(1 - \frac{d_s}{d_p}\right)^3} \quad (3-3)$$

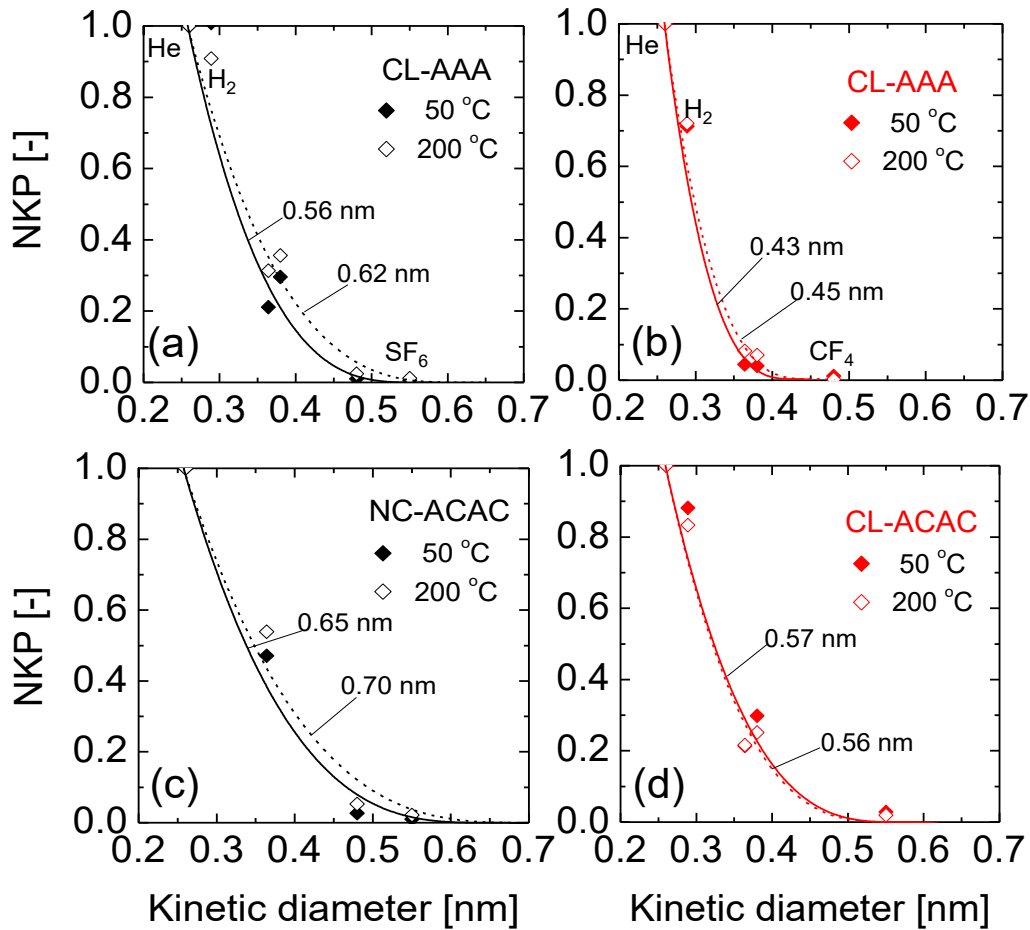


Fig. 3-14 NKP as a function of kinetic diameter fitted to Equation 4 for non-crosslinked and organic crosslinked MAPTMS-SZ-AAA and MAPTMS-SZ-ACAC. The solid and dashed lines are theoretical curves.

An alternative approach for estimating the mean pore diameter of membranes is the k_0 plot [46]. The k_0 plot presents a temperature-independent method for calculating the pore size by employing the apparent activation energies of gas permeation, E_p , and pre-exponential factors, k_0 , of a gaseous species, as expressed in Equation 3-4.

$$k_{0,i}^{1/3} = a^{1/3}d_p - a^{1/3}d_i \quad (3-4)$$

Therefore, the estimated pore diameters are the pore sizes for an infinite range of temperatures. Fig. 3-15 (a) and (b) show the k_0 plots as a relationship between the $k_{0,i}^{1/3}$ and the kinetic diameter for NC-AAA, CL-AAA, NC-ACAC and CL-ACAC-derived membranes, respectively. It is interesting to note that the estimated mean pore diameters of CL-AAA and CL-ACAC-derived membranes according to k_0 (CL-AAA: 0.48 nm; CL-ACAC: 0.55 nm) were very similar to the NKP-estimated pore diameters at both 50 and 200 °C. On the other hand, the k_0 -estimated mean pore diameters for NC-AAA and NC-ACAC-derived membranes (NC-AAA: 0.76 nm; NC-ACAC: 0.84 nm) were considerably higher than those estimated via NKP. These observations establish that the NKP method of estimating the mean pore diameters of NC-AAA and NC-ACAC-derived membranes more accurately defines the high selectivity of small gases over that of large gases, which cannot be expected from pore diameters that are estimated using the k_0 plots.

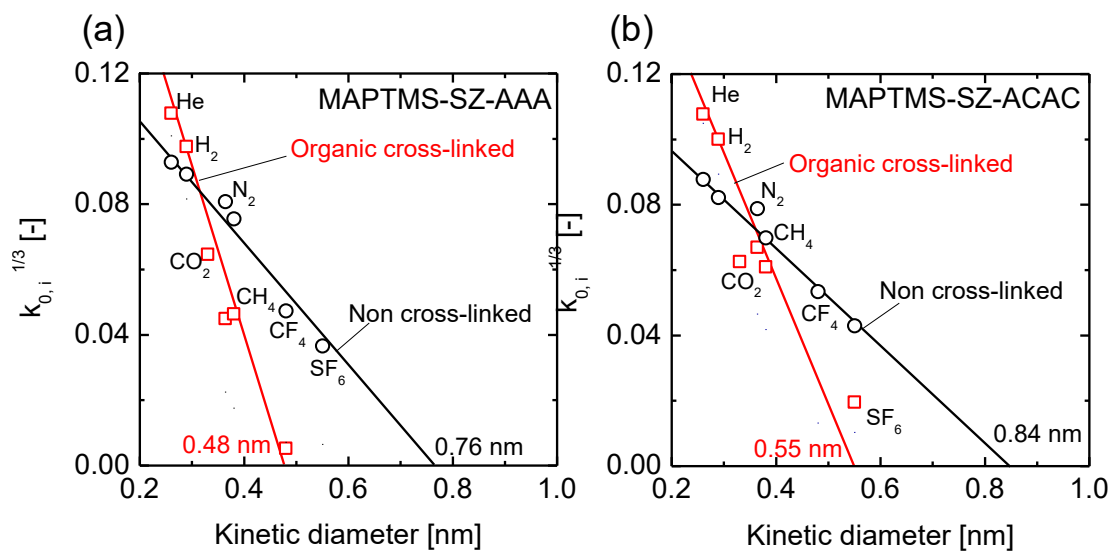


Fig. 3-15 Relationship between $k_{0,i}^{1/3}$ and kinetic diameter for (a) non-crosslinked and organic crosslinked MAPTMS-SZ-AAA and (b) non-crosslinked and organic crosslinked MAPTMS-SZ-ACAC.

3.3.3.3 Analysis of microporous structures via the gas permeance ratio and activation energy

The microstructures of membranes can be evaluated by examining the relationship between the permeation properties of gas molecules. Specifically, the relationship between He and H₂ permeation behaviors give insight into the sub-ultra-microporous nature of membranes [47]. Fig. 3-17 (a) and (b) plot the activation energy of He permeance and the He/H₂ permeance ratio as functions of the activation energy of H₂ permeance, and the activation energy of N₂ permeance along with the H₂/N₂ permeance ratio as functions of the activation energy of H₂ permeance, respectively. The activation energies were calculated by fitting the plots of the temperature dependence of gas permeance (shown in Fig. 3-16 (a)-(d) for NC-AAA, CL-AAA, NC-ACAC and CL-ACAC-derived membranes, respectively) to Equation 2-1, using activation energy, E_p , and k_0 as fitting parameters. Fig. 3-17 (a) and (b) show that the results of this work, which were reproduced, compare with various other state-of-the-art membranes such as glassy polymer membranes [48-51] rubbery polymer membranes [51] and silica-based membranes [52-54]. All related data are presented in Table 3-4. These various state-of-the-art membranes were carefully chosen to represent various membrane types and microstructures.

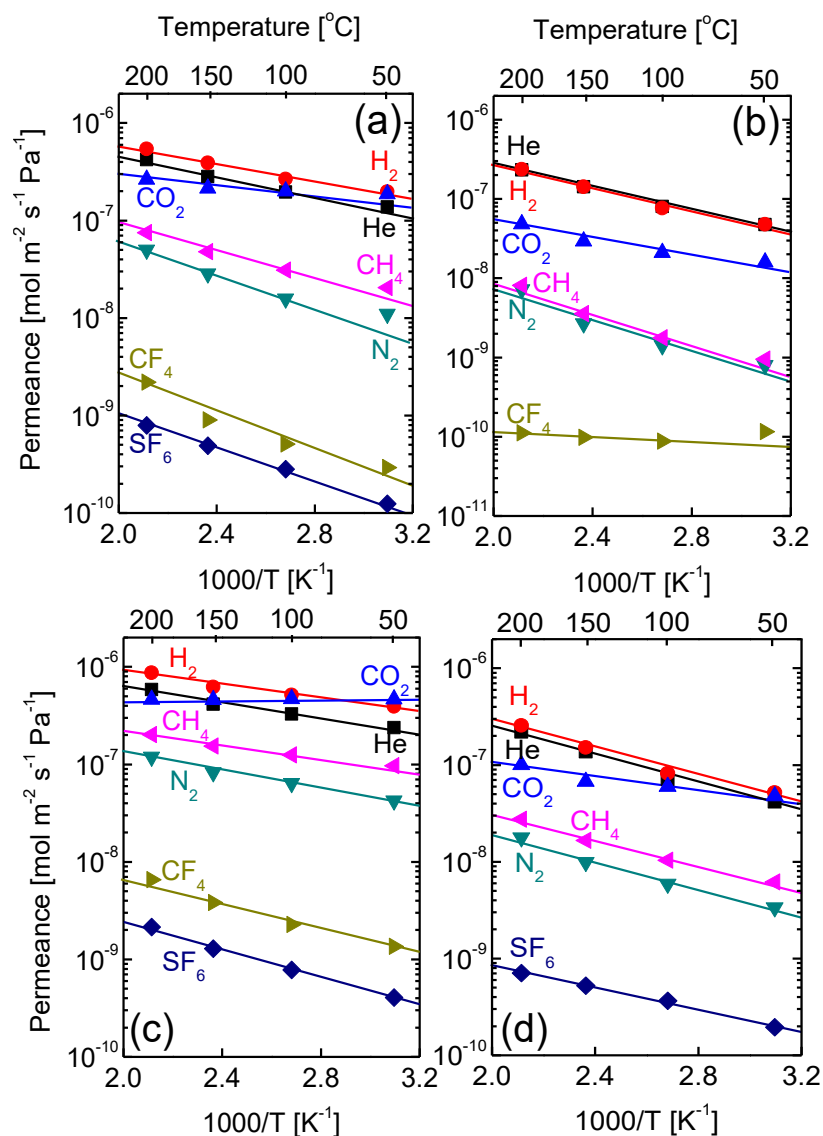


Fig. 3-16 Plots of the temperature dependence of single-gas permeance for membranes derived from (a) non-crosslinked MAPTMS-SZ-AAA, (b) organic crosslinked MAPTMS-SZ-AAA, (c) non-crosslinked MAPTMS-SZ-ACAC, and (d) organic crosslinked MAPTMS-SZ-ACAC.

Fig. 3-17 (a) shows that all membranes displayed very similar He-H₂ correlations without substantial deviations, which suggests that the activation energies of permeance, and by extension the permeation paths, for He and H₂ are very similar irrespective of membrane type. Fig. 3-17 (a) also shows that the He/H₂ permeance ratio generally increased as the activation energy of H₂ permeance increased for all membranes with polymer membranes showing the highest values. Therefore, in this respect, non-crosslinked and organic crosslink-derived membranes follow a similar trend.

A deviation in the characteristics of the membranes began to appear, however, as shown in Fig. 3-17 (b) as H₂ and N₂ began to permeate via different paths. As shown by the dashed lines, the non-crosslink-derived membranes showed a different trend from the organic-crosslink-derived membranes. The trends for NC-AAA and NC-ACAC tended towards that of polymer membranes that show a very high E_p for N₂ with respect to the E_p for H₂. This provided direct evidence of the similarities in the microstructural behavior of non-crosslinked organic moieties and polymer matrices. On the other hand, however, the trends for CL-AAA and CL-ACAC followed that of silica-based membranes, as evident from Fig. 3-17 (b). In this case, both values for E_p (N₂ and H₂) tended to be similar. Fig. 3-17 (b) also shows that, irrespective of the membrane type, the H₂/N₂ permeance ratio increased as the E_p (H₂) of a membrane became higher. It is worth noting that CL-AAA-derived membranes displayed better performance than CL-ACAC-derived membranes because of a greater amount of extended crosslinking, which combined with the parent -Si-O-Zr- network to form better molecular sieving networks.

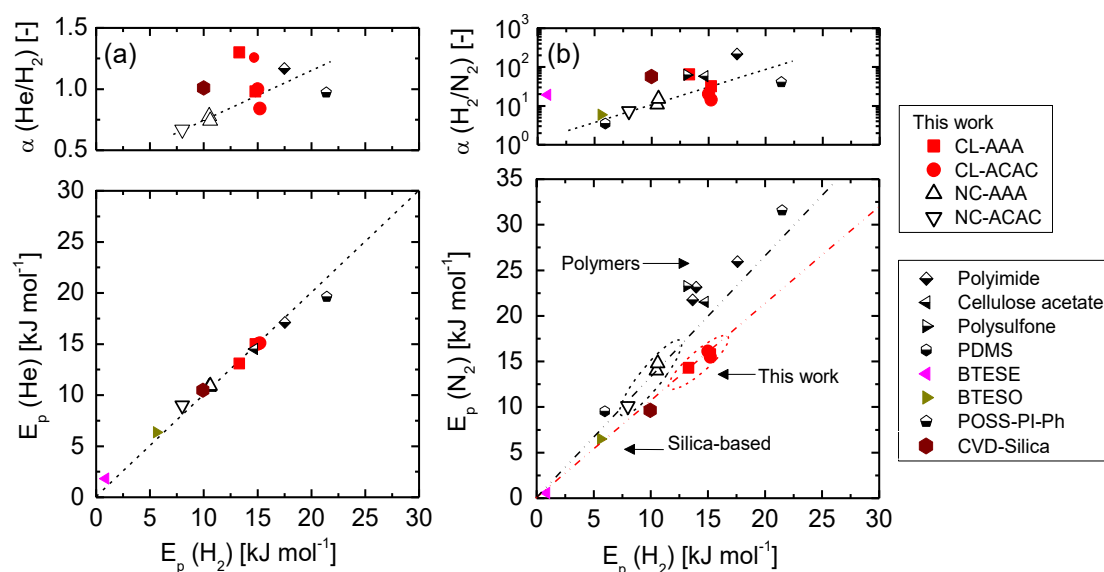


Fig. 3-17 (a) Activation energy of He permeance and the He/H₂ permeance ratio at 200 °C as functions of the activation energy of H₂ permeance; and, (b) Activation energy of N₂ permeance and H₂/N₂ permeance ratios at 200 °C as functions of the activation energy of H₂ permeance. Dashed lines are for a visual aid.

Table 3-4 Apparent activation energies of H₂ and N₂ permeation for different reference membranes

Membrane	Activation energy [kJ mol ⁻¹]			Permeance ratios [-]		Reference
	He	H ₂	N ₂	He/H ₂	H ₂ /N ₂	
Polyimide	17.0	17.6	25.9	1.2	162.7	[48]
Polyimide	-	14.1	23.1	-	-	[49]
Polyimide	-	13.7	21.7	-	-	[49]
Cellulose acetate	14.4	14.8	21.5	1.3	46.7	[50]
Polysulfone	-	13.2	23.2	-	50.0	[51]
PDMS	-	6.1	9.5	-	3.3	[51]
BTESE	1.8	1.0	0.6	-	16.2	[52]
BTESO	6.3	5.7	6.6	-	5.3	[52]
POSS-PI-Ph	19.5	21.5	31.5	1.0	33.3	[53]
CVD-silica	10.4	10	9.6	1.0	53.0	[54]

Fig. 3-18 (a) and (b) show the plots of H₂ and N₂ permeance and H₂/N₂ selectivity as functions of temperature for CL-AAA and CL-ACAC-derived membranes and NC-AAA and NCL-ACAC-derived membranes, respectively. The H₂-N₂ pair was chosen since they possess very different kinetic diameters and thus travel through different permeation paths. As expected, the H₂/N₂ selectivity for all membranes was slightly reduced with temperature while the H₂/N₂ selectivity showed greater temperature dependence NC-AAA and NC-ACAC-derived membranes. Close examination of the plots also reveals that for both CL-AAA- and CL-ACAC-derived membranes H₂ and N₂ permeance showed a higher dependence on temperature with corresponding higher apparent activation energies compared with the non-crosslinked alternatives, as shown in Fig. 3-18. It is generally agreed that higher activation energy is required to permeate smaller pores [47] and the higher level of activation energy values for CL-AAA- and CL-ACAC-derived membranes support the estimations for mean pore diameters. Associating a smaller pore size accompanied by higher apparent activation energies of gas permeation with the membrane microstructural characteristics may be misleading, however, when comparing membranes—particularly those of different classes.

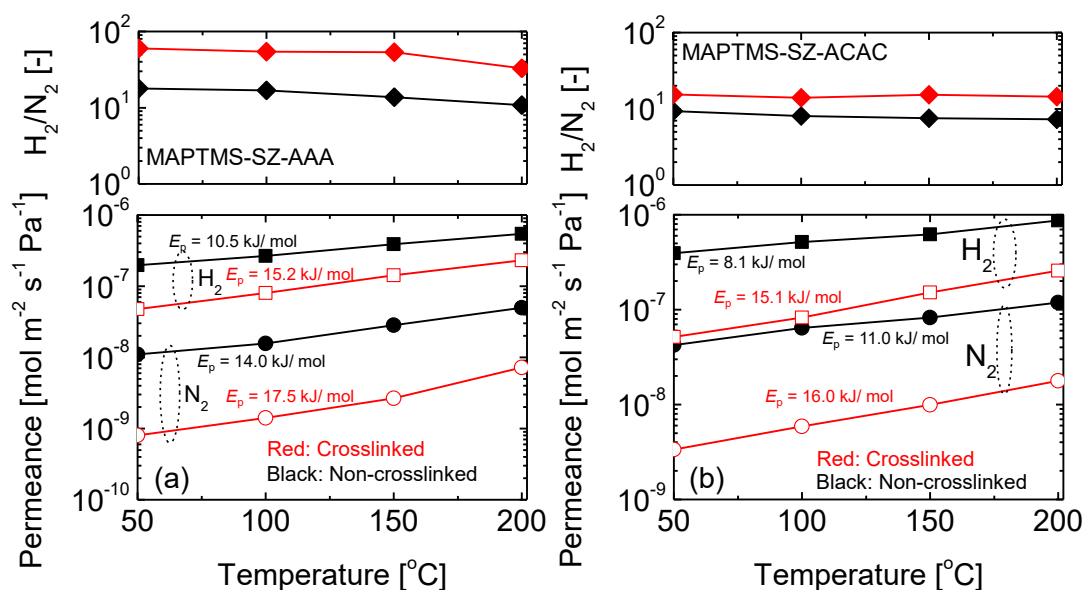


Fig. 3-18 H_2 and N_2 permeance and H_2/N_2 selectivity as functions of temperature for (a) non-crosslinked and organic crosslinked MAPTMS-SZ-AAA; and (b) non-crosslinked and organic crosslinked MAPTMS-SZ-ACAC.

Resolving this problem with comparisons required defining the intrinsic microstructural characteristics based on the normalized values of the apparent activation energies of the chosen gas pairs. An intrinsic characteristic is the ‘intrinsic rigidity’ (or flexibility). For membranes with very flexible microstructures such as rubbery polymer membranes, the activation energy of gas permeance increases with kinetic diameter. In rigid microstructures such as glassy polymer membranes, the gas kinetic diameter has less influence on the activation energies [3]. Based on this, the intrinsic rigidity of a membrane can be defined as the normalized difference in the activation energies of the permeance of a large gas and that of a smaller gas through a membrane—in this case, $1 - [E_p(H_2) / E_p(N_2)]$. The relative rigidity is determined by the value of this expression.

Fig. 3-19 plots the defined ‘intrinsic rigidity’ as a function of $E_p(N_2) / E_p(H_2)$ for various membranes. Details of the activation energy values are presented in Table 3-4. A correlation was established such that increasingly ‘flexible’ membranes show increasingly polymer-like characteristics. On the other hand, increasingly ‘rigid’ membranes show increasingly silica-like microstructures. Organosilica membranes are regarded as rigid, porous membranes with some degree of flexibility depending on the bridging organic group, and the greater the length of the organic C-C bridge

between Si atoms the more flexibility it will demonstrate [52, 55]. In Fig. 3-19, a BTESO-derived membrane with an octyl hydrocarbon bridge tended towards a more flexible and dense structure compared with a BTESE-derived membrane with an ethyl hydrocarbon bridge. The NC-AAA- and NC-ACAC-derived membranes showed a trend closer to polymer membranes confirming the theory of flexible non-crosslinked moieties. The CL-AAA- and CL-ACAC-derived membranes on the other hand tended towards more 'rigid' structures.

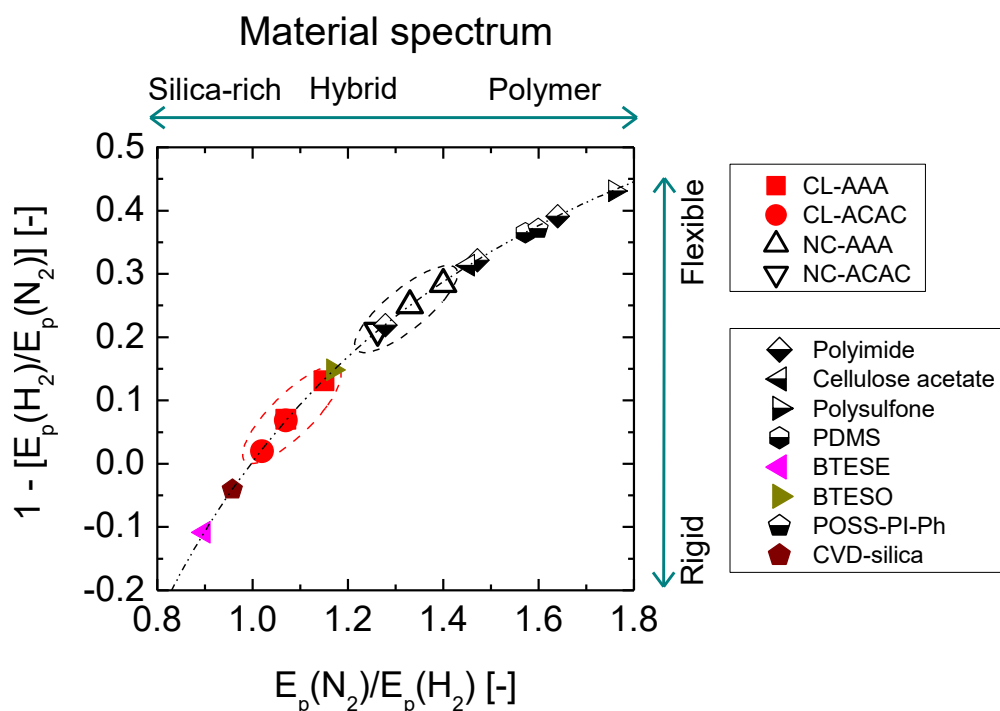


Fig. 3-19 The correlation between 'intrinsic rigidity' $1 - [E_p(H_2) / E_p(N_2)]$ and material class calculated based on $E_p(N_2) / E_p(H_2)$ values for different membranes. Absolute values are shown in Fig. 3-18 and Table 3-4.

3.4 Conclusions

In this work, $\text{SiO}_2\text{-ZrO}_2$ -based organically crosslinked hybrid membranes were fabricated from class II hybrid inorganic-organic polymer materials prepared via the sol-gel crosslinking of ligand (AAA or ACAC)-chelated zirconium oxide networks and MAPTMS derived siloxane networks. The membrane microstructural characteristics were evaluated by analyzing the results of single-gas permeation experiments for temperatures ranging from 50 to 200 °C. The following conclusions were drawn.

1. The AAA-chelated system generated a copolymerization crosslinking with the Si precursor- 3-methacryloxypropyltriethoxysilane (MAPTMS)- while the ACAC-chelated system generated only a homopolymerization within the MAPTMS.

2. New pore structures were formed as organic crosslinked materials showed a significant increase in measured BET surface areas (OCL-AAA: $\approx 320 \text{ m}^2 \text{ g}^{-1}$, OCL-ACAC: $\approx 40 \text{ m}^2 \text{ g}^{-1}$) compared with non-crosslinked samples ($< 1 \text{ m}^2 \text{ g}^{-1}$).

3. The organic crosslink-derived membranes showed better molecular sieving properties with higher H_2/N_2 selectivity (OCL-AAA: 33, OCL-ACAC: 20) compared with non-crosslink-derived membranes (H_2/N_2 selectivity; NCL-AAA: 11, NCL-ACAC: 7).

4. Organic-crosslinked and non-crosslink-derived membranes revealed different membrane microstructures. Two different mean pore diameters were estimated for the NCL-AAA- (0.56 and 0.62 nm) and NCL-ACAC-derived (0.65 and 0.70 nm) membranes, respectively, at 50 and 200 °C. On the other hand, the estimated mean pore diameters for both OCL-AAA- and OCL-ACAC-derived membranes at 50 and 200 °C were very similar.

5. Finally, characterization of the membrane microstructure based on the permeation properties of H_2 and N_2 revealed that organic crosslink-derived membranes showed a change in microstructural properties from a flexible to a rigid structure that ranged between that of silica-rich materials and polymer materials.

Considering that a facile method was established to fabricate and tune the microstructure of supported class II hybrid inorganic-organic highly permeable membranes, this study should serve as a template for future work where tailored network tuning and functionalization can be achieved for specific applications.

Cited literature

1. W. J. Koros, Evolving beyond the thermal age of separation processes: membranes can lead the way, *AIChE J.*, 50 (2004) 2326-2334
2. W. J. Koros, A more aggressive approach is needed for gas separation membrane development, *Membrane*, 31 (2006) 157-160
3. M. R. Abdul Hamid, H. -K. Jeong, Recent advances on mixed-matrix membranes for gas separation: opportunities and engineering challenges, *Korean J. Chem. Eng.* 35 (2018) 1577-1600

4. L. M. Robeson, Polymer membranes for gas separation, *Curr. Opin. Solid St. M.* 4 (1999) 549-552
5. L. M. Robeson, The upper bound revisited, *J. Membr. Sci.*, 320 (2008) 390-400
6. H. L. Castricum, A. Sah, R. Kreiter, D. H. A. Blank, J. F. Vente, J. E. ten Elshof, Hydrothermally stable molecular separation membranes from organically linked silica, *J. Mater. Chem.*, 18 (2008) 2150-2158
7. K. Yoshida, Y. Hirano, H. Fujii, T. Tsuru, M. Asaeda, Hydrothermal stability and performance of silica-zirconia for hydrogen separation in hydrothermal conditions, *J. Chem. Eng. Jpn.* 34 (2001) 523-530
8. G. P. Fotou, Y. S. Lin, S. E. Pratsinis, Hydrothermal stability of pure and modified microporous silica membranes, *J. Mater. Sci.*, 30 (1995) 2803-2808
9. Y. Li, H. Zhou, G. Zhu, J. Liu, W. Yang, Hydrothermal stability of LTA zeolite membranes in pervaporation, *J. Membr. Sci.*, 297 (2007) 10-15
10. T. Tsuru, Nano/subnano-tuning of porous ceramic membranes for molecular separations, *J. Sol-Gel Sci. Technol.*, 46 (2008) 349-361
11. N. K. Raman, C. J. Brinker, Organic “template” approach to molecular sieving silica membranes, *J. Membr. Sci.*, 105 (1995) 273-279
12. Y. Ohta, K. Akamatsu, T. Sugawara, A. Nakao, A. Miyoshi, S. -I. Nakao, Development of pore size-controlled silica membranes for gas separation by chemical vapor deposition, *J. Membr. Sci.*, 315 (2008) 93-99
13. M. Kanezashi, M. Kawano, T. Yoshioka, T. Tsuru, Organic-inorganic hybrid silica membranes with controlled silica network size for propylene/propane separation, *Ind. Eng. Chem. Res.*, 51 (2012) 944-953
14. P. Judeinstein, C. Sanchez, Hybrid organic-inorganic materials: a land of multidisciplinary, *J. Mater. Chem.*, 6 (1996) 511-525
15. C. Sanchez, J. de A. A. Soler-Illia, F. Ribot, T. Lalot, C. R. Mayer, V. Cabuil, Designed Hybrid organic-inorganic nanocomposites from functional nanobuilding blocks, *Chem. Mater.* 13 (2001) 3061-3083
16. K. -H. Haas, Hybrid inorganic-organic polymers based on organically modified Si-alkoxides, *Adv. Eng. Mater.*, 2 (2000) 571-582
17. L. Yu, M. Kanezashi, H. Nagasawa, J. Oshita, A. Naka, T. Tsuru, Pyrimidine-bridged organoalkoxysilane membrane for high-efficiency CO₂ transport via mild affinity, *Sep. Purif. Technol.*, 178 (2017) 232-241

18. K. -H. Haas, H. Wolter, Synthesis, properties and applications of inorganic-organic copolymers (ORMOCERs), *Curr. Opin. Solid St. M.*, 4 (1999) 571-580
19. S. M. Kumbar, T. Selvam, C. Gellermann, W. Storch, T. Ballweg, J. Breu, G. Sextl, ORMOCERs (organic-inorganic hybrid copolymers)-zeolite beta (BEA) nanocomposite membranes for gas separation applications, *J. Membr. Sci.*, 347 (2010) 132-140
20. C. Sanchez, B. Julian, P. Belleville, M. Popall, Applications of hybrid organic-inorganic nanocomposites, *J. Mater. Chem.* 15 (2005) 3559-3592
21. G. Schottner, K. Rose, U. Posset, Scratch and abrasion resistant coatings on plastic lenses-state of the art, current developments and perspectives, *J. Sol-Gel Sci. Technol.*, 27 (2003) 71-79
22. S. Amberg-Schwab, H. Katschorek, U. Weber, A. Burger, Inorganic-organic polymers as migration barriers against liquid and volatile compounds, *J. Sol-Gel Sci. Technol.*, 26 (2003) 699-703
23. M. Popall, J. Kappel, M. Pilz, J. Schulz, G. Feyder, A new inorganic-organic polymer for the passivation of thin film capacitors, *J. Sol-Gel Sci. Technol.*, 2 (1994) 157-160
24. R. Houbertz, G. Domann, J. Schulz, B. Olsowski, L. Frohlich, W. -S. Kim, Impact of photoinitiators on the photopolymerization and the optical properties of inorganic-organic hybrid polymers, *Appl. Phys. Lett.*, 84 (2004) 1105
25. J. F. Velez, J. M. Aparicio, J. Mosa, Covalent silica-PEO-LiTFSI hybrid solid electrolytes via sol-gel for Li-ion battery applications, *Electrochim. Acta.*, 213 (2016) 831-841
26. K. Prater, The renaissance of the solid polymer fuel cell, *J. Power Sources.*, 29 (1990) 239-250
27. B. Bonnet, D. J. Jones, J. Roziere, L. Tchicaya, G. Alberti, M. Casciola, L. Massinelli, B. Bauer, A. Peraio, E. Rammuni, Hybrid organic-inorganic membranes for a medium temperature fuel cell, *J. New Mat. Electrochem. System.*, 3 (2000) 87-92
28. O. Soppera, C. Croutxe-Barghorn, D. J. Lougnot, New insights into photoinduced processes in hybrid sol-gel glasses containing modified titanium alkoxides, *New J. Chem.*, 25 (2001) 1006-1014

29. O. Soppera, C. Croutxe-Barghorn, Real-time Fourier transform infrared study of free-radical UV-induced polymerization of hybrid sol-gel. I. Effect of silicate backbone on photopolymerization kinetics, *J. Polym. Sci. A1.*, 41 (2003)716-724
30. J. M. Guissi, I. Blaszczyk-Lezak, B. Sanz, P. E. Allegretti, C. Mijangos, M. S. Cortizo, Tautomeric acetoacetate monomers as building units of functional copolymers, *Eur. Polym. J.*, 59 (2014) 84-93
31. K. Grzybowska, Z. Wojnarowska, A. Grzybowski, M. Paluch, J. M. Guissi, M. S. Cortizo, I. Blaszczyk-Lezak, C. Mijangos, Effect of polymer structure on the molecular dynamics and thermal behavior of poly (allyl acetoacetate) and copolymers, *Polymer*, 55 (2014) 1040-1047
32. S. Lawal, M. Kanezashi, H. Nagasawa, T. Tsuru, Development of an acetylacetonate-modified silica-zirconia composite membrane applicable to gas separation, *J. Membr. Sci.*, 599 (2020) 117844
33. M. ten Hove, A. Nijmeijer, L. Winnubst, Facile synthesis of zirconia doped hybrid organic inorganic silica membranes, *Sep. Purif. Technol.*, 147 (2015) 372-378
34. N. Moriyama, H. Nagasawa, M. Kanezashi, T. Tsuru, Bis(triethoxysilyl)ethane (BTESE)-derived silica membranes: pore size formation mechanism and gas permeation properties, *J. Sol-Gel Sci. Technol.*, 86 (2018) 63-72
35. S. T. Balke, T. H. Mourey, Local polydispersity detection in size exclusion chromatography: method assessment, *J. Appl. Polym. Sci.*, 81 (2001) 370-383
36. M. Danaei, M. Dehghankhold, S. Ataei, F. H. Davarani, R. Javanmard, A. Dokhani, S. Khorasani, M. R. Mozafari, Impact of particle size and polydispersity index on the clinical applications of lipidic nanocarrier systems, *Pharmaceutics*, 10 (2018) 57
37. X. Le Guevel, C. Palazessi, P. Proposito, G. D. Giustina, G. Brusatin, Influence of chelating agents on the photopolymerization of hybrid Ti-based waveguides *J. Mater. Chem.*, 18 (2008) 3556-3562
38. A. Matsumoto, T. Kumagai, H. Aota, H. Kawasaki, R. Arakawa, Reassessment of free-radical polymerization mechanism of allyl acetate based on end-group determination of resulting oligomers by MALDI-TOF-MS spectrometry, *Polym. J.*, 41 (2009) 26-33

39. R. Joseph, W. T. Ford, S. Zhang, M. P. Tsyurupa, A. V. Patsukhov, V. A. Davankov, Solid-state ^{13}C -NMR analysis of hypercrosslinked polystyrene, *J. Polym. Sci. A: Polym. Chem.*, 35 (1997) 695-701
40. B. Li, R. Gong, Y. Luo, B. Tan, Tailoring the pore size of hypercrosslinked polymers *Soft Matter*, 7 (2011) 10910-10916
41. C. Morterra, G. Cerrato, C. Emanuel, End-on surface coordinated (adsorbed) CO_2 : a specific ligand for surface Lewis acidic centres, *Mater. Chem. Phys.*, 29 (1991) 447-456
42. S. Lawal, L. Yu, H. Nagasawa, T. Tsuru, M. Kanezashi, A carbon-silica-zirconia membrane with CO_2 flow-switching behavior promising high-temperature H_2/CO_2 separation, *J. Mater. Chem. A*, 8 (2020) 23563
43. H. H. Horowitz, G. Metzger, A new analysis of thermogravimetric traces, *Anal. Chem.*, 35 (1963) 1464-1468
44. A. Gronowski, Z. Wojtczak, The thermal decompositions of some transition metal acrylates and polyacrylates, *J. Thermal Anal.*, 26 (1983) 233-244
45. H. Schmidt, *Sol-gel: science and technology; proceedings of the winter school on glass and ceramics from gels, São Carlos (SP), Brazil, 14 - 19 August 1989. Ed. by M. A. Aegerter. Singapore: World Scientific. 1989, 432-469*
46. H. R. Lee, M. Kanezashi, Y. Shimomura, T. Yoshioka, T. Tsuru, Evaluation and fabrication of pore-size-tuned silica membranes with tetraethoxydimethyl disiloxane for gas separation, *AIChE J.*, 57 (2011) 2755-2765
47. P. Hacıoğlu, D. Lee, G. V. Gibbs, S. T. Oyama, Activation energies for permeation of He and H_2 through silica membranes: An ab initio calculation study, *J. Membr. Sci.*, 313 (2008) 277-283
48. K. Haraya, K. Obata, T. Hakuta, H. Yoshitome, The permeance of gases through a new type of polyimide membrane, *Membrane*, 11 (1986) 48-52
49. Y. Yampolskii, S. Shishaskii, A. Alentiev, K. Loza, Correlations with and prediction of activation energies of gas permeation and diffusion in glassy polymers, *J. Membr. Sci.*, 148 (1998) 59-69
50. K. Haraya, K. Obata, T. Hakuta, T. Yoshitome, Permeation of gases through a symmetric cellulose acetate membrane, *J. Chem. Eng. Jpn.*, 19 (1986) 464-466
51. X. Feng, P. Shao, R. Y. M. Huang, G. Jiang, R. -X. Xu, A study of silicone rubber/polysulfone composite membranes: H_2/N_2 and O_2/N_2 permselectivities, *Sep. Purif. Technol.*, 27 (2002) 211-223

52. H. L. Castricum, G. G. Paradis, M. C. Mittelmeijer-Hazeleger, R. Kreiter, J. F. Vente, J. E. ten Elshof, Tailoring the separation behavior of hybrid organosilica membranes by adjusting the structure of the organic bridging group, *Adv. Funct. Mater.*, 21 (2011) 2319-2329
53. M. Kanezashi, Y. Tomarino, H. Nagasawa, T. Tsuru, Tailoring the molecular sieving properties and thermal stability of carbonized membranes containing polyhedral oligomeric silsesquioxane (POSS)-polymer via the introduction of norbornene, *J. Membr. Sci.*, 582 (2019) 59-69
54. H. Nagasawa, Y. Yamamoto, M. Kanezashi, T. Tsuru, Atmospheric-pressure plasma-enhanced chemical vapor deposition of hybrid silica membranes, *J. Chem. Eng. Jpn.*, 51 (2018) 732-739
55. M. Kanezashi, Y. Yoneda, H. Nagasawa, T. Tsuru, Gas permeation properties for organosilica membranes with different Si/C ratios and evaluation of microporous structures, *AIChE J.*, 63 (2017) 4491-4498

Chapter 4

Enhanced H₂-permselectivity in a carbon-silica-zirconia membrane derived from an acetylacetonate-ceramic composite pyrolysis

4.1 Introduction

A 2015 report estimates that the world's energy demand satisfied by fossil fuels such as gas, coal and oil stand at about 85 % [1]. Global annual energy demand of 12 billion tons equivalent of oil (BTOE) results in the emission of about 40 giga tons of CO₂ [1] while the energy forecasted to be demanded by just 8 countries (China, the USA, India, Brazil, Japan, South Korea, Canada, and Mexico) will be as high as 12.5 BTOE by 2035, the equivalent of 2015 total CO₂ emission-resulted consumptions [2]. With the continued dependence on fossil fuel and the ever-increasing demand of energy, the danger of increased CO₂ emission looms. Moreover, other factors driving the move towards alternative fuel sources are energy security and climate change [3]. Hydrogen is widely considered as a sustainable and clean alternative source of energy [3, 4].

Hydrogen not being a primary energy source needs to be produced from other sources. The chemical industry serves as a good source of hydrogen production [5]. However, it is required to purify hydrogen from other gases encountered in typical industrial gas mixtures. Several techniques exist for gas separation in the chemical industries including but not limited to traditional processes such as pressure swing adsorption (PSA), cryogenic distillation [6-8], and in recent decades the energy conservative membrane separation [7, 8].

Diverse membrane types such as polymeric membranes, metallic membranes, porous inorganic membranes (silica, zeolites, metal oxides) and carbon molecular sieve membranes have been studied for hydrogen separation and extensive reviews have been made [7, 9]. Porous inorganic membranes are considered as having superior molecular permselectivity compared to polymeric membranes, durable over longer periods and can be operated at much higher temperatures [10]. Particularly, silica membranes have shown very high H₂-permselective ability [11, 12]. However, a significant problem with pure silica-derived membranes has to do with network

densification at elevated temperatures [10, 13]. According to the work of de Vos and Verweij, H₂ permeance in a silica membrane prepared at 600 °C was about 5×10^{-7} mol m⁻² s⁻¹ Pa⁻¹ at 200 °C which is one order of value lower compared to that measured for a silica membrane prepared at 400 °C (1.7×10^{-6} mol m⁻² s⁻¹ Pa⁻¹) [11]. Lin also demonstrated that by subjecting an unsupported silica to 600 °C for 30 hours, the pore volume of silica reduced significantly [13]. The densification of silica at very high temperatures is attributed to the continued thermal condensation of -Si-OH groups [13, 14]. Vahlas and co-workers processed silica films at 400 °C and observed a continuous decrease in the -Si-OH peaks detected by FTIR as temperature increased until completely disappearing at 550 °C [14].

Several techniques have thus been proposed to solve this issue. Such includes spacer methods (incorporating an alkyl group to bridge Si atoms in the precursor) [15, 16], templating methods (incorporating unhydrolyzable organic group attached as a pendant to the Si atom) [17, 18], anion/cation doping [19, 20] and the use of stable metal oxides such as Al₂O₃, ZrO₂ and TiO₂ as co-composites [21-23]. At temperatures reaching 550-600 °C, the most potent means of inhibiting the thermal densification of silica is by compositing with metal oxides because of their extreme thermal stability. The modification of pure silica with a metal oxide to form a ceramic composite has been well studied and the most popular oxide being ZrO₂ [22, 24, 25]. The stability of silica is greatly improved, and stability improvement increased as Zr content was increased. Yoshida and co-workers [22] as well as Choi and co-workers [24] showed that for the best results, a mixture ratio of 1:1 was desired. A SiO₂-ZrO₂ (1:1) membrane prepared by Choi and co-workers by the CVD method at 600 and 650 °C only reduced in H₂ permeance from 7.3 to 2.7×10^{-8} mol m⁻² s⁻¹ Pa⁻¹. Thereafter, the membrane kept a stable value at 700 °C. However, increasing the ZrO₂ content resulted in loss of selectivity and a low initial H₂ permeance [22]. This is borne out of the difficulty in achieving an ideal mixed composite because the hydrolysis rate of the zirconia precursor is much faster than a silica precursor [26]. This can result in a quick formation and aggregation of ZrO₂ nanoparticles thereby forming an uneven composite.

Therefore, to achieve even hydrolysis reactivity, a modification of the zirconium precursor with an organic coordination ligand has been suggested and proven [27, 28].

Utilizing organic coordination/complexing ligands offers another advantage as reported by Spijksma and co-workers [29]. They showed that by modifying Ti and Zr atoms in a TiO₂-ZrO₂ composite with diethanolamine (DEA), a membrane's permselectivity could be improved. Since then, the successful improvement of a SiO₂-ZrO₂ composite membrane with an acetylacetonate ligand has been reported [30]. But the ligands do not remain intact at the elevated temperatures in which a SiO₂-ZrO₂ composite membrane is needed.

Recently, our group studied an acetylacetonate-modified SiO₂-ZrO₂ composite (1:1) after carbonization by the pyrolysis of the acetylacetonate ligand at 550 °C in a nitrogen atmosphere [31]. It was confirmed that the acetylacetonate ligands pyrolyzed to form free carbon nanoparticles within the SiO₂-ZrO₂ composite network. Characterizations revealed an interesting electrostatic interaction between the free carbon nanoparticles and CO₂ whereby a pressure-induced flow switching of CO₂ could be observed. Combined with an improved H₂ permeance over an unmodified SiO₂-ZrO₂ composite membrane, enhanced H₂/CO₂ separation ability was achieved. However, the pyrolysis of the highly concentrated acetylacetonate ligands resulted in formation of faults in the membrane. Hoebbel and co-workers however demonstrated that by utilizing the same stoichiometric water/alkoxide molar ratio during the hydrolysis process, different β -diketone and β -ketoester-type coordination ligands chelated to Zr displayed different hydrolytic stability with the most stable being acetylacetonate [32]. It is thus reasonable to theorize that utilizing different water/alkoxide molar ratios beyond the stoichiometric amount for hydrolysis could tune the eventual concentration of an acetylacetonate ligand within the resulting SiO₂-ZrO₂ composite. This may be able to control the extent and severity of the defect-forming pyrolysis.

In this study, the combination of compositing metal oxide and carbonization of acetylacetonate ligand for the modification of silica microstructure was investigated. Specifically, the effect of hydrolysis water/alkoxide molar ratio (WR) on the resulting carbonized SiO₂-ZrO₂ composite network was investigated and optimized. Based on the optimized water ratio, the synergistic combination of the relative amounts of SiO₂ over ZrO₂ and the residual free carbon for H₂-permselectivity was investigated and compared to the state-of-the-art sol-gel-derived SiO₂-ZrO₂ membrane. It is resolved

that free residual carbon deposited within the SiO₂-ZrO₂ composite provided microstructural benefits.

4.2 Experimental

4.2.1 Materials preparation by sol-gel

5 wt% in ethanol medium of SiO₂-ZrO₂-acetylacetonone (represented as SZA hereafter) sols were prepared according to a previous report [30]. In this work however, two different sol-gel experiments were made.

In the first experiment, SZA sols of different Si/Zr molar ratios were prepared. First, 80% pure zirconium (iv) tert-butoxide (ZrTB, Aldrich) dissolved in ethanol (Aldrich) was modified with a 99% pure acetylacetonone (ACAC, Aldrich) (ACAC/ZrTB molar ratio = 4/1) for one hour at room temperature. Subsequently, a 98% pure tetraethoxysilane (TEOS, Aldrich) dissolved in ethanol was co-hydrolyzed with the previously acetylacetonone-modified ZrTB in four places so that the atomic ratios of Si/Zr were 9/1, 7/3, 5/5 and 3/7. For hydrolysis, deionized water (water/alkoxide molar ratio = 60) and hydrochloric acid (37%, Nacalai Tesque) as a catalyst (acid/alkoxide molar ratio 0.25) were used. Hydrolysis and poly-condensation were carried out in a closed vial by stirring the mixture at 550 rpm for more than 12 hours at room temperature.

In the second sol-gel experiment in a similar manner but fixing the atomic ratio of Si/Zr at 5/5, three different SZA sols were prepared depending on the water/alkoxide molar ratio (WR). Hydrolysis proceeded using three different WR of 4, 60 and 240. The acid/alkoxide ratio was still fixed at 0.25.

Films, powders and membranes were subsequently prepared from these sols. To prepare films, 50 µl of the respective sols were drop-coated on UV-pretreated silicon wafers and allowed to dry at room temperature. The dried films were then calcined at the needed temperatures before characterization. Powders were prepared by a slow drying process whereby the sol was allowed to dry freely under a controlled temperature range of 50-80 °C giving rise to unsupported xerogels. These were subsequently crushed and calcined appropriately. All calcinations were done in a N₂

atmosphere. The samples prepared at 300 °C are referred to as SiO₂-ZrO₂-ACAC (SZA) while those prepared at 550 °C are referred to as carbon- SiO₂-ZrO₂ (CSZ).

4.2.2 Preparation of membrane separation layers

Membranes were fabricated on support layers fabricated according to the description in section 2.2.1. Two types of membrane separation layers were fabricated based on the calcination temperature. The first type was the membrane derived from SiO₂-ZrO₂-ACAC. A 5 wt% SiO₂-ZrO₂-ACAC sol prepared as described earlier was diluted to a 0.5 wt% with ethanol and wipe-coated onto the SiO₂-ZrO₂ intermediate layer. This was followed by firing in 600 ml min⁻¹ nitrogen gas stream at 300 °C for 20 min. This process was repeated several times to obtain the top separation layer.

The second type of membrane layer was the carbon-SiO₂-ZrO₂ separation layer based on a carbonization/pyrolysis process. The same 0.5 wt% sol was wipe-coated on the SiO₂-ZrO₂ intermediate layer in the same manner. After this, the membrane was allowed to dry at 50 °C in a stream of nitrogen gas for a few minutes before flash firing at the carbonization temperature of 550 °C for 20 minutes. This process was also repeated several times.

4.2.3 Material characterizations

The particle sizes of the as-prepared sols were measured at room temperature via dynamic light scattering (DLS) using a Malvern Zetasizer Nano ZS (Malvern Instruments Ltd.). The presence and intensities of different functional groups were detected on film-coated silicon wafers via Fourier Transform Infrared Spectroscopy (FTIR, FTIR-4100, JASCO, Japan). The thermogravimetric profiles of powders were analyzed using Differential Thermogravimetry/Thermogravimetric Analysis (DTG-TGA, TG-50 Shimadzu Co., Japan) under nitrogen or air gas flow of approximately 60 ml min⁻¹ and a heating rate of 10 °C min⁻¹.

Furthermore, the lattice structures were analyzed using the x-ray diffractometry (XRD, D2 PHASER X-Ray Diffractometer, Bruker, Germany) with Cu K α as the radiation source at a wavelength of 1.54 Å. The microporosities of the powders were evaluated by N₂ adsorption-desorption experiments at -196 °C (BELSORP MAX,

BEL Co., Japan). Prior to this measurement, samples were evacuated of adsorbed gases and vapors at 200 °C for at least 12 hours.

4.2.4 Evaluation of membrane gas permeation characteristics

A schematic representation of the gas permeation measurement setup is shown in Fig. 2-2. Water vapor adsorbed into the membrane pores after fabrication was desorbed by flowing He gas through the membrane module setup at 200 °C for 12 hours.

The single gas performance of membranes was evaluated with high-purity gases (H₂, He, CO₂, N₂, CH₄, CF₄, SF₆ in that order) similar to the procedure described in section 2.2.3.

4.3 Results and discussion

4.3.1 Control and optimization of ligand chelation degree via hydrolysis

Since Hoebbel *et al* [32] demonstrated that more than 97% of ACAC chelating ligand remained bonded to Zr after 7 days of hydrolysis with a water/alkoxide molar ratio of 6, ACAC ligand is a very hydrolytically stable chelating ligand. Therefore, by replacing the butoxyl groups in the Zr precursor by ACAC chelating ligands, the hydrolysis rate can be considerably slowed down [26, 27]. Nonetheless, it is expected that this resistance can be finely controlled by varying the water/alkoxide molar ratio other than the stoichiometric amount and the concentration of the ligand chelated to Zr in a SiO₂-ZrO₂-ACAC composite may be tuned. Three different water/alkoxide molar ratios (WR) have been adopted: 4, 60 and 240 to determine the optimal WR required to form a carbon-SiO₂-ZrO₂ membrane. On one hand, it is anticipated that a lower WR will result in retaining a higher amount of ligand and therefore possibly result in a higher amount of residual carbon, on the other hand, a higher WR result in higher microporosity for a better molecular sieving effect. For this purpose, the ratio of Si to Zr was kept at 1:1.

4.3.1.1 Characterization of sols, films, and powders before carbonization

Fig. 4-1 shows the sol size measured by intensity for SZA sols prepared at WR 4, 60 and 240. The mean values and standard deviations are presented in Table 1. It can be observed that the sol size increased as WR increased from 4 (3.4±1.0 nm) to 60

(8.1 ± 1.5 nm) and then to 12 ± 0.3 nm for a WR of 240. This therefore points to more condensations between hydrolyzed groups (-SiOH and -ZrOH) as WR increased resulting from increased hydrolysis.

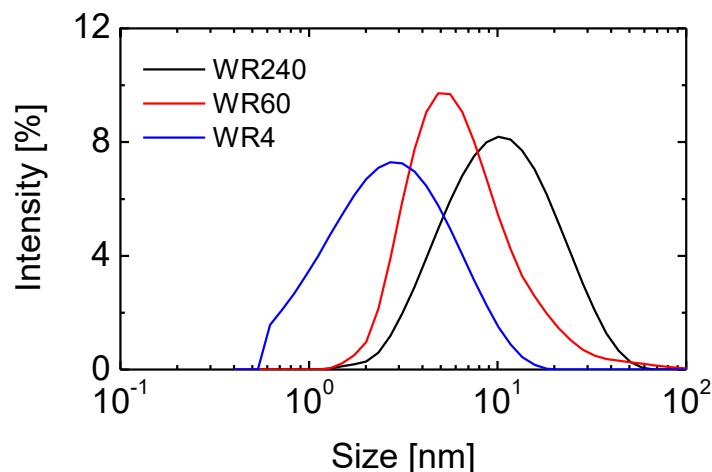


Fig. 4-1 Sol size by intensity measured by DLS for different water/alkoxide molar ratios.

Table 4-1 Average sol size by intensity values of SiO₂-ZrO₂-ACAC sols prepared at different water/alkoxide molar ratios.

Water ratio [-]	Average size [nm]	Standard deviation (+/-)
4	3.4	1.0
60	8.1	1.5
240	12	0.3

FT-IR provides definitive evidence for the observation made with the sol size measurement. Fig. 4-2 (a) shows the observed FT-IR spectra in the range of 3200 to 400 cm⁻¹ measured for as-prepared SZA films before and after firing at 300 °C in N₂ atmosphere. The two peaks that appear around 1,600 cm⁻¹ and 1,525 cm⁻¹ are assigned to the enol C=O and C=C bonds that are characteristic of the acetylacetone, respectively [34]. The peak observed around 1000 cm⁻¹ can be assigned to the siloxane bond -Si-O-Si- [35]. This indicates that hydrolysis-produced -Si-OH species were able to undergo condensation with other -Si-OH species or -Si-OEt species. The spectra of the unfired films show that acetylacetone remained chelated irrespective of the WR used only differing in intensity. Fig. 4-2 (b) shows the plot of evaluated

absorbance ratios of the -C=C- peak of chelating ACAC ligand to siloxane as a function of water/alkoxide molar ratios. The -C=C- peak intensity reduced as WR increases. Therefore, the increased hydrolysis and condensation between SiO_2 and ZrO_2 inferred from Fig. 4-1 indicates that the amount of ACAC chelated to Zr was reduced by increasing the WR.

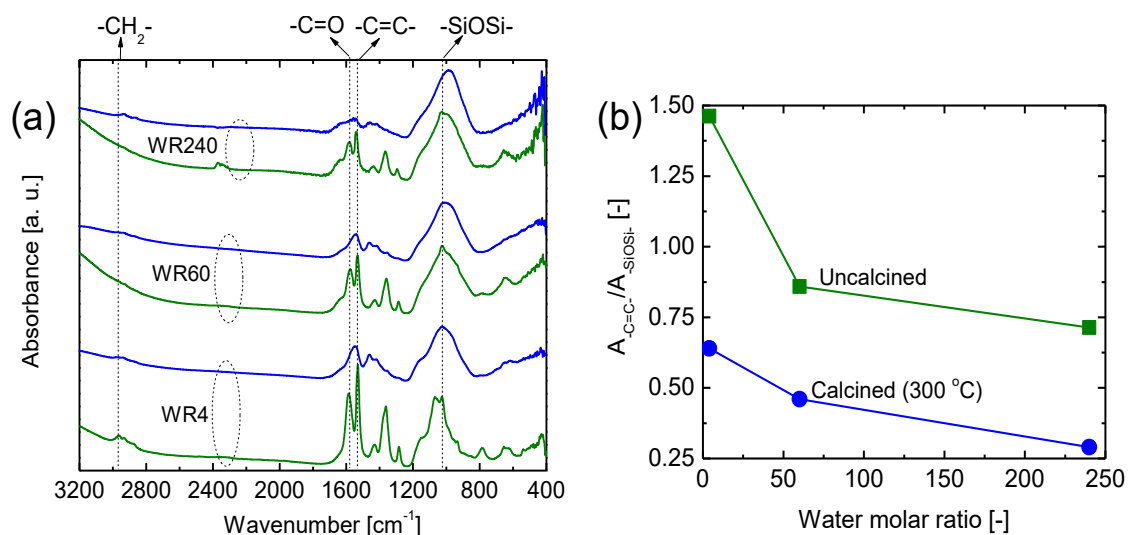


Fig. 4-2 (a) FT-IR spectra observed within a range of 3200- 400 cm^{-1} for uncalcined (green line) and calcined (300 °C in N_2 ; blue line) $\text{SiO}_2\text{-ZrO}_2\text{-ACAC}$ films prepared with different water/alkoxide molar ratios; (b) plot of the evaluated absorbance ratios of the representative peaks of the chelating ACAC ligand to siloxane as a function of water/alkoxide molar ratios.

The same comparisons were made for films fired at 300 °C in N_2 atmosphere (represented by the blue solid lines). After firing at 300 °C, the intensities of the representative acetylaceton peaks reduced irrespective of WR. This is consistent with the thermogravimetric profile reported for a SZA powder prepared with a WR of 4 which showed weight loss at 300 °C [30]. However, the characteristic peaks belonging to ACAC can still be observed and the relative ACAC content followed the same trend as the unfired films.

Fig. 4-3 shows the N_2 adsorption-desorption isotherms for SZA powders prepared with different water/alkoxide molar ratios and fired at 300 °C. This figure shows that the amount of N_2 adsorbed increased as WR for hydrolysis increased. At WR of 4 the amount of N_2 adsorbed was small because the high amount of ACAC ligands present

in the SiO₂-ZrO₂ matrix based on Fig. 4-2 (b). These occupied the intra-particle network spaces that allowed only a little amount of N₂ adsorbed. At WR of 240 however, the high amount of hydrolysis that caused a reduced amount of ACAC ligands improved the amount of N₂ adsorbed. Nonetheless, WR of 240 still resulted in the highest microporous volume.

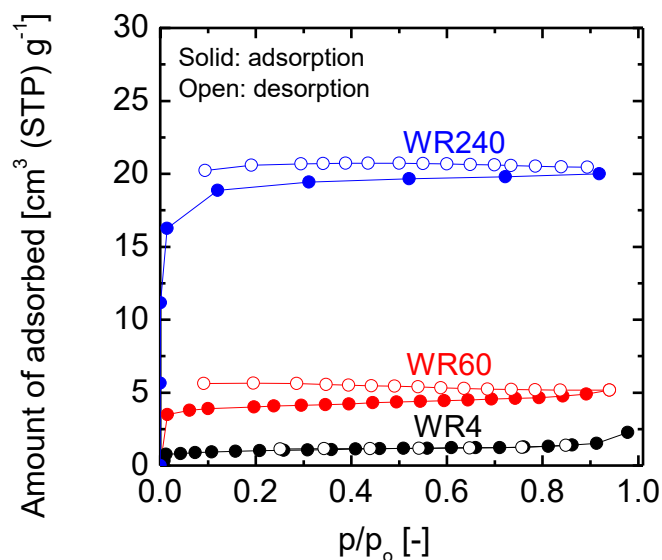


Fig. 4-3 N₂ adsorption-desorption isotherms at -196 °C for SiO₂-ZrO₂-ACAC powders prepared with different water/alkoxide molar ratios and fired at 300 °C.

The gas permeation properties of membranes fabricated from SZA at the different WR were also examined at 200 °C. Fig. 4-4 (a) shows the kinetic diameter dependence of single gas permeance of different gases (He (0.26 nm), H₂ (0.289 nm), CO₂ (0.33 nm), N₂ (0.364 nm), CH₄ (0.38 nm), CF₄ (0.48 nm), and SF₆ (0.55 nm)) for SZA-derived membranes fabricated at 300 °C. Fig. 4-4 (b) shows the dimensionless permeance normalized on the basis of He permeance in Fig. 4-4 (a) as a function of kinetic diameter. It is obvious that the permeance values of all gases increased as WR increased from 4 to 240. However, the ideal selectivity of H₂ over larger gases reduced with WR but still well above Knudsen-based values as presented in Table 4-2.

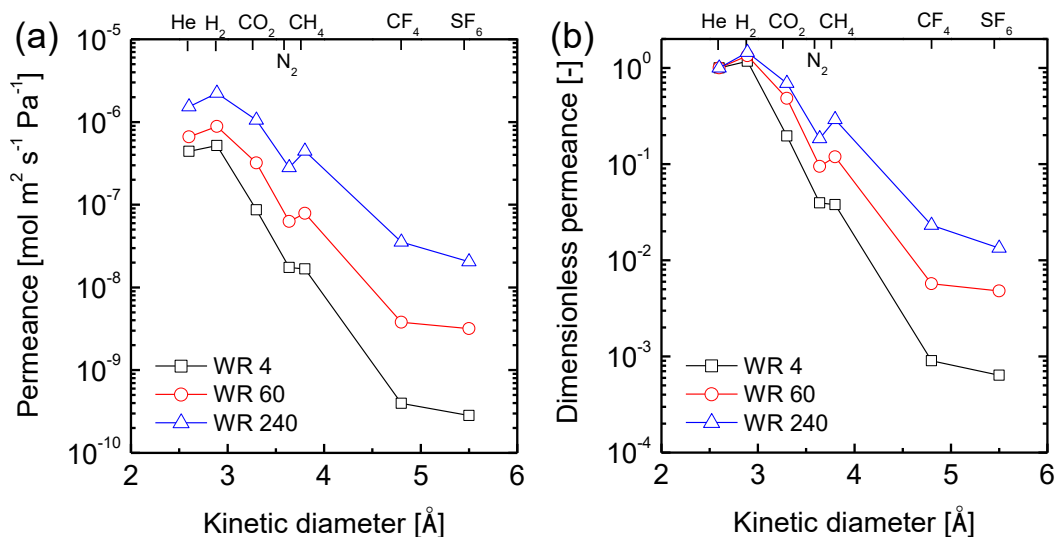


Fig. 4-4 (a) Single gas permeance at 200 °C as a function of kinetic diameter of SiO₂-ZrO₂-ACAC-derived membranes fabricated at 300 °C under N₂ for different water/alkoxide molar ratios. (b) corresponding dimensionless permeance as a function of kinetic diameter normalized by He permeance.

Table 4-2 Gas permeance of H₂, N₂ and SF₆ gases at 200 °C; ideal selectivity of H₂ over N₂ and SF₆ for SiO₂-ZrO₂-ACAC-derived membranes prepared with different water/alkoxide molar ratios.

WR	Permeance [10^{-7} mol m ⁻² s ⁻¹ Pa ⁻¹]			Ideal selectivity [-]	
	H ₂	N ₂	SF ₆	H ₂ /N ₂	H ₂ /SF ₆
4	5.2	0.2	0.003	30	1600
60	8.8	0.6	0.032	14	280
240	22	2.8	0.21	8	110
Knudsen	-	-	-	4.3	8.5

Furthermore, Fig 4-4 (b) which can reveal the pore size distribution comparison of the membranes showed that a membrane prepared with a WR of 4 showed the narrowest distribution compared with water/alkoxide molar ratios of 60 and 240. This trend is opposite to that observed for organosilica membranes whereby an increase in WR increased the selectivity of membranes. For example, a triethoxysilane (TRIES)-derived membrane showed that membranes prepared with water ratio of 240 exhibited the narrowest pore distribution compared to a WR of 60 and 6 (having the broadest

pore distribution) as reported by Kanezashi *et al.* [36]. Kanezashi and co-workers opined a “template effect” to explain this phenomenon. At low water ratio, the incomplete hydrolysis of ethoxy groups (-SiOEt) resulted in the persistence of these ethoxy groups in the networks. At a high water/alkoxide molar ratio however, these ethoxy groups were completely hydrolyzed and therefore replaced by an abundance of hydroxyl groups (silanol -Si-OH). After calcination at elevated temperatures, the silanol (-Si-OH) rich, high WR-derived membrane underwent a thermal condensation of silanol into siloxane crosslinks thereby resulting in a -Si-O-Si- dense network. On the other hand, after calcining an ethoxy-rich network derived from low WR, the thermally unstable ethoxy groups simply decompose without a condensation crosslinking, resulting in a loose network. This trend was also reported for a bis(triethoxysilyl propoxy)pyridine (BTTP)-derived membrane by Yu and co-workers utilizing water/BTTP ratios of 12, 40 and 240 [37].

In a chelating ligand-ceramic composite however, the mechanism of thermal network formation is different. Fig. 4-5 summarizes the effect of water/alkoxide molar ratio on the ligand concentration and network formation in SiO₂-ZrO₂-ACAC before and after calcination. FT-IR results in Fig 4-2 (a) and (b) revealed that even after calcination at 300 °C, a substantial amount of ligands was still present. A WR of 4 retains the highest amount of ligands, and these network-occupying ligands result in a quasi-dense network that behaves like a polymer-derived structure [38] that gives a narrow pore distribution. On the other hand, when the WR is increased, the amount of hydroxyl groups increases but with a persistent presence of ligands in the network as Fig. 4-5 illustrates. At the calcination temperature, some -OH groups are removed but condensation to form -Si-O-Si-, -Si-O-Zr- or -Zr-O-Zr- linkages is inhibited because the ligands still present prevented the proximity of condensable species. Therefore, it might be reasonably concluded that for a coordination ligand-ceramic composite network, an increase in WR results in membranes with looser network and vice versa.

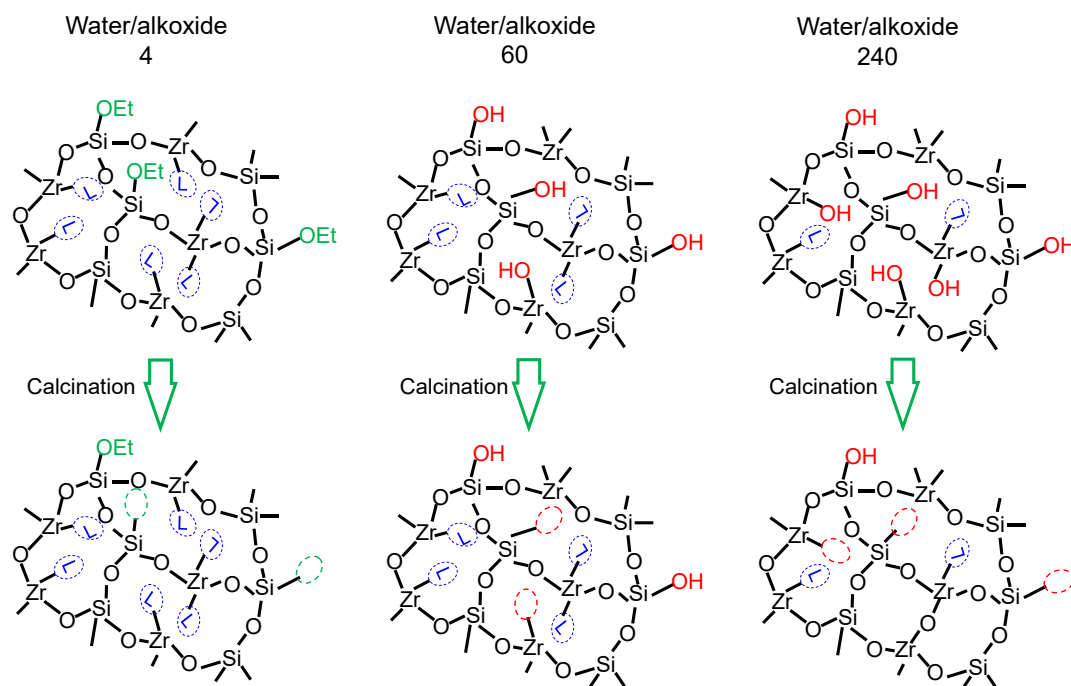


Fig. 4-5 Schematic illustration of the effect that the water/alkoxide molar ratio exerts on the relative ligand population before and after calcination.

4.3.1.2 Characterization after carbonization

The results of characterizations before carbonization have revealed that the concentration of ACAC ligand in the membrane can be successfully determined by the water/alkoxide molar ratio applied for hydrolysis and affects SZA membranes' pore size distribution. However, the optimal WR required for a carbonized SiO₂-ZrO₂ can only be determined by analyzing the results of characterization after carbonization at 550 °C.

The amount of residual carbon after 550 °C pyrolysis can be evaluated by measuring the thermogravimetry in N₂ and air atmospheres. Fig. 4-6 (a) – (c) show the thermogravimetric profiles in N₂ and air. The amount of residual carbon (evaluated as mg of carbon per mg of residual material) is assumed to be the difference between the normalized residual weight in N₂ at 550 °C and the normalized residual weight in air at 1000 °C after all carbon is removed. From Fig. 4-6 (a) – (c) it can be observed that the amount of residual carbon estimated was the highest for WR of 4 and smallest for the WR of 240. This is consistent with the ACAC ligand content

from the precursor material. Therefore, WR of 240 is not suitable to retain a high amount of carbon material in the $\text{SiO}_2\text{-ZrO}_2$ matrix.

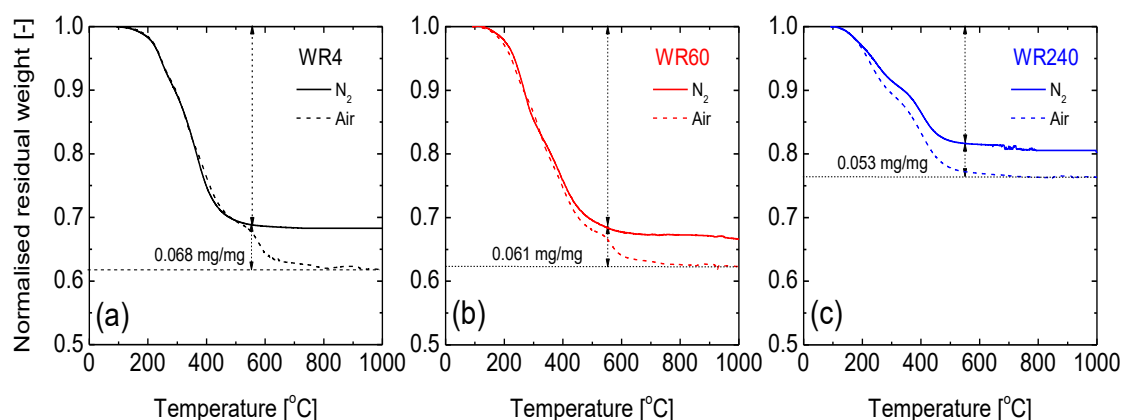


Fig. 4-6 Thermogravimetric profiles of $\text{SiO}_2\text{-ZrO}_2\text{-ACAC}$ powders under N_2 (solid line) and air (dash line) up to 1000 °C.

Furthermore, the XRD diffractograms of carbon- $\text{SiO}_2\text{-ZrO}_2$ powders prepared at 550 °C as shown in Fig. 4-7 (a) and (b) shows that the WR of 240 resulted in aggregation of tetragonal ZrO_2 nanoparticles. WR of 4 and 60 retained amorphous structures when compared to the powders before carbonization shown in Fig. 4-7 (a). Therefore, WR 4 and 60 are more likely to form defect-free thin separation layers. However, despite a WR of 4 retaining the highest residual carbon but resulting in a very low microporosity as shown in Fig. 3, the WR of 60 serves as the best balance between microporosity, amorphousness and amount of residual carbon.

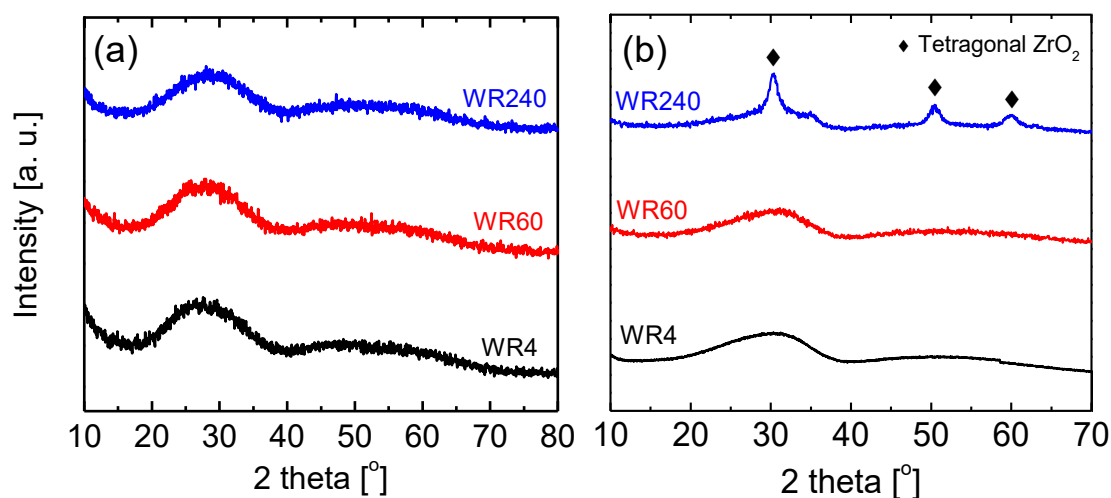


Fig. 4-7 XRD patterns of (a) $\text{SiO}_2\text{-ZrO}_2\text{-ACAC}$ powders prepared at different water/alkoxide molar ratios after firing under a N_2 atmosphere at 300 °C (b) carbon- $\text{SiO}_2\text{-ZrO}_2$ powders prepared at different water/alkoxide molar ratios after firing under a N_2 atmosphere at 550 °C.

4.3.2 Microstructural transformation between $\text{SiO}_2\text{-ZrO}_2\text{-ACAC}$ and Carbon- $\text{SiO}_2\text{-ZrO}_2$: effect of Si/Zr ratio

An optimal water/alkoxide molar ratio for preparing $\text{SiO}_2\text{-ZrO}_2\text{-ACAC}$ as the precursor to carbon- $\text{SiO}_2\text{-ZrO}_2$ has been chosen to be 60 at a fixed ratio of Si to Zr atoms of 1:1. However, the effects of the relative ratios of Si to Zr at a fixed WR of 60 on the microstructural properties of CSZ-derived bulk materials and membranes is very important. It is important to note that the theoretical amount of ACAC present in a given SZA matrix can also be dictated by the ratio of Si to Zr atoms present when at any given time the theoretical ACAC/Zr ratio is kept at 4:1. Therefore, in a silica-rich material the theoretical ACAC amount reduces and, for a zirconia-rich material, the ACAC amount increases, all while keeping the theoretical ACAC/Zr ratio at 4:1.

Fig. 4-8 shows the thermogravimetric profiles in an N_2 atmosphere for as-prepared SZA powders with different Si/Zr atomic ratios of 3/7, 5/5, 7/3 and 9/1. The final residual weight represents the undecomposable residual mass in the given thermal atmosphere. In consistence with the previous discussion, the amount of material decomposed corresponded with the amount of ACAC contained in the starting material. Therefore, the residual weight increased as Si/Zr ratio increased- the most silica-rich SZA powder (Si/Zr of 9/1) shows the highest residual weight and the most zirconia-rich SZA powder (Si/Zr of 3/7) shows the lowest residual weight. The CSZ materials considered in this work were prepared at 550 °C and the above observations hold at 550 °C on the thermogravimetric profile. However, the absolute amount of the residual carbon at 550 °C cannot be determined even if the residual weights correspond to the initial ACAC amount at each Si/Zr ratio.

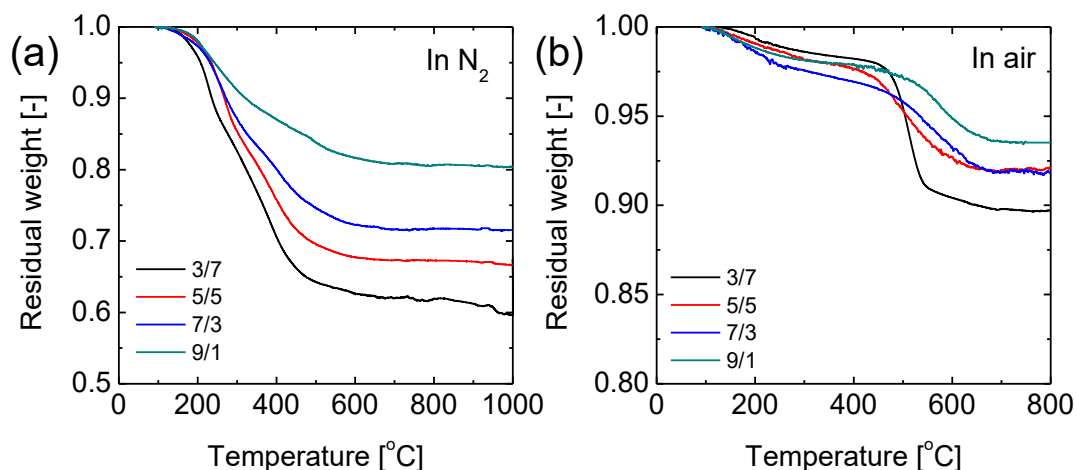


Fig. 4-8 Thermogravimetric profiles of (a) SiO₂-ZrO₂-ACAC powders (uncalcined) prepared at different Si/Zr atomic ratios under a N₂ atmosphere up to 1000 °C and (b) carbon-SiO₂-ZrO₂ powders (prepared at 550 °C under N₂) under an air atmosphere up to 800 °C. (Gas flow: 50-60 ml min⁻¹; Ramping rate: 10 °C min⁻¹.)

CSZ powders prepared by pyrolyzing SZA powders in N₂ atmosphere at 550 °C were thereafter subjected to a thermogravimetric process in an air atmosphere. The hot air atmosphere resulted in the complete oxidation and removal of the carbon nanoparticles in the CSZ powders. Therefore, the amount of mass reduction corresponds to the residual carbon in the starting CSZ powders prepared at 550 °C. Table 4-3 presents the results of this thermogravimetric experiment. The general trend is that the residual carbon amount increases with the zirconia mole fraction. For the most zirconia-rich precursor where the theoretical C/Si atomic ratio is 28/3, the result is the highest residual carbon of 0.103 mg of carbon per mg of CSZ. The most silica-rich precursor with theoretical C/Si atomic ratio of 4/9 resulted in the lowest residual carbon of 0.065 mg of carbon per mg of CSZ.

Table 4-3 Evaluation of carbon content in carbon-SiO₂-ZrO₂ powders prepared at 550 °C

Si/Zr atomic ratio	Theoretical starting C/Si atomic ratio	Residual carbon at 550 °C
[-]	[-]	[mg/mg]
3/7	28/3	0.103
5/5	20/5	0.081
7/3	12/7	0.083
9/1	4/9	0.065

The microstructural transformation between SZA and CSZ was also examined by x-ray diffraction (XRD). Fig. 4-9 shows the x-ray diffractograms of SZA (green lines) powders and CSZ powders (red lines) prepared at different Si/Zr atomic ratios. Before carbonization, all the spectra of SZA show amorphous structures irrespective of Si/Zr atomic ratio. A broad peak is common to all the samples before carbonization which shifts very slightly from higher 2θ to a lower 2θ as Si/Zr ratio increases. The calculated d -spacing values are presented in Table 4-4 and reveal that the d -spacing value of 0.37 nm for SZA9/1 is only slightly higher than that of SZA3/7 at 0.34 nm. Nonetheless, the slightly lower d -spacing of SZA3/7 may be attributed to the lower inter-plane distance caused by the higher concentration of ACAC ligands between the lattices.

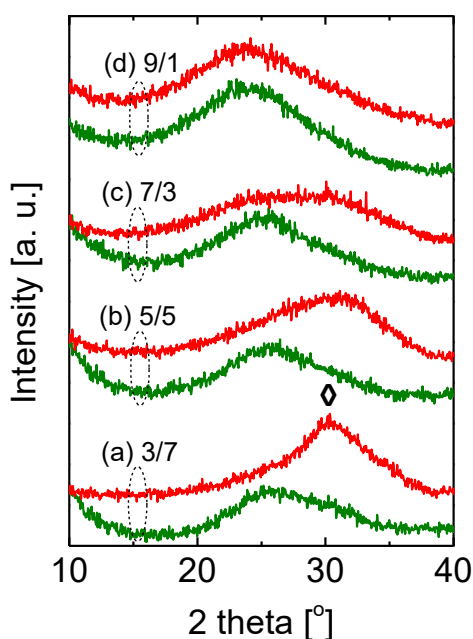


Fig. 4-9 X-ray diffractograms of SiO₂-ZrO₂-ACAC powders (before carbonization; green) and Carbon-SiO₂-ZrO₂ powders (after carbonization in N₂ at 550 °C; red) prepared at different Si/Zr atomic ratios. Symbol \diamond represents the appearance of aggregated tetragonal ZrO₂ particles.

The results recorded after for the CSZ powders reveal drastically different observations. It is important to note that all but the Si/Zr ratio of 3/7 have completely amorphous phases. CSZ3/7 showed a little aggregation of tetragonal ZrO₂ particles with a pointed peak at 2θ of 30 °.

According to the d -spacing calculated for CSZ powders a larger difference in the values can be observed compared to the uncarbonized SZA powders and the peak shifts are obvious in Fig 4-9. The d -spacing value of 0.37 nm for CSZ9/1 is much higher than that of CSZ3/7 at 0.29 nm. This indicates that a considerable microstructural differentiation can be achieved once carbonization takes place. A second interesting observation is revealed when comparing SZA and CSZ profiles at each Si/Zr ratio (from green to red). For example, the d -spacing of SZA3/7 at 0.34 nm is much higher than that of a corresponding CSZ3/7 at 0.29 nm. The CSZ7/3 powder showed only a slight shift compared to the SZA7/3 precursor resulting in d -spacing values of 0.32 nm and 0.35 nm, respectively. As for CSZ9/1, there was no observable peak shift compared to SZA9/1 corresponding to a similar d -spacing of 0.37 nm in both cases.

This result is also consistent with a N₂ adsorption experiment. Fig. 4-10 presents the N₂ adsorption-desorption isotherms measured at -196 °C for all SZA and CSZ powders with different Si/Zr ratios. The obtained BET surface areas are also shown in Table 4-4. Generally, it can be observed that a reduction of surface areas occurs from SZA powders to CSZ powders attributed to the densification of the networks by increased -Zr-O-Zr- thermal condensations [39] and the possible deposition of the free carbon products of pyrolysis. Nonetheless, this densification is more pronounced in zirconium rich cases than in the silica rich cases. SZA5/5 with BET surface area of 14 m² g⁻¹ became CSZ5/5 with $S_{a,BET}$ of 0.7 m² g⁻¹, representing about 95 % densification. On the other hand, SZA9/1 with a $S_{a,BET}$ of 456 m² g⁻¹ was transformed to CSZ9/1 with $S_{a,BET}$ of 413 m² g⁻¹, representing only about 9 % densification. Therefore, it is noteworthy that in a silica rich case, even if densification occurs, no

substantial change was effected on the ceramic composite superstructure. In contrast to this, a pure silica bulk prepared by Lin *et al* showed a surface area reduction of about 34 % and a reduction of 15 % for 6% aluminum-doped silica [21].

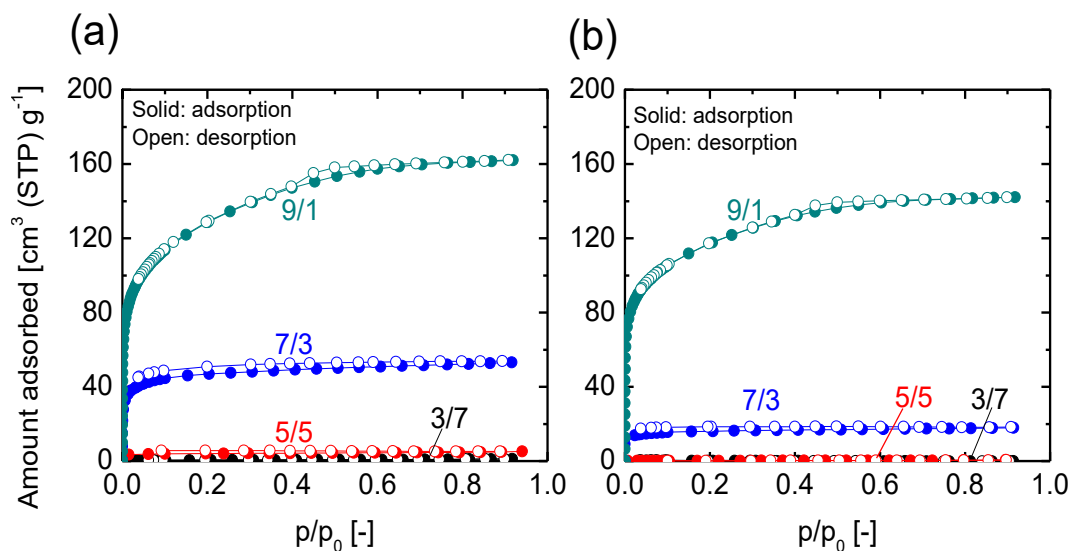


Fig. 4-10 N₂ adsorption-desorption isotherms at -196 °C for (a) SiO₂-ZrO₂-ACAC and (b) carbon-SiO₂-ZrO₂ powders prepared with different Si/Zr atomic ratios

Table 4-4 Effect of Si/Zr atomic ratio on microstructural properties of SiO₂-ZrO₂-ACAC and carbon-SiO₂-ZrO₂ powders

Si/Zr atomic ratio [-]	SiO ₂ -ZrO ₂ -ACAC		Carbon-SiO ₂ -ZrO ₂	
	<i>d</i> spacing [nm]	S _{a,BET} [m ² g ⁻¹]	<i>d</i> spacing [nm]	S _{a,BET} [m ² g ⁻¹]
3/7	0.34	2.0	0.29	0.9
5/5	0.34	14	0.29	0.7
7/3	0.35	178	0.32	43
9/1	0.37	456	0.37	413

S_{a,BET}- BET surface area

The effect of microstructural changes from SZA structure to CSZ structure on membrane performance was also determined by preparing SZA and CSZ membranes with the different Si/Zr atomic ratios. SZA membranes were fabricated at 300 °C

while CSZ membranes were fabricated at 550 °C based on the procedures previously described in this work.

Fig 4-11 (a) shows the kinetic diameter dependence of single gas permeance for SZA membranes measured at 200 °C while Fig. 4-11 (b) shows that for CSZ membranes measured at the same temperature. H₂ permeance and selectivities over CH₄ for the two classes of membranes are presented in Table 4-5. It is immediately evident from Fig. 4-11 (a) that all SZA membranes are capable of molecular sieving with H₂/CH₄ ideal selectivity ranging between 6.6 and 11 (Table 4-5) well above the Knudsen ratio of 2.8. At the same time, the H₂ permeances showed similar range of values between 4.4 to 12 x 10⁻⁷ mol m⁻² s⁻¹ Pa⁻¹. Therefore, it is difficult to observe any substantial difference in the performance of SZA membranes with different Si/Zr ratios. This can be explained by the fact that a SZA9/1 membrane prepared with a WR of 60 and calcined at 300 °C presents silica-rich phase that possesses a strong molecular sieving ability. On the other hand, a SZA3/7 membrane prepared at the same conditions presents ACAC-rich networks that also serve as molecular sieving agents within the quasi-dense networks.

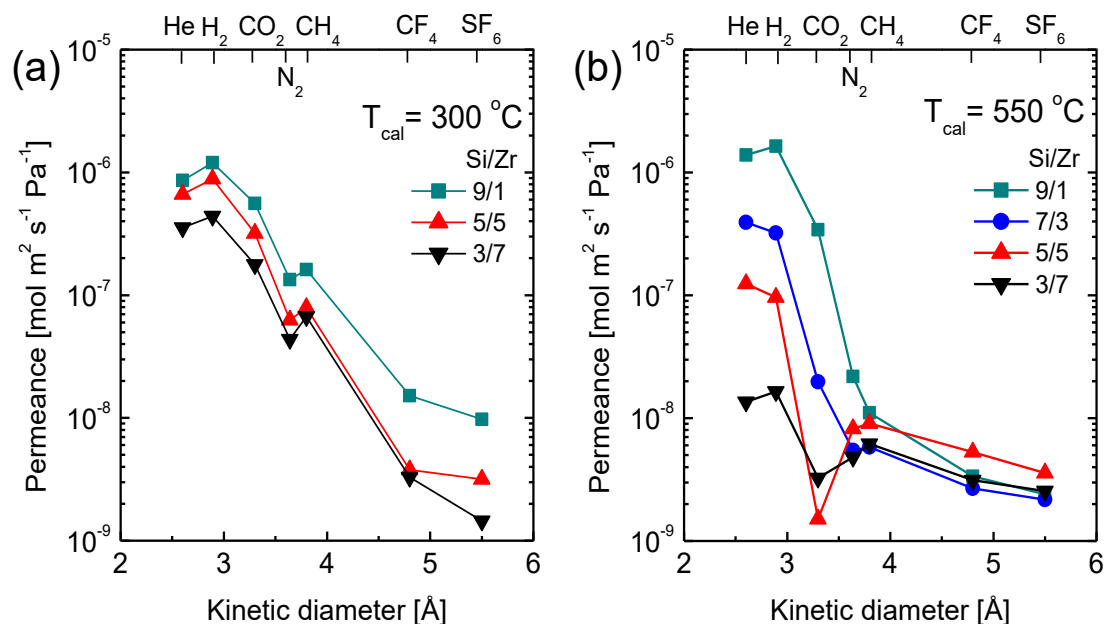


Fig. 4-11 (a) Single gas permeance at 200 °C as a function of kinetic diameter of SiO₂-ZrO₂-ACAC-derived membranes fabricated at 300 °C in N₂ for different Si/Zr atomic ratios. (b) Single gas permeance at 200 °C as a function of kinetic diameter of

carbon-SiO₂-ZrO₂-derived membranes fabricated at 550 °C in N₂ for different Si/Zr atomic ratios.

After carbonization however, CSZ membranes show an entirely different trend. The membrane performance depends on the Si/Zr ratio. A CSZ9/1 shows a very high H₂ permeance of $16 \times 10^{-7} \text{ mol m}^{-2} \text{ s}^{-1} \text{ Pa}^{-1}$ together with a similarly high H₂/CH₄ ideal selectivity of 148. The trend then follows that as Si/Zr ratio reduces, H₂ permeance and H₂/CH₄ ideal selectivity reduce as shown by the values in Table 4-5.

Table 4-5 Comparison of H₂ permeance and H₂/CH₄ permeance ratio of SiO₂-ZrO₂-ACAC and carbon-SiO₂-ZrO₂ membranes at 200 °C

Si/Zr atomic ratio [-]	SiO ₂ -ZrO ₂ -ACAC		Carbon-SiO ₂ -ZrO ₂	
	H ₂ permeance [10 ⁻⁷ mol m ⁻² s ⁻¹ Pa ⁻¹]	α (H ₂ /CH ₄) ^{a, b} [-]	H ₂ permeance [10 ⁻⁷ mol m ⁻² s ⁻¹ Pa ⁻¹]	α (H ₂ /CH ₄) ^{a, b} [-]
3/7	4.4	6.6	0.16	2.7
5/5	8.8	11	1.1	48
7/3	-	-	3.2	55
9/1	12	7.4	16	148

^a α = ideal selectivity, ^b H₂/CH₄ Knudsen ratio = 2.8

Fig. 4-12 summarizes the microstructural transformation from a SiO₂-ZrO₂-ACAC to carbon-SiO₂-ZrO₂ based on the relative Si/Zr atomic ratios. This illustration also visualizes the effect on membrane performance. At a low Si/Zr ratio, the medium is zirconium and therefore was ACAC rich. In this case, the high population of ACAC physically modifying the network size can result in a quasi-dense network providing molecular sieving. After carbonization, the high population of zirconium and ACAC give rise to a permanently dense network and at the same time resulting in defect formation during the pyrolysis process. These combine to result in low H₂-permselectivity.

At the other end of the spectrum, when Si/Zr ratio is high, the medium is silica rich with some ACAC still present as shown in Fig 4-12. The molecular sieving ability of silica rich medium combined with some ACAC ligands cause H₂-permselectivity. After carbonization, the resulting CSZ structure becomes more

siloxane (-Si-O-Si-) rich as a result of more thermal condensation. Also, since the content of zirconium and ACAC are limited in this case, defect formation is also minimal. These will greatly improve the H₂-permselectivity of the resulting membrane. An organosilica membrane has also been shown to improve H₂-perselectivity upon high temperature calcination up to 700 °C which was attributed to rearrangements of the silicon-carbon bonds upon pyrolysis of the organic linking units [40].

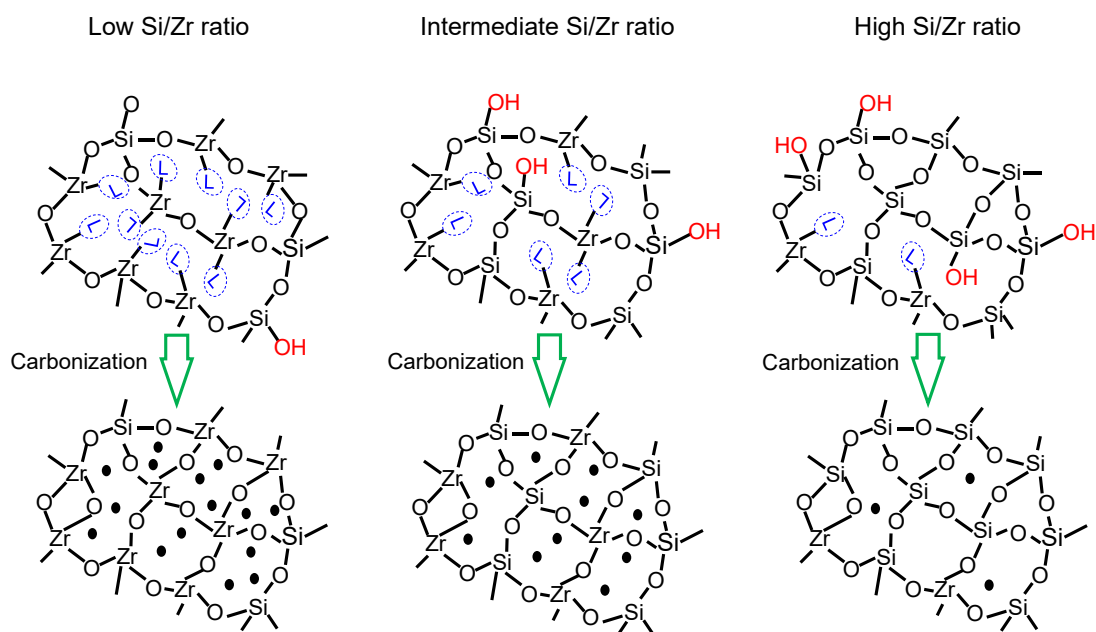


Fig. 4-12 Schematic illustration of the effect of Si/Zr atomic ratio on ligand-to-carbon and microstructural transformations.

4.3.3 Carbonization-enhanced H₂-permselectivity in a SiO₂-ZrO₂ composite membrane

Silica-derived membranes have impressively high H₂-permselectivity, that is, they can achieve simultaneous high H₂ permeance and selectivity of H₂ over larger gases. Higher selectivities can be achieved when silica-derived membranes are fabricated at even higher temperatures between 500 and 700 °C. However, the membranes begin to trade off H₂ permeance as a result of the densification and thus disappearance of H₂-permeating pores [14, 21]. For example, the H₂ permeance for a silica membrane prepared at 400 °C was 20 x 10⁻⁷ mol m⁻² s⁻¹Pa⁻¹ with H₂/N₂ selectivity of 64. When prepared at 600 °C however, the permeance reduced by 75 % to 5 x 10⁻⁷ mol m⁻² s⁻¹Pa⁻¹

¹ while the H₂/N₂ selectivity increased to more than 135 [12]. Kanezashi *et al* also demonstrated the densification effect of temperature on silica by evaluating the activation energies of gas permeation through silica 550 °C- and 750 °C-derived membranes. They observed almost double increase of activation energies of gases in 750 °C-derived membranes compared to 550 °C-derived [41]. These are consistent with the observation made by Lin *et al.* [21] regarding the microstructural properties of a bulk silica gel. A silica powder prepared at 40 °C had a pore volume of 0.458 cm³ g⁻¹ which reduced by 75 % to 0.114 cm³ g⁻¹ at 400 °C. In comparison to this, a SiO₂-ZrO₂ composite in the Si/Zr ratio 9/1 showed only a 21 % reduction in pore volume from 0.21 to 0.165 cm³ g⁻¹ when calcined through a similar range of temperatures (from 200 to 550 °C) [42].

Yoshida *et al.* [22] prepared a SiO₂-ZrO₂ membrane with a Si/Zr ratio of 9/1 at 570 °C. The single gas permeance as a function of kinetic diameter is displayed in Fig. 4-13 (a). At 3 x 10⁻⁷ mol m⁻² s⁻¹Pa⁻¹, the H₂ permeance is lower than a corresponding pure SiO₂ membrane prepared at 600 °C as reported by de Vos and Verweij. This is because ZrO₂ being crystalline is a naturally dense material and while the addition to SiO₂ to form a composite matrix reduces the densification rate at elevated temperatures, it reduces the H₂ permeance at the same time.

Fig. 4-13 (a) and (b) compare the CSZ9/1 and unmodified SiO₂-ZrO₂ (9/1) membranes. Fig. 4-13 (a) shows the comparison of single gas permeance at 200 °C as a function of kinetic diameter. By comparison, a SZA9/1 membrane prepared at 300 °C has an H₂ permeance of 12 x 10⁻⁷ mol m⁻² s⁻¹Pa⁻¹, while a CSZ9/1 membrane prepared at 550 °C has an H₂ permeance of 16 x 10⁻⁷ mol m⁻² s⁻¹Pa⁻¹ corresponding to almost no change in H₂ permeance. This is an interesting observation. The H₂ permeance for a pure SiO₂-ZrO₂ (9/1) membrane is 5 times lower at 3 x 10⁻⁷ mol m⁻² s⁻¹Pa⁻¹. Fig. 4-13 (b) also shows that both CSZ9/1 and SiO₂-ZrO₂ (9/1) membranes have similar distribution of small pores.

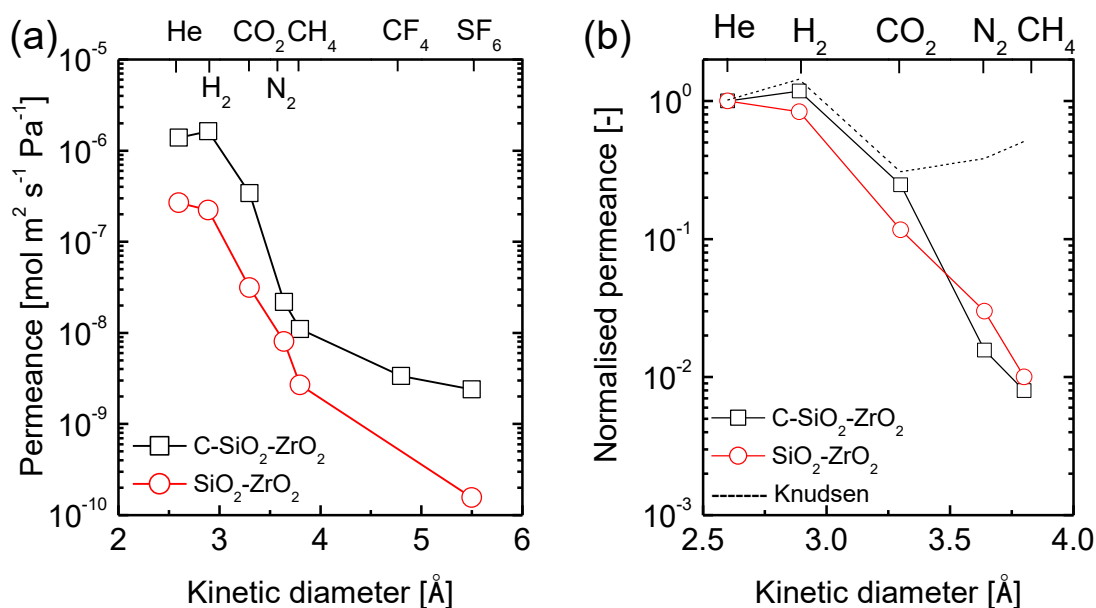


Fig. 4-13 (a) Single gas permeance at 200 °C as a function of kinetic diameter of carbon-SiO₂-ZrO₂-derived membranes (this work) compared with pure unmodified SiO₂-ZrO₂-derived membranes [22] prepared with a Si/Zr atomic ratio of 9/1. (b) Corresponding dimensionless permeance as a function of the kinetic diameter normalized by He permeance.

Fig. 4-14 shows the temperature dependence of single gas permeance for He, H₂, CO₂, N₂ and CH₄. All gases show increased permeance as temperature increases indicating activated diffusion mechanism. Table 4-6 presents the calculated apparent activation energy when the data points in Fig. 4-14 are fitted to the theoretical lines as expressed by Equation 2-1 [43]. The evaluated activation energies of He and H₂ for a CSZ9/1 membrane (8.3 and 7.1 kJ mol⁻¹, respectively) reveal very similar values to those evaluated for a pure SiO₂-ZrO₂ (9/1) membrane (8.1 and 7.0 kJ mol⁻¹, respectively). Therefore, it can be confirmed that both a CSZ9/1 and SiO₂-ZrO₂ (9/1) membrane possess similar distribution of small pores. In spite of this similarity in pore distribution, a CSZ9/1 displayed enhanced H₂-permselectivity compared to a SiO₂-ZrO₂ (9/1) membrane- H₂ permeance and H₂/CH₄ selectivity were higher for the CSZ9/1 membrane.

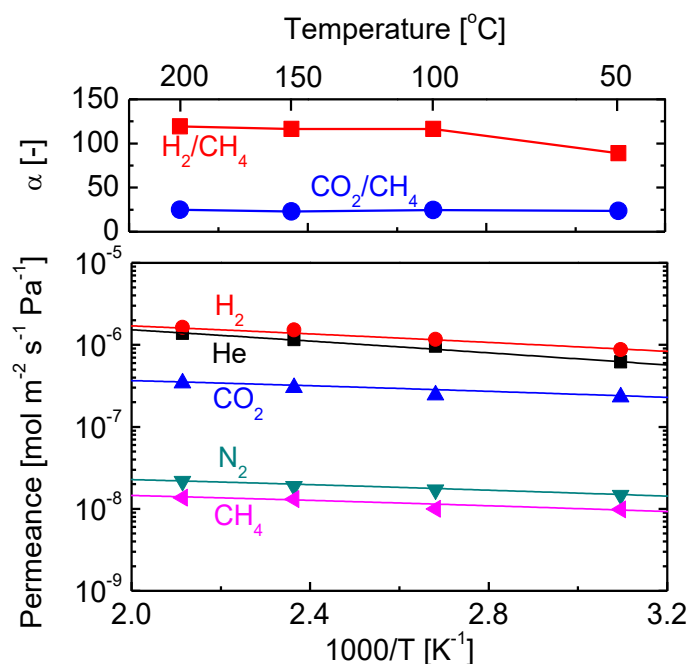


Fig. 4-14 Temperature dependence of gas permeance for carbon-SiO₂-ZrO₂ membranes prepared with a Si/Zr atomic ratio of 9/1.

Table 4-6 Comparison of He and H₂ permeance, activation energies and H₂/CH₄ permeance ratio for pure SiO₂-ZrO₂ [22] and Carbon-SiO₂-ZrO₂ membranes (this work); pore volume comparison between a SiO₂-ZrO₂ [42] and Carbon-SiO₂-ZrO₂ gels prepared at a Si/Zr atomic ratio of 9/1 at 550 °C.

Membrane type	Permeance [10 ⁻⁷ mol m ⁻² s ⁻¹ Pa ⁻¹]		Activation energy [kJ mol ⁻¹]		α at 200 °C [-]	Pore volume [cc g ⁻¹]
	He	H ₂	He	H ₂	H ₂ /CH ₄	
SiO ₂ -ZrO ₂ ^a	4.5	3	8.1	7.0	83	0.165
Carbon-SiO ₂ -ZrO ₂	14	16	8.3	7.1	148	0.236

^a Membrane data from ref. [21] and pore volume data from ref. [42]; α- ideal selectivity

A comparison of the pore volumes of bulk CSZ9/1 and SiO₂-ZrO₂ (9/1) materials thus explains the improved H₂-permselectivity of CSZ9/1 membrane. The respective pore volumes are indicated in Table 4-6. The CSZ9/1 with a pore volume of 0.236 cm³ g⁻¹ shows a much higher pore volume than a pure SiO₂-ZrO₂ by 43 %. This can be explained by the presence of carbon nanoparticles within the SiO₂-ZrO₂ structure.

As is widely reported, pyrolyzed carbon nanoparticles possess ultra-micropores and micropores which connect to provide combined molecular sieving and improved permeability and are attractive for application as carbon molecular sieve membranes [44, 45]. Fig. 4-15 illustrates the microstructural difference between a pure $\text{SiO}_2\text{-ZrO}_2$ composite and a CSZ composite. In the pure composite matrix, the likelihood of -Zr-O-Zr- linkages increase at high temperatures to form a crystalline tetragonal phase by sintering mechanism [46]. This tetragonal phase may be undetected in an XRD diffractogram as a result of the overwhelming silica amorphous phase. The carbon nanoparticles in the CSZ network prevents the densification of ZrO_2 into its crystalline phase and occupies the aggregation volume that would have been occupied by aggregated ZrO_2 nanoparticles. Thus, while providing increased permeation path for H_2 , larger gases are sieved out by the ultra-micropore-micropore connections.

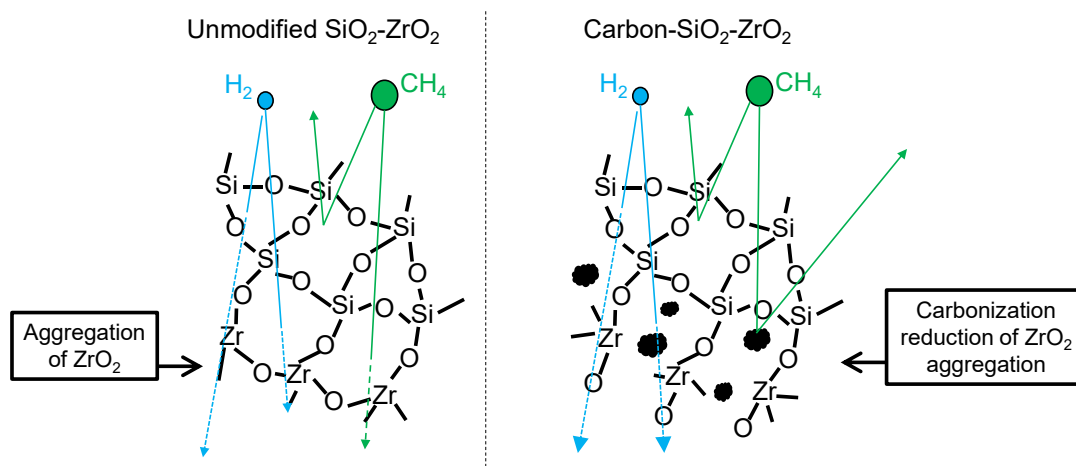


Fig. 4-15 Schematic illustration of enhanced H_2 -permeability enabled by the carbonization of a $\text{SiO}_2\text{-ZrO}_2$ microstructure

4.4 Conclusions

In this work an attempt was made to derive the best sol synthesis and chemo-structural parameters necessary for the fabrication of an H_2 -permeable carbon- $\text{SiO}_2\text{-ZrO}_2$ (CSZ) composite membranes by pyrolysis of a $\text{SiO}_2\text{-ZrO}_2\text{-ACAC}$ (SZA) composite at $550\text{ }^\circ\text{C}$ in N_2 atmosphere. The hydrolysis water/alkoxide molar ratio (WR) and relative Si/Zr atomic ratios were chosen as study parameters. The effects of water/alkoxide molar ratios of 4, 60 and 240 as well as the Si/Zr atomic ratios were studied and optimized.

Characterization of CSZ powders prepared with different WR by thermogravimetry, XRD and N₂ adsorption reveal that the most suitable WR to maintain the balance between carbon nanoparticles retention, amorphousness and microporosity is water/alkoxide molar ratio of 60.

Furthermore, fixing the WR at 60 and characterizing films, powders and membranes prepared using Si/Zr ratios of 9/1, 7/3, 5/5 and 3/7 reveal that a proper differentiation in microstructure and membrane performance will be achieved when SZA is pyrolyzed to CSZ. A CSZ9/1 membrane showed the best H₂-permselectivity with H₂ permeance of $16 \times 10^{-7} \text{ mol m}^{-2} \text{ s}^{-1} \text{ Pa}^{-1}$ and H₂/N₂ and H₂/CH₄ ideal selectivities of 75 and 148, respectively. Therefore, the best combination of parameters is a WR of 60 applied to prepare a carbon-SiO₂-ZrO₂ composite containing a relative Si/Zr of 9/1.

Lastly, the carbonization in a CSZ9/1 membrane improved the H₂-permselectivity over a pure unmodified SiO₂-ZrO₂ containing a similar Si/Zr ratio and similar distribution of the small pores. While the CSZ9/1 membrane showed an H₂ permeance of $16 \times 10^{-7} \text{ mol m}^{-2} \text{ s}^{-1} \text{ Pa}^{-1}$ the unmodified SiO₂-ZrO₂ membrane was $3 \times 10^{-7} \text{ mol m}^{-2} \text{ s}^{-1} \text{ Pa}^{-1}$. This was attributed to the increased pore volume afforded by the carbon nanoparticles through ultra-micropores inherent in them. It is therefore resolved that the densification of silica at elevated temperatures can be ameliorated by a combination of ZrO₂ composition and a carbonization of the resulting composite.

Cited literature

1. N. Abas, A. Kalair, N. Khan, Review of fossil fuels and future energy technologies, *Futures*, 69 (2015) 31–49
2. Y. Chang, J. Lee, H. Yoon, Alternative projection of the world energy consumption-in comparison with the 2010 international energy outlook, *Energ. Policy*, 50 (2012) 154-160
3. B. Johnston, M. C. Mayo, A. Khare, Hydrogen: the energy source for the 21st century, *Technovation*, 25 (2005) 569–585
4. G. Nicoletti, N. Arcuri, G. Nicoletti, R. Bruno, A technical and environmental comparison between hydrogen and some fossil fuels, *Energ. Convers. Manage.*, 89 (2015) 205–213

5. M. Ball, M. Wietschel, The future of hydrogen – opportunities and challenges, *Int. J. Hydrogen Energ.*, 34 (2009) 615 – 627
6. R. W. Rousseau, *Handbook of separation process technology*, John Wiley and Sons, New York, 1987
7. N. W. Ockwig, T. M. Nenoff, Membranes for hydrogen separation, *Chem. Rev.* 107 (2007) 4078-4110
8. A. P. Simpson and A. E. Lutz, Exergy analysis of hydrogen production via steam methane reforming, *Int. J. Hydrogen Energ.*, 32 (2007) 4811-4820
9. S. C. A. Kluiters, presented under the 5th Research Framework Programme of European Union, Intermediate report EU project MIGREYD NNE5-2001-670, Petten, December 2004
10. G. Q. Lu, J. C. Diniz da Costa, M. Duke, S. Giessler, R. Socolow, R. H. Williams, T. Kreutz, Inorganic membranes for hydrogen production and purification: a critical review and perspective, *J. Colloid Interf. Sci.* 314 (2007) 589–603
11. R. M. de Vos, H. Verweij, Improved performance of silica membranes for gas separation, *J. Membr. Sci.*, 143 (1998) 37-51
12. R. M. de Vos, H. Verweij, High-selectivity, high-flux silica membranes for gas separation, *Science*. 279 (1998) 1710-1711
13. Y. S. Lin, Microporous and dense inorganic membranes: current status and prospective, *Sep. Purif. Technol.* 25 (2001) 39–55
14. S. Ponton, F. Dhainaut, H. Vergnes, D. Samelor, D. Sadowski, V. Rouessac, H. Lecoq, T. Sauvage, B. Caussat, C. Vahlas, Investigation of the densification mechanisms and corrosion resistance of amorphous silica films, *J. Non-Cryst. Solids.*, 515 (2019) 34–41
15. A. P. Dral, J. E. ten Elshof, Organic groups influencing microporosity in organosilicas, *Micropor. Mesopor. Mater.* 267 (2018) 267–273
16. M. Kanezashi, Y. Yoneda, H. Nagasawa, T. Tsuru, K. Yamamoto, J. Ohshita, Gas permeation properties for organosilica membranes with different Si/C ratios and evaluation of microporous structures, *AIChE J.* 63 (2017) 4491-4498.
17. N. K. Raman, C. J. Brinker, Organic “template” approach to molecular sieving silica membranes, *J. Membr. Sci.*, 105 (1995) 273-279

18. Y. E. Lee, B. S. Kang, S. H. Hyun, C. H. Lee, Organic-templating approach to synthesis of nanoporous silica composite membranes (ii): MTES-templating and CO₂ separation, *Sep. Sci. Technol.*, 39 (2004) 3541–3557
19. M. Kanezashi, M. Asaeda, Hydrogen permeation characteristics and stability of Ni-doped silica membranes in steam at high temperature, *J. Membr. Sci.*, 271 (2006) 86–93
20. M. Takenaka, H. Nagasawa, T. Tsuru, M. Kanezashi, Hydrocarbon permeation properties through microporous fluorine-doped organosilica membranes with controlled pore sizes, *J. Membr. Sci.*, 619 (2021) 118787
21. G. P. Fotou, Y. S. Lin, S. E. Pratsinis, Hydrothermal stability of pure and modified microporous silica membranes, *J. Mater. Sci.* 30 (1995) 2803-2808
22. K. Yoshida, Y. Hirano, H. Fujii, T. Tsuru, M. Asaeda, Hydrothermal stability and performance of silica-zirconia membranes for hydrogen separation in hydrothermal conditions, *J. Chem. Eng. Jpn.*, 34 (2001) 523-530
23. C. Guizard, A. Ayral, A. Julbe, Potentiality of organic solvents filtration with ceramic membranes. A comparison with polymer membranes, *Desalination* 147 (2002) 275-280
24. H.-S. Choi, C.-H. Ryu, G.-B. Hwang, Obtention of ZrO₂-SiO₂ hydrogen permselective membrane by chemical vapor deposition method, *Chem. Eng. J.*, 232 (2013) 302-309
25. S.-J. Ahn, A. Takagaki, T. Sugawara, R. Kikuchi, S. T. Oyama, Permeation properties of silica-zirconia composite membranes supported on porous alumina substrates, *J. Membr. Sci.*, 526 (2017) 409-416
26. J. Livage, C. Sanchez, Sol-gel chemistry, *J. Non-Cryst. Solids.*, 145 (1992) 11-19
27. J. Livage, M. Henry, C. Sanchez, Sol-gel chemistry of transition metal oxides, *Prog. Solid St. Chem.*, 18 (1988) 25-341
28. D. A. Ward, E. I. Ko, Preparing catalytic materials by the sol-gel method, *Ind. Eng. Chem. Res.* 34 (1995) 421-433
29. G. I. Spijksma, C. Huiskes, N. E. Benes, H. Kruidhof, D. H. A. Blank, V. G. Kessler, H. J. M. Bouwmeester, Microporous zirconia–titania composite membranes derived from diethanolamine-modified precursors, *Adv. Mater.*, 18 (2006) 2165–2168

30. S. Lawal, M. Kanezashi, H. Nagasawa, T. Tsuru, Development of an acetylacetonate-modified silica-zirconia membrane applicable to gas separation, *J. Membr. Sci.* 599 (2020) 117844
31. S. Lawal, L. Yu, H. Nagasawa, T. Tsuru, M. Kanezashi, A carbon-silica-zirconia membrane with CO₂ flow-switching behavior promising high-temperature H₂/CO₂ separation, *J. Mater. Chem. A.* 8 (2020) 23563
32. D. Hoebbel, T. Reinert, H. Schmidt, E. Arpac, On the hydrolytic stability of organic ligands in Al-, Ti- and Zr-alkoxide complexes, *J. Sol-Gel Sci. Technol.*, 10 (1997) 115-126
33. W. Puthai, M. Kanezashi, H. Nagasawa, K. Wakamura, H. Ohnishi, T. Tsuru, Effect of firing temperature on water permeability of SiO₂-ZrO₂ membranes for nanofiltration, *J. Membr. Sci.*, 497 (2016) 348-356
34. D. Peter, T. S. Ertel, H. Bertagnolli, EXAFS study of zirconium alkoxides as precursors in sol-gel process: II. The influence of the chemical modification, *J. Sol-Gel Sci. Technol.*, 5 (1995) 5-14
35. S. K. Parida, S. Dash, S. Patel, B. K. Mishra, Adsorption of organic molecules on silica surface, *Adv. Colloid Interface Sci.*, 121 (2006) 77–110
36. M. Kanezashi, R. Matsugasako, H. Tawarayama, H. Nagasawa, T. Tsuru, Pore size tuning of sol-gel-derived triethoxysilane (TRIES) membranes for gas separation, *J. Membr. Sci.*, 524 (2017) 64-72
37. L. Yu, M. Kanezashi, H. Nagasawa, J. Ohshita, A. Naka, T. Tsuru, Fabrication and microstructure tuning of a pyrimidine-bridged organoalkoxysilane membrane for CO₂ separation, *Ind. Eng. Chem. Res.*, 56 (2017) 1316-1326
38. S. O. Lawal, H. Nagasawa, T. Tsuru, M. Kanezashi, Facile development of microstructure-engineered, ligand-chelated SiO₂-ZrO₂ composite membranes for molecular separations, *Mol. Syst. Des. Eng.*, 6 (2021) 429-444
39. Z.-G. Wu, Y.-X. Zhao, D.-S. Liu, The synthesis and characterization of mesoporous silica–zirconia aerogels, *Micropor. Mesopor. Mater.* 68 (2004) 127–132
40. X. Yu, H. Nagasawa, M. Kanezashi, T. Tsuru, Improved thermal and oxidative stability of bis(triethoxysilyl)ethane (BTESE)-derived membranes, and their gas-permeation properties, *J. Mater. Chem. A.* 6 (2018) 23378-23387
41. M. Kanezashi, T. Sasaki, H. Tawarayama, H. Nagasawa, T. Yoshioka, K. Ito, T. Tsuru, Experimental and theoretical study on small gas permeation

- properties through amorphous silica membranes fabricated at different temperatures, *J. Phys. Chem. C*, 118 (2014) 20323-20331
42. W. Puthai, M. Kanezashi, H. Nagasawa, T. Tsuru, SiO₂-ZrO₂ nanofiltration membranes of different Si/Zr molar ratios: stability in hot water and acid/alkaline solutions, *J. Membr. Sci.* 524 (2017) 700-711.
43. H. Nagasawa, T. Niimi, M. Kanezashi, T. Yoshioka, T. Tsuru, Modified gas-translation model for the prediction of gas permeation through microporous organosilica membranes, *AIChE J.*, 60 (2014) 4199-4210
44. M. Kiyono, P. J. Williams, W. J. Koros, Effect of pyrolysis atmosphere on separation performance of carbon molecular sieve membranes, *J. Membr. Sci.*, 359 (2010) 2-10
45. X. Ning, W. J. Koros, Carbon molecular sieve membranes derived from Matrimid[®] polyimide for nitrogen/methane separation, *Carbon*, 66 (2014) 511-522
46. Y.-S. Lin, C.-H. Chang, R. Gopalan, Improvement of thermal stability of porous nanostructured ceramic membranes, *Ind. Eng. Chem. Res.* 33 (1994) 860-870

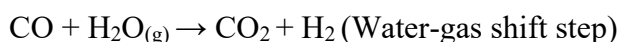
Chapter 5

CO₂ flow-switching behaviour in a pyrolysis-derived carbon-silica-zirconia membrane promises a versatile high-temperature H₂/CO₂ separation

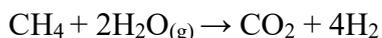
5.1 Introduction

Separation processes have already made a significant impact on the world [1]. The operating expenses of these processes, however, represent exorbitant investments of capital in industries such as petroleum, chemical, petrochemical, pharmaceutical, pulp, mineral and others [2]. Currently, about 80% of the world's energy demand is satisfied using fossil fuels [3]. These facts suggest that the world's industrial energy demand (and by extension fossil fuel consumption) derives from separation processes. By 2035, it is estimated that 8 countries (China, the USA, India, Brazil, Japan, South Korea, Canada, and Mexico) will demand as much as 5.24×10^{17} kJ (4.97×10^{17} BTU) of energy [4], and 37% of that is estimated to come from the industrial sector alone of which about 79% is foreseen to be fossil fuel-derived by 2030. 5 Therefore, two interwoven problems must be solved: 1) reliance on fossil fuels; and, 2) energy requirement for industrial separation processes. Fortunately, new separation techniques such as membrane separation have been developed over the years to tackle these problems. The development of hydrogen separation membranes could be a two-pronged solution to the problems highlighted above [6]. On the one hand, membrane separation could be an energy-efficient way to separate H₂ from different mixtures [2, 7-10], while on the other hand the resultant H₂ could provide a sustainable and 'cheap' source of energy [11, 12].

Hydrogen production from the steam reforming of natural gas currently produces levels of production efficiency that average between 65 and 75%, which is the highest of all non-renewable production sources [11]. Currently, steam reforming of natural gas also has the lowest cost, uses existing infrastructure [13], requires no oxygen for processing, and operates at the lowest temperature of all methods [14]. Obviously, steam reforming is the most widely used method for hydrogen production as it accounts for 80-85% of total hydrogen production [15]. As shown below, steam reforming of natural gas consists mainly of methane reforming and is basically accomplished in two steps [6, 16]:



The overall reaction becomes



The final step in steam methane reforming (SMR) is separation of the effluent stream, which is comprised mostly of H₂, H₂O and CO₂, the composition of which depends on factors such as the reformer operating temperature and pressure and the steam-to-carbon ratio [6, 16]. Techniques utilized for separation of H₂ from CO₂ and steam (for >99 % pure H₂ stream) have traditionally consisted of venerable energy intensive approaches such as the pressure swing adsorption (PSA) of H₂ or CO₂, cryogenic distillation [2, 6, 16, 17], and the more recent process of energy conservative membrane separation [6, 16].

The composition of the final effluent gas stream is dependent on variable conditions such as temperature, pressure, and the steam-to-carbon ratio, which means that the separation technique of choice must be versatile enough to deal with these composition variations. This poses a challenge for the development of membrane separation techniques, and researchers must develop robust and versatile materials that simultaneously deliver the core targets of viable H₂ separation. Integrated gasification combined cycle applications (IGCC) also utilize the water-gas shift (WGS), and candidate materials must achieve levels of H₂ recovery and H₂/CO₂ selectivity of 70-90% and 21-62, respectively, under high temperatures and pressures [18], although SMR/WGS targets in industrial sources of H₂ production have more stringent requirements for H₂ stream purity at > 99.99% [6, 16, 19]. In addition to these targets, we believe taking H₂ separation membranes a step further would entail versatility in order to deal with H₂/CO₂ mixtures of widely varying compositions.

Several H₂ separation membranes that are applicable in a wide variety of temperature ranges have been developed over the years. The developers of these membranes have aspired to meet the set targets, and beyond, with varying degrees of success, which is associated with the material make-up of the membranes. Various H₂ separating membrane materials and processes have been reviewed [2, 6, 20]. Overall, H₂ separating membranes have yet to meet the desired potential, and as of recently, only two industrial applications of H₂ separation membranes are known to exist (recovery of H₂ from off-gases in the ammonia industry and production of pure H₂ in the electronic industry) [20]. Thus, the principal driver of success in this quest is

confined to creativity in materials research. An interesting group of materials that have received much attention in recent times are flexible metal-organic frameworks (FL-MOFs) [21-28], specifically because of their ability to structurally respond to external stimuli such as pressure, temperature, light and electric fields [26]. Such ‘dynamic’ responses are exploitable in separation processes. For example, a fluorinated MOF derived from a self-assembly of 2,2’-bis(4-carboxyphenyl) hexafluoro propane and zinc nitrate hexahydrate has shown high selectivity of CO₂ over N₂ because perfluorinated compounds exhibit electrostatic interactions with CO₂ [23]. According to Kitagawa and Uemura [21], a construction of ‘dynamic’ porous coordination polymers is rational via the placement of weak ‘interaction devices’ such as van der Waals force, π - π stacks and hydrogen bonds between stiff 1-D, 2-D and 3-D building blocks. This strategy offers a viable design for new porous materials by utilizing existing ceramic materials that have shown promise for H₂ separation. Thus, the ‘interaction devices’ employed must selectively engage with the mixture to be separated.

Composite SiO₂-ZrO₂ ceramic membranes have exhibited desirable levels of hydrothermal stability for H₂ separation, but expensive molecular sieving is required [29]. Hence, our group recently reported the successful chemical modification of a composite SiO₂-ZrO₂ ceramic membrane capable of molecular sieving [30]. This membrane in its ligand-modified form offered no promise for H₂/CO₂ separation. A successful modification with a chelating ligand of acetylacetone, however, has opened the possibility for in-situ carbonization (pyrolysis of the organic ligand). If the deposited free carbon during pyrolysis approximates the anisotropic characteristics of graphite [31], then the resultant van der Waals forces between the π - π stacks of carbon layers could serve as ‘interaction devices’ and endow new ‘dynamic’ characteristics into the SiO₂-ZrO₂ matrix. Van der Waals interactions could also develop between the carbon particles and the metal centers due to shifts in the electron densities. Moreover, a recent report of the carbonization of a molecular sieve silica membrane has introduced interesting properties to ordinary molecular sieve silica [32, 33].

Herein, we describe how SiO₂-ZrO₂-acetylacetonate was successfully pyrolyzed to form a carbonized form of SiO₂-ZrO₂ (hereafter called C-SiO₂-ZrO₂). Fig. 5-1 presents the expected pyrolysis and network formation pathway. The in-situ

carbonization was evaluated by characterization methods. C-SiO₂-ZrO₂ interaction with CO₂ at various temperatures was investigated via sorption experiments. Single and binary gas mixture experiments at 50 and 300 °C were performed to determine the permeation characteristics of H₂ and CO₂ as well as the separation performance of an alumina-supported C-SiO₂-ZrO₂ membrane. Finally, we discuss the place of a C-SiO₂-ZrO₂ membrane in the scheme of H₂ separation in industrial H₂ production systems and postulate as to the possibility that a versatile H₂ separation can be achieved. In the present study, we believe that we achieved a rational design for selective dynamism in a porous ceramic membrane.

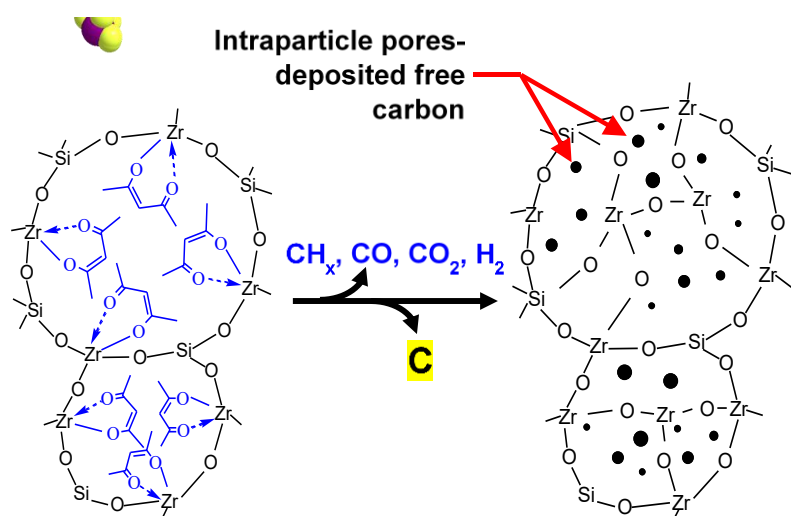


Fig.5-1 Illustration of expected pyrolysis and network formation pathway of SiO₂-ZrO₂-acac to C-SiO₂-ZrO₂

5.2 Experimental

5.2.1 Preparation and pyrolysis of SiO₂-ZrO₂-acac powder and C-SiO₂-ZrO₂ membrane fabrication

The preparation of SiO₂-ZrO₂-acac (SZa₄) sol was described in Chapter 2 section 2.2.1. SZa₄ (SiO₂-ZrO₂-acetylacetonate) powders were subsequently prepared from a SZa₄ sol by slowly drying the sol under an atmosphere controlled at 40-50 °C. Carbon-SiO₂-ZrO₂ (CSZ550) powders were then prepared from SZa₄ powders via calcination in a 3-zone furnace at 550 or 750 °C under a N₂ stream at 600 ml min⁻¹ for 20-25 min. For convenience the resultant pyrolyzed products will hereafter be referred to as CSZ550 or CSZ750 depending on the calcination temperature.

To prepare CSZ550 membranes, it was necessary to fabricate membrane supports. Details of this fabrication process has been described in Chapter 2 section 2.2.1. The active separation layer was prepared thus: 1 wt% SZa₄ sol in ethanol was wipe-coated onto the pre-prepared SiO₂-ZrO₂ intermediate layer followed by calcination under a 600 ml min⁻¹ nitrogen gas flow at 550 °C for 20-25 min. in a 3-zone continuous flow furnace. This process was repeated 6–8 times to obtain the final defect-free CSZ550 membrane ready for single-gas and binary-mixture permeation measurements. It should be noted that after fabrication the CSZ550 membrane was kept in the membrane module under a He flow for 12 hours at 200 °C.

5.2.2 Characterization of materials

The pyrolysis route of the acetylacetonate ligand in SZa₄ powders was analyzed and monitored using thermogravimetry and mass spectroscopy (TGA-DTA-PIMS 410/S, Rigaku, Japan; DTG-60 Shimadzu Co., Japan) under nitrogen or He gas flows of 80 ml min⁻¹ with a heating rate of 10 °C min⁻¹. In a similar manner, the combustion test for free carbon under air was performed using thermogravimetry (DTG-60 Shimadzu Co., Japan). The presence and the chemical state of free carbon was confirmed using Fourier Transform-Infrared spectroscopy (FT-IR, FTIR-4100, JASCO, Japan) and solid-state ¹³C cross polarization/dipolar decoupling magic-angle spinning nuclear magnetic resonance (CP/DD MAS-NMR), which was recorded using a NMR spectrometer (Varian 600PS, Agilent Inc., U. S. A.). ¹³C-CP/DD MAS-NMR measurement was carried out at a frequency of 150.87 Hz using both ¹³C-¹H dipolar coupling and decoupling modes. The spectra were acquired in 360 scans each with a 90° pulse of 3.2 μs and recycle delays of 70 s. Hexamethylbenzene was used as a reference against which the observed peaks were positioned, and a 6 mm zirconia rotor spun at a magic angle of 57.4° at 7 kHz contained the sample. The physical evidence of the presence of carbon nanoparticles was confirmed by obtaining the micrographs of the SZa₄ and CSZ550 particles using transmission electron microscopy. The samples to be resolved were prepared on ultra-high-resolution carbon supports (STEM 100Cu Grids) by dropping approximately 10 μl of a 2 wt% dispersion of the fine particles in butanol onto the grids. Prior to examination, the prepared grids were vacuum-dried at 50 °C for 48 hours. The crystal/amorphous structure and lattice spacing values of SZa₄ and CSZ550 powders were obtained using X-ray diffraction spectroscopy (D2 PHASER X-Ray Diffractometer, Bruker,

Germany) with Cu K α as the radiation source at a wavelength of 1.54 Å. Furthermore, the sorption behaviors of CO₂ on both SZa₄ and CSZ550 powders were analyzed with CO₂ adsorption/desorption experiments carried out at 25, 30 and 35 °C. Prior to this measurement, samples of adsorbed gases and vapors were evacuated: SZa₄ at 100 °C and CSZ550 at 300 °C for at least 6 hours. Temperature-programmed desorption of N₂ and CO₂ was carried out using a custom-built equipment setup fitted with a mass spectrometer (Dymaxion Dycor, Ametek Process Instruments, U. S. A.). Lastly, the cross-section morphology of the composite membrane was examined by Field Emission-Scanning Electron Microscopy (FE-SEM, Hitachi S-4800, Japan). Prior to examination, chipped samples of the membrane were attached to sample holders via carbon tape and vacuum-dried at 50 °C for 24 hours.

5.2.3 Gas permeation measurement

A schematic representation of the gas permeation measurement setup is shown in Fig. 5-2. Prior to the gas permeation measurement, a CSZ550 membrane was fitted into its module immediately after fabrication and placed inside the furnace in the gas permeation measurement rig at 200 °C under a moderate helium flow of 100 ml min⁻¹ for about 12 hours to remove the adsorbed vapor. Single-gas permeation tests of the CSZ550 membranes were made using high purity gases (H₂, He, CO₂, N₂, CH₄, CF₄, SF₆ in that order). Each gas was fed to the upstream of the closed-end membrane module at 200-500 kPa of absolute pressure under temperatures ranging from 50 – 300 °C. Permeate side pressure was kept at atmospheric pressure and the permeate gas flow was measured using a bubble film flow meter (HORIBA-STECH, Japan).

Binary mixture separation performance was evaluated using the setup shown in Figure 5-2 at 50 and 300 °C. In the measurement of binary gas mixture separation, H₂/CO₂ (80/20, 50/50, 20/80) mixtures were fed to the upstream of the module while maintaining the pressure by setting the retentate side needle valve at 200 and 500 kPa with the downstream kept at atmospheric pressure. The compositions of the feed, retentate and permeate streams were analyzed using a pre-calibrated gas chromatograph (GC-14B, Shimadzu, Japan) equipped with a TCD detector (column: Porapak N (GL Science, Japan)). To evaluate the transmembrane pressure-drop of each component, the log mean pressure difference ($\Delta P_{i,lm}$) was applied (Equation 5-1).

$$\Delta P_{i,lm} = \frac{\Delta P_{i,in} - \Delta P_{i,out}}{\ln(\Delta P_{i,in} / \Delta P_{i,out})} \quad (5-1)$$

In Equation 5-1, $\Delta P_{i,in}$ and $\Delta P_{i,out}$ represent the difference in partial pressures of component i between the retentate side and the permeate side at the inlet and outlet of the module, respectively.

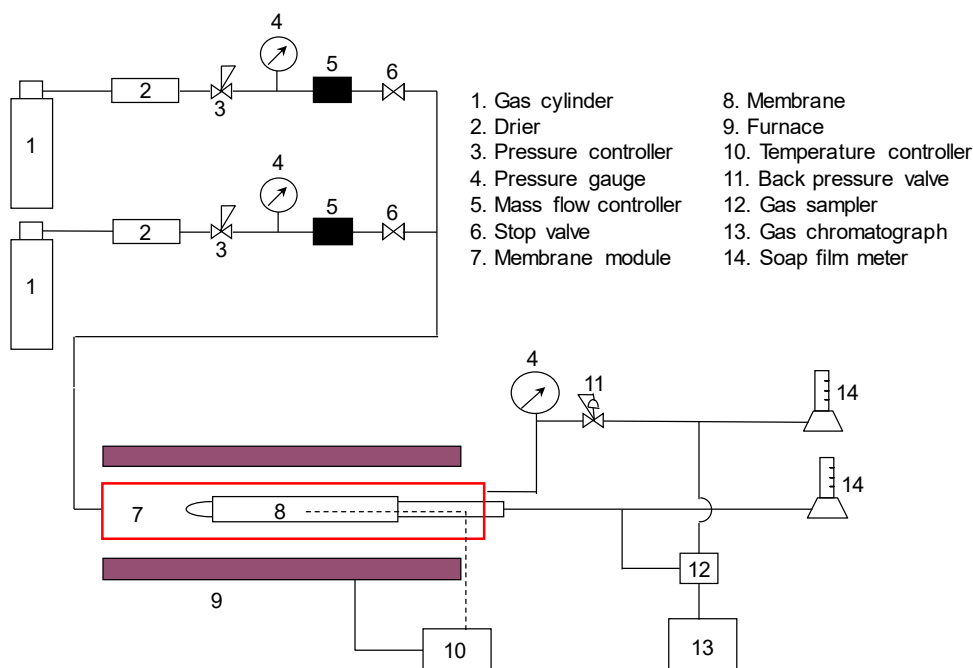


Fig. 5-2 Schematic flow diagram of the gas permeation testing setup (Test pressures: $P_u = 200\text{-}500$ kPa, $P_d = 100$ kPa)

5.3 Results and discussion

5.3.1 Carbonization of $\text{SiO}_2\text{-ZrO}_2\text{-acac}$ into $\text{C-SiO}_2\text{-ZrO}_2$ and identification of the carbon state

In Fig. 5-3 (a), the decomposition products of Acac^- (acetylacetonate) were confirmed via TG-MS (thermogravimetry-mass spectroscopy under an inert He atmosphere. In this figure the final decomposition temperature was around $500\text{-}550$ °C, which corresponds to the profile for $\text{SiO}_2\text{-ZrO}_2\text{-acac}$ thermal decomposition under an inert N_2 atmosphere, as presented in Fig. 5-3 (b), which shows the DTG-DTA profiles for the thermal decompositions of $\text{SiO}_2\text{-ZrO}_2\text{-acac}$ and $\text{C-SiO}_2\text{-ZrO}_2$ under N_2 and air, respectively. The final decomposition temperature for $\text{SiO}_2\text{-ZrO}_2\text{-acac}$ under N_2 was approximately $500\text{-}550$ °C with the DTA curve showing no exothermal peaks, which indicated no combustion reactions and possible deposition of non-volatile

decomposition products. Under air, C-SiO₂-ZrO₂ (prepared by pyrolyzing SiO₂-ZrO₂-acac under N₂ at 550 °C for 20 minutes, as discussed under the experimental section) showed thermal decomposition until the temperature reached 600 °C with exothermal peaks in the DTA curve indicating the combustion of deposited non-volatile carbon to CO and/or CO₂. The weight loss was calculated at 20%, which corresponded to 203 mg carbon/g of C-SiO₂-ZrO₂.

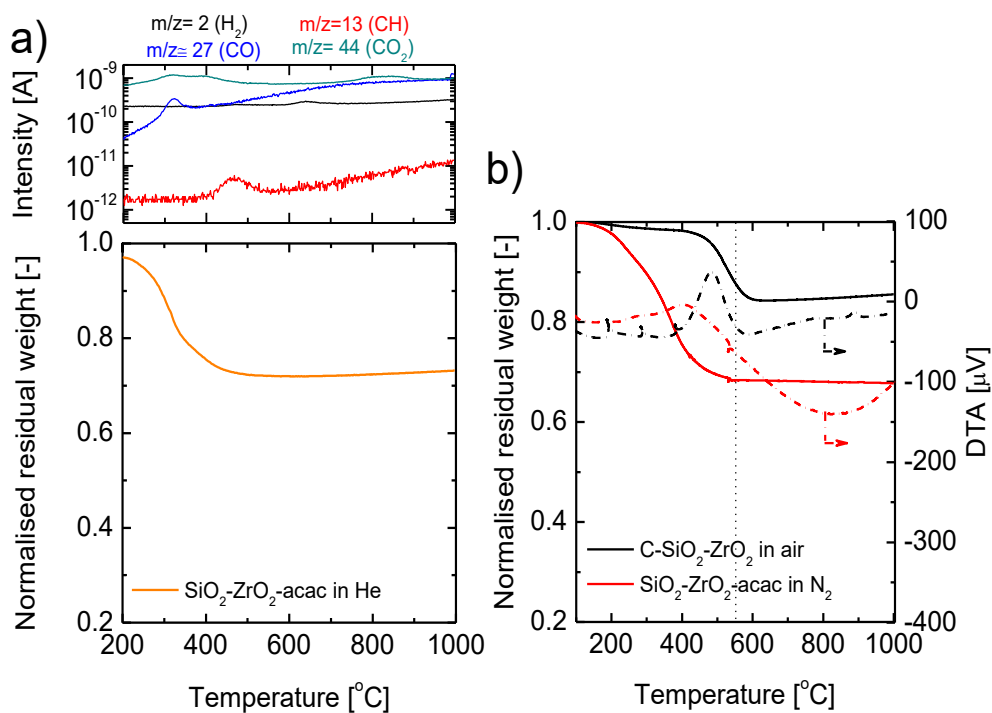


Fig. 5-3 Observed TG-MS profile of SiO₂-ZrO₂-acac under He, and (a) TGA-DTA profiles of SiO₂-ZrO₂-acac under N₂ and C-SiO₂-ZrO₂ under air (b) (ramping rate: 10 °C min⁻¹)

It is important to determine the state of carbon in the SiO₂-ZrO₂ matrix as this will aid in understanding the behavior of the composite material. Fig. 5-4 shows the change in the CP-MAS-¹³C-NMR (cross polarization) spectra of the SiO₂-ZrO₂-acac transformation to C-SiO₂-ZrO₂ (pyrolyzed at 550 and 750 °C). For the spectrum of SiO₂-ZrO₂-acac, the different peaks indicate the intensity of the different functional groups of the enol and keto forms of the acac⁻ chelate resulting from ¹³C-¹H dipolar coupling. Acetylacetone in its keto tautomer form exists with two carbonyl groups (C=O), and as such is not able to properly chelate with transition metals. However, in its enol form, acetylacetone presents with one carbonyl group (C=O) and one enol group (C=C-OH) that more easily forms acetylacetonate, thus facilitating chelation.

The magnified chemical shifts of peaks 5 and 6 on the $\text{SiO}_2\text{-ZrO}_2\text{-acac}$ spectra show very small intensities indicating that the enol forms of acac^- were adequately chelated to $\text{SiO}_2\text{-ZrO}_2$ by comparison with the spectrum of pure acetylacetone [35]. Furthermore, the spectra of 550 and 750 °C-pyrolyzed $\text{C-SiO}_2\text{-ZrO}_2$ showed broad peaks in the aromatic chemical shift region (~130 ppm) with two spinning side bands. The spinning side bands are peaks due to the chemical shift in anisotropy that is associated with sp^2 hybridized C species such as aromatic and carbonyl C [36, 37]. This indicates the transformation of acac^- into aggregated sp^2 hybridized graphitic carbon. The DD-MAS- ^{13}C -NMR (dipolar decoupling mode) that resolved the magnetic environment of ^{13}C by decoupling ^{13}C - ^1H revealed very sharp peaks (Fig. 5-5). This is reasonable since free carbon has no bonded ^1H . The 550 and 750 °C-pyrolyzed $\text{C-SiO}_2\text{-ZrO}_2$ samples showed similar spectra, further indicating that pyrolysis up to 750 °C results in little or no change in the chemical and physical states of the pyrolysis product.

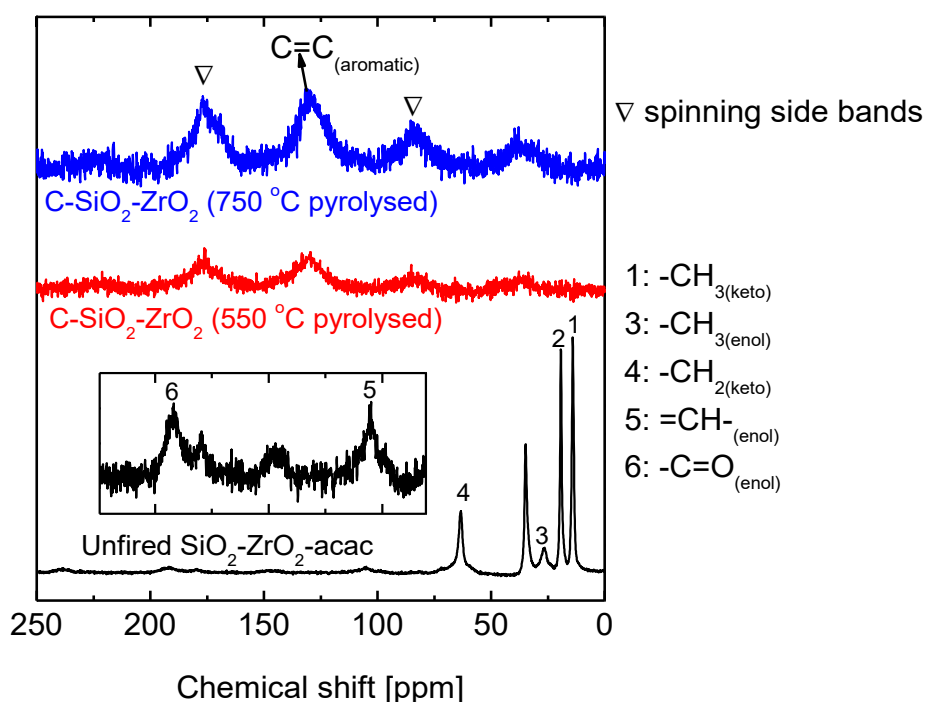


Fig. 5-4 CP-MAS- ^{13}C -NMR spectra of fresh $\text{SiO}_2\text{-ZrO}_2\text{-acac}$ and that pyrolyzed at 550 and 750 °C.

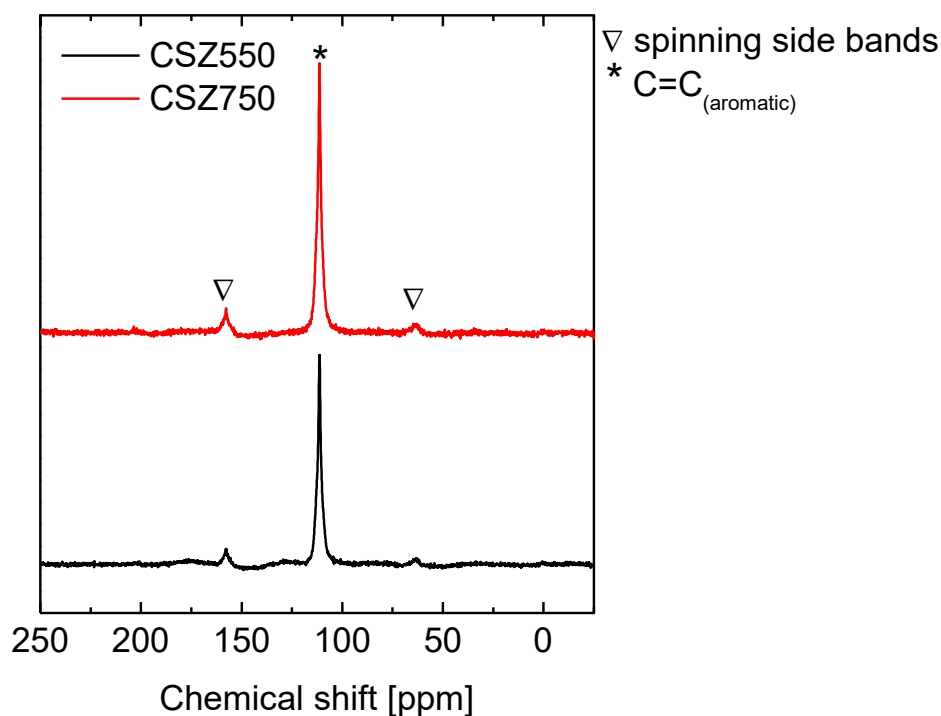


Fig. 5-5 DD-MAS- ^{13}C -NMR spectra of C-SiO₂-ZrO₂ prepared at 550 and 750 °C under N₂.

The physical evidence of the presence of free carbon was obtained by transmission electron microscopy. Fig. 5-6 (a)-(d) compare the electron diffraction patterns in the TEM micrographs of 5 nm-scale SiO₂-ZrO₂-acac (Fig. 5-6 (a) and (b)) and C-SiO₂-ZrO₂ (Fig. 5-6 (c) and (d)) that were used to detect the presence of carbon nanoparticles. Fig. 5-6 (b) and (d) are high-contrast conversions of Fig. 5-6 (a) and (c). The images show the edges of the particles. The micrographs reveal dark patches of ~1 nm or less dispersed in the C-SiO₂-ZrO₂ matrix. Similar TEM images have been reported for fluorescent carbon nanoparticles (CNPs) [38]. The inset images of both SiO₂-ZrO₂-acac and C-SiO₂-ZrO₂ show halo electron diffraction patterns indicating that the carbonization process had little effect on the amorphous structure of the SiO₂-ZrO₂ matrix.

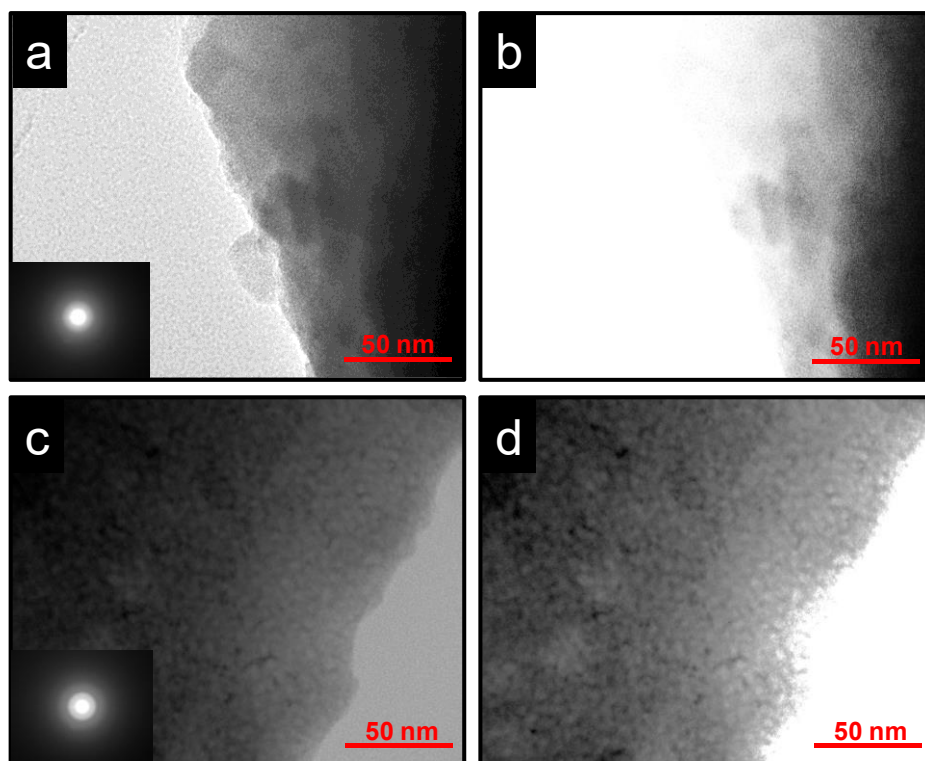


Fig. 5-6 TEM images of $\text{SiO}_2\text{-ZrO}_2\text{-acac}$: (a) original; (b) high-contrast and $550\text{ }^\circ\text{C}$ -derived $\text{C-SiO}_2\text{-ZrO}_2$: (c) original; (d) high-contrast. Insets: Electron Diffraction Images

5.3.2 Unique permeation properties of CO_2 in $\text{C-SiO}_2\text{-ZrO}_2$ membranes

5.3.2.1 Understanding the interaction between CO_2 and $\text{C-SiO}_2\text{-ZrO}_2$.

Fig. 5-7 (a) and (b) illustrate the observed evolution of the $\text{CO}_2/\text{C-SiO}_2\text{-ZrO}_2$ interaction. In Fig. 5-7 (a), the adsorption isotherms of $\text{SiO}_2\text{-ZrO}_2\text{-acac}$ and $\text{C-SiO}_2\text{-ZrO}_2$ powders at 25 and $35\text{ }^\circ\text{C}$ are shown. Both samples show gentle Langmuir-like (almost Henry) type I adsorption isotherms in the pressure range observed. The adsorption-desorption isotherms of $\text{SiO}_2\text{-ZrO}_2\text{-acac}$ at both 25 and $35\text{ }^\circ\text{C}$ follow reversible paths indicating almost no special effect of CO_2 adsorption on neither the $\text{SiO}_2\text{-ZrO}_2\text{-acac}$ structure nor the surface. In contrast, after carbonization of $\text{SiO}_2\text{-ZrO}_2\text{-acac}$ resulted in $\text{C-SiO}_2\text{-ZrO}_2$, the adsorption-desorption isotherms of CO_2 showed significant hysteresis despite the smaller amount of adsorbed CO_2 indicating a structural conformation of the $\text{C-SiO}_2\text{-ZrO}_2$ to allow CO_2 adsorption. The existence of this hysteresis at a temperature above the critical temperature of CO_2 ($31\text{ }^\circ\text{C}$) rules out the possibility of capillary condensation, and instead suggests this is the result of a

structural transformation [22]. Culp *et al.* [22] proposed that when host-guest interaction can energetically compensate for the shape transformation of the host lattice, the host structure could conform to the shape of the guest molecules.

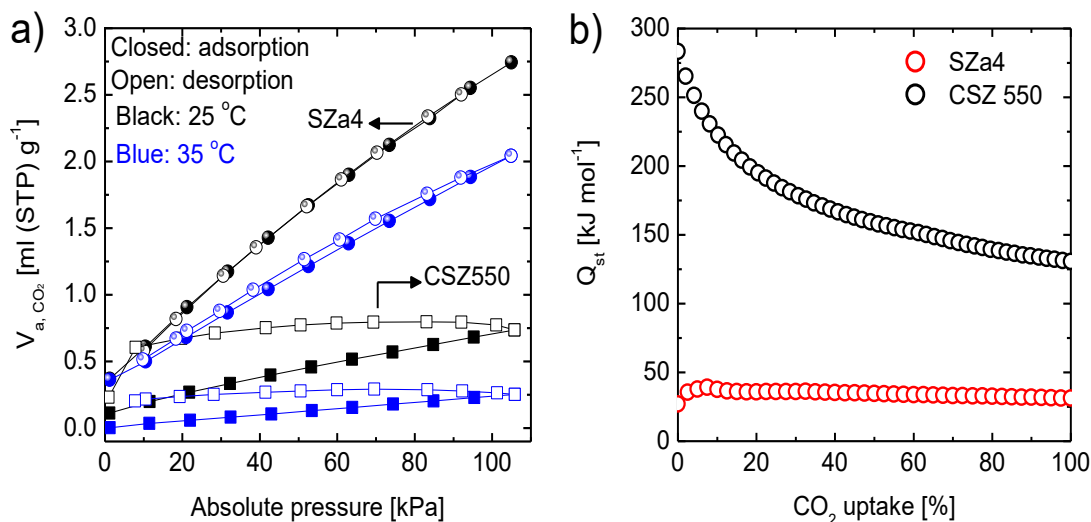


Fig. 5-7 (a) Adsorption-desorption isotherms of CO_2 onto $\text{SiO}_2\text{-ZrO}_2\text{-acac}$ and $\text{C-SiO}_2\text{-ZrO}_2$ powders measured at 25 and 35 °C; (b) Calculated isosteric heats of adsorption of CO_2 onto $\text{SiO}_2\text{-ZrO}_2\text{-acac}$ and $\text{C-SiO}_2\text{-ZrO}_2$ powders using temperatures of 25, 30 and 35 °C

Fig. 5-7 (b) presents the isosteric heat of the adsorption of CO_2 onto $\text{SiO}_2\text{-ZrO}_2\text{-acac}$ and $\text{C-SiO}_2\text{-ZrO}_2$ calculated using the adsorption isotherms at 25, 30 and 35 °C and the Clausius-Clapeyron equation. The isosteric heat of CO_2 adsorption for $\text{C-SiO}_2\text{-ZrO}_2$ shows an average value of $\sim 170 \text{ kJ mol}^{-1}$ compared with $\sim 34 \text{ kJ mol}^{-1}$ for $\text{SiO}_2\text{-ZrO}_2\text{-acac}$. Lin *et al* [39] calculated the theoretical potential energy surface (PES) barrier required for CO_2 chemisorption on a pristine graphite to be $\sim 350 \text{ kJ mol}^{-1}$ ($\sim 84 \text{ kcal mol}^{-1}$). With CO_2 adsorption on $\text{C-SiO}_2\text{-ZrO}_2$ releasing a maximum of $\sim 290 \text{ kJ mol}^{-1}$, this suggests that CO_2 adsorption onto $\text{C-SiO}_2\text{-ZrO}_2$ can produce enough energy to deform the lattice structure to allow adsorption. The drastic decrease in the Q_{st} of $\text{C-SiO}_2\text{-ZrO}_2$ indicates an energetic heterogeneity of the $\text{C-SiO}_2\text{-ZrO}_2$ surface.

Fig. 5-8 shows the observed XRD patterns and lattice spacing values calculated from the centers of the amorphous peaks of $\text{SiO}_2\text{-ZrO}_2\text{-acac}$, $\text{C-SiO}_2\text{-ZrO}_2$, and pure $\text{SiO}_2\text{-ZrO}_2$ powders (with and without firing) measured at room temperature. The d -

spacing value was reduced when SiO₂-ZrO₂-acac (0.356 nm) was pyrolyzed to C-SiO₂-ZrO₂ (0.295 nm) at 550 °C under N₂. On the other hand, pure SiO₂-ZrO₂ displayed a *d*-spacing shift from 0.314 nm to 0.291 nm after calcination at 550 °C. The resultant *d*-spacing of C-SiO₂-ZrO₂ was similar but somewhat higher in value compared with that of pure SiO₂-ZrO₂ (0.291 nm). The similar *d*-spacing values of C-SiO₂-ZrO₂ and pure SiO₂-ZrO₂ may suggest that free carbon layers are well integrated into the SiO₂-ZrO₂ lattice and do not form separate structures. The spacing between the successive layers of carbon can thus be safely assumed to be less than 0.295 nm. In Fig. 5-9, a scheme illustrating the interaction between CO₂ and C-SiO₂-ZrO₂ is shown. As established from characterization methods, free carbon is integrated in graphitic form in the C-SiO₂-ZrO₂ lattice. Graphitic carbon is anisotropic so that the layers of carbon are closely bound together in the vertical axis by weak van der Waals forces produced by delocalized π -orbital electrons (π - π stacking) and sp²-hybridized C-C σ -bonding in the horizontal direction [40]. These delocalized electrons can induce dipole moments on approaching CO₂ molecules specifically because of the known vibrational modes of CO₂ which make it susceptible to dipole induction. The induced CO₂ molecules become attracted and electronically adsorbed onto the graphitic carbon layers thereby undergoing structural changes because the weak van der Waals forces allow the lattice to conform to the functionality of CO₂ guest molecules [22].

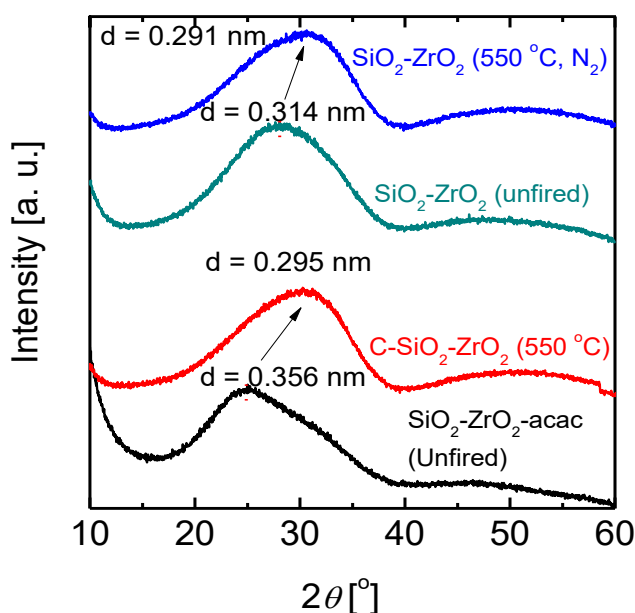


Fig. 5-8 Observed XRD patterns and calculated d -spacing values of $\text{SiO}_2\text{-ZrO}_2\text{-acac}$, $\text{C-SiO}_2\text{-ZrO}_2$ and pure $\text{SiO}_2\text{-ZrO}_2$ powders measured at room temperature.

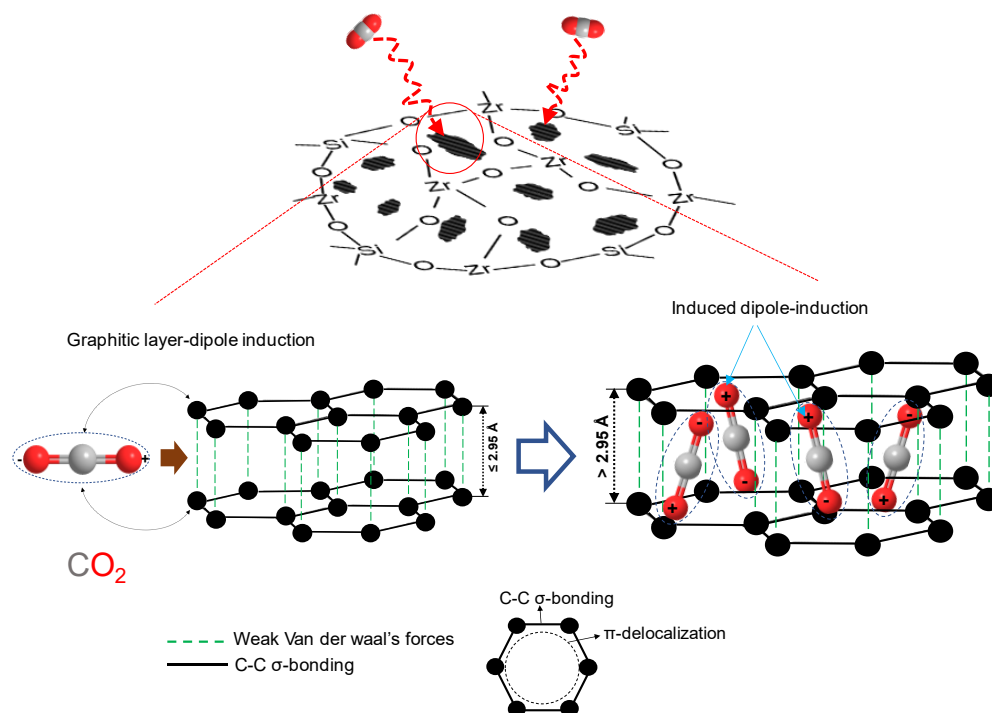


Fig. 5-9 Scheme illustrating the mechanism of the interaction between CO_2 and $\text{C-SiO}_2\text{-ZrO}_2$

5.3.2.2 Pressure-induced transition of CO_2 flow in $\text{C-SiO}_2\text{-ZrO}_2$ membranes

Fig. 5-10 (a) and (b) show the time courses for the single-gas permeance of He, H_2 and CO_2 at 50 and 300 °C, respectively, through an alumina-supported $\text{C-SiO}_2\text{-ZrO}_2$ membrane, as measured at an upstream pressure of 200 kPa. In both cases, a dynamic permeation trend is observed for CO_2 whereby the permeance reduces drastically with time before reaching a steady state. This points to a strong permeation hindrance to CO_2 flow due to blocking by adsorbed immobilized CO_2 . At 50 °C, He and H_2 recovered about 65 and 79% of their initial values, respectively, after the feeding of CO_2 , which effectively blocked certain pores due to adsorption by the $\text{C-SiO}_2\text{-ZrO}_2$ pores. This shows that adsorbed CO_2 has a blocking effect on the permeation paths of He and H_2 and that He, H_2 and CO_2 share same permeation paths. At 300 °C the values for He and H_2 permeance are recovered at rates of 80 and 83%, respectively, and it would be safe to assume that the recovery ratio increases as temperature increases so that adsorption would be stronger at 50 °C than at 300 °C given the continued occurrence of adsorption.

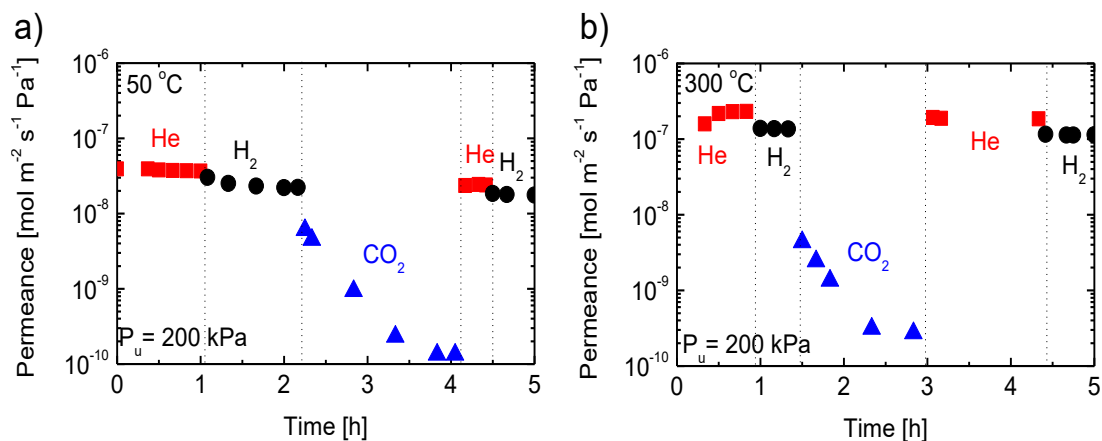


Fig. 5-10 Time courses for single-gas (He, H₂ and CO₂) permeation at 50 (a) and 300 °C (b)

Fig. 5-11 (a) shows the single-gas permeance for a C-SiO₂-ZrO₂ membrane as a function of the kinetic diameter of different gases (He (0.26 nm), H₂ (0.289 nm), CO₂ (0.33 nm), N₂ (0.364 nm), CH₄ (0.38 nm), CF₄ (0.48 nm), and SF₆ (0.55 nm)) measured at 300 °C under 200 and 500 kPa of upstream pressure. Also shown in Fig. 5-11 (a) are the calculated values for permeance according to the Knudsen mechanism based on SF₆, as indicated by the broken lines. The experimentally obtained values for He and H₂ permeance far exceeded those calculated via the Knudsen mechanism, which suggests the existence of pores so small that only H₂ and He could permeate them, which indicates a bimodal pore distribution in C-SiO₂-ZrO₂ membranes. It should be noted that pressures are presented in absolute values. For the measurement made at 200 kPa of upstream pressure, the gas permeance followed a trend such that permeance was decreased with an increase in the kinetic diameter, which generally indicates a molecular sieving property. CO₂ is the exception, and deviates from the trend with a permeance lower than other gases irrespective of the kinetic diameter. At 500 kPa of upstream pressure, however, gas permeance follows a trend whereby it decreases with an increase in the kinetic diameter without exception as opposed to gas permeance at 200 kPa. It was noted that values for gas permeance at 200 kPa remained either approximately the same (He, H₂, CH₄, CF₄, SF₆) at 500 kPa or somewhat less (N₂), but CO₂ permeance at 500 kPa ($1.5 \times 10^{-9} \text{ mol m}^{-2} \text{ s}^{-1} \text{ Pa}^{-1}$) was increased by almost one order compared with that at 200 kPa ($1.7 \times 10^{-10} \text{ mol m}^{-2} \text{ s}^{-1} \text{ Pa}^{-1}$). To further investigate this CO₂-specific trend, the pressure-dependence of CO₂ permeance was investigated using a fresh C-SiO₂-ZrO₂ membrane calcined at 550 °C,

as shown in Fig. 5-11 (b). The measurement was made multiple times to ensure steady-state values and to verify accuracy. The data presented in Fig. 5-11 (b) are data recorded as soon as CO₂ reached steady state at 200 kPa. At subsequent pressures, the system response was quick and steady state was reached in a short time. In the initial feed of CO₂ gas to the upstream of the membrane at 200 kPa and 300 °C, it was required to wait approximately 2 hours for steady state to be reached before recording the results. The results obtained reveal that CO₂ permeance showed almost no dependence on upstream pressures that reached approximately 350 kPa. At 400 kPa and above, however, a positive slope in the permeance of CO₂ was almost linear with the slope of further increases in the pressure.

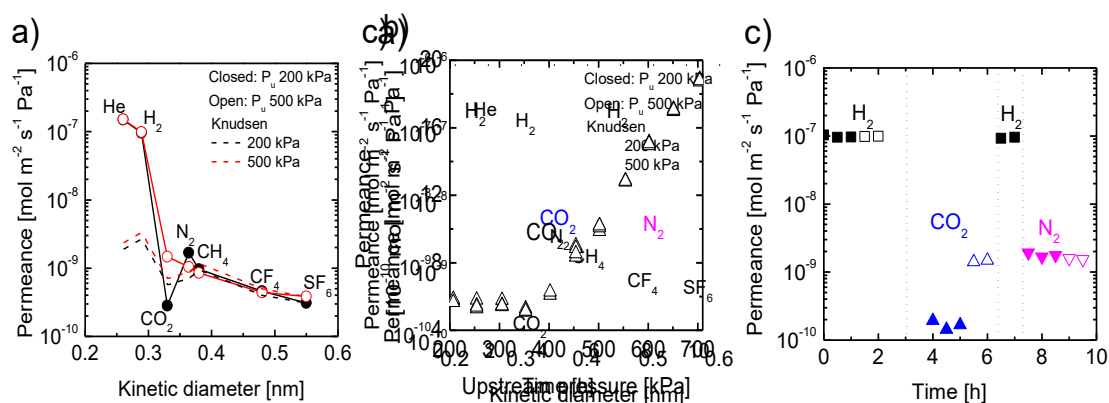


Fig. 5-11 (a) Single-gas permeance at 300 °C as a function of kinetic diameter at 200 and 500 kPa upstream pressures; (b) CO₂ permeance as a function of upstream pressure measured at 300 °C; (c) time course for the single-gas permeance of H₂, CO₂ and N₂ at 300 °C measured at upstream pressures of 200 and 500 kPa (closed symbols: 200 kPa; open symbols: 500 kPa).

This is consistent with the kinetic diameter dependence of single gas permeance measurements made at 200 and 500 kPa. In some cases, this type of trend can be associated with the development of defects in a membrane [41, 42]. In the works of DeSisto *et al* [41] and Barma and Mandal [42], defects appeared on SiO₂ membrane layers as thick as 7 μm and 6 μm respectively which happened to cause viscous flow. As shown in Fig. 5-11 (c), however, after CO₂ permeation at 200 and 500 kPa, the permeance of H₂ recovered as much as 99% of its levels before CO₂ flow (after desorption of adsorbed CO₂ in vacuum at 350 °C). Furthermore, the values for N₂ permeation at 200 and 500 kPa showed similar values following CO₂ permeation,

which is a sign of the absence of any defects. This suggests that the integrity of the membrane matrix was retained and was unaffected by the flow of CO₂. Therefore, it can be safely assumed that CO₂ only displayed a switching of flow regimes in the C-SiO₂-ZrO₂ membrane with 400 kPa being the transition pressure. Neither plasticization nor defects can be suggested in this case. It should be noted that since the measurement temperature (300 °C) was well above the critical temperature of CO₂ (31 °C), this phenomenon should not be ascribed to the flow of capillary condensate. We therefore suggest a pressure-induced multilayer diffusion mechanism. It has already been established in this section that adsorbed and immobilized CO₂ molecules prevent further permeation of gas-phase CO₂ molecules. This trend persists at low pressures. When the upstream pressure increases and the concentration of CO₂ exceeds a certain threshold where adsorbent-adsorbate interaction dominates, multilayer adsorption may occur and thus lead to a greater mobility of gas-phase CO₂ molecules [43].

Table 5-1 lists the calculations of activation energy for the temperature dependence of the gas permeation for different gases (H₂, CO₂, N₂ and SF₆), as regressed against Equation 2-1 and plotted in Fig. 5-12. Based on these calculations, H₂ exhibited an activated diffusion mechanism with activation energy of 5.96 kJ mol⁻¹, while other gases showed Knudsen permeation with activation energies of less than 1 kJ mol⁻¹. In Fig. 5-12, it is evident that the blocking effect of adsorbed CO₂ greatly contributes to a reduction in the apparent CO₂ permeance beyond the expected Knudsen value across the tested range of temperatures.

Table 5-1 Calculated activation energy for the permeation of different gaseous species through a C-SiO₂-ZrO₂ membrane regressed against Equation 2-1.

Gas	H ₂	CO ₂	N ₂	SF ₆
Activation energy [kJ mol ⁻¹]	5.96	0.55	-0.88	0.88

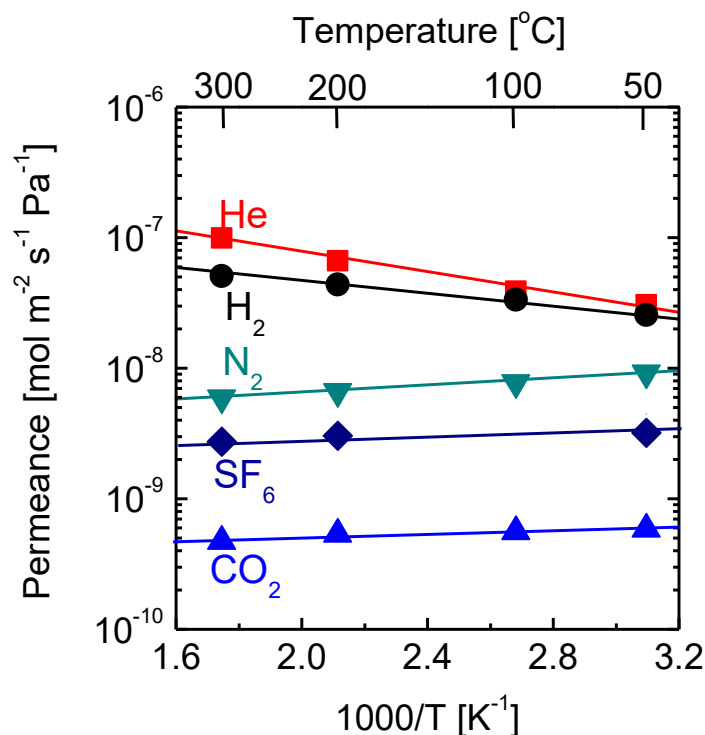


Fig. 5-12 Temperature dependence of single-gas permeance and permeance ratios at temperatures ranging from 50 to 300 °C for a C-SiO₂-ZrO₂ membrane prepared at 550 °C.

Establishing the flow transition of CO₂ presents an interesting phenomenon whereby a C-SiO₂-ZrO₂ membrane could switch the flow of CO₂ based on a pre-designed threshold pressure. It is rational to assume that the threshold pressure for the transition of CO₂ flow would depend on the average pore size of the C-SiO₂-ZrO₂ membrane. Fine-tuning the average pore size to pre-design a threshold switching pressure, however, is a subject for future investigation. To establish the recyclability of CO₂-flow switching and the reliability of a C-SiO₂-ZrO₂ membrane over time, 3 cycles of the sequential pressure dependence of CO₂ permeance at 200 and 500 kPa upstream pressures were carried out at 300 °C for 16 hours, as shown in Fig. 5-13. The two regimes of CO₂ flow before and after transition were perfectly repeatable over the 3 cycles without a significant difference in permeance. Also, N₂ permeation was carried out to further stress the fact that the flow-switching behavior is specific to CO₂. The permeance of N₂ remained the same at 200 and 500 kPa, which indicated no pressure dependence for N₂ permeation through the C-SiO₂-ZrO₂ membrane. Both experiments further verified that no defects were formed during this switching of the CO₂ flow.

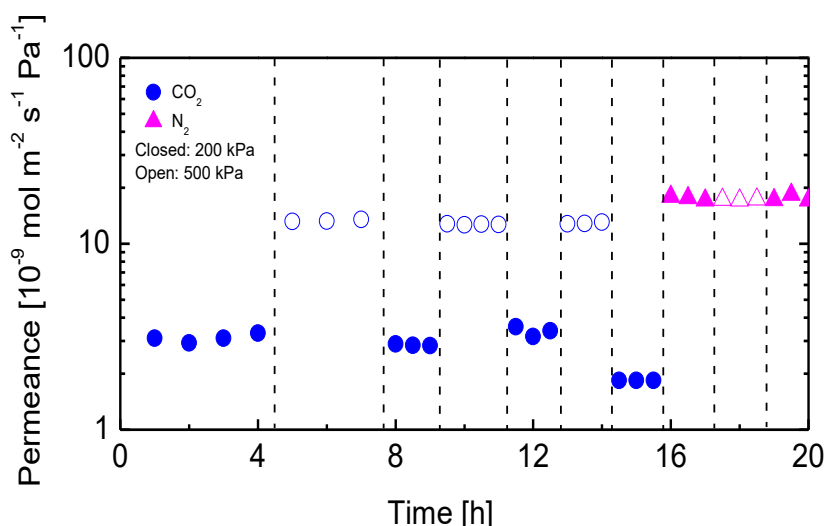


Fig. 5-13 Pressure-induced switching cycles of CO₂ flow represented by the time course of CO₂ and N₂ permeance under sequential pressurization at 200 and 500 kPa.

5.3.3 Binary H₂/CO₂ mixture separation performance of a C-SiO₂-ZrO₂-derived membrane

5.3.3.1 Effects of temperature, pressure, and CO₂ feed mole fraction on the binary mixture separation performance.

Fig. 5-14 (a) shows the values for the permeance of H₂ and CO₂ through a C-SiO₂-ZrO₂ membrane as a function of the CO₂ mole fraction in the feed (and by extension CO₂ upstream partial pressure) measured at 50 °C. At 50 °C and 200 kPa, H₂ and CO₂ permeance was decreased as the CO₂ mole fraction in the feed increased. This trend resembles that of silica membranes where the permeance of the adsorptive gas is expected to slightly increase as its mole fraction in the feed decreases [44]. The same trend was observed at 50 °C and 500 kPa. Fig. 5-14 (b) illustrates the separation of a binary gas mixture of H₂ and CO₂ at 300 °C. At 200 kPa, the permeance of H₂ maintained a high value of $7 \times 10^{-8} \text{ mol m}^{-2} \text{ s}^{-1} \text{ Pa}^{-1}$ up to a CO₂ mole fraction of 0.5 after which the permeance was reduced drastically to $4 \times 10^{-9} \text{ mol m}^{-2} \text{ s}^{-1} \text{ Pa}^{-1}$ at a CO₂ mole fraction of 0.8. At 500 kPa, however, only a slight decrease in H₂ permeance occurred even up to a CO₂ feed mole fraction of 0.8. This underscores the fact that at high values of both temperature and pressure, less CO₂ is adsorbed, and the pressure-induced multilayer diffusion of CO₂ presents less of a hindrance to the permeation of H₂, and, thereby, high H₂/CO₂ selectivity is maintained across all levels of CO₂ concentration.

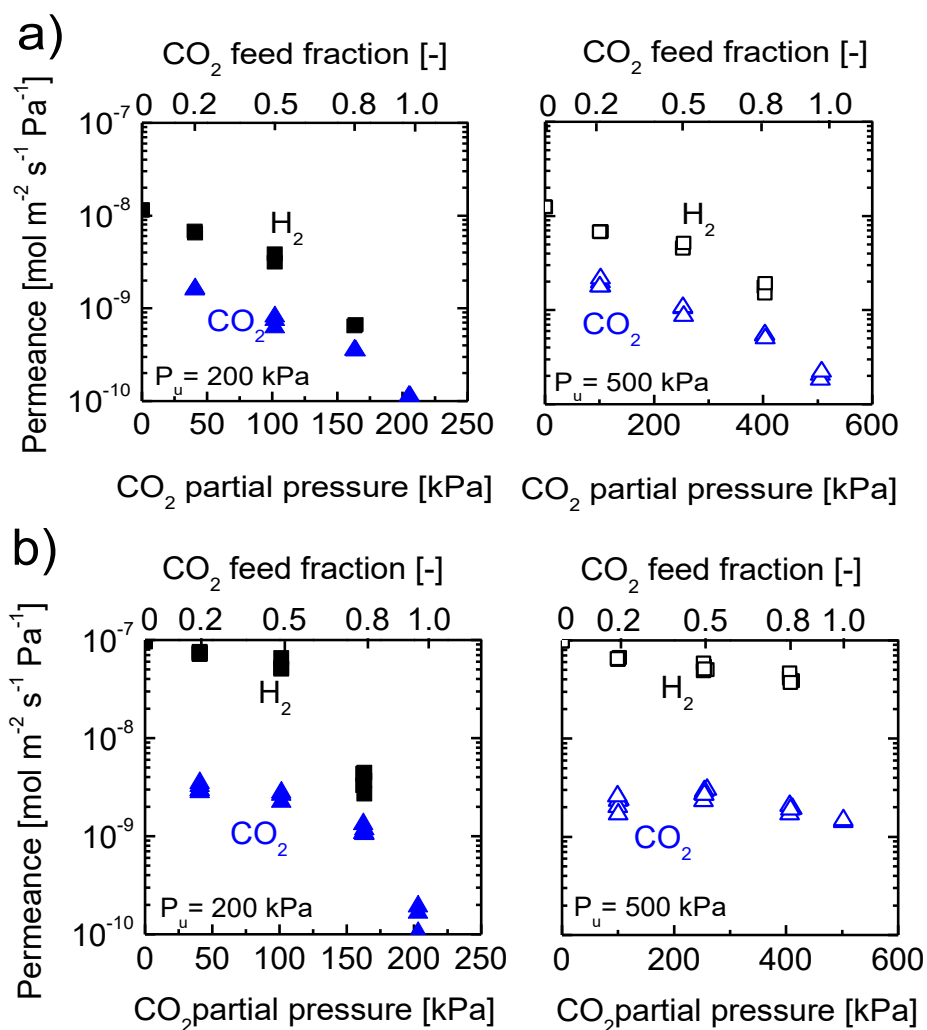


Fig. 5-14 Gas permeance as a function of CO₂ feed mole fraction and feed partial pressure at 50 °C (a) and 300 °C (b). Closed symbols: 200 kPa total upstream pressure; Open symbols: 500 kPa total upstream pressure.

As mentioned earlier in this section, the permeance increase as the concentration of CO₂ in the feed decreased was similar to that observed for silica membranes in a surface diffusion mechanism. The increases in CO₂ permeance shown in Fig. 5-14 (a) and (b), however, were more substantial. In addition, the permeance of the CO₂ in a binary mixture through the membrane was greater than that observed during single permeation at the same feed pressure. This can be explained by the fact that H₂ has a much higher flux than the slower permeating component CO₂, which exerts a ‘sweeping’ effect, and CO₂ is ‘swept’ along in the permeation paths. The same phenomenon was observed for a polypyrrolone membrane where the much slower permeating CH₄ molecules were ‘swept’ along by the much faster CO₂ molecules [45].

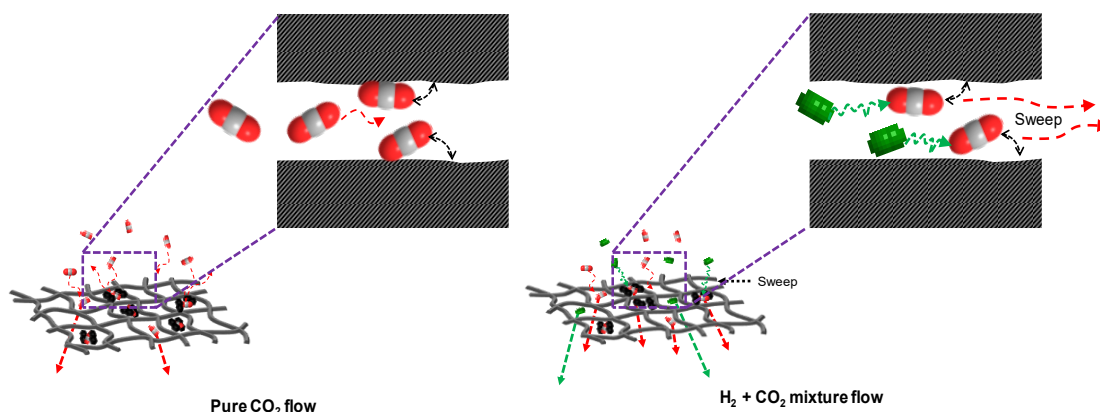


Fig. 5-15 Schematic illustration of the H₂ ‘sweeping’ effect on CO₂ permeation.

Such a ‘sweeping’ effect can be explained by considering the co-existence of two gas species with different molecular sizes and adsorptive tendencies moving through a common permeation path. The molecules of the fast and less-adsorptive permeating gas continually collide with the slow permeating and more-adsorptive gas molecules and therefore displace them from the adsorbent surface thereby increasing the gas phase flow of the adsorbate gas molecules. Fig. 5-15 features a schematic illustration of the effect of H₂ presence on the adsorption-flux balance of CO₂ through C-SiO₂-ZrO₂ membrane pores. In the case of a binary mixture of H₂ and CO₂ gases, faster H₂ molecules sweep slower CO₂ molecules and therefore there is a considerable contribution of CO₂ to the overall bulk phase transport of the gas mixture. The fraction of the bulk mass flux contributed by each component in the gas mixture can be calculated based on a set of equations presented by Kamaruddin and Koros [45], which compares to the gas-phase flux in single-gas permeation systems. When these equations were applied to single and binary H₂/CO₂ systems at 300 °C and 500 kPa, the results revealed that the fraction of the bulk-phase flux contribution by CO₂ is much higher in the permeation of a gas mixture than in that of pure CO₂ as shown in Fig. 5-16, which was predicted by Kamaruddin and Koros [45].

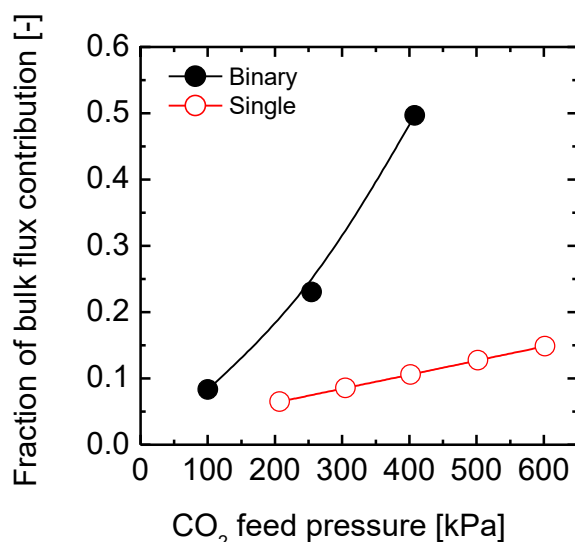


Fig. 5-16 Calculated fraction of the CO₂ bulk flux contribution at 300 °C as a function of the CO₂ feed pressure in single and binary systems (at total $P_u = 500$ kPa).

5.3.4 Outlook on the practical application of a C-SiO₂-ZrO₂ membrane for H₂/CO₂ separation.

There are reports of membranes that separate H₂ and CO₂ by utilizing strong CO₂ adsorption to create reverse CO₂/H₂ permselectivity at low temperature [46]. In this process, the more adsorptive CO₂ molecules permeate at the expense of blocked non-adsorptive H₂ molecules. In these membranes, as permeation temperature increases, molecular sieving properties dominate and achieve a level of H₂ permselectivity that is suitable for high-temperature applications such as steam methane reforming/water-gas shift reactions (SMR/WGS) and the integrated gasification combined cycle (IGCC). In the present work, however, the molecular sieving properties at 300 °C with 200 kPa of upstream pressure seemed inadequate to achieve sufficient H₂ permselectivity across all CO₂ concentrations due to persistent CO₂ blocking. This is a drawback for practical and versatile high-temperature applications. This drawback is eliminated with a high pressure of 500 kPa where high H₂ permselectivity can be achieved across various CO₂ concentrations, as Fig. 5-14 (b) shows. For practical high-temperature, high-pressure H₂/CO₂ separation purposes where membrane versatility may be of paramount importance as a result of fluctuating CO₂ concentrations, a C-SiO₂-ZrO₂ membrane could be useful. Fig. 5-17 compares the H₂ permeance-H₂/CO₂ mixture selectivity trade-off of high-temperature separation membranes (details in Table 5-2). Most of the high-temperature H₂/CO₂ separation

membranes include a range of versions from zeolitic to ceramic that achieve separation by means of molecular sieving (size exclusion of CO₂) of a 1:1 binary H₂-CO₂ mixture. Thus, it would be a novel occurrence to achieve comparable separation (good H₂ permeance-H₂/CO₂ selectivity trade-off) with a CO₂ adsorptive-type membrane across several H₂-CO₂ mixture ratios. Fig. 5-17 clearly shows that C-SiO₂-ZrO₂ membranes can achieve a separation performance that is comparable to many molecular sieving membranes at high temperatures even with most CO₂-concentrated feed stock. This ability is a result of the pressure-induced transition of CO₂ flow in C-SiO₂-ZrO₂ membranes (as previously established), which results in less hindrance to the flow of H₂ and promotes activated H₂ permeation.

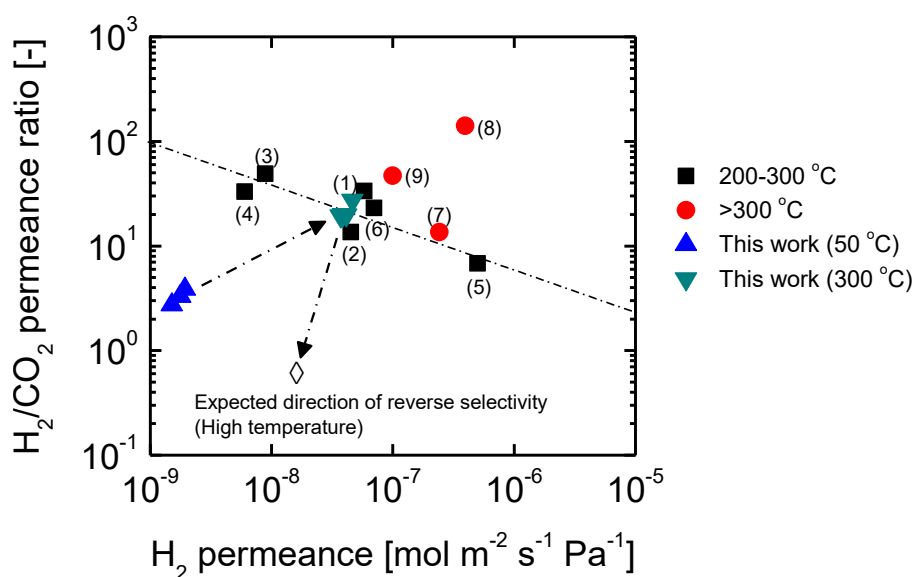


Fig. 5-17 Trade-off plot of H₂/CO₂ mixture selectivity versus H₂ permeance values for different high-temperature separation membranes

Table 5-2. Comparison of H₂ permeance-H₂/CO₂ mixture selectivity trade-off of high-temperature H₂/CO₂ separation membranes

No.	Membrane type	H ₂ permeance [10 ⁻⁸ mol m ⁻² s ⁻¹ Pa ⁻¹] 1]	α (H ₂ /CO ₂) [-]	Reference
200-300 °C				
1	Zeolite (SAPO-34)	7	23	[47]
2	ZIF-7	4.5	13.6	[48]
3	Zeolite (B-ZSM-5)	0.6	33	[49]
4	SiC	0.89	49	[50]
5	Si	50	6.8	[51]
6	Pd-organosilica	5.8	33.5	[52]
>300 °C				
7	SiO ₂ -TiO ₂	24.2	13.6	[53]
8	MFI-type Zeolite	39.6	141	[54]
9	Zeolite (B-ZSM-5)	10	47	[49]
300 °C, 500 kPa				
	C-SiO ₂ -ZrO ₂	7	20-30	This work

α - selectivity

5.4 Conclusions

In this work we set out to investigate the possible unique properties that could evolve during the in-situ carbonization of acetylacetonate ligands in a SiO₂-ZrO₂ network and the resultant contribution to H₂/CO₂ separation. The in-situ carbonization of SiO₂-ZrO₂-acac to C-SiO₂-ZrO₂ was confirmed by TG-

MS, DTG-TGA, FT-IR, CP/DD-MAS-¹³C-NMR, and TEM. The carbon content in C-SiO₂-ZrO₂ promoted the adsorption of CO₂, which resulted in a maximum heat of adsorption at 290 kJ mol⁻¹ and provided energy sufficient to allow the carbon layers in C-SiO₂-ZrO₂ to conform to the CO₂ molecules. This development revealed that CO₂ could be trapped. The CO₂ permeance of the C-SiO₂-ZrO₂ membrane demonstrated a significant level of dependence on the feed pressure, but little dependence on either temperature or the CO₂ feed concentration under conditions of 300 °C and 500 kPa, which allowed for an interesting separation performance when used in binary H₂/CO₂ systems. The C-SiO₂-ZrO₂ membrane achieved a H₂/CO₂ separation performance comparable to molecular sieving membranes irrespective of the CO₂ feed content. In this study, we fabricated a two-parameter CO₂-switchable ceramic membrane. The switching parameters were the feed side pressure and the use of a fast permeating gas component.

Cited literature

1. D. S. Sholl, R. P. Lively, Seven chemical separations to change the world, *Nature*, 532 (2016) 435-437
2. R. W. Rousseau, *Handbook of separation process technology*, John Wiley and Sons, New York, 1987
3. S. Adhikari, S. Fernando, Hydrogen membrane separation techniques, *Ind. Eng. Chem. Res.*, 45 (2006) 875-881
4. Y. Chang, J. Lee, H. Yoon, Alternative projection of the world energy consumption-in comparison with the 2010 international energy outlook, *Energ. Policy*, 50 (2012) 154-160
5. E. A. Abdelaziz, R. Saidur, S. Mekhilef, A review on energy saving strategies in industrial sector, *Renew. Sust. Energ. Rev.*, 15 (2015) 150-168
6. N. W. Ockwig, T. M. Nenoff, Membranes for hydrogen separation, *Chem. Rev.* 107 (2007) 4078-4110
7. H. Li, Z. Song, X. Zhang, Y. Huang, S. Li, Y. Mao, H. J. Ploehn, Y. Bao, M. Yu, Ultrathin, molecular-sieving graphene oxide membranes for selective hydrogen separation, *Science*, 342 (2013) 95-98
8. T. Ji, Y. Sun, Y. Liu, M. Li, F. Wei, L. Liu G. He, Y. Liu, Facile in situ hydrothermal synthesis of layered zirconium phenylphosphonate molecular

- sieve membranes with optimized microstructure and superb H₂/CO₂ selectivity, *Acs. Appl. Mater. Inter.*, 2020, DOI: 10.1021/acsami.0c02789
9. M. Kanezashi, D. Fuchigami, T. Yoshioka, T. Tsuru, Control of Pd dispersion in sol-gel-derived amorphous silica membranes for hydrogen separation at high temperatures, *J. Membr. Sci.* 439 (2013) 78-86
 10. S-J. Ahn, A. Takagaki, T. Sugawara, R. Kikuchi, S. T. Oyama, Permeation properties of silica-zirconia composite membranes supported on porous alumina substrates, *J. Membr. Sci.* 526 (2017) 409-416
 11. E. Shoko, B. McLellan, A. L. Dicks D. da Costa, Hydrogen from coal: production and utilization technologies, *Int. J. Coal Geo.*, 65 (2006) 213-222
 12. P. P. Edwards, V. L. Kuznetsov, W. I. F. David, N. P. Brandon, Hydrogen and fuel cells: towards a sustainable energy future, *Energ. Policy*, 36 (2008) 4356-4362
 13. C. Acar and I. Dincer, Comparative assessment of hydrogen production methods from renewable and non-renewable sources, *Int. J. Hydrogen Energ.*, 39 (2014) 1-12
 14. C. Acar and I. Dincer, I., Review and evaluation of hydrogen production methods for better sustainability *Int. J. Hydrogen Energ.*, 40 (2015) 11094-11111
 15. D. R. Simbeck, Hydrogen costs with CO₂ capture. Presented at the 7th international conference on greenhouse gas control technologies (GHGT-7), Vancouver, British Columbia, Canada, September 6–10; 2004
 16. A. P. Simpson and A. E. Lutz, Exergy analysis of hydrogen production via steam methane reforming, *Int. J. Hydrogen Energ.*, 32 (2007) 4811-4820
 17. L. Barelli, G. Bidini, F. Gallorini and S. Servili, Hydrogen production through sorption-enhanced steam methane reforming and membrane technology: a review, *Energ.*, 33 (2008) 554-570
 18. A. K. Ku, P. Kulkarni, R. Shisler and W. Wei, Membrane performance requirements for carbon dioxide capture using hydrogen-selective membranes in integrated gasification combined cycle (IGCC) power plants, *J. Membr. Sci.*, 367 (2011) 233-239
 19. J. J. Stanislawski, M. J. Holmes, A. C. Snyder, S. G. Tolbert and T. J. Curran, Advanced CO₂ separation technologies: coal gasification, warm-gas cleanup, and hydrogen separation membranes, *Energ. Procedia*, 37 (2013) 2316-2326

20. S. C. A. Kluiters, presented under the 5th Research Framework Programme of European Union, Intermediate report EU project MIGREYD NNE5-2001-670, Petten, December 2004
21. S. Kitagawa and K. Uemura, Dynamic porous properties of coordination polymers inspired by hydrogen bonds, *Chem. Soc. Rev.*, 34 (2005) 109-119
22. J. T. Culp, M. R. Smith, E. Bittner and B. Bockrath, Hysteresis in the physisorption of CO₂ and N₂ in a flexible pillared layer nickel cyanide, *J. Am. Chem. Soc.*, 130 (2008) 12427-12434
23. C. A. Fernandez, P. K. Thallapally, R. K. Motkuri, S. K. Nune, J. C. Sumrak, J. Tian and J. Liu, Gas-induced expansion and contraction of a fluorinated meta-organic framework, *Crys. Growth Des.*, 10 (2010) 1037-1039
24. A. Boutin, F.-X. Coudert, M.-A. Springuel-Huet, A. V. Neimark, G. Férey and A. H. Fuchs, The behavior of flexible MIL-53(Al) upon CH₄ and CO₂ adsorption, *J. Phys. Chem. C*, 114 (2010) 22237-22244
25. J. van den Bergh, C. Gücüyener, E. A. Pidko, E. J. M. Hensen, J. Gascon and F. Kapteijn, Understanding the anomalous alkane selectivity of ZIF-7 in the separation of light alkane/alkene mixtures, *Chem. Eur. J.*, 17 (2011) 8832-8840
26. J. Wang, J. Luo, J. Zhao, D.-S. Li, G. Li, Q. Huo and Y. Liu, Assembly of two flexible metal-organic frameworks with stepwise gas adsorption and highly selective CO₂ adsorption, *Crys. Growth Des.*, 14 (2014) 2375-2380
27. Z.-J. Li, J. Lu, M. Hong and R. Cao, Metal-organic frameworks based on flexible ligands (FL-MOFs): structures and applications, *Chem. Soc. Rev.*, 43 (2014) 5867-5895
28. G. A. Craig, P. Larpent, S. Kusaka, R. Matsuda, S. Kitagawa and S. Furukawa, Switchable gate-opening effect in metal-organic polyhedral assemblies through solution processing, *Chem. Sci.*, 9 (2018) 6463-6469
29. K. Yoshida, Y. Hirano, H. Fujii, T. Tsuru, M. Asaeda, Hydrothermal stability and performance of silica-zirconia for hydrogen separation in hydrothermal conditions, *J. Chem. Eng. Jpn.* 34 (2001) 523-530.
30. S. Lawal, M. Kanezashi, H. Nagasawa, T. Tsuru, Development of an acetylacetonate-modified silica-zirconia membrane applicable to gas separation, *J. Membr. Sci.* 599 (2020) 117844

31. R. R. Dagastine, D. C. Prieve and L. R. White, Calculations of van der Waals forces in 2-dimensionally anisotropic materials and its application to carbon black, *J. Colloid Interf. Sci.*, 249 (2002) 78-83
32. M. C. Duke, J. C. Diniz da Costa, D. D. Do, P. G. Gray, G. Q. Lu, Hydrothermally robust molecular sieve silica for wet gas separation, *Adv. Funct. Mater.* 16 (2006) 1215-1220
33. M. C. Duke, J. C. Diniz da Costa, G. Q. Lu, M. Petch, P. G. Gray, Carbonized template molecular sieve silica membranes in fuel processing systems: permeation, hydrostability and regeneration, *J. Membr. Sci.* 241 (2004) 325-333
34. W. Puthai, M. Kanezashi, H. Nagasawa, K. Wakamura, H. Ohnishi, T. Tsuru, Effect of firing temperature on water permeability of SiO₂-ZrO₂ membranes for nanofiltration, *J. Membr. Sci.* 497 (2016) 348-356.
35. X. Tao, W. Qiu, H. Li, T. Zhao, Synthesis of nanosized zirconium carbide from preceramic polymers by the facile one-pot reaction, *Polym. Adv. Technol.*, 21 (2010) 300-304
36. K. Ikeya and A. Watanabe, Application of ¹³C ramp CPMAS NMR with phase-adjusted spinning sidebands (PASS) for the quantitative estimation of carbon functional groups in natural organic matter, *Anal. Bioanal. Chem.*, 408 (2016) 651-655
37. J. C. C. Freitas, F. G. Emmerich, G. R. C. Cernicchiaro, L. C. Sampaio and T. J. Bonagamba, Magnetic susceptibility effects on ¹³C MAS NMR spectra of carbon materials and graphite, *Solid State Nucl. Mag.*, 20 (2001) 61-73
38. D. Pan, J. Zhang, Z. Li, C. Wu, X. Yan and M. Wu, Observation of pH-, solvent-, spin-, and excitation-dependent blue photoluminescence from carbon nanoparticles, *Chem. Commun.*, 46 (2010) 3681-3683
39. S. C. Xu, S. Irle, D. G. Musaev and M. C. Lin, Quantum chemical prediction of reaction pathways and rate constants for dissociative adsorption of CO_x and NO_x on the graphite (0001) surface, *J. Phys. Chem. B*, 110 (2006) 21135-21144
40. D. D. L. Chung, Graphite, *J. Mat. Sci.*, 37 (2002) 1475 – 1489
41. B. A. McCool, N. Hill, J. DiCarlo and W. J. DeSisto, Synthesis and characterization of mesoporous silica membranes via dip-coating and hydrothermal deposition techniques, *J. Membr. Sci.*, 218 (2003) 55–67

42. S. Barma, and B. Mandal, Synthesis and characterization of ordered mesoporous silica membrane: role of porous support and gas permeation study, *Micr. Meso. Mater.*, 210 (2015) 10-19
43. J.-G. Choi, D. D Do and H. D. Do, Surface diffusion of adsorbed molecules in porous media: monolayer, multilayer, and capillary condensation regimes, *Ind. Eng. Chem. Res.*, 40 (2001) 4005-4031
44. M. Kanezashi, W. N. Shazwani, T. Yoshioka and T. Tsuru, Separation of propylene/propane binary mixtures by bis(triethoxysilyl) methane (BTESM)-derived silica membranes fabricated at different calcination temperatures, *J. Membr. Sci.*, 415-416 (2012) 478-485
45. H. D. Kamaruddin, and W. J. Koros, Some observations about the application of Fick's first law for membrane separation of multicomponent mixtures, *J. Membr. Sci.*, 135 (1997) 147-159
46. M. Hong, S. Li, J. L. Falconer and R. D. Noble, Modification of zeolite membranes for H₂ separation by catalytic cracking of methyldiethoxysilane, *J. Membr. Sc.*, 307 (2008) 277-283
47. M. Yu, H. Funke, R. D. Noble and J. L. Falconer, H₂ separation using defect-free, inorganic composite membranes, *J. Am. Chem. Soc.*, 133 (2011) 1748-1750
48. A. Huang, Y. Chen, Q. Liu, N. Wang, J. Jiang and J. Caro, Synthesis of highly hydrophobic and permselective metal-organic-framework Zn(BDC)(TED)_{0.5} membranes for H₂/CO₂ separation, *J. Membr. Sci.*, 454 (2014) 126-132
49. M. Hong, J. L. Falconer and R. D. Noble, Modification of zeolite membranes for H₂ separation by catalytic cracking of methyldiethoxysilane, *Ind. Eng. Chem. Res.*, 44 (2005) 4035-4041
50. B. Elyassi, M. Sahimi and T. T. Tsotsis, Silicon carbide membranes for gas separation applications, *J. Membr. Sci.*, 288 (2007) 290-297
51. R. M. de Vos and H. Verweij, High-selectivity, high-flux silica membranes for gas separation, *Science*, 279 (1998) 1710-1712
52. J. Lei, H. Song, Y. Wei, S. Zhao and H. Qi, A novel strategy to enhance hydrothermal stability of Pd-doped organosilica membrane for hydrogen separation, *Micr. Meso. Mater.*, 253 (2017) 55-63

53. Y. Gu and S. T. Oyama, Permeation properties and hydrothermal stability of silica-titania membranes supported on porous alumina substrates, *J. Membr. Sci.*, 345 (2009) 267-275
54. Z. Tang, J. Dong and T. M. Nenoff, Internal surface modification of MFI-type zeolite membranes for high selectivity and high flux of hydrogen, *Langmuir*, 25 (2009) 4848-4852

Chapter 6

Conclusions and considerations for further studies

6.1 Summary and conclusions

To summarize, the microporous structure and properties of a SiO₂-ZrO₂ composite has been tailored in 3 major ways:

1. The chemical modification of the transition metal component, Zr, by chelating with acetylacetonate ligand. This ligand performed two functions of arresting the hydrolysis rate of the Zr precursor and modifying the network of the resulting SiO₂-ZrO₂ composite.
2. By utilizing unsaturated Si precursor (3-(trimethoxysilyl)propyl methacrylate-MAPTMS) in combination with acetylacetonate (ACAC) or allyl acetoacetate (AAA), it was possible to crosslink the unsaturated moieties via a thermal radical polymerization.
3. The carbonization of the SiO₂-ZrO₂ composite by pyrolyzing acetylacetonate-modified SiO₂-ZrO₂. The effect of acetylacetonate concentration and Si/Zr ratio were investigated.

Thus, the major conclusions derived from these studies can be summarized into 4 items:

(i) Acetylacetonate-modified SiO₂-ZrO₂-derived membrane showed H₂ permeance of 9.9×10^{-7} with a H₂/SF₆ permeance ratio of 7,600, which was better than the results when using a pure SiO₂-ZrO₂-derived membrane (H₂ permeance: 1.4×10^{-6} mol m⁻² s⁻¹ Pa⁻¹, H₂/SF₆ permeance ratio: 11). When an acac⁻-modified SiO₂-ZrO₂-derived membrane prepared at 250 °C (H₂ permeance: 1.8×10^{-7} mol m⁻² s⁻¹ Pa⁻¹, H₂/CH₄: 100, CO₂/CH₄: 60 at 50 °C) was heat-treated at 550 °C, the result was improved H₂ permeance of 5.2×10^{-6} mol m⁻² s⁻¹ Pa⁻¹ with low permeance ratios (H₂/CH₄: 3, H₂/SF₆: 9) at 50 °C. The 250 °C-fired acac⁻-modified SiO₂-ZrO₂-derived membranes exhibited a gas permeation mechanism similar to polymer membranes, and the 300 °C-heat-treated version showed the best trade-off between H₂ permeance and the H₂/SF₆ permeance ratio.

(ii) SiO₂-ZrO₂-based organically crosslinked hybrid membranes were fabricated via the sol-gel crosslinking of ligand (AAA or ACAC)-chelated zirconium oxide networks and MAPTMS derived siloxane networks. The AAA-chelated system generated a copolymerization crosslinking with the Si precursor while the ACAC-chelated system generated only a homopolymerization within MAPTMS. New pore structures were formed as organic crosslinked materials showed a significant increase in measured BET surface areas (OCL-AAA: $\approx 320 \text{ m}^2 \text{ g}^{-1}$, OCL-ACAC: $\approx 40 \text{ m}^2 \text{ g}^{-1}$) compared with non-crosslinked samples ($< 1 \text{ m}^2 \text{ g}^{-1}$). The organic crosslink-derived membranes showed better molecular sieving properties with higher H₂/N₂ selectivity (OCL-AAA: 33, OCL-ACAC: 20) compared with non-crosslink-derived membranes (H₂/N₂ selectivity; NCL-AAA: 11, NCL-ACAC: 7). Finally, organic crosslink-derived membranes showed a change in microstructural properties from a flexible to a rigid structure that ranged between that of silica-rich materials and polymer materials. Considering that a facile method was established to fabricate and tune the microstructure of supported class II hybrid inorganic-organic highly permeable membranes, this study should serve as a template for future work where tailored network tuning and functionalization can be achieved for specific applications.

(iii) An attempt was made to derive the best sol synthesis and chemo-structural parameters necessary for the fabrication of carbon-SiO₂-ZrO₂ (CSZ) composite membranes by pyrolysis of a SiO₂-ZrO₂-ACAC (SZA) composite at 550 °C in N₂ atmosphere. The hydrolysis water/alkoxide molar ratio (WR) and relative Si/Zr atomic ratios were chosen as study parameters. The effects of water/alkoxide molar ratios of 4, 60 and 240 as well as the Si/Zr atomic ratios were studied and optimized. The most suitable WR to maintain the balance between carbon nanoparticles retention, amorphousness and microporosity is water/alkoxide molar ratio of 60. Also using Si/Zr ratios of 9/1, 7/3, 5/5 and 3/7, CSZ9/1 membrane showed the best H₂-permselectivity with H₂ permeance of $16 \times 10^{-7} \text{ mol m}^{-2} \text{ s}^{-1} \text{ Pa}^{-1}$ and H₂/N₂ and H₂/CH₄ ideal selectivities of 75 and 148, respectively. Therefore, the best combination of parameters is a WR of 60 applied to prepare a carbon-SiO₂-ZrO₂ composite containing a relative Si/Zr of 9/1 which showed improved H₂-permselectivity over a pure unmodified SiO₂-ZrO₂ containing a similar Si/Zr ratio and similar distribution of the small pores. This was attributed to the increased pore volume afforded by the

carbon nanoparticles through ultra-micropores inherent in them. It is therefore resolved that the densification of silica at elevated temperatures can be ameliorated by a combination of ZrO₂ composition and a carbonization of the resulting composite.

(iv) A carbon-SiO₂-ZrO₂ (CSZ) with Si/Zr ratio of 5/5 was further investigated. The carbon content in C-SiO₂-ZrO₂ promoted the adsorption of CO₂, which resulted in a maximum heat of adsorption at 290 kJ mol⁻¹ and provided energy sufficient to allow the carbon layers in C-SiO₂-ZrO₂ to conform to the CO₂ molecules. This development revealed that CO₂ could be trapped. The CO₂ permeance of the C-SiO₂-ZrO₂ membrane demonstrated a significant level of dependence on the feed pressure, but little dependence on either temperature or the CO₂ feed concentration under conditions of 300 °C and 500 kPa, which allowed for an interesting separation performance when used in binary H₂/CO₂ systems. The C-SiO₂-ZrO₂ membrane achieved a H₂/CO₂ separation performance comparable to molecular sieving membranes irrespective of the CO₂ feed content.

6.2 Considerations for further studies

So far, the studies undertaken during this research period, as pointed out earlier, have focused on ligand modification of ceramic composite, microstructural engineering of such modified composites by choosing specific network forming ligands and carbonization of the composite by pyrolysis. Based on the results and the conclusions drawn therefrom, the following considerations are put forward as future study subjects.

1. Ligand-ceramic composites from network-forming and functional moieties

In chapter 3, allyl acetoacetate as a network forming ligand was used in conjunction with an unsaturated Si precursor for the microstructural engineering of the ligand modified SiO₂-ZrO₂ composite. This microstructural tuning improved the molecular sieving and predictability of the network pore distribution. For future studies, the selection of a functional group bearing Si precursor is suggested in addition to the network forming Si precursor (MAPTMS) so that a combination of network engineering and functional interaction with permeating species could be explored. Suggested precursors and their potential functional behavior include

- (i) Phenyltriethoxysilane- PTEOS (hydrophobicity)
- (ii) Aminopropyltrimethoxysilane- APTMOS (hydrophilicity or CO₂ affinity)
- (iii) Tridekafluoro-tetrahydrooctyltriethoxysilane-TDFTHOTEOS (oleophobicity)

2. Formation of carbon-ceramic composites from thermosetting organic modifiers

The carbonization of SiO₂-ZrO₂ composites and the application to the formation of gas separation membranes were explored in chapters 4 and 5. One major challenge with carbonization by pyrolysis was the difficulty in preventing defect formation during pyrolysis. The thermal stability of the ligands employed were low allowing the material to lose a lot of mass at the final carbonization temperatures. Therefore, it is suggested that thermally stable and thermosetting organic ligands be employed for the modification of ceramic composites. Based on chapter 5, by retaining a very high amount of residual carbon in the carbon-ceramic composite, high-pressure CO₂/N₂ and CO₂/CH₄ separations could be possible.

In conclusion, ligand-ceramic combinations offer a lot of opportunities for the development of new membrane types that can be applied to a variety of needs.

List of publications

Journal articles

1. **Sulaiman Lawal**, Masakoto Kanezashi, Hiroki Nagasawa, Toshinori Tsuru, Development of an acetylacetonate-modified silica-zirconia composite membrane applicable to gas separation, *J. Membr. Sci.*, 599 (2020) 117844 (p.1-11)
2. **Sulaiman Lawal**, Liang Yu, Hiroki Nagasawa, Toshinori Tsuru, Masakoto Kanezashi, A carbon-silica-zirconia ceramic membrane with CO₂ flow switching behavior promising versatile high-temperature H₂/CO₂ separation, *J. Mater. Chem. A*, 8 (2020) 23563-23573
3. **Sulaiman Lawal**, Hiroki Nagasawa, Toshinori Tsuru, Masakoto Kanezashi, Facile development of microstructure-engineered, ligand-chelated SiO₂-ZrO₂ composite membranes for molecular separations, *Mol. Syst. Des. Eng.*, 6 (2021) 429-444
4. **Sulaiman Lawal**, Hiroki Nagasawa, Toshinori Tsuru, Masakoto Kanezashi, Enhancement of the H₂-permselectivity of a silica-zirconia composite membrane enabled by ligand-ceramic to carbon-ceramic transformation, *J. Membr. Sci.*, *Under review*, (July 2021)

Conferences

1. **Sulaiman Lawal**, Masakoto Kanezashi, Hiroki Nagasawa, Toshinori Tsuru, Effect of zirconium-acetylacetonate chelation on the molecular sieving properties of a SiO₂-ZrO₂ composite membrane, The 16th International Conference on Inorganic membranes (ICIM16), Taipei, Taiwan (Notification of acceptance on 2/27/2020), 2020/06/29–07/02
2. **Sulaiman Lawal**, Liang Yu, Hiroki Nagasawa, Toshinori Tsuru, Masakoto Kanezashi, Fabrication of a carbon-functionalized silica-zirconia ceramic membrane with pressure-induced CO₂ flow switching, The Membrane Society of Japan Membrane Symposium 2020 (Online Zoom platform), 2020/11/12-13

Acknowledgements

Alhamdulillah! I must first and foremost thank Allah, the Almighty, the Wise. Despite my many shortcomings in His worship and commands, He (Allah) has seen me through 3 years of rigorous studies and has held me up at trying times. There is no amount of gratitude I can express that comes close to appreciating His Mercies on me.

I must also thank my parents (**Alhaji Abdurrauf and Mrs. Kifayat Lawal**) who have shown me great understanding, love and support throughout my life. Between us they know when the goings were tough, and they were there to encourage and motivate me to keep pushing for my life goals. I am very glad that they are both alive to see me complete a major milestone in my life and see me accomplish the goals they have dreamt for me in their daily struggles. I cannot acknowledge them enough and I love them both for the sake of Allah.

Next, to my teachers, many of whom I have had since coming to Japan. I must first thank immensely **Professor Masakoto Kanezashi** who showed belief by accepting me to undertake a doctorate under his supervision despite having no concrete research background in the field of membrane science and technology. I would also like to appreciate the very kind, jovial and astute guidance of our head, **Professor Toshinori Tsuru**. He always has a positive outlook towards everything, and this quality is what drives the Separation and Technology laboratory at Hiroshima University. **Professor Hiroki Nagasawa** has also been very helpful for my daily life. He is down-to-earth and always ready to talk and be of help. I definitely could not have asked for any better research group to work with.

It would be very criminal to forget to mention the family of students in the Separation and Technology laboratory at Hiroshima University both past and present. I would like to appreciate the help of **Dr. Liang Yu** (now back in China at the Beijing Institute of Technology) who was always ready to discuss the progress of my work. He always created time to listen to me and give very enlightening advise and insights. He certainly is one of the smartest people I have met. I would also like to appreciate **Dr. Sofiatun Anisah** who was the person that taught me my first experimental works and showed patience towards me. The Japanese students have been of immense help to me throughout my stay in this laboratory and for my daily life. I would like to

particularly mention **Norihiro Moriyama**, **Naoya Hataoka** (my student guide), **Mari Takenaka** (she helped me so much sometimes I am ashamed of asking for more help), **Kenta Nakahiro**, **Kenta Watanabe**, **Takahiro Nagaoka**, **Mitsugu Kawasaki** and others that have shown me friendship over the years.

I also want to appreciate the Japanese government through the **Ministry of Education, Culture, Sports, Science and Technology (MEXT)** for providing me with the scholarship to study and live in Japan for three years and a half. I also want to mention the kind help of the Japanese Embassy and Ambassador in Nigeria for providing the required guidance during the scholarship application processes.

Last but definitely not the least, I want to appreciate and acknowledge my darling wife **Basirat Mojisola Ayinde** for being my companion through this journey. You have certainly made living in Japan a whole lot easier for me, and I would not have achieved many things if not for your understanding, strength and love. I have many a thing to apologize for, but I hope that you would overlook my faults. You are very strong, dedicated and caring. You gave birth to our son **Hudhayfah** with no family to assist us, you bathed him and fed him everyday for the past 18 months while also pursuing your doctorate degree. If that is not strength, I do not know what is. Thank you very much. JazaakiLlahu khayr! I love you very much.

Thank you all.